TESIS DE LA UNIVERSIDAD DE ZARAGOZA

2025 165

Nicoll Paulina Zeballos Lema

Site-directed immobilization of enzymes through surface engineering

Director/es
López Gallego, Fernando

ISSN 2254-7606

Prensas de la Universidad
Universidad Zaragoza

Universidad de Zaragoza
Servicio de Publicaciones

ISSN 2254-7606

Universidad Zaragoza
1542

Tesis Doctoral

SITE-DIRECTED IMMOBILIZATION OF ENZYMES THROUGH SURFACE ENGINEERING

Autor

Nicoll Paulina Zeballos Lema

Director/es

López Gallego, Fernando

UNIVERSIDAD DE ZARAGOZA
Escuela de Doctorado

Programa de Doctorado en Bioquímica y Biología Molecular

2023

Universidad Zaragoza
1542

Tesis Doctoral

SITE-DIRECTED IMMOBILIZATION OF ENZYMES THROUGH SURFACE ENGINEERING

Autor

Nicoll Paulina Zeballos Lema

Director/es

López Gallego, Fernando

UNIVERSIDAD DE ZARAGOZA
Escuela de Doctorado

Programa de Doctorado en Bioquímica y Biología Molecular
2023

Site-directed immobilization of enzymes through surface engineering

To obtain the degree of PhD in

Biochemistry and Molecular Biology

at the University of Zaragoza

Nicoll Paulina Zeballos Lema

2023

Thesis Supervisor:

Dr. Fernando López Gallego

Heterogeneous Biocatalysis Group, CIC biomaGUNE. San Sebastian (Spain)

University tutor:

Dr. Ramón Hurtado Guerrero

ARAID researcher at University of Zaragoza. Zaragoza (Spain)

Table of Contents

Index of figures

Index of table

Index of equations

List of abbreviations

3

3MB. 3-methyl-1-butanol

3MBA. 3 methyl-butylamine

A

AFM. alternating magnetic field

AG. Agarose microbeads

B

BSA. Albumin bovine serum standard

BsADH-H2.. Bs-ADH-Q8H/E11H

BsADH-H2-B. BsADH-E265H/E266H

BsADH-H3.. Bs-ADH-Q8H/K10H/E11H

BsADH-H4.. Bs-ADH-Q8H//E11H/E265H/E266H

BsADH-WT.. BsADH native with 6x histidines

C

C-ADH. Cohesin-ADH

CD. Circular-Dichroism

CLSM. 3.2.11 Confocal Laser Scanning Microscopy

Coh. Cohesin

COREX/BEST. Biology using Ensemble-based Structural Thermodynamics

D

DCM. Dichloromethane

D-ECFP-D. Dockerin-Enhanced cyan fluorescent protein-Dockerin

DF. Dilution factor

DMSO. Dimethyl sulfoxide

dNTPs. Deoxynucleotide triphosphates

Doc. Dockerin

DSF. Differential scanning fluorimetry

D-ωTA-D. Dockerin-ω-Transaminase-Dockerin

E

Ea. activation energy

EAA. Ethyl acetoacetate, ethyl acetoacetate

F

FAD^{+}. Flavin-adenine-dinucleotide sodium salt

FID. flame ionization detector

FTIC. Fluorescein isothiocyanate

FWHM. Full width half maximum

G

GC. Gas chromatography

GPMES. (3-glycidyloxypropyl) trimethoxysilane

H

Hd. High density

HdAG. High density agarose microbeads

His-BpCAT-C. Catalase from *Bordetella pertussis* with a 6xHistidine-tag at N-terminus and the cohesin at C-terminus

HPLC. High performance liquid chromatography

HSAB. Hard and soft acids and bases

I

ICQ. *in*tensity correlation coefficient

IDA. Iminodiacetic acid, iminodiacetate

IMAC. Immobilized metal-affinity chromatography

IPA. Isopropanol

IPTG. Isopropyl-β-D-thiogalactopyranoside

iSECel. immobilized scaffolded enzymatic cellulosome

L

LB. Luria-Bertani

Ld. Low density

LdAG. Low density agarose microbeads

M

MA. Mander coefficient A

MB. Mander coefficient B

MIP. Molecular imprinting polymerization

MNPs. Magnetic nanoparticles

N

NAD^+. Nicotinamide adenine dinucleotide

NADH. Nicotinamide adenine dinucleotide reduced

NPs. Nanoparticles

O

OD. Optical density

P

PCR. Polymerase Chain Reaction

PDB.. Protein Data Base

PEA. R-1-phenylethylamine

PLP. Pyridoxal 5'-phosphate monohydrate

Q

QC. Quick-Change

QCM-D. *3.2.10* Quartz crystal microbalance with dissipation

QMC-D. Quartz crystal microbalance with dissipation

R

Rh. Rhodamine B isothiocyanate

S

SDS-PAGE. sodium dodecyl sulfate–polyacrylamide gel electrophoresis

T

T_M. Melting-Temperature, Melting-Temperature

Trp. Tryptophan

Tt27-HBDH-H2. Tt27-HBDH-R129H/Y130H

Tt27-HBDH-H3. Tt27-HBDH-R99H/R129H/Y130H

Tt27-HBDH-H4. Tt27-HBDH-R99H/R129H/Y130H/R250H

Tt27-HBDH-loop. Tt27-HBDH-129 (6x H) 133

Tt27-HBDH-WT. Tt27-HBDH-WT native with 6x histidines

Acknowledgment

I still cannot believe I have come this far, but like everything in life there is an end. It has been an intense four years of my life with a lot of learning, both personal and professional.

First of all, I would like to express my sincere gratitude to my advisor, Dr Fernando Lopez Gallego, for his guidance, support, and encouragement throughout this journey. I will always be grateful for having his door open to ease any of my doubts, and answer my questions or concerns. Thank you for your advice and your motivation throughout all these years.

I am deeply indebted to Susana, for teaching me everything from scratch at the beginning of the path that lead me this PhD adventure. I appreciate you always being available to offer advice and pick your brains when I needed it.

I want to express my gratitude to a few individuals with whom I worked closely during the course of my PhD. I would like to thank Eleftheria, Susana, and Natalia for helping me create and analyse cellulosomes. Also, I want to express my gratitude to Prof. Claudia Schmidt-Dannert for collaborating with us on the edition of the Bioconjugate Chemistry article. Thank you, Javier and Daniel, for spending the time conducting reactions using the catalysts made for the operational studies of the histidine clusters variants. Thanks to Mikel and Eneko for your assistances in expressing proteins. I would also express my gratitude to Dr Ilaria Armenia and Dr Puerto Morales for kindly providing us with the nanoparticles used in this thesis.

I am thankful to the consortium of HOTZYMES for the funding to carry out this doctoral thesis and for the short stay in the US. Finally thanks to the CIC BiomaGUNE platforms and the proteomic service of CIC BioGUNE.

I feel very grateful to Dr Anabel Benitez and Dr Cintia W. Rivero for the gentle review of this manuscript to support my PhD thesis as international doctorate.

Thank you to all my lab colleagues in the Heterogeneous biocatalysis lab, Sergio, Eleftheria, Alejandro, Daniel A, Ainhoa, Maialen, Javier, Eneko, and especially Natalia and Mercedes, for your help and support every day and especially in my darkest days. Thanks also to those who lab mates that have become great friends Mariana, Daniel G., Idania and that have been a fundamental part of this adventure. Thank you for the time and support in this last stressful year of this journey.

I would also like to give thanks to Dr Joel Kaar and his group(Colorado, US) for kindly hosting me for 3 months(which turned out to be the coldest months in my life). I would like to

particularly acknowledge Hector and Evan for the time and attention dedicated to helping me during this period I learnt a lot about your expertise in non-natural amino acids and fluorescence during my stay in your lab.

To my dear friends María and Nicolette who have always been there for me, thank for your patience your kindness and for those words of support that you have always had for me. Thanks for being my friends inside and outside of CIC biomaGUNE.

To my friends back in Zaragoza, Marta, Celia, Elena, Gabi, Ivan, Jorge, Victor, Sergi, Diego, Paula and David thanks for being there in spite of the distance. Each time I have seen you, it has been as if time had not passe. Thank you for your calls and the beers.

To Tom, thank you to for having crossed my path when I least expect it. You are the best thing that I keep from San Sebastian, Thank you for being there since I met you and for all the support, encouragement, hugs and laughs that you have given me. You have contributed enormously in finishing this adventure and I am excited for the next one.

Finalmente agradecer a mi familia, sin ellos nada de esto sería posible, gracias por apoyarme siempre y en especial en esta última etapa que ha sido la más estresante. Gracias mamá y papá por haberme dado todo y por enseñarme a trabajar por lo que quiero. A mis hermanos, que a pesar de la distancia siempre han estado ahí para mí a tan solo una llamada

Thank you all.

Abstract

Enzyme immobilization is usually one of the unwritten requirements to enable biocatalyst to play a relevant role in the development of many chemical industries. To obtain an efficient biocatalyst through this process, it is key that enzyme immobilization is achieved in a functionally active form. The biological activity of these immobilized enzymes is influenced by certain factors such as the correct orientation of the immobilized enzymes or the spatial distribution between the enzymes in a multi-enzymatic process. Although many immobilization techniques have been reported throughout the last decades, only a few of them allow the control of the orientation of the enzyme. Typically, the insertion of target groups at the N- or C-terminal is used for this goal, limiting the possible orientations of the immobilized enzymes. Taking into account the widely described high selectivity between histidine tags and divalent metal chelates to attach the enzymes to carriers, several surface histidine cluster variants were developed to prove the possibility of controlling the orientation beyond the N- or C- terminus. The strategy was tested in two multimeric alcohol dehydrogenase enzymes after a previous rational analysis of the enzyme surface *in silico* using COREX/Best algorithm. The variants developed were tested on different porous carriers activated with different materials and metal densities. The best candidates were extensively studied spectrophotometrically, using fluorescence microscopy and proteomic techniques. These candidates were also tested on non-porous nanocarriers.

On the other hand, inspired by the natural organization of the hydrolytic enzymes in the Cellulosome, we developed synthetic scaffolds using the highest affinity protein-protein interaction between the Cohesin and Dockerin domains. Based on this concept, different immobilized scaffolded enzymatic cellulosome or (iSECel) system were developed to control the spatial distribution of the different multi-enzymatic processes. The effect of the integration of all the enzymes needed for complete biotransformation in the same carrier, as well as the position of one enzyme relative to the other is reflected in the biocatalyst performance.

In summary, the work developed here provides new tools for the optimization of new heterogeneous biocatalysts, whether they are composed of a single enzyme or more, opening a new path for the rational control of enzyme orientation and their spatial organization.

.

Resumen

El desarrollo industrial de nuestra sociedad ha llevado a incrementar exponencialmente la demanda de productos químicos en todos los ámbitos de la vida, desde agricultura, construcción, producción textil o medicina. Sin embargo, junto a esta demanda, se ha incrementado la necesidad de cambiar los clásicos métodos de producción a métodos más sostenibles y respetuosos con el medio ambiente. Así desde principios del siglo XXI se ha buscado evolucionar socio-económicamente pero de forma orientada a no comprometer el futuro de las generaciones con el consumo de materias primas fósiles o el aumento de desechos no degradables. En este contexto, la biocatálisis se ha establecido como un proceso alternativo tanto para la síntesis como para la biodegradación de compuestos de interés gracias a su continuo avance tecnológico.

La biocatálisis utiliza enzimas como herramienta catalítica biológica para la producción de diferentes productos de interés químico o farmacéutico así como para la degradación de desechos o compuestos tóxicos. Existen otros tipos de catalizadores no biológicos que pueden realizar funciones equivalentes, pero que no poseen las ventajas de estos biocatalizadores. Al ser compuestos biológicos, estos catalizadores se forman de forma natural en células, poseen excelente capacidad catalítica, generalmente trabajan en condiciones fisiológicas y con una selectividad exquisita. Otra de sus características es que permiten obtener productos con alto grado de pureza debido a que presentan quimio, regio y estereoselectividad, además de que por su origen natural son renovables y biodegradables.

Debido a este creciente interés industrial y a los grandes avances en ingeniería de proteínas, herramientas computacionales y genéticas se ha ampliado el abanico de sustratos capaces de ser utilizados por las enzimas más allá de sus compuestos naturales. Sin embargo, debido a su origen las enzimas presentan limitaciones al ser aplicadas a procesos industriales como son su baja estabilidad en presencia de disolventes no polares, altas temperaturas o cambios en el pH. Además de su baja recuperación y reutilización tras reacciones ya sean discontinuas o en flujo debido a su alta solubilidad en medios acuosos. Es así como la inmovilización de estos biocatalizadores en soportes sólidos (biocatalizadores heterogéneos) ha surgido como un proceso casi obligatorio para su posible reciclado y uso a nivel industrial. Si bien la inmovilización es de los biocatalizadores es necesaria, hacerlo con una conformación activa y con una orientación apropiada es la clave para lograr biocatalizadores eficientes y competitivos con los actuales.

En esta tesis doctoral se han desarrollado dos nuevas herramientas para la optimización en el proceso de inmovilización de enzimas en materiales sólidos. Por un lado, en sistemas complejos donde más de una enzima es necesaria, ya sea para llevar a cabo la reacción principal o para el reciclaje de los cofactores necesarios para la reacción. Estos sistemas, también llamados sistemas multienzimáticos, normalmente son rutas alternativas a procesos sintéticos tradicionales por etapas, donde se evita el aislamiento de subproductos e intermedios de reacción y, por tanto, aumentan la ecoeficiencia del proceso general. Inspirados en la distribución espacial en procesos multienzimáticos en la naturaleza como en la degradación de la celulosa por el Celulosoma se han diseñado andamios sintéticos de proteínas (iSECel) mediante interacciones cohesina-dockerina. Esta plataforma biológica ha servido para ensamblar diferentes cascadas multienzimáticas en fase sólida. Por un lado, un sistema bi-enzimático para la transformación de alcoholes en aminas donde se estudió la eficiencia de la cascada en inmovilizaciones segregadas vs. la co-inmovilización en el mismo soporte. Por otro lado, un sistema de tres enzimas para la conversión de dioles, donde se estudió el efecto del orden de las enzimas en el andamio sintético, así como del efecto en la limitación de carga de enzima en el primer paso de ensamblaje (Capítulo 3).

Por otro lado, centrándonos en una sola enzima y teniendo como modelo la interacción entre la etiqueta de histidinas y soportes activados con quelatos metálicos, se ha desarrollado un método para el control de la orientación de la enzima en soportes sólidos. Esta técnica se basa en la modificación racional de la superficie de la enzima insertando clúster de histidinas mediante ingeniería de proteínas. Este proceso consta de tres etapas: la primera de análisis *in silico* de las enzimas modelo, dos alcoholes deshidrogenasas una de *Bacillus steareothermophilus* (BsADH) y la otra de *Thermus Thermophiles* (Tt27-HBDH) usando la herramienta computacional COREX/Best. La segunda etapa de desarrollo de las variantes con clústeres de histidina y el cribado de las mismas en diferentes soportes porosos activados con cuatro diferentes metales. La tercera etapa compuesta por el estudio de los efectos en el biocatalizador final de los mejores candidatos con respecto a la misma enzima con etiqueta de histidina (Capítulo 4).

Finalmente, en el último capítulo experimental (Capítulo 5), se estudió el efecto de la orientación y la distancia de inmovilización en soportes no-porosos, donde problemas de difusión interna desaparecen. En este caso se utilizaron nanopartículas magnéticas las cuales, por un lado, incrementan la capacidad de carga de la enzima debido al tamaño y por otro debido a las propiedades intrínsecas al magnetismo pueden tener innovadoras salidas como la hipertermia localizada. Además de demostrar que la orientación afecta a los parámetros cinéticos y termodinámicos de los biocatalizadores.

GENERAL INTRODUCTION

Introduction

The work presented here aims to examinate and analyze the importance of two factors during the immobilization process in a general biocatalyst. In system where a single enzyme is involve, the importance of the orientation control upon de immobilization that plays a key role in the enzymatic activity and stability of the final biocatalyst. On the other hand, in the systems where more than one enzyme needs to be involve, either due to the reaction steps or the cofactor recycling needs, the spatial organization and the positions of the enzymes in those multi-enzymatic systems are essential for an efficient performance.

1.1 Biocatalysis

The chemical industry has long recognized the importance of considering environmental and economic metrics when developing a new process that will find application in chemical manufacture. Here, catalysts offer significant benefits, and today, increasing emphasis is being placed on biologically mediated chemical reactions, in other words, bioconversions or biocatalytic processes. Generally, the biological catalysts are enzymes, which catalyse the transformation of a chemical substance (substrate) into another one (product). Since enzymes are catalysts, they lower the energy barrier required to reach the transition state, speeding up chemical reactions. Remarkably, enzymes are unique catalysts as the present an exquisite chemo-, regio-, and enantioselectivity.[1]

Enzymes are protein-based compounds produced by living organisms to catalyse metabolic biochemical reactions, either catabolic or anabolic reactions, necessary to all life processes.[2] The use of enzymes has been seen in the preservation of food and beverages in the ancient Egyptians. In 1783 Spallanzani first mentioned the importance of this biomolecule as a life-generating force inherent to certain kinds of inorganic matter that, with time, could be used to create themselves. [3] In 1812 Kirchhoff shows in his work the application of these biomolecules as catalyst to convert starch into glucose, but association with the word “catalysis” was not coined for almost another 20 years by Berzelius, who hypothesized that enzymes were such catalysts. Later, in 1877, Kühne would go on to coin the word “enzyme”. At the end of the century, in 1897, Eduard Buchner demonstrated the conversion of glucose to ethanol by a cell-free extract from yeast. Moreover, the kinetic understanding of enzymes remained elusive until the appearance of the proposed hypothesis for enzyme reactions by Michaelis and Menten in 1913.[4]

In applied biocatalysis, biotransformations can be carried out under mild conditions making the biocatalyst an attractive approach to chemical reactions. In nature, biocatalytic processes can be performed by i) fermentation reactions using growth-associated whole cell

and ii) reactions mediated by isolated enzymes. Despite the whole-cell bioconversion being used as a process in the production of different products of interest, the isolated enzymes show significant benefits when compared to whole cells. For example, cross-reactions should not occur, and substrates do not have to be transported across the membranes avoiding diffusion related issues. [5-7]

Enzymes can continue their functions under *in vitro* conditions. The use of cell-free enzymes allows catalytic processes in conditions not suitable for cell growth, and this fact was exploited in different fields. In the 1950s the first target application of enzymes was used for producing steroids in the pharmaceutical market.[8] Hydrolytic enzymes were also used since the 1960s by detergent manufacturers.[9, 10] However, it was not until the advancement in biotechnology that new tools, such as recombinant DNA technology, improved production processes and made possible the production of enzymes commercially feasible. Protein engineering and direct evolution techniques allowed for improvement of enzyme production and also allow alteration of their properties which further revolutionized the commercialization of industrially important enzymes and radically changed the way to produce chemicals in the long-term future.[11]

Thus, enzymes may be excellent industrial catalysts in different areas of the chemical industry, including the production of antibiotic precursors and bulk chemicals like acrylamide among others.[12] However, they still show features inherent to their origin that are not very suitable for industrial applications. The high solubility of enzymes in aqueous solutions becomes a problem for efficiency of their recovery and use in recycling. Therefore biocatalysts are generally applied on a single-use basis,[13] and the process is considered economically and environmentally unattractive in industry. Additionally, for a successful application in an industrial process, the enzymes must be stable and fully functional under process conditions. However, normally the conditions of industrial processes, such as temperature, pH values or solvent conditions differ from the natural environment of enzymes and thus they are usually unstable. They can also be inhibited by substrates and products in the reaction bulk or they only work effectively with natural substrates, which significantly limits the range of industrial process that they are able to catalyse. Consequently, the utilization of enzymes in industrial processes needs a large process of optimization from biological usage to industrial usage. Thus approaches spanning over various disciplines are focused on the identification and production of robust, stable biocatalysts in order to be suitable for application in a broader range of industry settings.[10]

Within the new alternatives for rational development of biocatalysts *in silico* analysis helps to sort out some of these drawbacks. The use of molecular biology techniques may improve

the enzyme properties. Also, immobilization and post-immobilization techniques could upgrade the enzymes properties.[14] Moreover, the increase in the number of accessible enzymes expands the list of possible catalytic reactions and the possibility to work in multi-enzyme cascades reactions which makes it more feasible to access more efficient and cleaner chemical synthesis.[15]

1.2 Immobilization

Enzyme immobilization refers to many techniques aimed to attach or entrap enzymes physically onto solid matrices while retaining at least part of their catalytic activity which can be used repeatedly and continuously.[16]

The first scientific observation that led the discovery of enzyme immobilization was made in 1916 by Nelson and Griffin.[16] They demonstrated that the invertase enzyme is able to exhibit catalytic activity when it is absorbed onto charcoal or aluminium hydroxide. Initial immobilization techniques were focused on isolated enzymes usually with adsorption techniques. During the 1950s and 1960s different covalent immobilization techniques were developed. In the 1970s the immobilization of two enzymes systems became possible, and new immobilization techniques were developed for example affinity binding, coordination binding, etc. In the 1990s the design of immobilized enzymes become more rational, where site-specific enzyme immobilization became the focus of attention. Also, in this period it was observed that the performance of enzymes can be improved using post-immobilization techniques, and multipoint attachment emerged as a new strategy. Studies using nanoscale structures for immobilization were published in the 2000s reducing diffusional limitations and maximizing the functional area which led to increased enzyme loading. Additionally, during this period other improvements were reported such as the covalent attachment of NAD(H), co-immobilization of enzymes and its auxiliary cofactors and the use of a wide range of nanoparticles as immobilizing supports. Nevertheless, this is still an area of interest which contains many unanswered questions for future applications.[17, 18]

Immobilization is one of the most powerful tools to deal with the main problems of the industrial application of enzymes; lack of long-term stability and difficulty in reusing them. This process also simplifies the manipulation of the biocatalyst and allows control over the reaction process as the immobilized biocatalysts are more easily separated from reactants once the reaction is complete. However, immobilization of enzymes may cause modifications to the enzyme properties, such as, changes in the intrinsic activity of the immobilized enzyme or changes in the way that the enzyme interacts with the substrate. In other words, changes in the micro-environment when the enzyme is immobilized to when it is soluble in

the bulk conditions. As a result, these properties are determined by the characteristics of the immobilization as well as the characteristics of the solid support (particle size, pore size, hydrophilic or hydrophobic nature), the nature of the immobilization (covalent or non-covalent) and the number of interactions between the enzyme and the carrier due to the possibility of the enzyme multivalence. [14, 19] However, until now, and even with significant advances in the different immobilization techniques, there is not a universal immobilized protocol for the enhancement of enzyme activity and stability of different types of enzymes. That is why immobilization is still an empirical exercise requiring trial-and-error experiments.[20]

1.2.1 Methods of immobilization

The different immobilization techniques are based on the physical adsorption, entrapment or encapsulation, covalent bindings, crosslinked aggregates, and affinity immobilization.[21] Throughout the years within these techniques, physical adsorption was commonly employed because of its simplicity but in many cases the enzymes are leaching from the surface of the carrier. Covalent cross-linking appears to be a solution for the leaching issues, where they employ natural lysine residues and cross-linking agents. However, the proteins typically have multiple lysine residues producing random surface orientation of the enzymes. This prompts enzyme unfolding, and issues in diffusion of the substrates and products to the active site of the enzyme. [20, 22, 23] In Figure 1 we show the different techniques and the degree of control of the orientation they can offer. These techniques are also described as follows:

Cross-linked:

The cross-linked enzymes aggregates or CLEA is a relatively recent technique that does not require the use of solid carriers. The formation of these non-soluble CLEAs occurs through aggregation of proteins using a precipitant agent followed by crosslinking of these aggregates through the primary amines of proteins and using a bifunctional linking agent.[23] However, precipitation is a random process which could result in enzymes in an inactive orientation.

Physical adsorption:

This is the most common and oldest technique used to immobilize enzymes due to its simplicity and where the enzyme is physically absorbed onto the surface carrier. This process can be carried out without specificity or through week non-specific forces such as hydrophobic interactions, Van der Waals, etc. Therefore, with these interaction it is possible,

in some cases to control the region of the enzyme through where is going to be absorbed by ionic binding.[24]

Entrapment:

The entrapment or encapsulation technique physically confines the enzyme into the carrier structure, but the substrate and products can pass through the carrier. This technique allows the modification of the encapsulating material which could improve the orientation of the enzymes into the carrier.[24] An example of this are the metal organic frameworks which are able to drive the direction of the immobilization though the reactive groups of the enzyme. [25]

Covalent binding:

Covalent binding is one of the most widely employed immobilization techniques, specifically in industrial applications, due to the operational stability of this technique. [26] The natural or mutated cysteines and lysine residues in the surface of the enzyme are the reactive groups employed. These residues allow orientation control during immobilization and multivalent attachment. [27]

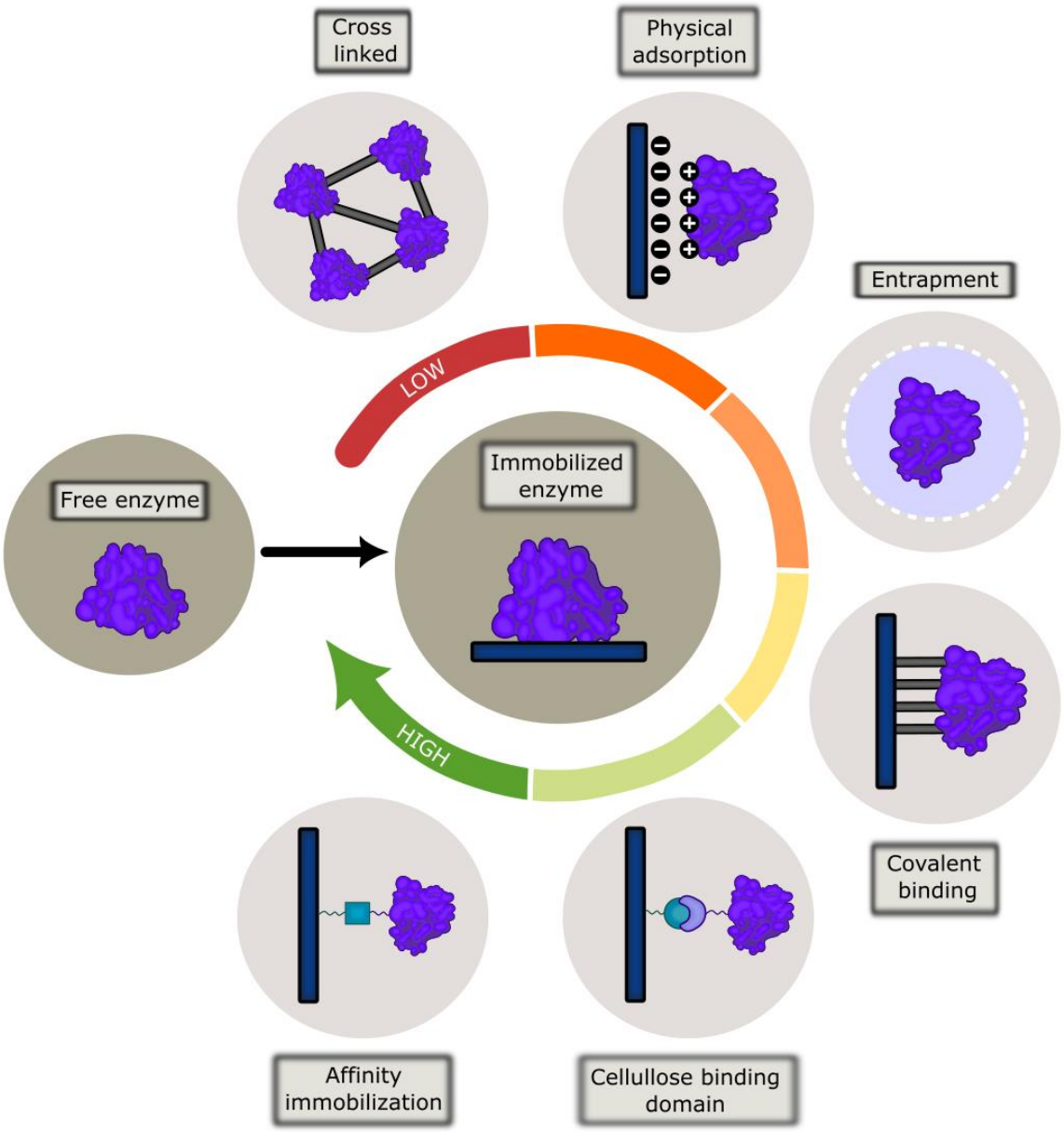

Figure 1: Immobilization techniques and their degree of orientation control during the immobilization process.

The colour bar shows the grade of orientation control during the immobilization, from low control in red to high orientation control in green.

1.3 Factors that influencing the biological activity in immobilized enzymes

During the immobilization of enzyme on carriers, uncertain unavoidable changes can occur in the enzyme that could affect either, the active sites of the enzyme or the enzyme structure which may negatively impact the activity. [28] There are several factors to consider when obtaining the amplification activity of the immobilized enzymes. Thus, it is not only the

method of immobilization chosen - with specific designed interactions between the carriers and the enzymes, substrate or reaction media - that plays an important role in obtaining a prominent catalytic reaction. [29]

1.3.1 Orientation

Uncontrolled immobilization could cause the unproductive binding of the enzyme with a bad orientation or in a too rigid conformation that may cause the complete loss of the enzymatic activity. Hence, a promising strategy to optimize the recovered activity of the heterogeneous biocatalyst is controlling the enzyme´s orientation on the solid surface of the carrier.[20, 28] This factor will be discussed in greater detail in Chapter 4.

1.3.2 Diffusion:

In single enzyme catalysis, the interactions between enzyme and substrate or products can influence enzymatic activity. To obtain an efficient catalytic reaction the substrates should diffuse through the reaction media to reach the active site of the immobilized enzyme, but also the products should diffuse away from the active site to facilitate a new catalytic cycle. [30] Heterogeneous biocatalysts are typically in a different phase from the reactants/products. For the biocatalytic process to occur, the reactant molecules must be in contact with the active site, so the molecules must diffuse though the fluid layer surrounding the heterogeneous biocatalyst. This layer is the external diffusion barrier and enzymatic activity depends on the fluid dynamics and the thickness of this layer. [20, 31] However the internal diffusion barrier, could occur in parallel with external diffusion, and is highly dependent on the carrier employed, the size and the porosity. Dey and colleagues reports how the apparent Km values decrease with smaller sizes of carriers which increase V_{max} due to the internal diffusion barrier decrease. [32]

1.3.3 Carrier choice:

The characteristics of the carrier takes a leading role in the performance of the biocatalyst, as well as in their further application. As was described above, the carriers could interact with the enzymes, substrate and/or products and affect some of the enzymatic kinetic parameters. [29] For that reason there are a large list of properties that an ideal carrier has to have, such as the physical resistance, inertness toward the enzymes, bio-compatibility and availability at low cost.[33] However, other characteristics such as the size or the porosity depends on the application and the immobilization process and there are not general rules for selecting the optimums carrier for all the biocatalysts. The carriers can be classified into two big groups: porous carriers and non-porous carriers.

Porous carriers:

Porous carriers are generally preferred due to their high surface area that allows a higher enzyme loading and therefore a high enzymatic productivity compared with the non-porous carriers. Also, the immobilized enzyme inside the porous carriers is more protected from the environment (harsh conditions) which could inactivate the enzymes. However, this type of carrier has diffusional limitations which is provoked by concentration gradients inside the pores of the carries. These concentration gradients can be larger or smaller due to the heterogeneity of the immobilized enzyme distribution inside the pores or the size of the pores themselves. [20, 34] In this group agarose carriers have been extensively used not only for its high porosity but also for other advantages such as ease of functionalization - which increases the possible binding chemistry, has a hydrophilic character and thus have a greater affinity for the protein, and the possibility for regeneration and reuse. This type of carriers will be used in Chapters 3 and 4.

Non-porous carriers:

Normally the non-porous carriers have low surface areas which affect the capacity of protein loading. Moreover, considering that the specific area of these supports depends on the particle size, to increase the enzyme loading capacity the carriers should be on a nanoscale level.[35] Thus, the of use of non-porous nano-particles may be a solution, because if the enzyme is correctly oriented, no diffusion problems will exist.[35] These nanoparticles have unique properties such as photoconversion, luminescence or magnetism between others, that could be combined with the enzymes to exploit new paths to enhance the enzymatic activity of the nano-biocatalyst.[36] Claussen and colleagues provided the hyperactivation of an alkaline phosphatase when immobilized on semiconductor quantum dots nano-particles.[37] As was described above due to the nanoparticles having different properties, some external stimulus are testing such the light to control the enzyme activity[38] or the magnetics ones applying an alternative magnetic field.[39] This last type of non-porous nano-carriers, will be used in Chapter 5.

1.3.4 Spatial distribution

The first studies about enzyme immobilization were focused on single enzyme immobilization. However, there are many biotransformations where it is necessary to have more than one enzyme working together in a cascade to complete the reaction. These systems, called multi-enzymatic systems, are widely found in the nature and consist of a highly ordered assemblies of enzymes. [40] Thus, the general considerations discussed above are also applicable to multi-enzyme systems, but there are also other features that

affect the overall system such as the spatial distribution of the enzymes on the carrier and between the enzymes involved in the biotransformation. [29] The control of the position of the different enzymes on the carrier allows the co-localization of the enzymes allowing direct substrate transport among the enzymes avoiding diffusion into the bulk. This increases the concentration of the intermediate products and protects the unstable products or cofactors. [41] Additionally, the control of the position of the enzymes on the carrier affects the overall activity of the biocatalyst. [42]

1.4 Calculation of immobilization Parameters

To fully understand the effects of immobilization on enzyme activity, some experimental data should be calculated. The experiments performed should monitor evolution of enzyme activity throughout the entire immobilization process.

If possible, it is necessary to determine the concentration and activity of the enzyme.

Specific activity soluble (Ae_s U x mg^{-1}): The activity expressed per milligram of soluble enzyme in determined conditions.

$$Ae_{soluble}\ (U\ x\ mg^{-1}) = \frac{U\ x\ mL^{-1}}{mg\ x\ mL^{-1}{}_{enzyme}}$$

Eq (1): Specific Activity Ae_s

Offered protein (mg x $g^{-1}_{carrier\ offered}$) & Offered activity (U x $g^{-1}_{carrier\ offered}$): Refers to the amount of protein/activity that has been offered per gram of carrier.

$$\mathrm{mg}_{protein}\ x\ g^{-1}{}_{carrier} = mg\ x\ mL^{-1}\ x\ DF$$

$$\mathrm{U}_{enzyme}\ x\ g^{-1}{}_{carrier} = U\ x\ mL^{-1}\ x\ DF$$

Eq (2): Offered protein & offered activity

Where DF (Dilution Factor) is the relation between the carrier mass and the soluble protein solution.

Immobilization Yield (%): Percentage of enzyme that has been immobilized. This parameter can be calculated by using values of either, activity (U x mL^{-1}) or protein concentration (mg x mL^{-1}).

$$\Psi\ \%_{activity/protein} = 100 - \left(\frac{enzyme\ {}_{supernatan}}{enzyme\ {}_{offered}}\ x\ 100\right)$$

Eq (3): Immobilization yield

Protein load (mg x $g^{-1}_{carrier}$) & Activity load: Refers to the amount of protein/activity that has been theoretically immobilized per gram of carrier.

$$mg\ x\ g^{-1}_{carrier} = Offered\ protein\ (mg\ x\ g^{-1})\ x\ \left(\frac{10^3}{MW_{enzyme}}\right)\left(\frac{Immobilization\ yield}{100}\right)$$

$$U\ x\ g^{-1}_{carrier} = Offered\ activity\ (U\ x\ g^{-1})\ x\ \left(\frac{Immobilization\ yield}{100}\right)$$

Eq (4): Protein & activity load

Recovered activity (U x g-1 carrier): Also called expressed activity, gives the immobilized enzyme activity expressed on the carrier experimentally.

$$U\ x\ g^{-1}_{carrier} = U\ x\ mL^{-1}\ _{carrier\ suspention}\ x\ DF$$

Eq (5): Recovered activity

Notice that Eq (5) is only applicable if the carrier suspension is the same as the ratio between the carrier mass and the soluble enzyme offered, if not, the activity value (U x mL^{-1}) should be considered the dilution.

Specific activity immobilized (Aei): The activity immobilized per milligram of immobilized enzyme.

$$Ae_i\ (U\ x\ mg^{-1}) = \frac{Recover\ activity\ (\ U\ x\ g^{-1})}{Protein\ load\ (mg\ x\ g^{-1})}$$

Eq (6): Specific activity immobilized (Ae_i)

Relative recovered activity (%): The percentage gives the effectiveness of the immobilized biocatalyst compared with the reference in solution.

$$rRA\ (\%) = \frac{Ae_i}{Ae_s}\ x\ 100$$

Eq (7): Relative recovered activity or immobilization effectiveness

1.5 Bibliography

[1] R.A. Sheldon, The road to biorenewables: carbohydrates to commodity chemicals, ACS Sustainable Chemistry & Engineering, 6 (2018) 4464-4480.

[2] C.C. De Carvalho, Enzymatic and whole cell catalysis: finding new strategies for old processes, Biotechnology advances, 29 (2011) 75-83.

[3] R. Vallery, R. Devonshire, Life of Pasteur, Kessinger Publishing, LCC, 2003.

[4] N. Gurung, S. Ray, S. Bose, V. Rai, A broader view: microbial enzymes and their relevance in industries, medicine, and beyond, BioMed research international, 2013 (2013).

[5] S. Huf, S. Krügener, T. Hirth, S. Rupp, S. Zibek, Biotechnological synthesis of long-chain dicarboxylic acids as building blocks for polymers, European Journal of Lipid Science and Technology, 113 (2011) 548-561.

[6] S. Picataggio, K. Deanda, J. Mielenz, Determination of Candida tropicalis acyl coenzyme A oxidase isozyme function by sequential gene disruption, Molecular and cellular Biology, 11 (1991) 4333-4339.

[7] H.-P. Meyer, K.T. Robins, Large scale bioprocess for the production of optically pure L-carnitine, Monatshefte für Chemie/Chemical Monthly, 136 (2005) 1269-1277.

[8] A.S. Spirin, Cell-free protein synthesis, Cell-Free Translation Systems, (2002) 3-20.

[9] S. Gürkök, Microbial enzymes in detergents: a review, Int. J. Sci. Eng. Res, 10 (2019) 75-81.

[10] J. Chapman, A.E. Ismail, C.Z. Dinu, Industrial applications of enzymes: Recent advances, techniques, and outlooks, Catalysts, 8 (2018) 238.

[11] B. Turanli-Yildiz, C. Alkim, Z.P. Cakar, Protein engineering methods and applications, Protein Engineering, Citeseer2012.

[12] J.R. Cherry, A.L. Fidantsef, Directed evolution of industrial enzymes: an update, Current opinion in biotechnology, 14 (2003) 438-443.

[13] X. Pei, Z. Luo, L. Qiao, Q. Xiao, P. Zhang, A. Wang, R.A. Sheldon, Putting precision and elegance in enzyme immobilisation with bio-orthogonal chemistry, Chemical Society Reviews, (2022).

[14] J.M. Guisan, Immobilization of enzymes and cells, Springer2006.

[15] J. Fernández-Lucas, Multienzymatic synthesis of nucleic acid derivatives: a general perspective, Applied microbiology and biotechnology, 99 (2015) 4615-4627.

[16] J. Nelson, E.G. Griffin, Adsorption of invertase, Journal of the American Chemical Society, 38 (1916) 1109-1115.

[17] A.A. Homaei, R. Sariri, F. Vianello, R. Stevanato, Enzyme immobilization: an update, Journal of chemical biology, 6 (2013) 185-205.

[18] J.S. Melo, A. Tripathi, J. Kumar, A. Mishra, B.P. Sandaka, K.C. Bhainsa, Immobilization: then and now, Immobilization Strategies, Springer2021, pp. 1-84.

[19] M. Piumetti, S. Bensaid, Nanostructured Catalysts for Environmental Applications, Springer2021.

[20] J.M. Bolivar, I. Eisl, B. Nidetzky, Advanced characterization of immobilized enzymes as heterogeneous biocatalysts, Catalysis Today, 259 (2016) 66-80.

[21] J.M. Guisan, J.M. Bolivar, F. López-Gallego, J. Rocha-Martín, Immobilization of enzymes and cells: Methods and protocols, Springer2020.

[22] L. Cao, Immobilised enzymes: science or art?, Current opinion in chemical biology, 9 (2005) 217-226.

[23] S. Velasco-Lozano, F. López-Gallego, J.C. Mateos-Díaz, E. Favela-Torres, Cross-linked enzyme aggregates (CLEA) in enzyme improvement–a review, Biocatalysis, 1 (2016) 166-177.

[24] N.R. Mohamad, N.H.C. Marzuki, N.A. Buang, F. Huyop, R.A. Wahab, An overview of technologies for immobilization of enzymes and surface analysis techniques for immobilized enzymes, Biotechnology & Biotechnological Equipment, 29 (2015) 205-220.

[25] S. Escobar, S. Velasco-Lozano, C.-H. Lu, Y.-F. Lin, M. Mesa, C. Bernal, F. López-Gallego, Understanding the functional properties of bio-inorganic nanoflowers as biocatalysts by deciphering the metal-binding sites of enzymes, Journal of Materials Chemistry B, 5 (2017) 4478-4486.

[26] F. López-Gallego, G. Fernandez-Lorente, J. Rocha-Martin, J.M. Bolivar, C. Mateo, J.M. Guisan, Stabilization of enzymes by multipoint covalent immobilization on supports activated with glyoxyl groups, Immobilization of Enzymes and Cells: Third Edition, (2013) 59-71.

[27] A.A. Karyakin, G.V. Presnova, M.Y. Rubtsova, A.M. Egorov, Oriented immobilization of antibodies onto the gold surfaces via their native thiol groups, Analytical chemistry, 72 (2000) 3805-3811.

[28] K. Hernandez, R. Fernandez-Lafuente, Control of protein immobilization: Coupling immobilization and site-directed mutagenesis to improve biocatalyst or biosensor performance, Enzyme and microbial technology, 48 (2011) 107-122.

[29] Y. Zhang, J. Ge, Z. Liu, Enhanced activity of immobilized or chemically modified enzymes, AcS catalysis, 5 (2015) 4503-4513.

[30] M. Seenuvasan, K.S. Kumar, A. Kumar, R. Parthiban, Review on surface modification of nanocarriers to overcome diffusion limitations: An enzyme immobilization aspect, Biochemical engineering journal, 158 (2020) 107574.

[31] R. Klaewkla, M. Arend, W.F. Hoelderich, A review of mass transfer controlling the reaction rate in heterogeneous catalytic systems, INTECH Open Access Publisher Rijeka2011.

[32] G. Dey, S. Bhupinder, R. Banerjee, Immobilization of alpha-amylase produced by Bacillus circulans GRS 313, Brazilian Archives of Biology and Technology, 46 (2003) 167-176.

[33] V.L. Sirisha, A. Jain, A. Jain, Enzyme immobilization: an overview on methods, support material, and applications of immobilized enzymes, Advances in food and nutrition research, 79 (2016) 179-211.

[34] B. Brena, P. González-Pombo, F. Batista-Viera, Immobilization of enzymes: a literature survey, Immobilization of Enzymes and Cells: Third Edition, (2013) 15-31.

[35] C. Garcia-Galan, Á. Berenguer-Murcia, R. Fernandez-Lafuente, R.C. Rodrigues, Potential of different enzyme immobilization strategies to improve enzyme performance, Advanced Synthesis & Catalysis, 353 (2011) 2885-2904.

[36] B.J. Johnson, W.R. Algar, A.P. Malanoski, M.G. Ancona, I.L. Medintz, Understanding enzymatic acceleration at nanoparticle interfaces: Approaches and challenges, Nano Today, 9 (2014) 102-131.

[37] J.C. Claussen, A. Malanoski, J.C. Breger, E. Oh, S.A. Walper, K. Susumu, R. Goswami, J.R. Deschamps, I.L. Medintz, Probing the enzymatic activity of alkaline phosphatase within quantum dot bioconjugates, The Journal of Physical Chemistry C, 119 (2015) 2208-2221.

[38] H.R. de Barros, I. Garcia, C. Kuttner, N. Zeballos, P.H. Camargo, S.I.s.C. de Torresi, F. Lopez-Gallego, L.M. Liz-Marzan, Mechanistic insights into the light-driven catalysis of an immobilized lipase on plasmonic nanomaterials, AcS catalysis, 11 (2020) 414-423.

[39] I. Armenia, M.V.G. Bonavia, L. De Matteis, P. Ivanchenko, G. Martra, R. Gornati, M. Jesus, G. Bernardini, Enzyme activation by alternating magnetic field: Importance of the bioconjugation methodology, Journal of colloid and interface science, 537 (2019) 615-628.

[40] F. Jia, B. Narasimhan, S. Mallapragada, Materials-based strategies for multi-enzyme immobilization and co-localization: a review, Biotechnology and bioengineering, 111 (2014) 209-222.

[41] Y.-H.P. Zhang, Substrate channeling and enzyme complexes for biotechnological applications, Biotechnology advances, 29 (2011) 715-725.

[42] P. Pescador, I. Katakis, J.L. Toca-Herrera, E. Donath, Efficiency of a bienzyme sequential reaction system immobilized on polyelectrolyte multilayer-coated colloids, Langmuir, 24 (2008) 14108-14114.

BACKGROUND & OBJECTIVES

Background & Objectives

2.1 Background

During recent decades, the chemical industry has been constantly search for “green” and environmentally friendly alternatives to replace conventional manufacturing that often requires complex synthetics steps, a great deal of energy and fossil raw materials. Biocatalysis, using enzymes as catalytic tools, has emerged as an alternative to produce a wide range of fine chemicals and pharmaceutical ingredients. Furthermore, protein engineering and enzymatic cascades have boosted the range of synthetic schemes with industrial interest. On one hand, enzyme immobilization is one of the unwritten industry requirements to be more economically attractive due to reduced recycling, improving the separation of the biocatalyst from the reaction bulk, and enhancing the robustness of the biocatalyst. However, this process sometimes has the drawback of losing some or all catalytic activity due to the low control of enzyme orientation during immobilization and the lack of orchestration and tuning between the enzymes that form the biocatalyst. Whereby, the immobilization becomes an empirical exercise for each enzyme. In this context, it is necessary to develop, design and study alternative techniques for immobilization on solid supports that allow better control of the orientation and the spatial organization of the enzymes to fabricate more efficient heterogeneous biocatalysts. New technological development and the fundamental knowledge on this subject will contribute to establishing novel rational approaches for the enzyme immobilization, moving this process towards a rational rather than empirical approach.

2.2 Objectives

The thesis, here presented, has as its main aims **the developing and studying novel techniques for the rational immobilization of enzymes and multi-enzymatic systems on solid carriers.** To achieve the main objective, this PhD thesis has addressed the following goals:

I) Immobilization of a multi-enzyme system through protein scaffolds based on cellulosomes to control the spatial organization and orientation of the different enzymes involved in the system. Characterization and performance study in batch (stirred tank reactor) and continuous (packed bed reactor) reactions. **Chapter 3**

II) Engineering the surface of enzymes with histidine clusters to orient them on carriers functionalized with metal chelates (different type of metals and different metal densities) beyond the N- and C- terminus. Structural and functional characterization of the oriented heterogeneous biocatalysts. **Chapter 4**

III) Studying the operational performance and stability of these oriented heterogeneous biocatalysts for industrially relevant biotransformations. **Chapter 4**

IV) Tunning the orientation and immobilization distance to immobilize enzymes on Magnetic Nanoparticles (MNPs). **Chapter 5**

COHESIN-DOCKERIN SYSTEM

3.1 Introduction

Biocatalytic processes can either involve a single enzyme that catalyzes the desired reaction or more than one enzyme operating sequentially or simultaneously to obtain the desired compound, which are normally products of higher complexity.[1] Thus, multi-enzyme systems are gaining momentum for chemical manufacturing as they allow executing complex synthetic routes to yield highly pure products without requiring intermediate purification and protection/deprotection steps.[2] The simultaneous operation of several enzymes can also increase the overall production yield and system efficiency by pulling the cascade towards the final product while preventing the accumulation of potentially toxic and inhibitory intermediates.[3] However, achieving high fluxes through a biocatalytic cascade requires optimal coupling of enzyme reactions.[4] Biological living systems orchestrate fluxes of biosynthetic pathways through a variety of mechanisms including e.g. gene regulation,[5] allosteric control[6] and spatial compartmentalization[7] of enzyme activities; strategies which have been adopted for cellular engineering of metabolic pathways[8]. Far fewer approaches and tools are available for the efficient orchestration of enzyme cascades in cell-free (in vitro) reactions. In vitro synthetic biology or cell-free metabolic engineering is an emerging approach aimed at assembling artificial biosynthetic cascades using isolated enzymes. Such in vitro systems can operate under non-physiological conditions and are unimpeded by mass transfer, inhibitory (e.g. high substrate concentration, toxic reaction compounds) and side reaction issues, common to cellular systems. Cell-free operation also allows for the rapid proto-typing of cascades and isolation of purer products.[9, 10]

A major drawback of cell-free reactions is that they are based on isolated enzymes working under dilute conditions rather than the crowded and spatially organized environment of cells.[11] Several groups including ours, have successfully demonstrated confinement and co-immobilization of enzyme cascades on solid materials.[12] These co-localization strategies, however, lack the precision required to organize biocatalysts at the nanometre scale afforded by the biological systems. Different self-assembling supramolecular structures have been fabricated based on protein,[12, 13] DNA/RNA[14] or nanoparticle [15] building blocks to which target enzymes are attached via genetic fusions, engineered interaction domains or chemical modification. Such scaffolding approaches were shown to enhance the reaction efficiency of the multi-enzyme systems for chemical synthesis.[16]

Nature employs its own supramolecular scaffolds to organize enzymes into metabolomes. One such type of metabolome is the bacterial cellulosome that co-localizes and positions a cohort of glycosidases at the extracellular membrane for the degradation of the recalcitrant plant cell wall polymer cellulose.[17] Cellulosomes have highly modular architectures where

a scaffolding protein anchored to the cell wall displays cohesin (Coh) domains to which secreted glycosidases attach via cognate dockerin (Doc) domains. Binding of the metabolomes to cellulose is facilitated by cellulose binding domains (Figure 2, A). Inspired by their plug-and-play organization, synthetic cellulosomes have been engineered mostly for cell-based applications including metabolic engineering and/or biorefinery processes.[18] For in vitro applications, mini-cellulosomes have been designed for the selective assembly of multi-enzyme systems through the calcium-dependent interactions of Coh/Doc pairs (Figure 2, B).[12, 19, 20] These mini-cellulosomes have also been immobilized on cellulose-based or cellulose-coated solid materials for recycling. However, the structural diversity of such engineered cellulosome scaffolds used to organize multi-enzyme systems in the space is limited by the low number of available highly specific Coh/Doc pairs. Another challenge is the cellulosome assembly using large and/or multimeric enzymes causing molecular crowding and steric hindrances.[21] In this chapter, we sought to develop an alternative strategy where we use porous agarose microbeads for the construction of a cellulosome inspired, artificial metabolome (dubbed immobilized scaffolded enzymatic cellulosome or short, iSECel) that is genetically programmable.

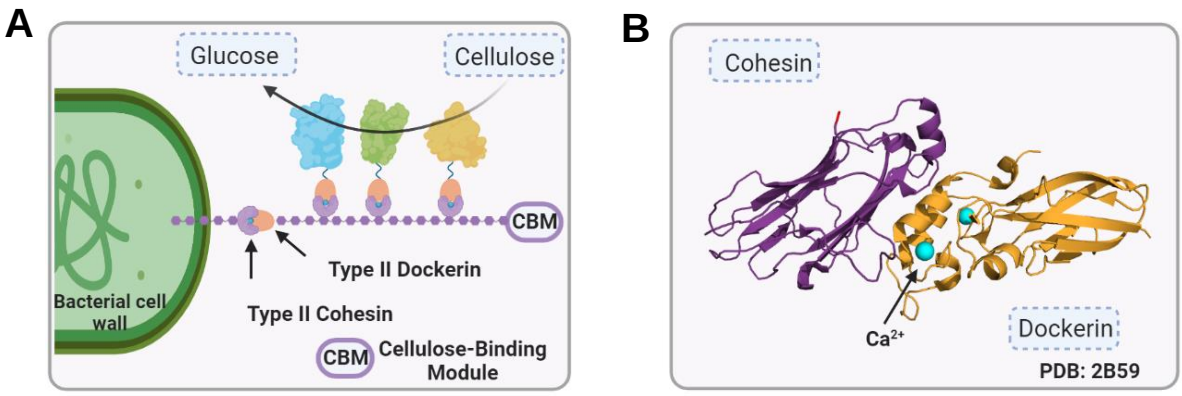

Figure 2: Schematic illustration of enzyme assembly through the system cohesin-dockerin.

A. *Cellulose-binding module in the nature to metabolize the cellulose.* ***B.*** *Cohesin-dockerin type I structure interaction mediated by calcium.*

3.2 Materials & Methods

3.2.1 Chemicals

LB (Luria-Bertani) Broth medium, Tris-HCl base buffer, sodium hydroxide and cobalt (II) chloride were purchased from Fisher Scientific (Waltham, MA, USA). R-1-phenylethylamine (PEA), 3-methyl-1-butanol (3MB), 3 methyl-butylamine (3MBA), acetone, acetophenone, ethanol, benzylalcohol, kanamycin sulfate, sodium pyruvate, pyridoxal 5'-phosphate

monohydrate (PLP), calcium chloride, sodium pyruvate, eicosane, (3-glycidyloxypropyl) trimethoxysilane (GPMES), fluorescein isothiocyanate (FTIC), rhodamine B isothiocyanate (Rh), sodium bicarbonate, sodium phosphate dibasic dehydrate, HEPES sodium salt, 1,5-pemtanediol, albumin bovine serum standard (BSA), flavin-adenine-dinucleotide sodium salt (FAD^+) and iminodiacetic acid (IDA) were purchased from Sigma-Aldrich (St. Louis, IL, USA). Nicotinamide adenine dinucleotide sodium salt (NAD^+), nicotinamide adenine dinucleotide reduced disodium salt (NADH)and the inductor Isopropyl-β-D-thiogalactopyranoside (IPTG) were acquired from Gerbu Biotechnik GmbH (Wieblingen, Germany). Acetonitrile, dimethyl sulfoxide (DMSO) and dichloromethane (DCM) were purchased from Scharlau (HPLC grade, Barcelona, Spain). Bradford protein assay dye reagent and micro Bio-spin columns were purchased from BIORAD (Biorad. Hercules, CA, USA). Cobalt-activated agarose microbeads 6BCL (AG-Co^{2+}, 15 µmol Co^{2+}/mL (A-1061S-X)) were acquired from ABT technologies (Madrid, Spain).

3.2.2 Sequences, plasmids and cloning

Synthetic genes encoding the enzymes and proteins (C-His, C-ADH, D-ECFP-D, D-ωTA -D) used in the iSECel-I system and the (His-D, D-NOX and His-BpCAT-C) were obtained from Genscript Biotech (Piscataway, NJ, USA) and cloned into the multi cloning site of pET28b (+). All nucleotide sequences encoding the primary sequences of all proteins herein used in the iSECel-I system are described in Table A 1 and the ones used in the iSECel-II and iSECel-III system are described in the Table A 2. All the plasmids were transformed and propagated in the *E. coli* DH5α following standard molecular biology protocols.[22]

3.2.3 Protein expression

Single colonies of recombinant *E. coli* BL21 (DE3) were used to inoculate 3 mL of LB medium supplemented with 30 µg x mL^{-1} kanamycin that were incubated overnight at 37 ºC. Then 50 mL of LB medium supplemented with the same antibiotic concentration as above were inoculated with 1 mL of the overnight cultures in a 250 mL flask and grown at 37 ºC and 250 rpm until the optical density (OD_{600nm} = 0.6). These cultures were then induced with IPTG under different conditions depending on the protein to be expressed them (Table 1) after the IPTG induction the culture were grown at 250 rpm. Bacteria were collected by centrifugation at 1503 x g for 30 min at 4 ºC and pellets were stored at – 20 ºC until use.

Table 1: Optimal conditions for the protein expression

Proteins for the iSECel-I system				
Protein	T (ºC) before IPTG	T (ºC) after IPTG	Optimal IPTG concentration	Optimal induction time
C-His	37 ºC	37 ºC	1 mM	3 hours

C-ADH	37 ºC	37 ºC	1 mM	3 hours
D-ECFP-D	37 ºC	21 ºC	0.1 mM	Over night
D-ωTA-D	37 ºC	21 ºC	0.1 mM	Over night

Proteins for the iSECel-II and iSECel-III system

Protein	T (ºC) before IPTG	T (ºC) after IPTG	Optimal IPTG concentration	Optimal induction time
C-ADH	37 ºC	37 ºC	1 mM	3 hours
His-D	37 ºC	21 ºC	0.1 mM	Over night
D-NOX	37 ºC	21 ºC	1 mM	Over night
His-BpCAT-C	37 ºC	21 ºC	1 mM	24 hours

3.2.4 Cell-free extract preparation

Cell pellets were resuspended in Tris-HCl buffer 25 mM at pH 7 and then lysed by sonication (Bondelin Somo plus sonicator) on ice for 20 min (40 % amplitude, 5 sec pulse). The sonicated lysate was centrifuged at 9391 x g at 4 ºC for 30 min to obtain a soluble protein lysate. In the case of D-ωTA-D, bacteria were resuspended in 25 mM Tris buffer and 0.1 mM of PLP at pH 10 and then lysed as described above. Immediately after the sonication step the D-ωTA-D cell lysate was adjusted to pH 7.5 prior to centrifugation.

3.2.5 Purification of C-His, His-ECFP-D, His-D and His-BpCAT-C

His-tagged proteins were purified from 5 ml crude cell extracts by metal-affinity binding to 500 mg AG-Co^{2+} resin via gravity-flow purification. After loading, the resin was washed with 5 mL of 25 mM Tris-HCl and the proteins were eluted with 1 mL of 500 mM imidazole in 25 mM Tris-HCl buffer and dialysed against 25 mM Tris-HCl, pH 7.

3.2.6 Protein quantification

Enzyme quantification and enzyme activity were spectrophotometrically measured in transparent 96-well microplates using a Microplate Reader Epoch 2 BioTek ®. The raw data were analysed with Gen 5 software (BioTek ®).

The protein concentrations were measured using Bradford´s protein assay.[23] All the experiments were performed in 96 well plates. Briefly, 5 µL of pure enzyme solution were mixed with 200 µL of Bradford reagent and incubated at room temperature for 5 min. The absorbance was measured at 595 nm. A standard curve using BSA as standard was utilized to calibrate the absorbance with the protein concentration.

3.2.7 Colorimetric enzyme assays

Transaminase assay: Transaminase activity of D-ωTA-D crude extract was measured by monitoring absorbance increase at 245 nm due to the formation of acetophenone (ε = 12 mM^{-1} x cm^{-1}), at different times under orbital shaking (567 rpm) within the reader. The cell-

free extracts and the immobilized enzyme suspensions were incubated with 2 mM of amino donor racemic phenylethylamine (*rac*-PEA), 0.1 mM of PLP and 10 mM of the assayed amine acceptor (3-methyl butanal or acetone) in 5% DMSO 100 mM HEPES buffer at pH 8. One transaminase activity unit (U) is defined as the amount of the enzyme that catalyses the formation of 1 µmol of acetophenone per minute.

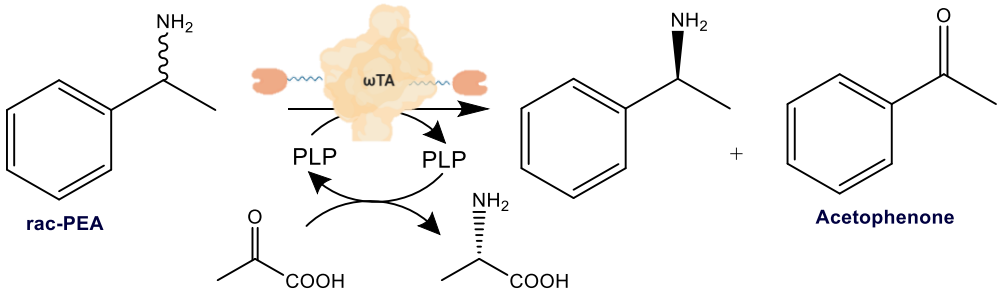

Alcohol dehydrogenase assay: Dehydrogenase activity of C-ADH was measured by monitoring the absorbance at 340 nm (ε= 6.22 mM^{-1} x cm^{-1}) at different times under orbital shaking (567 rpm) within the reader. Changes in absorbance were due to either the consumption or production of NADH in the reduction and oxidation reactions, respectively. Where, one unit of activity corresponds to the amount of the enzyme that catalyses either the reduction or oxidation of 1 µmol of NAD^+ or NADH per minute, respectively.

The oxidation reactions in the iSECel-I system, cell-free extracts and immobilized enzymes 5 µL of sample were incubated with 100 mM of 3-methyl butanol and 1 mM NAD^+ in 100 mM sodium phosphate buffer at pH 8 (scheme reaction A). For the reduction reaction, cell-free extracts and immobilized enzyme suspensions were incubated with 100 mM acetone and 1 mM NADH in 100 mM sodium phosphate at pH 7. The oxidation in the iSECel-II and iSECel-III systems were performed using 200 µL of reaction mix containing 100 mM of EtOH or 10 mM of 1,5 pentanediol and 1 mM of NAD^+ in 100 mM sodium phosphate buffer at pH 8 (scheme reaction B and C, respectively). To these reactions mixes, 5 µL of the different samples were added previous monitoring at 30 ºC.

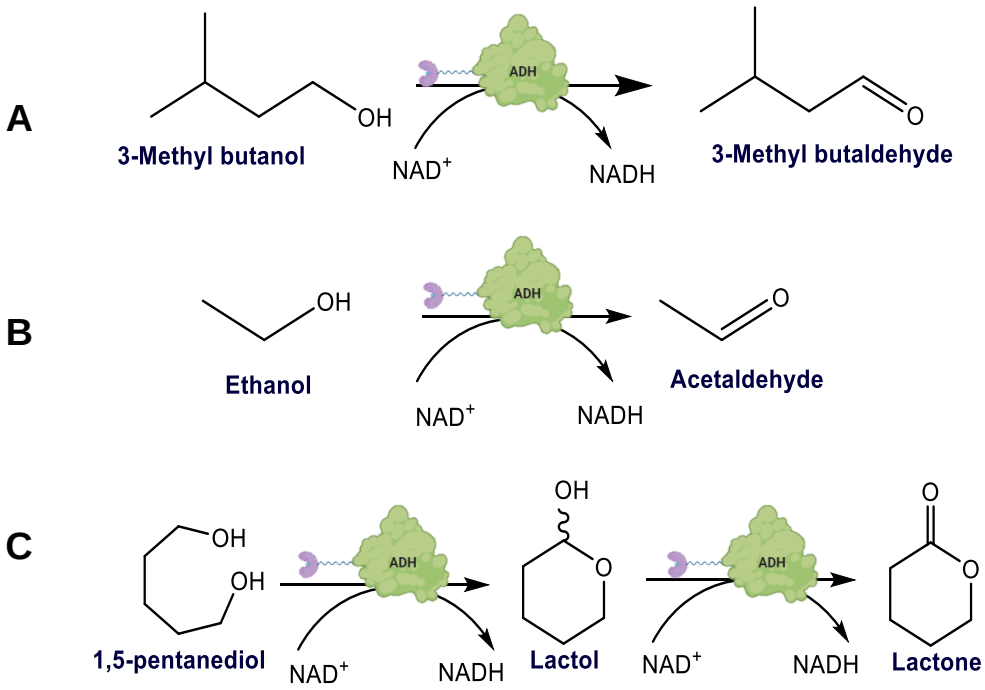

NADH Oxidase assay: The NADH oxidase activity of D-NOX for the iSECel-II and iSECel-III was measured by monitoring the decrease in the absorbance at 340 nm (ε= 6.22 mM-1 x cm-1) at different times under orbital shaking (567 rpm) within the reader. The cell-free extracts and the immobilized enzyme suspensions (5 µL) were incubated with 0.2 mM of NADH and 1.5 mM of FAD+ in 50 mM sodium phosphate buffer at pH 8 and 30 ºC. One unit of activity corresponds to the amount of the enzyme that catalyses the oxidation of 1 µmol of NADH to NAD^+ per minute.

Catalase assay: The catalase activity of either His-BpCAT-C or BpCAT-C for the iSECel-II and iSECel-III was measured by monitoring the decrease in the absorbance at 240 nm. The cell-free extracts, pure enzyme and the immobilized enzyme suspensions (5 µL) were incubated with a reaction mixture containing 35 mM of Hydrogen peroxide in sodium phosphate buffer at pH 8 and 30 ºC. One unit of catalase activity corresponds to the amount of the enzyme that catalyse the disproportionation of 1 µmol of hydrogen peroxide per minute.

Hydrogen peroxidase accumulation assay: The catalase activity in the full assembly iSECel-II or iSECel-III could be measured following the protocol described elsewhere,[24] by monitoring the absorbance increase at 560 nm due to the formation of resorufin. The iSECel-II or iSECel-III systems were incubated with a reaction mix containing 0.5 µL x mL^{-1} HRP (Peroxidase from Horseradish), 20 mM of 1,5-pentanediol, 1 mM NAD^+, 0.15 mM of FAD^+, 50 µM AmplifluRED in sodium phosphate buffer 100 mM pH8.

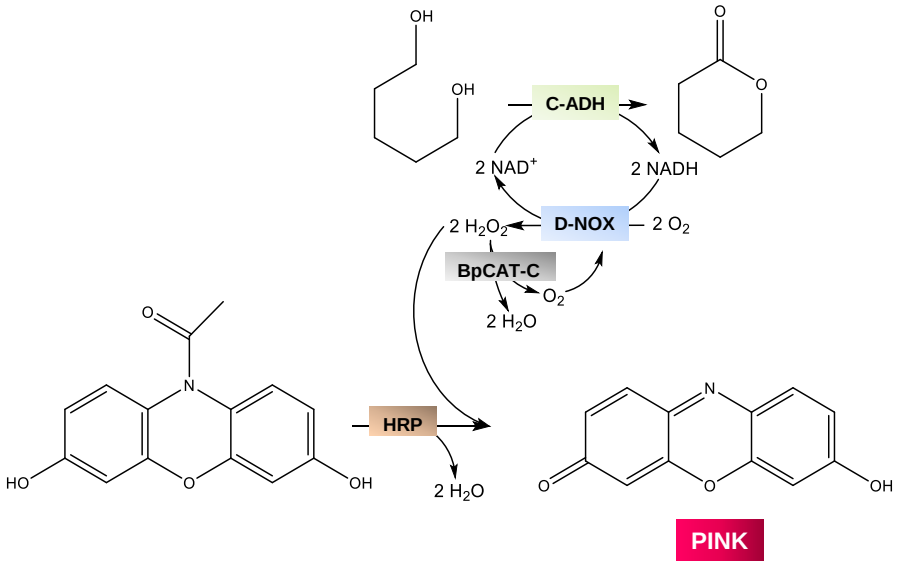

Figure 3: Enzymatic assay to determine the coupling efficiency in iSECel-II and iSECel-III using amplifluRED reactant

Colorimetric assay to determine the coupling efficiency in iSECel systems II and III. The cascade reactions of the first two enzymes (C-ADH and D-NOX) generate hydrogen peroxide as by-product. If the iSECel systems are working efficiently, the hydrogen peroxide will be consumed by the catalase (BpCAT-C or His-BpCAT-C), generating water and oxygen that could be recycled by D-NOX. However, if the catalase does not work efficiently, the system accumulates hydrogen peroxide and the HRP enzyme in the mix reaction will be able to react with the amplifluRED and generate a pink solution that we indeed monitor spectrophotometrically.

3.2.8 Solid-phase assembly of dockerin and cohesion fusion proteins as iSECel (iSECel-I system)

1 mL of purified C-His (0.18 - 0.3 mg x mL^{-1}) was incubated with 100 mg of AG-Co^{2+} placed in a micro Bio-spin column under orbital rotation for 1 hour at room temperature. Then, the suspension was filtered and AG-Co^{2+} functionalized with C-His was washed with 2 mL of assembly buffer (25 mM Tris-HCl buffer at pH 7 and 1 mM $CaCl_2$) to remove non-specifically bound proteins and equilibrate the carrier for the following assembly step. Next, 1 mL of crude extracts containing the dockerin fused cargo proteins (D-ωTA-D or D-ECFP-D) diluted in assembly buffer were incubated with 100 mg of AG-Co^{2+} functionalized with C-His for 1 hour at 4 ºC under orbital rotation, afterwards the carrier was washed with 2 mL of assembly buffer to remove non-specifically bound proteins. Before binding, 1 mL of D-ECFP-D pure protein (0.37 mg x mL^{-1}) was incubated with 1.32 µL of thrombin at 5.6 mg x mL^{-1} in 25 mM Tris-HCl at pH 7 and 4 ºC to remove the N-terminal histidine-tag and further use it as dockerin cargo protein as described above. In a final step, the solid-phase assembly was completed by incubating the obtained C-His/D-ωTA-D or C-His/D-ECFP-D carrier (100 mg)

with 1 mL of C-ADH crude extract following the same process as described in the previous step.

All washed, final carrier obtained from the solid-phase assembly process were analysed by SDS-PAGE (sodium dodecyl sulfate–polyacrylamide gel electrophoresis**)**. Briefly, a 1:3 (w:v) suspension of carrier and Laemmli buffer was boiled in a water bath for 5 min. Then, the samples were centrifuged at 9391 x g and the supernatant was withdrawn, loaded onto a SDS-PAGE gel and run as described in standard molecular biology protocols.[22] In parallel, all washed carriers were similarly suspended in a 25 mM Tris-HCl, pH 7 buffer with 500 mM imidazole, and the supernatant was collected and analysed by Bradford and SDS-PAGE to determine eluted protein concentrations.

3.2.9 Solid-phase assembly of the iSECel-II and iSECel-III systems

In the case of the iSECel-II systems, 2 mL of purified His-D (0.2 mg x mL^{-1}in system A and 0.1 mg x mL^{-1}in the system B) were incubated with 200 mg of AG-Co^{2+} placed in a micro Bio-spin column respectively and incubated under orbital rotation for 1 hour at room temperature. Then, the suspensions were filtered and AG-Co^{2+} functionalized with His-D were washed with 5 mL of assembly buffer (25 mM Tris-HCl buffer at pH 7 and 1 mM $CaCl_2$) to remove non-specifically bound proteins and equilibrate the carriers for the following assembly step, the C-ADH assembly. So, 2 mL of crude extracts containing the cohesin-ADH enzyme in assembly buffer were incubated with 200 mg of AG-Co^{2+} functionalized with their corresponding His-D for 1 hour at 4 ºC under orbital rotation. Afterwards, the carrier was washed with 5 mL of assembly buffer to remove non-specifically bound proteins. Next, the crude extracts containing the D-NOX enzyme were incubated with the corresponding carriers functionalized with the His-D/C-ADH (system A and system B) for 1 hour at 4 ºC under orbital rotation and washed using the 5 mL of the assembly buffer. Finally, 2 mL of the crude extract of His-BpCAT-C that was previously incubated overnight with thrombin in a ratio (1:50) in 25 mM Tris-HCl at pH 7 and 4 ºC to remove the N-terminal histidine-tag was incubated, were incubated with the corresponding carriers (system A and system B) for 1 hour at 4 ºC and washed with 5 mL of assembly buffer.

The iSECel-III systems were assembled as was described before, using 2 different initial protein concentrations (0.2 mg x mL^{-1}in system C and 0.1 mg x mL^{-1}in system D). Where the first pure protein assembled was His-BpCAT-C, next, the crude extract of D-NOX and followed by the assembly of the C-ADH from the crude extract.

3.2.10 Analysis of mass and molar ratio of the protein assembled in the iSECel systems

The quantity of assembled proteins and both mass and molar ratio of the protein domains forming the scaffold were determined by densitometry analysis of SDS-PAGE gels using an in-gel BSA calibration curve (1-0.04 mg x mL^{-1}) in the case of iSECel-I system. Samples were prepared as follows: 5 mg of iSECel-I carrier were incubated with 15 µL of Tris-HCl 25 mM at pH 7 and the resulting suspension was incubated with 15 µL Laemmli buffer at 100 ºC for 5 min. Then, the suspension was centrifuged at 9391 x g and 10 µL of the supernatant was analysed by SDS-PAGE according to standard molecular biology methods.[22] The gel was stained with Coomassie and imaged Gel Doc EZ Gel documentation system (BIORAD) for densitometric analysis using FIJI software .[25]

A similar protocol as the one described above was employed for the protein quantification of the proteins in iSECel-II and iSECel-III systems. However, in these cases, we used the molecular weight from Promega that gives the exact concentration of protein in the band corresponding with the 50 kDa molecular weight instead used the BSA calibration curve.

3.2.11 Quartz crystal microbalance with dissipation (QCM-D) to monitor the assembly of iSECel-I

QCM-D measurements were conducted to monitor the solid-phase iSECel-I assembly through mass deposition. These assays were performed with an E4 QCM-D (Q-sense, Biolin Scientifc) at 23 ºC employing SiO_2 coated (50 nm) quartz crystals (5 MHz) from Q-Sense as described in detail elsewhere.[26] Quartz crystals were functionalized prior to the iSECel-I immobilization. Initially, crystals were exposed to 3 M NaOH aqueous solution for 30 min and then rinsed with distilled water for 10 min. Subsequently, sensor disks were incubated for 16 hrs at 23 ºC with GPMES at 5 % v/v in aqueous solution at pH 8.5 to activate the surface with epoxy groups. Then, they were rinsed with distilled water and incubated for 3 hours with 0.5 M of IDA aqueous solution at pH 11. Finally, crystals functionalized with IDA groups were incubated with $CoCl_2$ 30 mg x mL^{-1} for 1 h to enrich the sensor surfaces with Co^{2+} chelates. Afterwards, the functionalized crystals were placed in the QCM-D chamber and equilibrated with 25 mM Tris-HCl at pH 7 for 10 min. For the assembly of the iSECel-I each protein domain was flowed through the chamber until stable values of frequency reached a plateau. Every immobilized protein domain was then rinsed with its immobilization buffer, which was 25 mM Tris-HCl at pH 7 for C-His and 25 mM Tris-HCl with 1 mM of $CaCl_2$ at pH 7 for D-ωTA-D and C-ADH. Finally, when the immobilization of the iSECel-I was completed, the chamber was rinsed with 0.5 M of imidazole.

3.2.12 Confocal Laser Scanning Microscopy (CLSM) of iSECel-I

The spatial distribution and co-immobilization of the fluorescently labelled protein domains immobilized on AG-Co^{2+} beads, was followed by CLSM with a Spectral ZEISS LSM 880 microscope and excitation lasers of λ_{ex} = 488 nm and λ_{ex} = 561 nm for FITC and or Rhodamine B, respectively.

Fluorescent labelling of protein domains was based on procedures reported elsewhere for optimal fluorochrome bioconjugation.[27] Briefly, the reaction mixture of 1 mg x mL^{-1} enzyme solution in 100 mM of sodium bicarbonate buffer at pH 8 was mixed with the corresponding fluorophore functionalized with an isocyanate group (1 M FITC and Rhodamine B isothiocyanate stocks were prepared in DMSO) at 1:10 molar ratio. The labelling reaction was then incubated for 1 h under gentle shaking at 25 ºC. Subsequently, the unreacted fluorophore was removed through a tangential ultrafiltration unit (10 kDa) with a 25 mM sodium phosphate solution at pH 7 until no coloration was observed in the filtered solution. C-ADH was labelled with Rhodamine B isocyanate (C-$ADH_{Rh,}$ red) and D-ωTA -D was labelled with FTIC (D-ωTA-D_{FTIC}, green). Labelled proteins were assembled in iSECel-I system following the protocol described in section 6 with C-His primed AG-Co^{2+} microbeads and 1.8 mg of protein per gram of carrier.

A 1:200 (w:v) buffered (25 mM sodium phosphate pH 7) suspension containing the carrier with the iSECel-I system was analyzed by CLSM using 10X and 40X objectives. The resulting micrographs were analyzed with FIJI using the corresponding plugins to determine co-localization and the fluorescence profile along the radius of single beads. First, from the confocal images, we obtained an average and normalized fluorescence profile, using FIJI software and its plugin module for radial profile generation (developed by Paul Baggethun). Subsequently, a Gaussian fit was applied to the obtained profiles of 10 single beads of similar size (Figure 4, A). Then, we searched for the fitted data point that corresponds to the 50% of the maximum normalized fluorescence fitted peak ($y_{max}/2$), and the corresponding radius coordinate (*x*) to that data point was then subtracted from the radius of the analysed bead to finally obtain the FWHM (full width half maximum) (Figure 4, B).

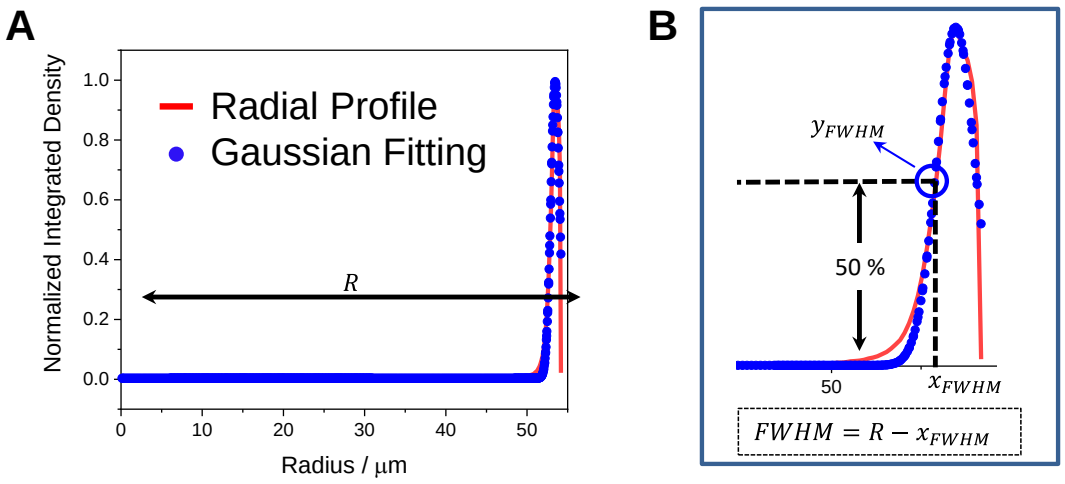

Figure 4: Explanatory illustration of FWHM calculation

A. *Representation of fluorescence radial profile (blue dots) together with the corresponding Gaussian fitting (red line) (R represents the particle radius).* ***B.*** *Explanatory illustration of FWHM estimation derived from the obtained fitted radial profile.*

The relative occupied radius (% FWHM) was estimated by dividing the FWHM by the average radius of the analysed beads. Furthermore, Pearson Manders and correlation intensity coefficients were determined through analysing the CLSM micrographs with JaCop plugin in FIJI.[28] Pearson coefficient expresses the intensity correlation of two fluorophores in two fluorescence micrographs. Mander coefficient A (MA) shows the proportion of fluorescein labelled enzymes that overlap in the space with the rhodamine labelled enzymes, while Mander coefficient B (MB) shows the opposite; the proportion of rhodamine labelled enzymes that overlap in the space with the fluorescein labelled ones. The intensity correlation coefficient (ICQ) informs us about the same with Pearson coefficient but eliciting the differences in the intensity between the two fluorophores.

3.2.13 Recovered activity of the enzymes assembled in the iSECel-I system

The alcohol dehydrogenase and transaminase activities recovered upon the assembly process were determined using the colorimetric enzymatic assayed described in 3.2.6

3.2.14 Biotransformation of alcohol into amines catalysed by free enzymes and iSECel-I systems with different spatial organization.

Batch reaction: 60 and 50 mU x mL^{-1} (measured by colorimetric assays, see section 3.2.7) of either soluble or iSECel-I immobilized ωTA and ADH, respectively, were incubated with 10 mM of 3-methyl butanol, 2 mM of *rac*-1-phenylethylamine, 100 mM of acetone, 1 mM of $CaCl_2$ and 0.01-1 mM of NAD^+ in 25 mM Tris-HCl buffer at pH 7 for 24 hrs at 30 ºC and 250 rpm. For the immobilized samples, the corresponding activity was added as 100 mg of the

co-localized iSECel-I (50 mg of Ag-Co^{2+} loading C-His/D-ωTA-D/C-ADH and 50 mg of the same carrier loading no protein) or segregated iSECel-I (50 mg of Ag-Co^{2+} loading C-His/D-ωTA-D and 50 mg of the same carrier loading C-His/D-ECFP-D/C-ADH). The reaction courses were monitored by measuring the acetophenone production by both absorbance at 254 nm and liquid chromatography. After 24 hrs, the enzymes were removed by either vacuum filtration (for the immobilized systems) or tangential ultrafiltration (for free enzymes) and the reaction crudes were extracted for further gas chromatography analysis. In particular, the co-localized iSECel-I preparation was vacuum filtered after each 24 hrs cycle and re-used in consecutive reaction cycles.

Flow reaction: 200 mg of co-localized iSECeI-I were packed into a plug-flow column (2 x 0.4 cm) and fed with 10 mM of 3-methyl butanol, 2 mM of rac-1-phenylethylamine, 100 mM of acetone, 1 mM of CaCl2 and 0.5 mM of NAD+ in 25 mM Tris-HCl buffer pH 7 at 10 µL x min-1 flow and 25 ºC. The outcome fractions were collected every 30 minutes and analysed by HPLC.

3.2.15 Kinetic studies and operational stability assays of the iSECel-II and iSECel-III systems for the bioconversion of 1,5-pentanodiol

Kinetic reactions were done in batch using 50 mg of the each iSECel systems (A to D systems), which were placed into Bio-spin columns. 600 µL of the reaction mixture containing 10 mM of Diol, 1 mM of NAD^+ and 0.15 mM of FAD in 100 mM phosphate buffer at pH 8 were added to the biocatalysts and to facilitate the oxygen diffusion to the reaction, an open syringe needle were added to the columns. The reactions were incubated at 30 ºC at 250 rpm inside an orbital incubator. The reactions courses were monitoring by removing samples at periodic intervals and further analyzed them by chromatographic methods. The batch recycling reaction were done followed the same protocol but taking all the sample after 24 hours of reaction.

3.2.16 Chromatographic methods

High performance liquid chromatography (HPLC):

For the iSECel-I system, the samples from reaction crudes were filtered and then analysed by HPLC (Waters 2690) equipped with a PDA detector using a ACQUITY UPLC® BEH C18 1.7 µm (2.1 x 50 mm) Waters column. Analytes were eluted with a linear gradient of 5 min with gradient mobile phases composed of formic acid 0.1% in water and acetonitrile. The gradient was set from 1 % acetonitrile to 99 % acetonitrile at a flow rate of 0.5 mL x min^{-1}. Chromatograms were recorded at 245 nm and the acetophenone exhibited a retention time

of 2.3 min. Concentration of acetophenone in samples was determined by using a calibration standard curve of different concentrations of pure acetophenone.

In the case of the iSECel-II and iSECel-III systems, the HPLC was employed to quantify the 5-hydroxipentanal through the derivatization into the corresponding *O*-benzylhydroxylamine derivative as was previously described by our group.[29] To achieve these, 10 µL of aqueous reaction sample was mixed with 50 µL *O*-benzylhydroxylamine hydrochloride (30 mM in pyridine/methanol/water 33:15:2) and incubated for 5 min at 25 °C. Afterwards, 500 µL of methanol was added and then centrifuged for 5 min at 13 450 x g. HPLC analysis was conducted in an Agilent Technologies 1260 Infinity II chromatograph equipped with a Poroshell EC-C18 column (4.6 × 100 mm^2, 2.7 µm). Samples were detected at 215 nm and were eluted at 1 $mL \cdot min^{-1}$ flow rate employing two mobile phases: phase A composed of trifluoroacetic acid 0.1% in water and phase B composed of trifluoroacetic acid 0.095% in 4:1 acetonitrile/water. Elution conditions: 10−100% of B over 30 min, followed by 10 min to recover the initial conditions. The retention time of *O*-benzylhydroxylamine derivatized 5-hydroxypentanal was 14.4 min.

Gas chromatography (GC):

For the iSECel-I system prior to GC analysis, liquid-liquid extractions were done. Briefly, 120 µL of sample were mixed with 24 µL of NaOH 10 M and 244 µL of dichloromethane containing 2 mM eicosane as internal standard. Then, the mixture was vigorously shaken and centrifuged to remove and discard the aqueous phase. The organic phase was recovered and mixed with 30-50 mg of $MgSO_4$ to dry the samples before GC analysis on an Agilent 8890 GC equipped with a 7693A Agilent Technologies autosampler injector and flame ionization detector (FID). Samples were separated on a phenyl silicone 5 % column (HP-5 30 m, 0.32 mm, 0.25 µm, Agilent Technologies). Helium was used as carrier gas with a flow of 1.35 mL x min^{-1}. Injector temperature was set at 250 ºC, split ratio was set to 6:1 with a split flow of 8.11 mL x min^{-1}. FID flame temperature was set at 300 ºC. Separation of compounds was done using the following temperature ramp: initial temperature was set at 60 ºC and maintained for 1 min, then followed by a ramp until 110 ºC with a rate of 3.5 ºC x min^{-1}, then the temperature was kept at 110 ºC for 2 min and then followed by another ramp up to 280 ºC at a rate of 25 ºC x min^{-1}. Finally, the temperature was kept at 280 ºC for 6 min.

In the case of the iSECel-II and iSECel-III systems, the GC method employed was also described previously by our group.[29] Briefly, prior to GC analysis a liquid−liquid extraction of the compounds of interest was performed. To achieve that, 50 µL of the reaction sample was mixed with 200 µL of ethyl acetate containing 2 mM eicosane as the external standard.

After the extraction, 30−50 mg of anhydrous $MgSO_4$ was added to dry samples before GC analysis. Gas chromatography analyses were carried out in the same equipment and column described above. Helium was employed as the support gas and equipped with a flame ionization detector (FID). The injector was set at 280 °C and the FID at 300 °C. Separation of extracted compounds in ethyl acetate was done by the following temperature program: the initial temperature at 60 °C, maintained for 2 min, ramp to 160 °C at a rate of 10 °C x·min^{-1}, ramp 2− 240 °C at a rate of 20 °C·x min$^{-1.}$ and finally maintained 4 min.

3.3 Results & Discussion

The first system tested only requires one type of cohesin-dockerin pair to assemble multi-enzyme systems which yet allows easy control over the assembly (density and ratios) of enzymes on microbead surfaces. This first model system allows the spatial organization of a two-step cascade for one-pot transformation of alcohols into amines concurrently catalyzed by a NADH-dependent alcohol dehydrogenase (ADH) and an ω-transaminase (ωTA). In this first system we demonstrate the capability to orderly assemble the dual enzyme system in solid phase by sequential binding of cohesin-dockerin pairs genetically fused to recombinant enzymes (Figure 5).

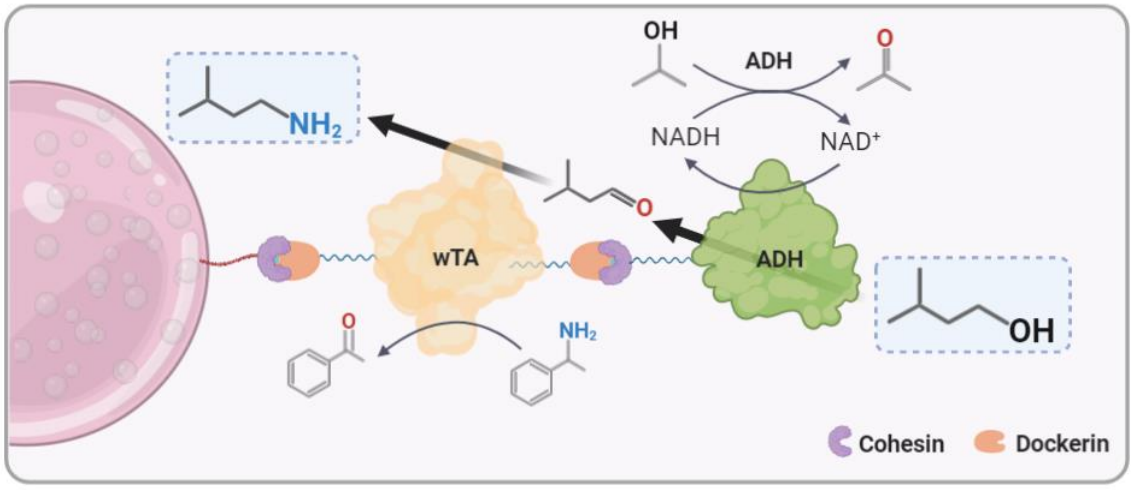

Figure 5: Schematic representation of immobilized scaffolded enzymatic cellulosome (iSECel-I) assembled in solid phase.

Porous agarose microbead (pink) functionalized with cobalt chelating groups bind His-tagged cohesin domains as priming units to which enzymes are bound via cognate dockerin domains as shown. ***ωTA:*** *ω-transaminase.* ***ADH:*** *Alcohol dehydrogenase.*

From the increasing number of described cohesin-dockerin pairs, we chose the well-characterized type II cohesin-dockerin pair from *Clostridium thermocellum.*[30, 31] The 20 kDa cohesin (Coh) domain was fused to the N-terminus of a tetrameric ADH from *Bacillus*

(Geobacillus) stearothermophilus[32] (~56 kDa monomer of C-ADH), while the 18 kDa dockerin (Doc) domain was fused to both the N- and C-terminus of a dimeric PLP-dependent (R)-ωTA from *Aspergillus terreus*[33] (~74 kDa monomer of D-ωTA-D) (structures shown in Figure A 1). As a proxy element for D-ωTA-D, we also fused Coh domains to both termini of a monomeric enhanced cyan fluorescent protein (~68 kDa D-ECFP-D). Furthermore, flexible GS-linkers were inserted between the cellulosome domains and the enzymes to reduce potential steric hindrances during the interaction (Table A 1). The presumed multimeric fusion protein complexes therefore display 4 Doc (~148 kDa D-ωTA-D dimer) and 4 Coh (~226 kDa C-ADH tetramer) sites for the interaction with their cognate binding domains. Finally, to prime the solid-phase assembly of the iSECel-I system, we fused a 6xHistine-tag to the C-terminus of the Coh domain (~ 21 kDa C-His) for its binding to agarose porous microbeads functionalized with cobalt chelates (AG-Co^{2+}) (Figure 6). Each modified protein was overexpressed in *E. coli BL21(DE3)* cells and their corresponding cell-free protein extracts were incubated with AG-Co^{2+} microbeads. The binding selectivity and strong affinity of the cohesin-dockerin interaction enables solid-phase assembly of the iSECel system directly from crude cell lysates using therefore non-purified enzymes. In three sequential steps, microbeads were first incubated with C-His and then followed by incubations with D-ωTA-D and C-ADH. In this iSECel-I system, the enzymes themselves are part of the scaffolding unlike other reported mini-cellulosome systems (Figure 5).[18]

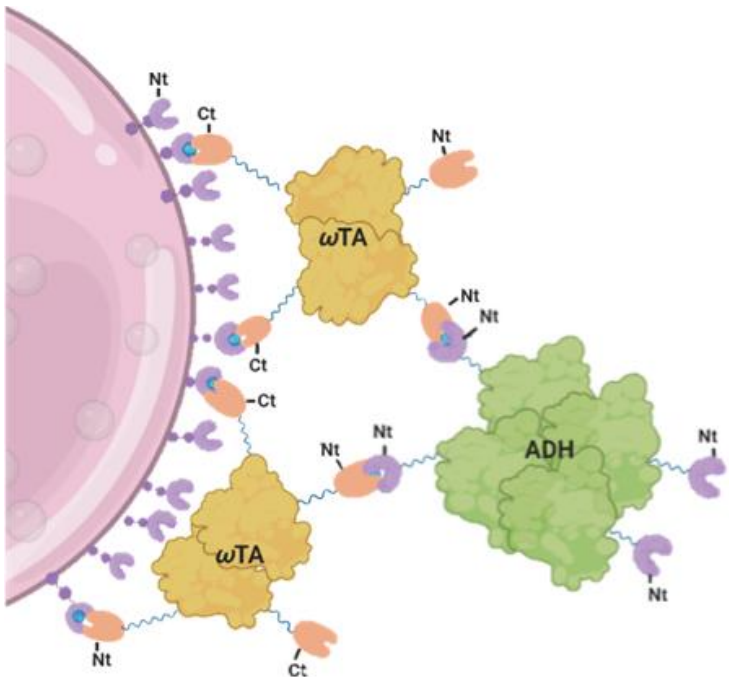

Figure 6: Interaction model of the cohesin-dockerin domains in the iSECel-I system.

Representation of the artificial cellulosome assembly immobilized on AG-Co^{2+} , referred as iSECel-I. Components are not drawn to scale and are exaggerated in size for the illustration proposes.

3.3.1 Binding specificity of the Coh/Dock pair to drive the iSECel-I assembly

To test and optimize the assembly of the first iSECel system, we first incubated D-ωTA-D with AG-Co^{2+} functionalized with C-His in presence of 1 mM $CaCl_2$. Herein, we demonstrated that D-ωTA-D is immobilized on microbeads displaying C-His, but not on naked ones (Figure 7, A and B). We obtained similar results with the monomeric D-ECFP-D, suggesting that this method will also work for other proteins (Figure 7, C).

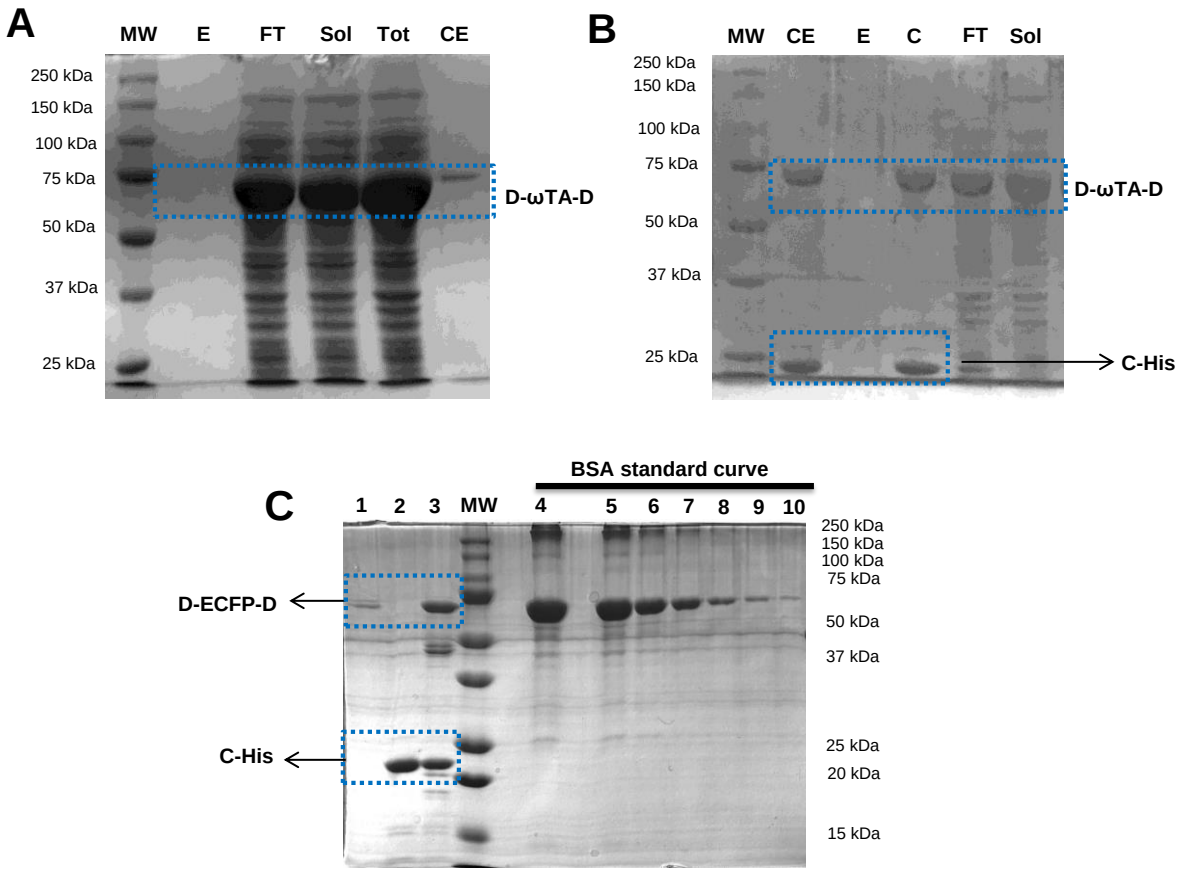

Figure 7: SDS-PAGE analysis of D-ωTA-D immobilization on agarose microbeads.

A. *Immobilization of D-ωTA on AG-Co^{2+}initial carrier.* ***B.*** *AG-Co^{2+}carrier functionalized with His-C and immobilization of D-ωTA driven by Coh/Dock interaction.* ***C:*** *Immobilization of D-ECFP-D and BSA standard curve. For panels A and B,* ***Tot:*** *Total cell-free extract after sonication lysis;* ***Sol:*** *Soluble cell-free extract after centrifugation of the cell lysate;* ***FT:*** *Flow-through of the soluble cell-free extract after incubation with the carrier;* ***C:*** *Carrier before imidazole elution;* ***E:*** *Elution with imidazole.* ***CE:*** *Carrier after elution with imidazole. In panel C;* ***Lane 1:*** *AG-Co^{2+} carrier after the incubation with D-ECFP-D.* ***Lane 2:*** *AG-Co^{2+} carrier after the immobilization of C-His.* ***Lane 3:*** *AG-Co^{2+} carrier functionalised with C-His after the immobilisation of D-ECFP-D.*

Lane 4 to10: *BSA standard curve (1 to 0.04 mg x mL-1).* ***MW****: Protein molecular weight marker. BSA standard curve (y=7269.5x – 89, R2=0.99).*

3.3.2 Optimization of the C-His loading

Next, we investigated the effect of C-His functionalization density (i.e. load) on the D-ωTA-D immobilization yield. To do this, we incubated AG-Co^{2+} with different concentrations of purified C-His, offering 1.8 to 3.7 mg of C-His per gram of carrier, achieving a quantitative immobilization yield in all cases. The functionalized microbeads were then incubated with the same amounts of D-ωTA-D in cell-free extracts and the immobilized proteins were analyzed by SDS-PAGE and quantified by densitometry as it is shown in the (Figure 8).[34]

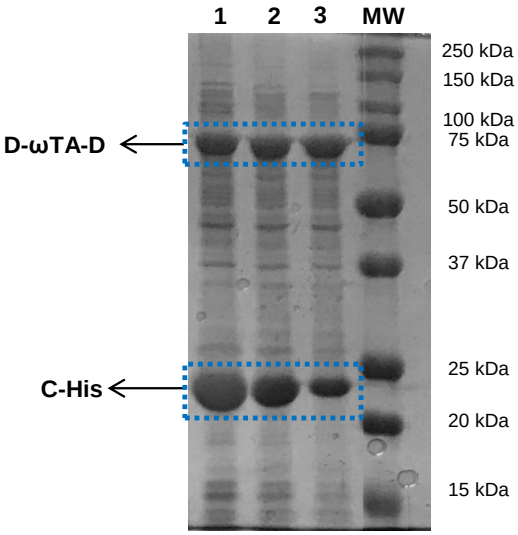

Figure 8: Optimization of the C-His immobilization on AG-Co^{2+} agarose microbeads.

Line1:*Carrier loaded with 3.7 mg of C-His;* ***lane 2:*** *carrier loaded with 3 mg of C-His;* ***line 3:*** *carrier loaded with 1.8 mg of C-His per gram of carrier after the immobilization step with D-ωTA-D.* ***MW:*** *Protein molecular wight marker.*

We found that the immobilization yield of D-ωTA-D minimally increased at higher C-His functionalization density. Binding of D-ωTA-D was already maximal at the lowest C-His load (1.8 mg C-His x g^{-1} microbeads) herein tested. These results suggest that the overall assembly efficiency of the soluble D-ωTA-D is limited by the density and the crowding of the Coh priming unit at the surface of the AG-Co^{2+}. Similar insights were found with mini-cellulosomes displayed on yeast cells surfaces, where molecular crowding was shown to limit multi-enzyme assembly efficiency.[21]

3.3.3 Assembly of the iSECel-I system

To complete the assembly of the dual enzyme cascade for our iSECel-I system, we therefore opted to use microbeads functionalized with 1.8 mg C-His x g^{-1} microbeads that

were saturated with D-ωTA-D (Figure 8) for subsequent C-ADH assembly. SDS-PAGE analysis confirmed successful solid-phase assembly of the iSECel-I system as all protein units were disassembled and desorbed from the microbeads under denaturing conditions (Figure 2A).

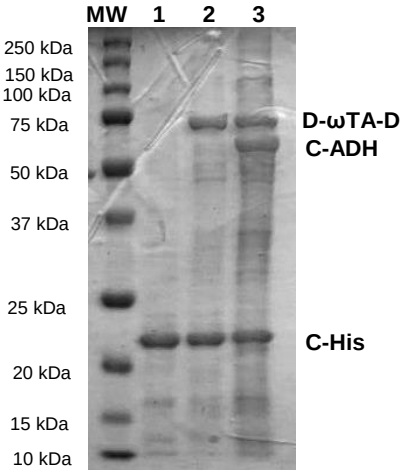

Figure 9: SDS-PAGE analysis of proteins attached to AG-Co^{2+} microbeads after each assembly step in the iSECel system.

Lane 1: *C-His released upon the first assembly step.* ***Lane 2:*** *C-His and D-ωTA-D released upon the second assembly step.* ***Lane 3:*** *C-His, D-ωTA-D and C-ADH released upon the third assembly step.* ***MW:*** *Molecular weight marker.*

Quantification of protein bands by densitometry estimated a mass ratio of 1.1:1.3:1 for C-His:D-ωTA-$D_{(2\text{-mer})}$:C-$ADH_{(4\text{-mer})}$ (corresponding to a molar ratio of 12:2:1) at the microbead surface (see section 3.2.10). These ratios reflect the size differences of the monomeric (C-His) and quaternary structures of the interacting enzymes in the iSECel. In this supramolecular assembly, each C-ADH tetramer (4 Coh domains) appears to be attached to two D-ωTA-D dimmers (4 Doc domains). We noted that the assembled iSECel-I could not be eluted from the microbeads upon incubation with imidazole and only harsh denaturing conditions used for SDS-PAGE analysis were capable to disassemble the scaffolded multi-enzyme system. This suggested a dense coverage of the microbeads and strong multivalent interactions between Coh and Doc domains of the assembled proteins.

Table 2: Mass and molar ratio of assembled proteins in iSECel-I immobilized on AG-Co^{2+} determined by densitometry of the SDS-PAGE electrophoresis gel.

	C-His	D-ωTA-D (dimer)	C-ADH (tetramer)
$^{a}mg \times g^{-1}_{carrier}$ [a]	1.8	2.06	1.61
$^{a}nmol \times g^{-1}_{carrier}$ [b]	85	14	7

Mass ratio	1.1	1.3	1
Molar ratio	12	2	1

[a] Concentration of protein bands shown in Figure 9.

[b]Molar concentrations were calculated using the molecular weights of multimeric proteins: C-His = 21 kDa, D-ωTA-D (2-mer): 148 kDa, C-ADH (4-mer): 226 kDa

3.3.4 Characterization of the iSECel through QMC-D

To further characterize the iSECel assembly in more detail, we monitored the sequential iSECel assembly by QMC-D (quartz crystal microbalance with dissipation) on cobalt chelate functionalized silica surfaces following the same stepwise protocol used for microbeads functionalization (Figure 10). Each adsorption step decreases the frequency (increasing in mass deposition) and increases the energy dissipation factor (increase of surface viscoelasticity) of the system. Frequency changes reflected the adsorption of C-His (Δf=17.7 Hz) onto the sensor surface and the subsequent binding of D-ωTA-D (Δf=39.3 Hz) and C-ADH (Δf=28.7 Hz). Larger frequency changes correspond to higher mass adsorption, pointing out that the calculated mass ratio of the adsorbed C-His: D-ωTA-D:C-ADH (0.6:1.4:1) through QMC-D were similar to that ratio obtained by SDS-PAGE densitometry (1.1:1.3:1)) (Table 2). Upon iSECel assembly, the total differences in frequency and energy dissipation (Δf= 85.7 Hz and ΔD = 9.69 x 10^{-6}) confirm the adsorption of a large macromolecular complex and the formation of a soft hydrated film. Remarkably, rinsing the sensor surface with 0.5 M imidazole caused only a small decrease in frequency (Δf= 4.23 Hz), confirming the results obtained with microbeads upon imidazole elution.

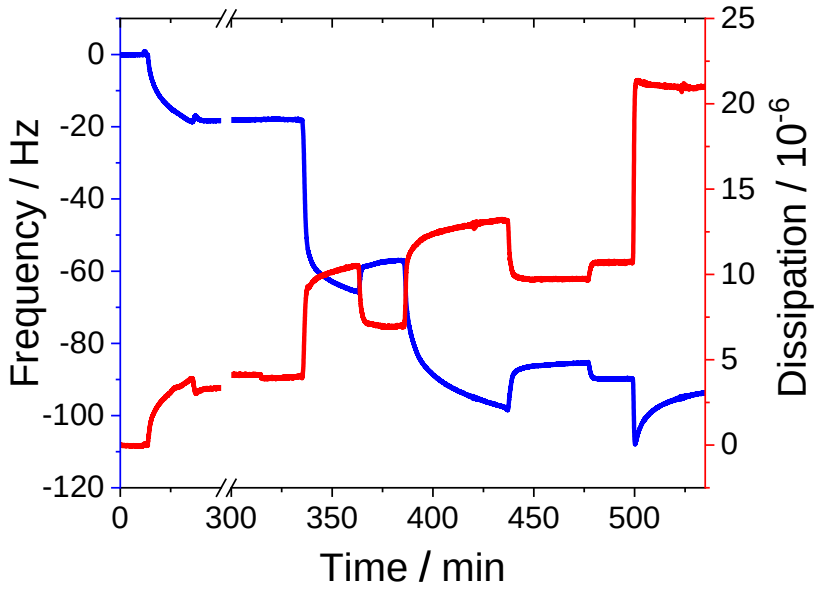

Figure 10: Real-time QMC-D measurements of the iSECel sequential assembly.

Assemble of C-His, D-ωTA-D and C-ADH on Co^{2+} functionalized quartz sensor surface. Imidazole means a 0.5 M imidazole wash.

3.3.5 Characterization of the iSECel through CLSM

We then performed the iSECel assembly with fluorescently labelled D-ωTA-D and C-ADH to analyse their spatial location within the microbeads by confocal laser scanning microscopy (CLSM) (Figure 11, A). Both enzymes occupied the outer surface of the microbeads, representing 4.45 ± 1.56 % of the particle radius (Figure 11, B).

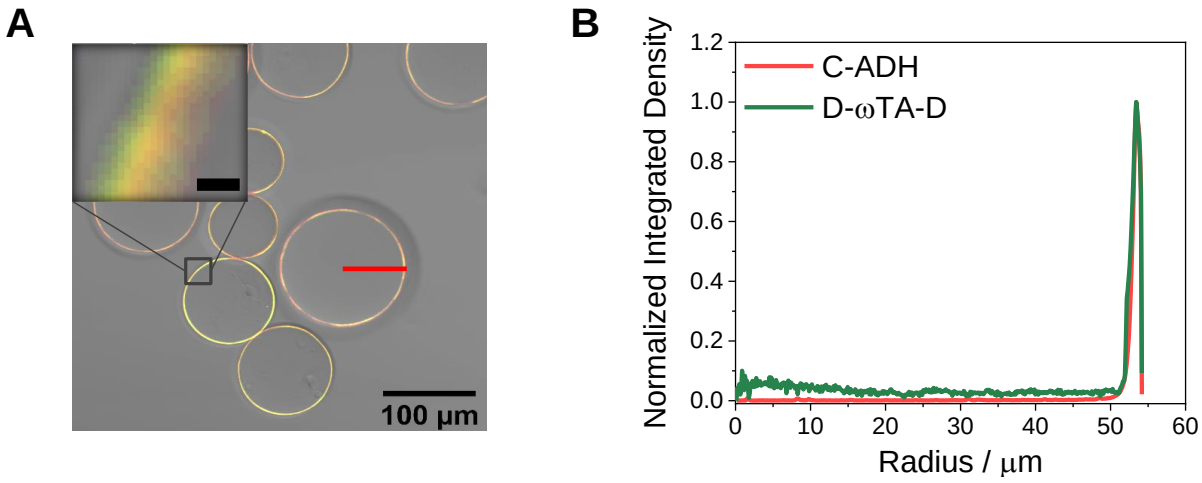

Figure 11: Assembly analysis by CLSM.

A. *Co-localization of D-ωTA-D (green, fluorescein labelled) and C-ADH (red, rhodamine labelled) on C-His functionalized microbeads (50-150 µm diameter) by CLSM. Red line depicts the radial cross-section of one selected microbead. Top left inset is the magnification of the outer surface of the microbead; scale (black line) is 0.5 µm.* ***B.*** *Average (n = 10) radial cross-section fluorescence profile of D-ωTA-D and C-ADH co-immobilized on AG-Co2+ microbeads (for more details see 3.2.12).*

Quantitative image analysis confirmed that 93% of the two enzymes co-localized at the outer 3-4 µm of the microbeads according to Pearson´s coefficient (Table 3).[35]

Table 3: Infiltration and co-localization parameters of the multi-enzyme system assembled and immobilized agarose porous microbeads AG-Co^{2+}

Protein infiltration within porous particles		**Co-localization parameters**	
Labelled Enzyme (Fluorophore)	**% FWHM[a]**	Coef. Pearson	0.93
		Coef. MA	0.96
D-wTA-D (Fluorescein)	4.45 ± 1.56	Coef. MB	0.91
C-ADH (Rhodamine B)	4.22 ± 1.48	ICQ	0.48

[a] % FWHM was calculated as described in section 3.2.12 and Figure 4.

3.3.6 Immobilization parameters for the iSECel

After characterizing iSECel solid-phase assembly, we next determined the immobilization parameters for each enzyme during the iSECel assembly using colorimetric assays. About 90% of the D-ωTA-D activity (immobilization yield Ψ%) in the cell-free extract was bound to the microbeads activated with C-His. 94% of loaded D-ωTA-D was active upon attachment to the microbeads, recovering an activity of 0.51 U x g^{-1} of microbeads. Subsequent attachment of C-ADH achieved a 35% immobilization yield, but the immobilized enzyme recovered only 7% of the loaded activity (corresponding to 0.033 U g^{-1} of microbeads) upon immobilization. While the activity of D-ωTA-D was only slightly reduced upon assembly, the activity of C-ADH was significantly reduced once assembled to the iSECel (Table 4).

Table 4: Apparent activity of the enzymes assembled in the iSECel.

Assembly Product	Enzyme	[a]Ψ %	[b]Load (U x g^{-1})	[c]RA (U x g^{-1}) (%)
Co-localized iSECel (His-C/D-ωTA-D/C-ADH)	ωTA	89 ± 0.3	[d] 0.61	[d] 0.44 (72)
	ADH	35 ± 4	[d] 0.52	[d] 0.033 (6)
Segregated iSECel (His-C/D-ωTA-D + His-C/D-ECFP-D/C-ADH)	ωTA	89 ± 0.3	[d] 0.61	[d] 0.51 (94)
	ADH	36 ± 7	[d] 0.41	0.18± 0.08 (58)

[a.] Immobilization yield (Ψ) % = (100 – ((Activity remaining in supernatant after immobilization / Activity in cell-free extract prior to immobilization) x 100).

[b.] Load represents the theoretically immobilized activity per gram of microbeads according to Ψ and considering the offered activity per gram of carrier.

[c.] Recovered activity (RA) is the measured activity per gram of microbeads after immobilization. The relative recovered activity (%) is the percentage of the loaded activity recovered after the immobilization (% RA = (RA/Load) x 100).

All mean values are the averages of three replicates with their corresponding standard deviation (SD). [d.] SD lower than the 5% of the mean value.

In contrast, C-ADH was 8 times more active using D-ECFP-D as a proxy for D-ωTA-D despite both dockerin cognates immobilized similar C-ADH yields (Table 4). We hypothesize that the more crowded environment of the co-localized iSECel within the agarose pores might induce conformational changes in ADH structure and/or impede the diffusion of co-factors/substrates towards its active site. We previously observed a similar activity reduction for this enzyme when co-immobilized with three other enzymes on porous microbeads.[36] The final ratio of activity of C-ADH: D-ωTA-D immobilized on the co-localized iSECel is 1:13

despite their 1:2 molar ratio, indicating that the alcohol oxidation will likely be the rate limiting step of this cascade.

3.3.7 Operational analysis

Once the activities of the two enzymes in the iSECel were confirmed, we applied this dual enzyme cascade for the one-pot, two step biotransformation of 3-methyl-1-butanol (3-MB) into 3-methyl-1-butylamine (3-MBA) (Figure 5). As auxiliary co-substrates, we used acetone as electron acceptor to regenerate NAD^+ for ADH catalysis and *rac*-phenylethylamine (*rac*-PEA) as amine donor to shift the transaminase reaction equilibrium towards the amine formation. We determined that the scaffolded C-ADH catalyzes the reduction of the co-substrate acetone 13 times faster than the oxidation of 3-MB thereby ensuring efficient NAD^+ co-factor regeneration for the first step of the biotransformation (Table 5). Then, we established that acetone is not a suitable substrate for the scaffolded D-ωTA-D and therefore does not compete with the aldehyde intermediate of the cascade reaction as its shown in the Table 5.

Table 5: Activity of the iSECel system towards different substrates.

Co-localized iSECel system	Substrate	Activity (U x g^{-1} carrier)
ADH activity	3-Methyl-1-butanol (3MB)	0.034
	Acetone	0.44
ωTA activity	3-Methyl-1-butanal	0.487
	Acetone	n.d

Enzyme activities were determined by colorimetric assays as described in section 3.2.7.

Therefore, during the concurrent transamination reaction, the R-selective D-ωTA-D transfers the amine group of R-1-phenylethyl amine (PEA) of the racemic co-substrate only to the aldehyde intermediate to yield 3-MBA and acetophenone. When the iSECel was incubated for 24 hrs (pH 7, 30 °C, 250 rpm) with 10 mM of 3-MB, 0.5 mM of NAD+, 100 mM of acetone and 2 mM of rac-PEA, we obtained 0.64±0.1 mM 3-MBA, representing 64% of the maximum theoretical conversion as the enantioselective D-ωTA-D only utilizes the half (R-isomer) of the amine donor rac-PEA (Figure 12). The overall iSECel catalyst productivity, in batch, was 4.4 nmol of 3-MBA min^{-1} g^{-1} under the conditions described above.

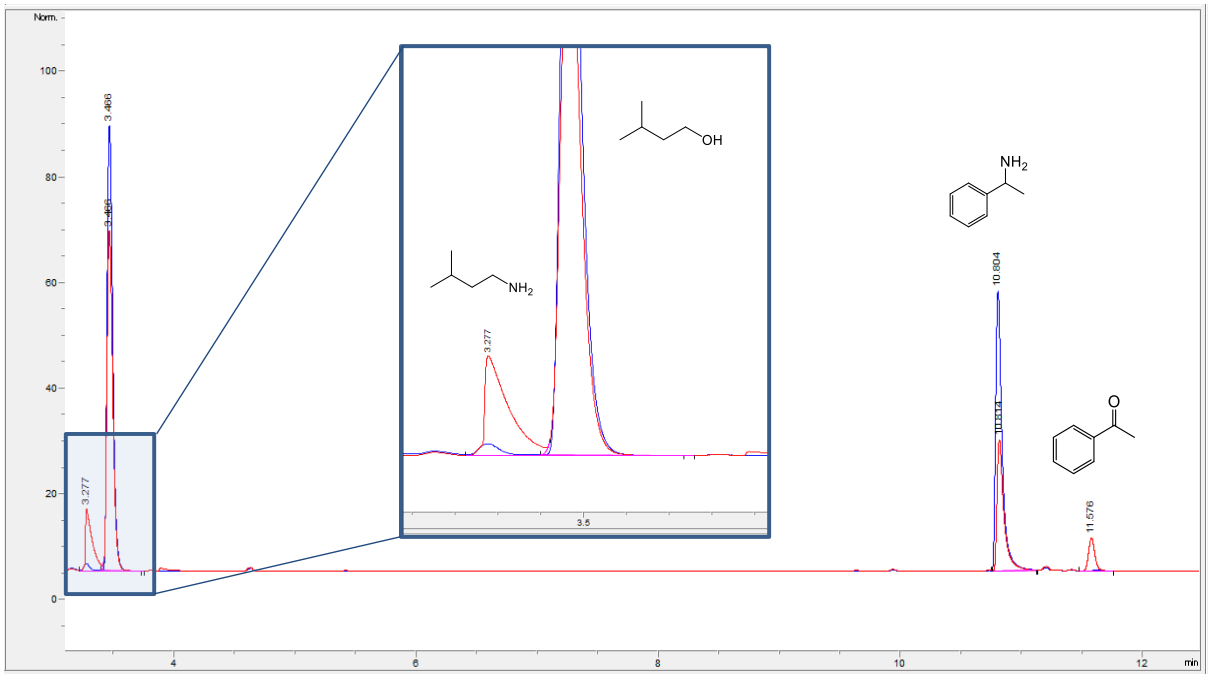

Figure 12: GC analysis of 3-MB biotransformation into 3-MBA.

Reaction crudes without (blue line) and with (red line) immobilized enzymes (as co-localised iSECel) were analyzed after 24 hrs of reaction by GC. Retention times: ***3-MBA*** *at 3.27 min;* ***3-MB*** *at 3.46 min;* ***PEA*** *at 10.8 min;* ***Acetophenone*** *at 11.58 min.*

3.3.8 Kinetic analysis of the different spatial distributions

To demonstrate that the physical proximity of both C-ADH and D-ωTA-D enhances the overall efficiency of the bio-cascade, we separately immobilized both enzymes through cohesin/dockerin interactions on two different microbeads of AG-Co^{2+}. To that aim D-ωTA-D was immobilized on one single microbead functionalized with C-His, while C-ADH was immobilized on another one but functionalized with the complex His-C/D-ECFP-D. Even though C-ADH was more active when immobilized by its own (Table 5), the segregated system yielded 25% less 3-MBA (0.45 ± 0.05 mM) than the co-localized one. In contrast, the free multi-enzyme system only reached 10% of the theoretical conversion (0.07 ± 0.01 mM).

The acetophenone production courses of the two-step oxidative amination catalyzed by iSECel with different spatial organizations confirm that co-localized iSECel catalyzed the step-wise transformation of 3-MB to 3-MBA more efficiently than the two enzymes separately immobilized on AG-Co^{2+} (segregated iSECel) (Figure 13, A). Furthermore, we observed no lag time in the acetophenone production when using co-localized iSECel unlike in the cascade performed with the segregated iSECel. The absence of lag phase in cascade reactions is one of the sings of substrate channelling,[37] supporting the physical proximity of the two enzymes in the co-localized iSECel architecture.

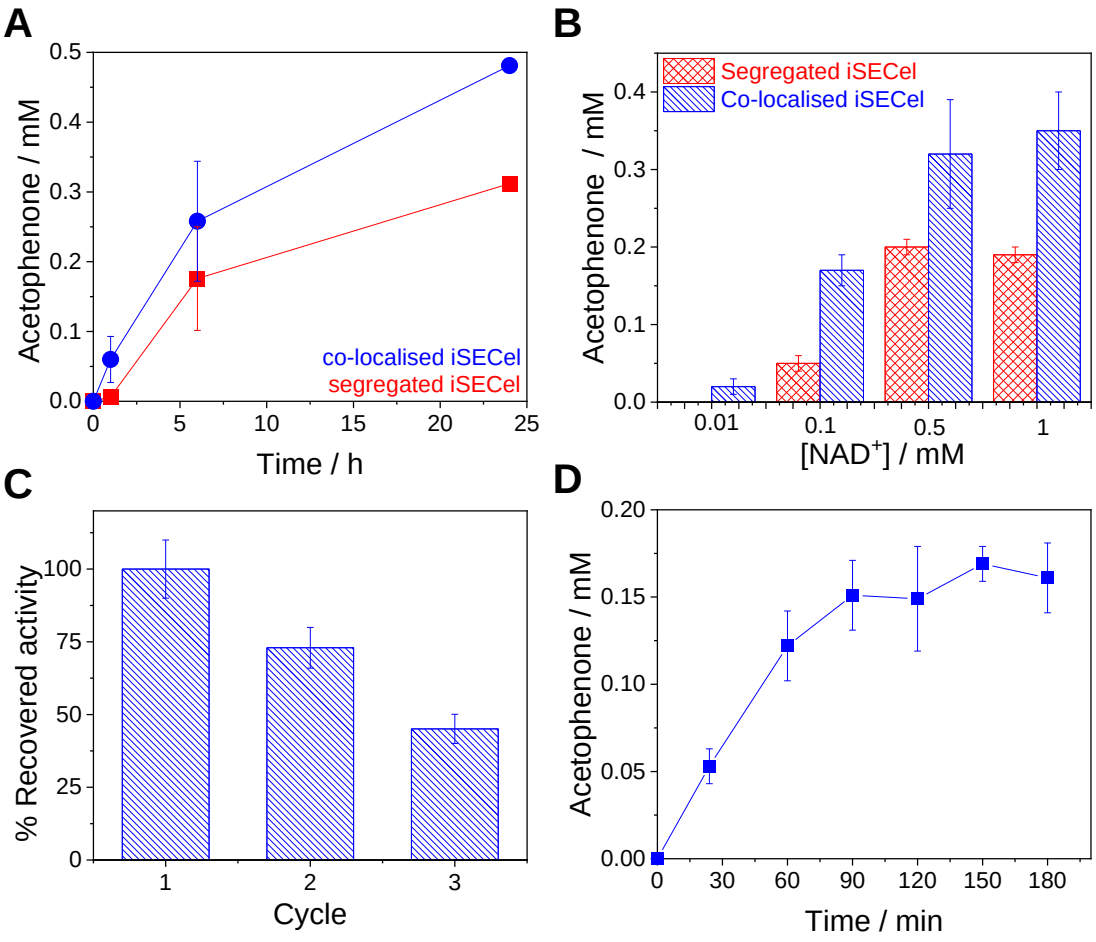

Figure 13: Kinetic study of the iSECel system.

A. *Reaction course of the oxidative amination of 3-MB into 3-MBA by monitoring the acetophenone titre during the biotransformation catalyzed by iSECels with different spatial organization.* ***B.*** *Acetophenone produced after 24 h at different NAD^+ concentrations.* ***C.*** *Recycling of co-localized iSECel in consecutive batch cycles* ***D.*** *Continuous reaction performed by co-localized iSECel packed into a plug-flow column at 10 µL x min^{-1} flow rate. In all panels, co-localized iSECels and segregated iSECels are shown as blue and red lines and bars, respectively. All reactions were performed in 10 mM of 3-MB and 1 mM of rac-PEA with 0.5 mM NAD^+ but in panel B, where NAD^+ concentrations varied. Plotted data are the mean values of three replicates with their corresponding standard deviation (error bars).*

Furthermore, the co-localized iSECel yielded 50% and 500% higher acetophenone titres compared to the segregated iSECel system with 0.5 and 0.1 mM NAD^+, respectively (Figure 13, B). At low NAD^+ concentrations, less aldehyde is produced by ADH and its transport to the physically segregated ωTA microbeads becomes rate-limiting. In contrast, the physical proximity in the co-immobilized iSECel minimizes this limitation. Therefore, the intermediate utilization was more efficient when the two enzymes were assembled into the synthetic cellulosome and co-immobilized on the same microbead. Such different was more drastic at

NADH concentration as low as 0.01 mM where acetophenone was only detected when iSECel was used. Similar effects were reported for a comparable enzyme cascade co-immobilized on porous agarose microbeads for the conversion of diols into aminoalcohols.[36]

Finally with this first system, we tested the reusability of our iSECel dual enzyme system. Figure 13 C shows that the multi-enzyme system can be recycled in batch, but its overall operational activity is reduced to 60% after 3 reaction cycles. To further expand the application of our system, we integrated the iSECel into a plug-flow column for continuous transformation of 3-MB into 3-MBA. Figure 13, D demonstrates that iSECel catalyst can operate in flow with a maximum production rate of 8 nmol of 3-MBA x min^{-1} x g^{-1} carrier, representing 2-times higher specific productivity than the batch operated system.

3.3.9 Expanding the concept of the iSECel system to a three-enzyme cascade

After testing the first iSECel system with a bi-enzymatic cascade, we decided to test the viability of utilising a different multi-enzymatic system containing three enzymes. Within this system, the three enzymes have been organized with two different spatial nanometric arrangements. We did this with the objective of studying the effect of the relative position of enzymes within the assembly on the overall cascade performance. (Figure 14). These new iSECel systems were designed for the bio-conversion of 1,5-pentanodiol (Diol in our scheme) to the corresponding lactone (same cascade as described in Chapter 4).

We firstly designed the fusion proteins which allow the cohesin-dockerin interaction to assemble our system. In this new iSECel system II, the cohesin-dockerin type II pairs from *Clostridium thermocellum* were employed similarly to the iSECel-I system. For the alcohol dehydrogenase, we used the construction C-ADH designed previously in this chapter. Unlike iSECel-I, the priming unit was the 6xHistidine-tag was fused to the dockerin domain (His-D). In the case of the NADH oxidase from *Thermus thermophilus,* the Doc domain was fused to the N-terminus (D-NOX) and the Coh domain was fused to the C-terminus of a tetrameric catalase from *Bordetella pertussis* that contains a 6xHistidine-tag at its N-terminus (His-BpCAT-C)

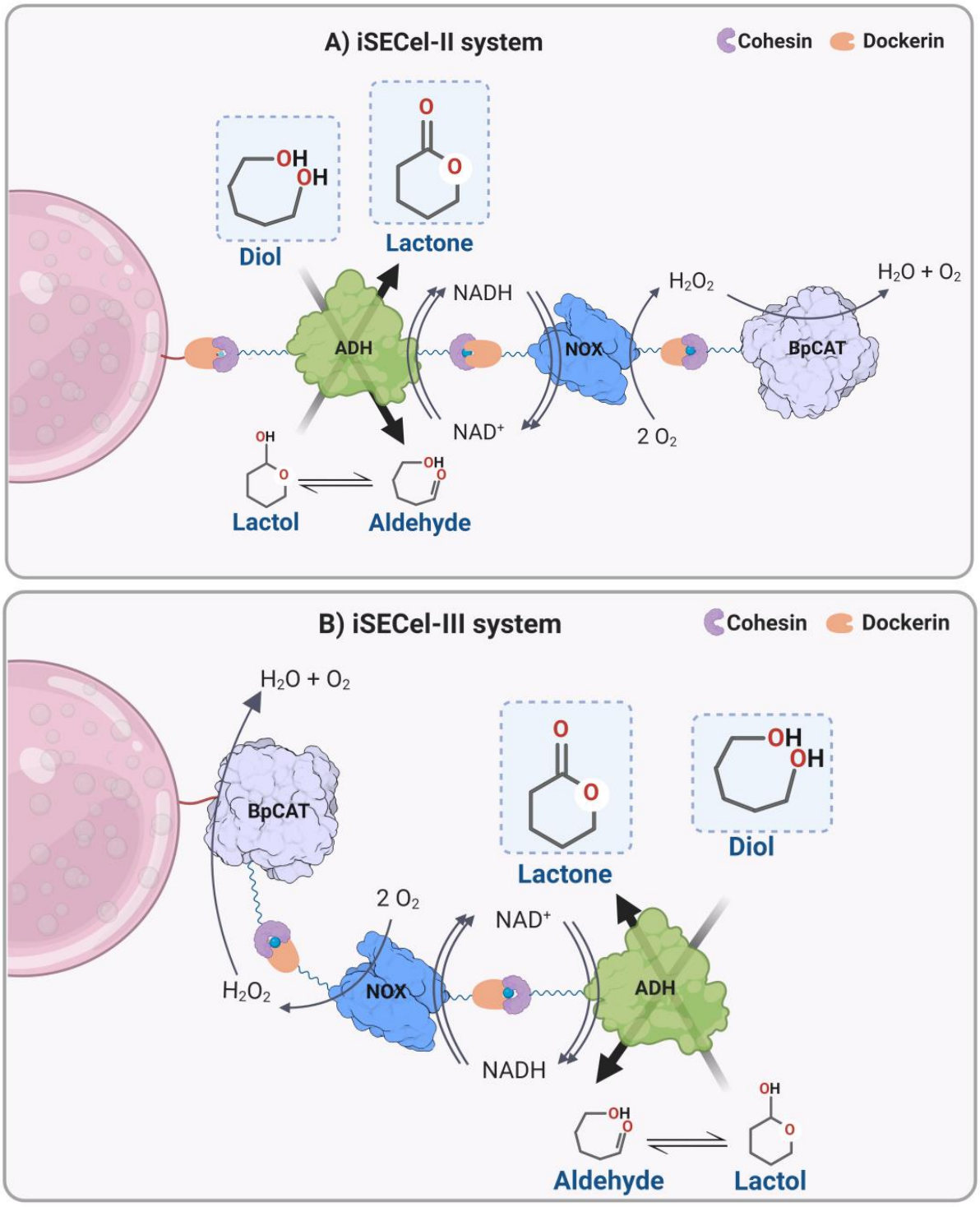

Figure 14: Schematic illustration for iSECel systems with three enzymes and two optional spatial distributions.

A. *Schematic illustration of the iSECel-II system with the assembly of the enzymes using as the first anchored point the His-D, which allows the assembly of the C-ADH, followed by the D-NOX and finally the His-BpCAT-C.* ***B.*** *Schematic illustration of the iSECel-III system assembled by the histidine tag of the His-BpCAT-C, followed by the D-NOX and the C-ADH.*

A similar multi-enzymatic system as the one proposed here was previously reported by our group, where three enzymes were immobilized on agarose microbeads activated with aldehyde, amino and cobalt chelates. This was done with the objective of irreversibly immobilizing three enzymes (NOX, BsADH and BlCAT),[29] and demonstrating that the co-immobilization of enzymes in an enzymatic cascade improves the total turnover number (TTN) during the consecutive reaction in batch.

Taking into account the previous results of the multi-enzymatic cascade assembled in iSECel-I, we wanted to further control of the spatial arrangement at the molecular level. To this aim, we propose two different sequences of immobilizing iSECel; 1) iSECel-II where AG-Co^{2+} are primed with His-D, then C-ADH is bound, followed by D-NOX and BpCAT-C without his-tag, 2) iSECel-III where the beads are primed with His-BpCAT-C, followed by the sequential binding of D-NOX and C-ADH. This two sequences would allow controlling the position of one enzyme relative to another through dockerin-cohesin interactions. Also, unlike the iSECel-I, we can study differences in the substrate channelling between iSECel-II and III (Figure 14).

As mentioned above, to study the spatial distribution of the multi-enzymatic enzymes we designed two approaches. In the first one, iSECel-II system, the C-ADH enzyme, responsible for the bio-conversion of the substrate (diol) into the corresponding product (lactone), is close to the AG-Co^{2+} microbead surface using as His-D as an anchor point. The enzyme responsible for the cofactor recycling is followed by NAD^+ dependent enzyme in both approaches, and the last coupled enzyme, BpCAT-C, responsible for the H_2O_2 elimination and *in situ* oxygen supply is in third position (Figure 14, A). The BpCAT-C enzyme, as was previously mentioned, contains a 6xHistidine tag at the N-terminus and a thrombin proteolysis recognition sequence between the histidine-tag and the enzyme sequence, which allows the histidine tag to be protolyzed in the iSECel-II system. However, such histidine-tag is employed as the first anchored point in the iSECel-III, which combined with the Coh domain in the C-terminus allows the assembly of the following enzymes, with the D-NOX in second position and the C-ADH as the last enzyme in iSECel-III (Figure 14, B).

3.3.10 Assembly of the iSECel-II system on AG-Co^{2+}

As we optimized for iSECel-I system (see section 3.3.2), the initial concentration of the anchored point was in excess (1.8 mg of protein) regarding the other enzymes. In this case we tested with lower initial concentrations to optimize the enzymatic assembly. Thus, both systems, iSECel-II and iSECel-III (section 3.3.11), were assembled using different initial anchored protein concentrations: iSECel-II system A at 1.6 mg x $g^{-1}_{carrier}$ of pure protein and

iSECel-III system B at 0.8 mg x $g^{-1}_{carrier}$ of pure protein. The immobilization parameters for the iSECel-II system are reported in Table 6.

Table 6: iSECel-II system: His-D/C-ADH/D-NOX/BpCAT-C immobilization parameters

iSECel-II system A: Initial offered protein concentration 1.6 mg x $g^{-1}_{carrier}$						
Protein immobilized	**Ψ % (Protein)**	**mg x $g^{-1}_{immobilized}$**	**U x $g^{-1}_{offered}$**	**Ψ % (Activity)**	**U x $g^{-1}_{immobilized}$**	**U x $g^{-1}_{recovered}$**
His-D	100 ± 0	0.98 ± 0		-	-	
His-D/**C-ADH**	-	-	18 ± 4.2	24 ± 1.4	4.31 ± 0.06	0.58 ± 0.75
His-D/**C-ADH**/D-NOX	-	-		-	-	0.03 ± 0.03
His-D/**C-ADH**/D-NOX/BpCAT-C	-	-		-	-	1.86 ± 0.53
His-D/C-ADH/**D-NOX**	-	-	49.7 ± 5.6	36.9 ± 6.7	18.3 ± 0.38	0.70 ± 0.02
His-D/C-ADH/**D-NOX**/BpCAT-C	-	-		-	-	0.59 ± 0.01
His-D/C-ADH/D-NOX/**BpCAT-C**	-	-	5934 ± 91	0	0	436.2 ± 123
iSECel-II system B: Initial offered protein concentration 0.8 mg x $g^{-1}_{carrier}$						
	Ψ % (Protein)	**mg x $g^{-1}_{immobilized}$**	**U x $g^{-1}_{offered}$**	**Ψ % (Activity)**	**U x $g^{-1}_{immobilized}$**	**U x $g^{-1}_{recovered}$**
His-D	100 ± 0	0.32 ± 0		-	-	
His-D/**C-ADH**	-	-	14.6 ± 0.3	0	0	0.39 ± 0.5
His-D/**C-ADH**/D-NOX	-	-	-	-	-	2.8 ± 0.5
His-D/**C-ADH**/D-NOX/C-BpCAT	-	-	-	-	-	0.66 ± 0.5
His-D/C-ADH/**D-NOX**	-	-	49.7 ± 5.6	37.1 ± 2.4	18.5 ± 0.14	1.14 ± 0.42
His-D/C-ADH/**D-NOX**/C-BpCAT	-	-	-	-	-	0.50 ± 0.08
His-D/C-ADH/D-NOX/**BpCAT-C**	-	-	5934 ± 91	25.3 ± 0.5	1503 ± 0.43	373 ± 136.4

The recovered activity of each enzyme was measured after each assembly step using colorimetric assays (section 3.2.7) to monitor how each step of assembly affected the enzyme activity. The immobilization of the His-D protein yielded 100 % regardless offered load, which allows further assembly of the consecutive proteins in the iSECel-II system. The yield of the second protein C-ADH in the iSECel-II system A (initial offered protein 1.6 mg x $g^{-1}_{carrier}$) was only 24 % of the activity offered with a recovered activity of 0.58 U x g^{-1}. However, this activity seems to increase by 3 times with the addition of D-NOX and BpCAT-C to complete the iSECel-II A assembly. In iSECel-II system B (initial offered protein 0.8 mg x $g^{-1}_{carrier}$), C-ADH immobilization was almost not detected through the spectrophotometric assay, but it was possible to follow the amount of protein immobilized by SDS-PAGE electrophoresis (Figure 15, B). Here, the recovered activity of C-ADH after the immobilization and after the completed assembly of iSECel-II system B increased only 1.5 times.

In the case of D-NOX, the immobilization yield was the same in both cases near to 37 %, but the initial recovered activity doubled (1.14 U x g^{-1}) in the case of iSECel-II system B compared with iSECel-II system A. However, the activity drops to similar values after the complete assembly of both iSECel-II systems (Table 6). Finally, the BpCAT-C immobilization yield was not detected by spectrometric measurements in the case of iSECel-II system A, however its activity was detected in the fully assembled biocatalyst. Here, the activity was 1.2 times higher than the activity recovered in iSECel-II system B which shows a 25 % of immobilization yield.

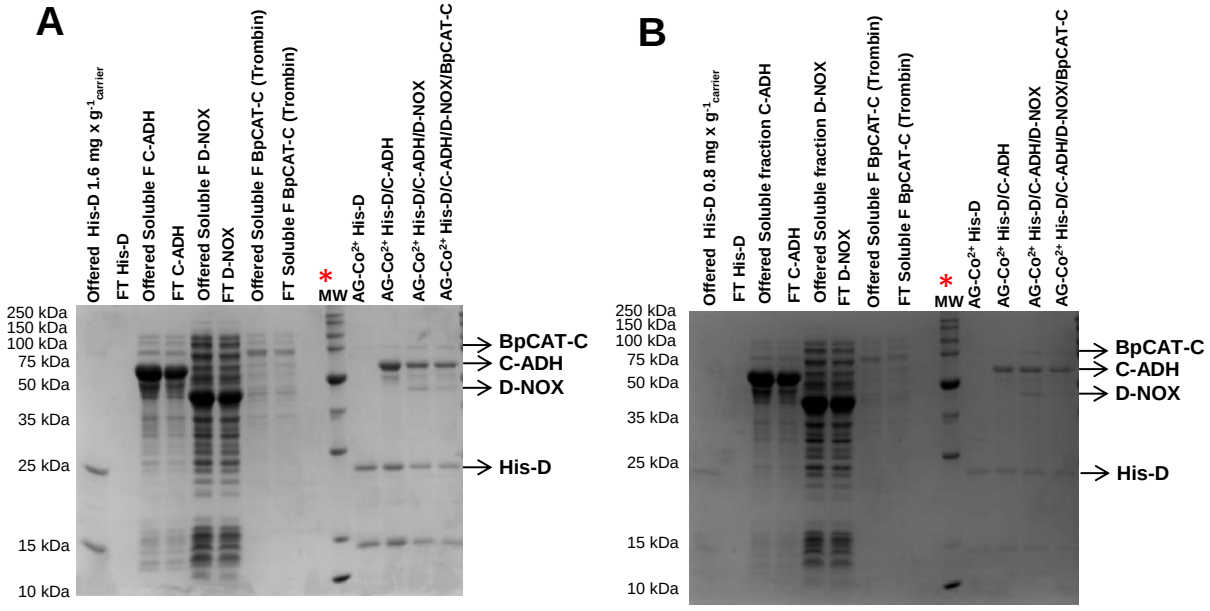

Figure 15: SDS-PAGE electrophoresis of the immobilization assembly of the iSECel-II system.

A. *Assembly of iSECel-II system A (initial offered protein at 1.6 mg x $g^{-1}_{carrier}$).* ***B.*** *Assembly of iSECel-II system B (initial offered protein at 0.8 mg x $g^{-1}_{carrier}$). In red asterisks are the Promega MW used to quantify the amount of protein immobilized.*

In the immobilization of the last assembled protein of both iSECel-II systems (BpCAT-C), there are a low concentration of protein, which in the case of the iSECel-II system B is not possible quantify it by densitometry. The gels in Figure 15 also allow us to calculate the immobilized protein in each immobilization step using as a reference an already known band concentration from the molecular weight (MW) of Promega (50 kDa which corresponds to 0.3 mg x mL^{-1}) and the Image J software tool (Table 7).

Table 7: Protein assembly quantification of the different proteins in the iSECel-II system.

iSECel-II system A:Initial offered protein concentration 1.6 mg x $g^{-1}_{carrier}$						
Protein assembled	**1st step**	**2nd step**	**3rd step**	**4th step**	**Molar ratio[1]**	**Activity expressed ratio[2]**
	mg x $g^{-1}_{carrier}$	**mg x $g^{-1}_{carrier}$**	**mg x $g^{-1}_{carrier}$**	**mg x $g^{-1}_{carrier}$**		
His-Dock	1.12	1.07	0.52	0.42	3.42	-
C-ADH		2.41	1.32	1.19	1	1
D-NOX			0.25	0.17	0.38	0.32
C-BpCAT				0.05	0.03	234
iSECel-II system B: Initial offered protein concentration 0.8 mg $g^{-1}_{carrier}$						
Protein assembled	**1st step**	**2nd step**	**3rd step**	**4th step**	**Molar ratio[1]**	**Activity expressed ratio[2]**
	mg x $g^{-1}_{carrier}$	**mg x $g^{-1}_{carrier}$**	**mg x $g^{-1}_{carrier}$**	**mg x $g^{-1}_{carrier}$**		
His-Dock	0.32	0.24	0.20	0.15	3.16	-
C-ADH		0.78	0.76	0.47	1	1
D-NOX			0.22	0.03	0.17	0.75
C-BpCAT				NQ	NQ	565

The protein quantity were calculated using as reference the Promega MW (50 KDa band correspond to 0.3 mg x mL^{-1}). [NQ] non quantifiable. [1] Molar ratio were calculated using the molecular weights of multimeric protein: His-D (mon):22.8 kDa; C-ADH (4-mer): 226 kDa; D-NOX (2-mer): 84.4 and BpCAT-C (4-mer): 300 kDa. [1 and 2] Calculated using the value of C-ADH as a reference

The quantification of the protein bands by densitometry estimates the molar ratio of the iSECel-II systems A and B (His-D:C-$ADH_{(4\text{-}mer)}$:D-$NOX_{(2\text{-}mer)}$:BpCAT-$C_{(4\text{-}mer)}$) of (3.42: 1: 0.38: 0.03) in the case of system A and (3.16: 1: 0.17: NQ) in the case of system B. The molar ratio shows again that the ratio between the first step of the assembly is the same no matter the initial protein loaded of the priming His-D. Where each C-ADH tetramer (4 Coh domains)

seems to be attached to 3 His-D, leaving only one domine per C-ADH to be able to attach the D-NOX.

3.3.11 Assembly of the iSECel-III system on AG-Co^{2+}

The same study described above was performed with the iSECel-III system, where two anchored protein concentrations (His-BpCAT-C) were employed: iSECel-III system C (1.6 mg x $g^{-1}_{carrier}$) and iSECel-III system D (0.8 mg x $g^{-1}_{carrier}$). The immobilization parameters for these assembly systems are shown in the Table 8.

Table 8: iSECel-III system: His-BpCAT-C/ D-NOX/C-ADH immobilization parameters

iSECel-III system C: Initial offered protein concentration 1.6 mg per $g^{-1}_{carrier}$						
Protein immobilized	**Ψ % (Protein)**	**mg x g^{-1} immobilized**	**U x g^{-1} offered**	**Ψ % (Activity)**	**U x g^{-1} immobilized**	**U x g^{-1} recovered**
His-BpCAT-C	100 ± 0	1.65 ± 0.2	2396 ± 136	97 ± 3	2325 ± 3.9	348 ± 6.4
His-BpCAT-C/D-NOX	-	-	-	-	-	248 ± 180
His-BpCAT-C/D-NOX/C-ADH	-	-	-	-	-	449 ± 123.5
His-BpCAT-C**/D-NOX**	-	-	50 ± 5.6	18 ± 11	8.9 ± 0.6	0.8 ± 0.03
His-BpCAT-C/**D-NOX**/C-ADH	-	-	-	-	-	0.52 ± 0.28
His-BpCAT-C/D-NOX/**C-ADH**	-	-	14.9 ± 3	0	0	1.07 ± 0.19
iSECel-III system D: Initial offered protein concentration 0.8 mg x $g^{-1}_{carrier}$						
	Ψ % (Protein)	**mg x g^{-1} immobilized**	**U x g^{-1} offered**	**Ψ % (Activity)**	**U x g^{-1} immobilized**	**U x g^{-1} recovered**
His-BpCAT-C	100 ± 0	0.097 ± 0.0	1076.8 ± 141	90 ± 7.6	966.48 ± 10.7	390 ± 275.7
His-BpCAT-C/D-NOX	-	-	-	-	-	323 ± 59.1
His-BpCAT-C/D-NOX/C-ADH	-	-	-	-	-	324.2 ± 44.1
His-BpCAT-C**/D-NOX**	-	-	50 ± 5.6	13 ± 6.6	6.5 ± 0.4	1.9 ± 0.1
His-BpCAT-C/**D-NOX**/C-ADH	-	-	-	-	-	0.62 ± 0.22
His-BpCAT-C/D-NOX/**C-ADH**	-	-	14.9 ± 3	0	0	0.9 ± 0.14

The anchored protein used in the iSECel-III was the histidine-tagged enzyme His-BpCAT-C. It had almost 100 % effectiveness in the immobilization yield measured by protein or activity in the case of iSECel-III system C. But in the case of iSECel-III system D there is a small differences between the immobilization yields measured by protein or activity. However, even when the amount of protein immobilized in iSECel-III system C is 1.7 times higher than in iSECel-III system D, the recovered activity is almost the same after immobilization. When the systems were fully assembled, the final recovered catalase activity expressed by iSECel-III system C increased and was almost 1.4 times higher than iSECel-III system D.

The cofactor recycling enzyme D-NOX showed a low immobilization yield for both iSECel-III systems around 13-18 % compared with the 37 % obtained for both iSECel-II system. However, the final activity expressed after the completed iSECel-III assembly were similar to the values obtained in the iSECel-II systems, where the D-NOX enzyme was in the third position of the assembly. The final assembled enzyme was C-ADH, where it was not possible to quantify spectrophotometrically the amount of protein immobilized. We were, however, again able to detect the protein attached by electrophoresis gel (Figure 16) and quantify by densitometry using Image J software (Table 9).

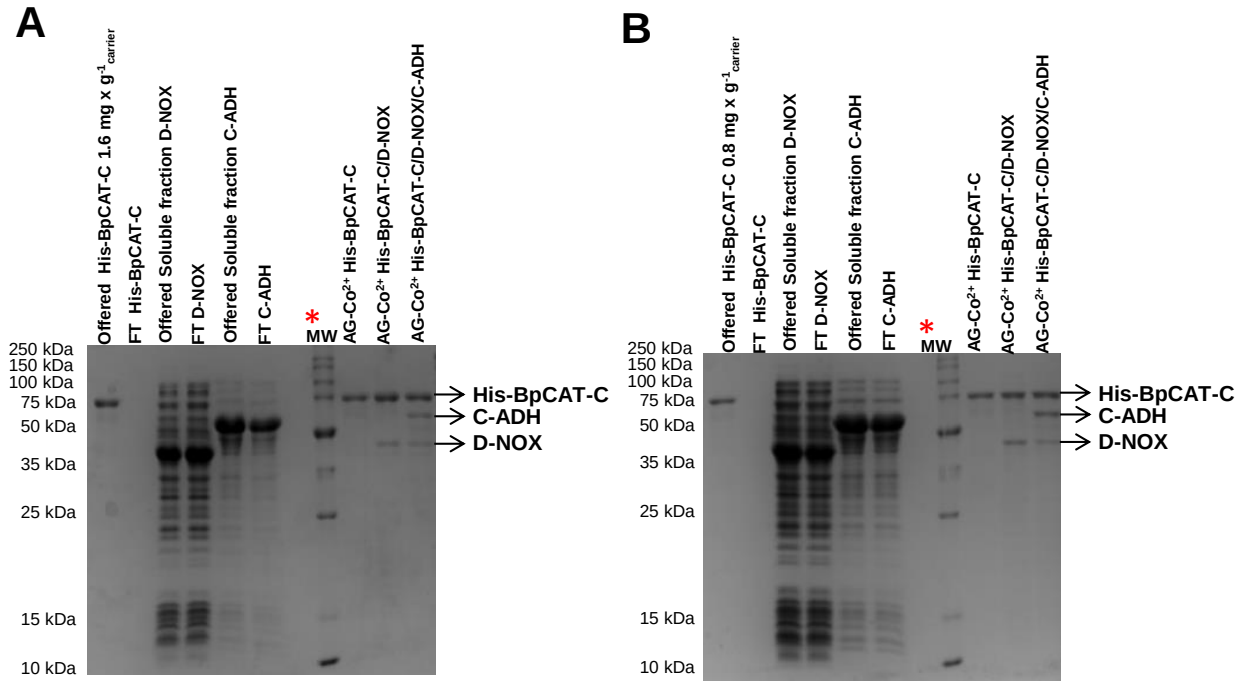

Figure 16: SDS-PAGE electrophoresis of the immobilization assembly of the iSECel-III system

A. *Assembly of iSECel-III system C (initial offered protein at 1.6 mg x $g^{-1}_{carrier}$).* ***B.*** *Assembly of iSECel-III system B (initial offered protein at 0.8 mg x $g^{-1}_{carrier}$). In red asterisks are the Promega MW used to quantify the amount of protein immobilized.*

Table 9: Protein assembly quantification of the different proteins in the iSECel-III system

iSECel-III system C: Initial offered protein concentration 1.6 mg x $g^{-1}_{carrier}$					
Protein assembled	**1st step**	**2nd step**	**3rd step**	**Molar ratio[1]**	**Activity expressed ratio[2]**
	mg x $g^{-1}_{carrier}$	**mg x $g^{-1}_{carrier}$**	**mg x $g^{-1}_{carrier}$**		
His-BpCAT	1.22	1.76	1.52	3.38	419
D-NOX		0.27	0.18	1.46	0.49
C-ADH			0.33	1	1
iSECel-III system D: Initial offered protein concentration 0.8 mg x $g^{-1}_{carrier}$					
Protein assembled	**1st step**	**2nd step**	**3rd step**	**Molar ratio[1]**	**Activity expressed ratio[2]**
	mg x $g^{-1}_{carrier}$	**mg x $g^{-1}_{carrier}$**	**mg x $g^{-1}_{carrier}$**		
His-BpCAT	0.89	1.02	0.96	1.44	360
D-NOX		0.37	0.19	1.04	0.69
C-ADH			0.49	1	1

The protein quantity were calculated using as reference the Promega MW (50 KDa band correspond to 0.3 mg x mL^{-1}). [NQ] non quantifiable. [1] Molar ratio were calculated using the molecular weights of multimeric protein: His-BpCAT-C (4-mer): 308.3 kDa; C-ADH (4-mer): 226 kDa and D-NOX (2-mer): 84.4 kDa. [1 and 2] Calculated using the value of C-ADH as a reference

The molar ratio of the iSECel-III systems C and D (His-BpCAT-$C_{(4\text{-mer})}$: D-$NOX_{(2\text{-mer})}$: C-$ADH_{(4\text{-mer})}$) of (3.38: 1.46: 1) in the case of system C and (1.44: 1.04: 1) in the case of system D. In these case each C-ADH seems to be is attached to 1.5 D-NOX in the system C and only 1 D-NOX in the system D.

3.3.12 Spectrophotometric assay for the scaffolded system coupling efficiency

The iSECel systems II and III, were designed to couple reactions in order to improve the overall reaction efficiency. Thus, after the individual characterization of the enzymes in the different iSECel systems, we evaluated the effect of each iSECel approach (with different immobilization order and protein load) in the efficiency of each enzyme working together. For C-ADH the activity was measured with 1,5-penanediol, and for D-NOX with the NADH as is described in section 3.2.7. To determine the catalase efficiency in iSECel systems II and III to remove H2O2, we coupled the system to HRP to determine the amount of hydrogen peroxide that was not converted by the BpCAT-C as described in Figure 3.

The results suggest that iSECel-III systems C and D accumulate 5 times less hydrogen peroxide during the multi-enzymatic cascade than both iSECel-II systems. This effect may be explained by the 4 and 2 times higher ADH activity measured in iSECel-II systems A and B respectively, that supply with more and faster NADH to NOX, ultimately accumulating more and faster H_2O_2. Although in all cases NADH is not accumulated, demonstrating that the cofactor recycling is very efficient, the removal of hydrogen peroxide is however limited by very active C-ADH assembled with a very low D-NOX:C-ADH activity ratios. Therefore, the differences in C-ADH activities between iSECell-II and III may rely on the more efficient channelling of cofactor at the expense of accumulating more H_2O_2. Hence we suggest that the spatial arrangement or a better spatial conformation of the C-ADH and the optimal activity ratio of the assembled C-ADH and D-NOX are key to have an efficient multi-enzyme system.

Table 10: Scaffolded system coupling efficiency.

Enzymatic activity	iSECel-II		iSECel-III	
	System A	System B	System C	System D
C-ADH activity (U x g^{-1})	0.71	0.38	0.17	0.17
D-NOX activity (U x g^{-1})	0.96	0.77	0.59	0.45
NADH accumulaton (U x g^{-1})	0	0	0	0
H_2O_2 accumulation (U x g^{-1})	1.06	0.64	0.20	0.17

The activities were measured following the protocols described in section 3.2.7.

3.3.13 Kinetic reaction in batch

The kinetics of the different iSECel systems were studied in batch reactions. The different biocatalysts were incubated with the reaction mix and samples were withdrawn after different times for their further GC analysis. The results reveal that in general the iSECel-II systems seem to be more efficient biocatalysts for the diol conversion than the iSECel-III systems, consuming more than 60 % of the diol after one hour of reaction in the case of iSECel-II system A and 50 % in the case of iSECel-II system B. This data are consistent with the higher activity of C-ADH observed before (Table 10). In addition, this higher activity of the A system seems to favour the second oxidation of the cascade from the intermediate lactol to the final product lactone, which in turn could spontaneously hydrolyzed into their ω-hydroxy acid.[38] The product yields of lactone was 15 % at 24 hours of reaction in iSECel-II system A and 10 % in the case of iSECel-II system B, second biocatalyst more active. Unfortunately, the lower activity in the diol conversion for both iSECel-III systems does not allow the second oxidation to lactone and shifts the equilibrium from the 5-hydroxypentanal (aldehyde) to the lactol intermediate after 24 hours of reaction.

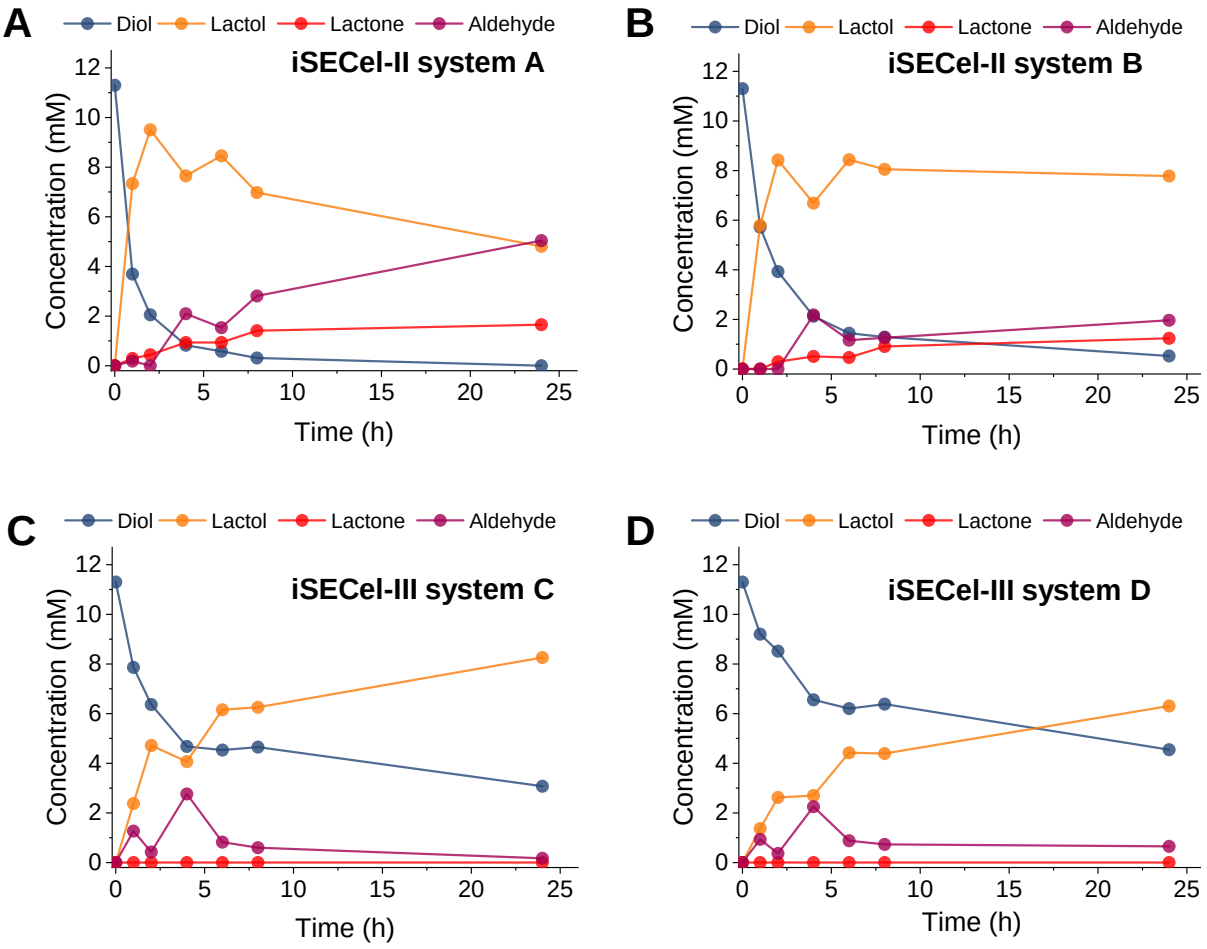

Figure 17: Kinetic course of reaction for the multi-enzymatic cascade in the different iSECel systems.

A. *Kinetic reaction course in batch for iSECel-II system A.* ***B.*** *Kinetic reaction course in batch for iSECel-II system B.* ***C.*** *Kinetic reaction course in batch for iSECel-III system C.* ***D.*** *Kinetic reaction course in batch for iSECel-III system D*

3.3.14 Operational stability of the iSECel-II and iSECel-III

The operational stability of the four iSECel systems were compared in batch after 24 hours of reaction. The results showed in the Figure 18 also contain the composition of each batch cycle at the final point. On one hand, the iSECel-II spatial organization with systems A and B shows the higher diol conversion in the first cycle (Figure 18, A and B). The conversion of diol, however, was reduced gradually until the percentage was almost 20 % in both cases. iSECel-II system A performed better than system B, converting more than 50 % of the residual diol until the third reuse cycle (Figure 19). The lactone production was detectable in the first and second batch cycle for iSECel-II system A and only the first cycle for iSECel-II system B with a low concentration. The trend of ratio of final product seen in systems A and B are similar, as shown in Figure 18, A and B. The maximum lactol concentration is

observed in the second cycle and no aldehyde is observed in this same cycle for both these systems. On the other hand, the iSECel-III spatial organization within systems C and D shows a lower conversion of the diol maintaining almost 20-25% conversion in the last three cycles (Figure 18, C and D). In both systems C and D, the lactol intermediate product is the major product only in the two first cycles, which also had the lower concentration of the aldehyde in equilibrium. In the last three cycles the major product of the reaction was the aldehyde compound, 5-hydroxyaldehyde.

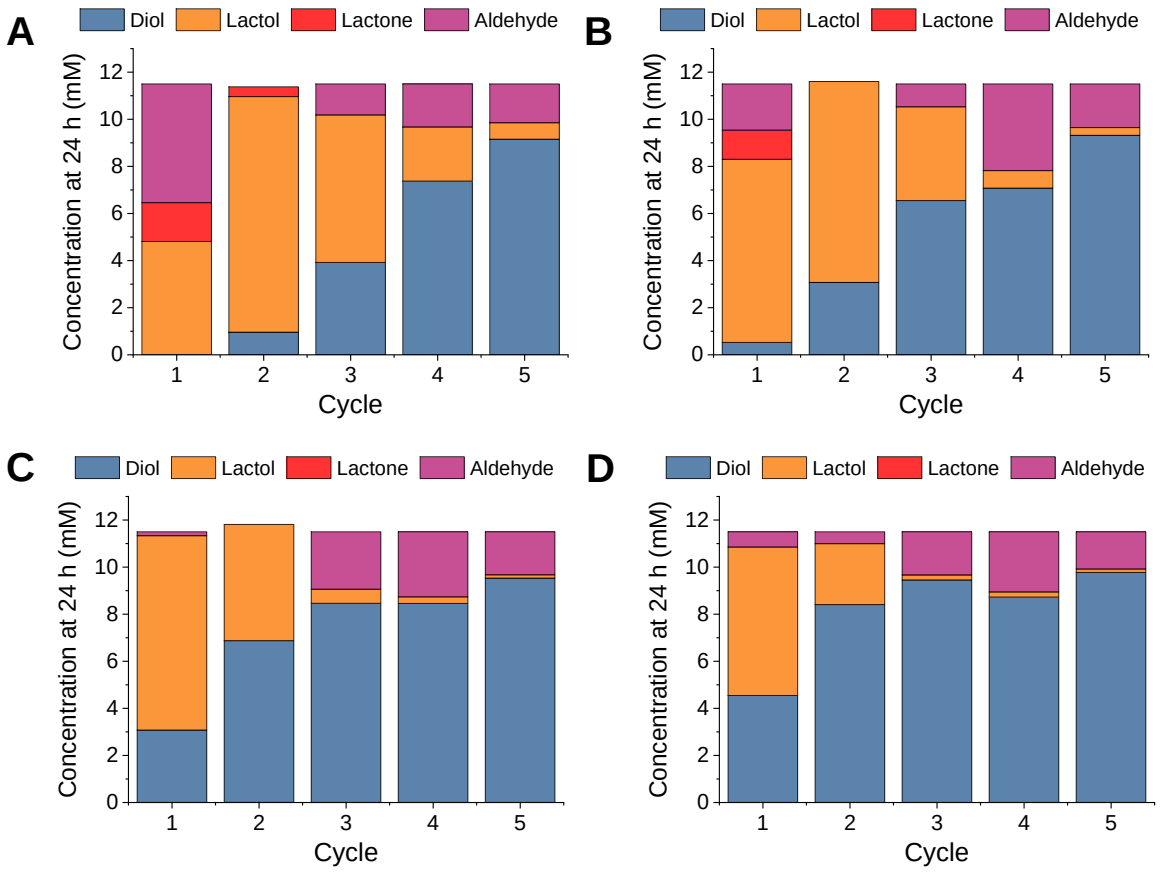

Figure 18: Product compounds after each batch cycle analyzed by GC.

A. *Compounds of iSECel-II system A after each 24 hour of batch reaction.* ***B.*** *Compounds of iSECel-II system B after each 24 hour of batch reaction.* ***C.*** *Compounds of iSECel-III system C after each 24 hour of batch reaction.* ***D.*** *Compounds of iSECel-III system D after each 24 hour of batch reaction.*

The high diol conversion in the iSECel-II systems A and B are correlated with the higher activity of the C-ADH as documented above (Table 10). Aside from the first cycle in the iSECel-II spatial organization, it seems that after each cycle of reaction the equilibrium between the lactol and the aldehyde was moving towards the aldehyde compound.

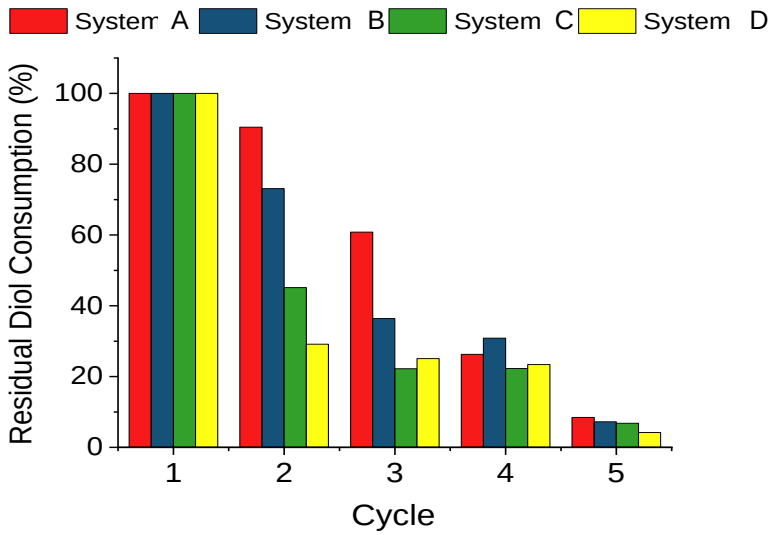

Figure 19: Residual diol consumption of the iSECel-II and iSECel-III systems

The consumed diol in the first cycle were: 100 % with iSECel-II system A; 95 % with iSECel-II system B; 69 % with iSECel-III system C and 55 % with the iSECel-III system D.

Finally to determine the cause of the loss of activity of the iSECel biocatalysts we performed SDS-PAGE electrophoresis and compared the used biocatalysts after the batch reaction cycles with two sample controls. On one hand, we used the same biocatalyst used for the recycling experiments but stored for 9 days at 4 ºC and on the other hand, we used a fresh biocatalyst assembled in the same conditions. With these two sample controls, we were able to determine the stability of the biocatalyst itself (storage stability without reaction) and the stability after the reaction (final biocatalyst recycling experiments). Thus, the gel shows that the enzymes are lixiviated from the carrier after 5 batch cycles, which explains the low reaction conversion (Figure 18). Also the biocatalyst storage at 4 ºC shows the storage stability of the different biocatalyst and shows that the spatial organized with four proteins in iSECel-II system A and system B are not stable enough, since some degradation is observed from the first assembled protein His-D to the last one BpCAT-C (Figure 20).

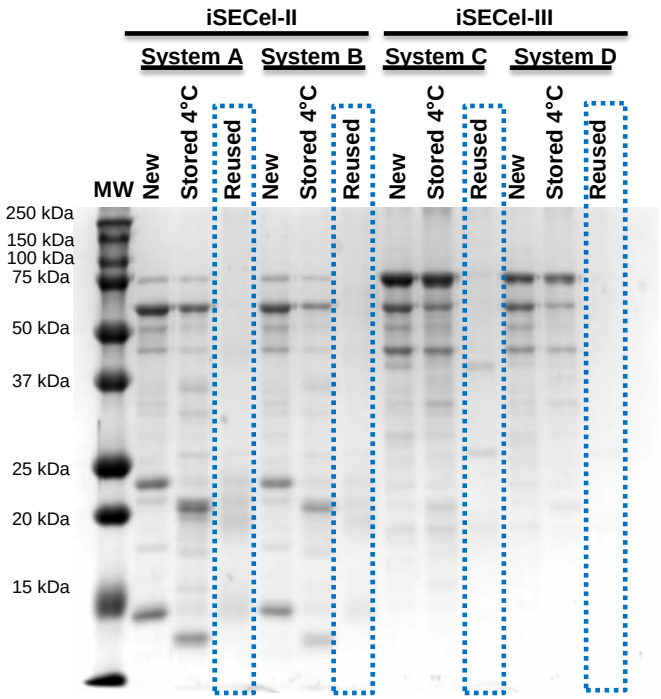

Figure 20: SDS-PAGE electrophoresis of the biocatalysts after 5 batch reaction cycles.

New: *Fresh biocatalyst;* ***Stored 4ºC:*** *the same biocatalyst employed for the reusability experiments but stored without reaction at 4 ºC per 9 days and* ***Reused:*** *The biocatalysts after 5 cycles of reaction.*

3.4 Conclusions

In summary, we have developed three genetically programmable solid-phase enzyme assembly systems. The first one iSECel-I system with which we demonstrated its potential with a dual enzyme cascade for amination of alcohols. We further show with this first system that the nanometric proximity of the two ordered scaffolded enzymes in porous agarose microbeads enhances the heterogeneous cascade performance. This system was also integrated into a flow-reactor for continuous synthesis of 3-MBA. Furthermore we developed two other iSECel systems, system II which contain four proteins, three of which are enzymes, and system III which contains three enzymes. We did this to demonstrate the versatility of these artificial cellulosome scaffolds for multi-enzymatic cascades. With these systems we also demonstrated that not only the proximity, but the different spatial organizations of the enzymes and their position in the assembly is important in the overall reactivity and stability of the system. This work establishes the basis of a new concept to organize multi-enzyme systems at the nanoscale level within solid matrices that can be readily expanded to other biocatalytic cascade reactions and enrich the toolbox for cell-free biotransformations.

3.5 Bibliography

[1] A. Bruggink, R. Schoevaart, T. Kieboom, Concepts of nature in organic synthesis: cascade catalysis and multistep conversions in concert, Organic process research & development, 7 (2003) 622-640.

[2] S. Wu, R. Snajdrova, J.C. Moore, K. Baldenius, U.T. Bornscheuer, Biocatalysis: enzymatic synthesis for industrial applications, Angewandte Chemie International Edition, 60 (2021) 88-119.

[3] W.-D. Fessner, Systems Biocatalysis: Development and engineering of cell-free “artificial metabolisms” for preparative multi-enzymatic synthesis, New biotechnology, 32 (2015) 658-664.

[4] C. Schmidt-Dannert, F. Lopez-Gallego, A roadmap for biocatalysis–functional and spatial orchestration of enzyme cascades, Microbial biotechnology, 9 (2016) 601-609.

[5] R.W. Carthew, Gene Regulation and Cellular Metabolism: An Essential Partnership, Trends Genet., (2020).

[6] G.P. Lisi, J.P. Loria, Allostery in enzyme catalysis, Curr. Opin. Struct. Biol., 47 (2017) 123-130.

[7] D.L. Schmitt, S. An, Spatial Organization of Metabolic Enzyme Complexes in Cells, Biochemistry, 56 (2017) 3184-3196.

[8] J.L. Avalos, G.R. Fink, G. Stephanopoulos, Compartmentalization of metabolic pathways in yeast mitochondria improves the production of branched-chain alcohols, Nat. Biotechnol., 31 (2013) 335-341.

[9] M.W. Ullah, W.A. Khattak, M. Ul-Islam, S. Khan, J.K. Park, Metabolic engineering of synthetic cell-free systems: Strategies and applications, Biochem. Eng. J., 105 (2016) 391-405.

[10] S. Burgener, S. Luo, R. McLean, T.E. Miller, T.J. Erb, A roadmap towards integrated catalytic systems of the future, Nat. Catal., 3 (2020) 186-192.

[11] A. Küchler, M. Yoshimoto, S. Luginbühl, F. Mavelli, P. Walde, Enzymatic reactions in confined environments, Nat. Nanotechnol., 11 (2016) 409.

[12] C. You, Y.H. Zhang, Self-assembly of synthetic metabolons through synthetic protein scaffolds: one-step purification, co-immobilization, and substrate channeling, ACS Synth. Biol., 2 (2013) 102-110.

[13] W. Kang, T. Ma, M. Liu, J. Qu, Z. Liu, H. Zhang, B. Shi, S. Fu, J. Ma, L.T.F. Lai, S. He, J. Qu, S. Wing-Ngor Au, B. Ho Kang, W.C. Yu Lau, Z. Deng, J. Xia, T. Liu, Modular enzyme assembly for enhanced cascade biocatalysis and metabolic flux, Nat. Comm., 10 (2019) 4248.

[14] C. Wang, L. Yue, I. Willner, Controlling biocatalytic cascades with enzyme–DNA dynamic networks, Nat. Catal., 3 (2020) 941-950.

[15] J.N. Vranish, M.G. Ancona, E. Oh, K. Susumu, G. Lasarte Aragonés, J.C. Breger, S.A. Walper, I.L. Medintz, Enhancing Coupled Enzymatic Activity by Colocalization on Nanoparticle Surfaces: Kinetic Evidence for Directed Channeling of Intermediates, ACS Nano, 12 (2018) 7911-7926.

[16] G.A. Ellis, W.P. Klein, G. Lasarte-Aragonés, M. Thakur, S.A. Walper, I.L. Medintz, Artificial Multienzyme Scaffolds: Pursuingin VitroSubstrate Channeling with an Overview of Current Progress, ACS Catal., 9 (2019) 10812-10869.

[17] L. Artzi, E.A. Bayer, S. Moraïs, Cellulosomes: bacterial nanomachines for dismantling plant polysaccharides, Nat. Rev. Microbiol., 15 (2017) 83-95.

[18] B.-B. Hu, M.-J. Zhu, Reconstitution of cellulosome: Research progress and its application in biorefinery, Biotechnology and Applied Biochemistry, 66 (2019) 720-730.

[19] Y. Mori, H. Nakazawa, G.A.L. Gonçalves, T. Tanaka, M. Umetsu, N. Kamiya, One-dimensional assembly of functional proteins: toward the design of an artificial cellulosome, Mol. Syst. Des. Eng., (2016).

[20] A. Szczupak, D. Aizik, S. Moraïs, Y. Vazana, Y. Barak, E.A. Bayer, L. Alfonta, The Electrosome: A Surface-Displayed Enzymatic Cascade in a Biofuel Cell's Anode and a High-Density Surface-Displayed Biocathodic Enzyme, Nanomaterials, 7 (2017) 153.

[21] M.R. Smith, H. Gao, P. Prabhu, L.F. Bugada, C. Roth, D. Mutukuri, C.M. Yee, L. Lee, R.M. Ziff, J.-K. Lee, F. Wen, Elucidating structure–performance relationships in whole-cell cooperative enzyme catalysis, Nat. Catal., 2 (2019) 809-819.

[22] H. Malke, J. SAMBROCK, EF FRITSCH and T. MANIATIS, Molecular Cloning, A Laboratory Manual , Volumes 1, 2 and 3. 1625 S., zahlreiche Abb. und Tab. Cold Spring

Harbor 1989. Cold Spring Harbor Laboratory Press. $115.00. ISBN: 0-87969-309-6, Wiley Online Library, 1990.

[23] M.M. Bradford, A rapid and sensitive method for the quantitation of microgram quantities of protein utilizing the principle of protein-dye binding, Analytical biochemistry, 72 (1976) 248-254.

[24] L.K. Morlock, D. Böttcher, U.T. Bornscheuer, Simultaneous detection of NADPH consumption and H 2 O 2 production using the Ampliflu™ Red assay for screening of P450 activities and uncoupling, Applied microbiology and biotechnology, 102 (2018) 985-994.

[25] J. Schindelin, I. Arganda-Carreras, E. Frise, V. Kaynig, M. Longair, T. Pietzsch, S. Preibisch, C. Rueden, S. Saalfeld, B. Schmid, Fiji: an open-source platform for biological-image analysis, Nature methods, 9 (2012) 676-682.

[26] D.R. Gagnon, T.J. McCarthy, Polymer surface reconstruction by diffusion of organic functional groups from and to the surface, Journal of applied polymer science, 29 (1984) 4335-4340.

[27] K.L. Holmes, L.M. Lantz, Protein labeling with fluorescent probes, Methods in cell biology, 63 (2001) 185-204.

[28] S. Bolte, F.P. Cordelières, A guided tour into subcellular colocalization analysis in light microscopy, Journal of microscopy, 224 (2006) 213-232.

[29] J. Santiago-Arcos, S. Velasco-Lozano, F. López-Gallego, Multienzyme Coimmobilization on Triheterofunctional Supports, Biomacromolecules, (2022).

[30] V.D. Alves, C. Fontes, P. Bule, Cellulosomes: Highly Efficient Cellulolytic Complexes, Subcell Biochem, 96 (2021) 323-354.

[31] J.J. Adams, G. Pal, Z. Jia, S.P. Smith, Mechanism of bacterial cell-surface attachment revealed by the structure of cellulosomal type II cohesin-dockerin complex, Proc Natl Acad Sci U S A, 103 (2006) 305-310.

[32] C. Ceccarelli, Z.-X. Liang, M. Strickler, G. Prehna, B.M. Goldstein, J.P. Klinman, B.J. Bahnson, Crystal Structure and Amide H/D Exchange of Binary Complexes of Alcohol Dehydrogenase from Bacillus stearothermophilus: Insight into Thermostability and Cofactor Binding, Biochemistry, 43 (2004) 5266-5277.

[33] A. Lyskowski, C. Gruber, G. Steinkellner, M. Schurmann, H. Schwab, K. Gruber, K. Steiner, Crystal structure of an (R)-selective omega-transaminase from Aspergillus terreus, PLoS One, 9 (2014) e87350.

[34] S.M. Alonso Villela, H. Kraïem, B. Bouhaouala-Zahar, C. Bideaux, C.A. Aceves Lara, L. Fillaudeau, A protocol for recombinant protein quantification by densitometry, MicrobiologyOpen, 9 (2020) e1027.

[35] J. Adler, I. Parmryd, Quantifying colocalization by correlation: The Pearson correlation coefficient is superior to the Mander's overlap coefficient, Cytometry Part A, 77A (2010) 733-742.

[36] S. Velasco-Lozano, J. Santiago-Arcos, J.A. Mayoral, F. López-Gallego, Co-immobilization and Colocalization of Multi-Enzyme Systems for the Cell-Free Biosynthesis of Aminoalcohols, ChemCatChem, 12 (2020) 3030-3041.

[37] N.C. Dubey, B.P. Tripathi, Nature Inspired Multienzyme Immobilization: Strategies and Concepts, ACS Applied Bio Materials, 4 (2021) 1077-1114.

[38] S. Kara, D. Spickermann, J.H. Schrittwieser, A. Weckbecker, C. Leggewie, I.W. Arends, F. Hollmann, Access to lactone building blocks via horse liver alcohol dehydrogenase-catalyzed oxidative lactonization, AcS catalysis, 3 (2013) 2436-2439.

HISTIDINE CLUSTERS

4.1 Introduction

The greener approach of the industry towards finding new biocompatible, bioactive, reusable and environmentally friendly biocatalysts has boosted the use of enzyme immobilization in combination with protein engineering methods and recombinant DNA technology. These techniques allow for fine-tuning of proteins to solve drawbacks reported in the literature for heterogeneous biocatalysts.[1, 2] Designed amino acid sequences can be constructed and inserted to produce the desired peptides and proteins in the recombinant form using synthetic genes or site-direct mutagenesis. This tuning allows modulation and optimization of the binding chemistry for site-specific and oriented immobilization on the solid carriers. [3-5]

The enzyme immobilization, generally required for industrial application, involves deep investigation into both the carrier and protein functionality, as is already reported in several reviews.[6, 7] Looking into enzyme function on the biocatalyst, the active site needs to be in a specific conformation and accessible to the target substrate with the labile region of the surface protein stabilized through anchored point to the carrier. Thus, enzyme orientation on the support surface may be critical. Enzyme immobilization randomly oriented on solid carriers may result in enzyme denaturalization, partial or complete loss of its activity due to a blocking of the active site, steric hindrance, or changes in the conformation during the immobilization. Consequently, oriented enzyme immobilization has attracted attention as an improved strategy in the biocatalyst field. Nowadays, the strategies available for oriented protein immobilization can be classified in chemical covalent immobilization, molecular imprinting technique based immobilization and bio/chemical affinity-mediated immobilization. [8]

4.1.1 Chemical covalent immobilization

Covalent-oriented immobilization is generally driven by cysteine and lysine residues. The thiol group (-SH) naturally present in the cysteine residues normally create internal disulfide bonds in the protein as a structural point of stabilization or is involved in the catalytic function in metalloproteins.[9] Thus, for site-specific oriented immobilization through thiol groups the indigenous disulfide bound needs to be reduced. Unfortunately, for many enzymes those cysteines are critical to maintaining structure or activity. In cases where a unique cysteine residue is incorporated by genetic modification, it’s possible to achieve covalent-oriented immobilization through maleimide reactivity[10] (Figure 21 A), with carriers activated with disulfide-glyoxyl groups[11] or the immobilization on gold nanoparticles.[12] The insertion of a unique cystein residue may affect the immobilization efficiency, for example the insertion of a cystein-tag with cysteins in tandem allows a high capture and immobilization efficiency.[13, 14] Thus, the orientation of enzymes can be likely controlled using cysteins, but present a

series of problems such as limited number of accessible thiol groups, the funtionality of the native cysteins in the protein is susceptible to sulfhydryl groups to be oxidised and formation of disulfide crosslinks in solution. There are reports that chelating agens such as ethylenediaminetetracetic acid (EDTA) are used to reduce metal-catalysed oxidation of sulfhydryls. These solutions unfortunately cannot be applied to metalloenzymes.[15] The amine groups present on the lysine residues and N-terminus have been exploited as anchoring points to aldehyde surfaces using Schiff base reactivity that requires, at least, the formation of two simultaneous bounds.[16] This approach has been only successful when the enzyme has lysine residues present on its surface.[17, 18] However, only the non-ionized amino groups are good nucleophiles to react with the support and this process depends greatly on the pKa of the surface lysines. Thus, in general, to immobilize the enzymes via their amine groups, an alkaline pH is necessary. Although, there are reports where immobilization has been achieved through areas with a high concentration of lysines with low pKa values in the same spatial plane of interaction with the support at neutral pH.[16] Also, carriers activates with epoxy groups, that are more versatile than the aldehydes, can react wit other nucleophiles in the protein surface such are cysteine, lysine and tyrosine residues, however therir reactivity is lower than the aldehyde and they need a first adsorbtion step of the protein to the surface to react. [19]

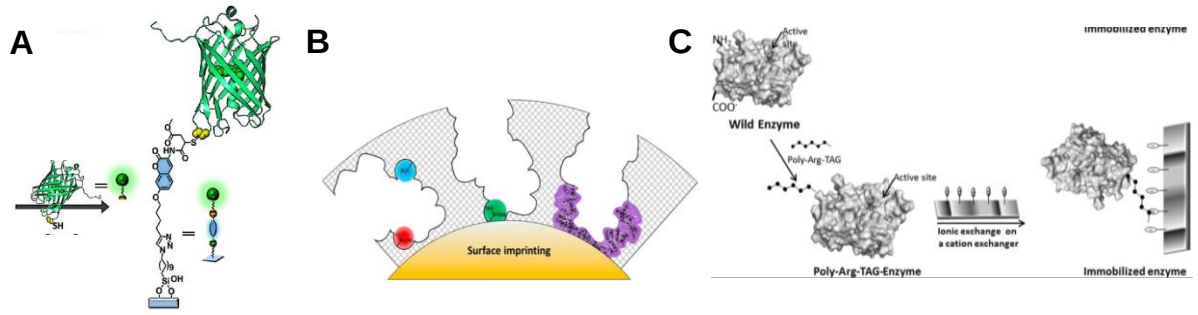

Figure 21: Oriented immobilization described in the literature.

A. *Covalent immobilization using cysteine residues (Wasserberg, Nicosia et al 2013).* ***B.*** *Molecular imprinting polymerization for oriented immobilization (Kalecki et al 2020).* ***C.*** *Immobilization through the insertion of poly-Arg tag (Barbosa et al 2015).*

4.1.2 Molecular imprinting polimerization (MIP) for oriented immobilization

Molecular imprinting polymerization is a technology that allows the creation of tailor-made binding sites on a polymer matrix with memory of the shape, size and functional group of the template molecule (Figure 21 B).[20] The designed functionalities allow the protein to be site-directed assembled homogeneously with a preferable orientation. The boronic acid group, single stranded oligonucleotides or aptamers are used as interactions for covalent

protein immobilization.[21] However, the molecular imprinting of proteins is still a challenge due to the harsh polymerization conditions employed for the imprinting, where conformational changes frequently occurs. Also, to template remove the proteins from the highly cross-linked polymer networks is difficult due to their large size. Another drawback of this molecular imprinting technology is that the enzyme needs multiple binding sites to have an ideally oriented protein immobilization. [22]

4.1.3 Affinity- mediated oriented immobilization

The discovery of fusion partners or “tags”, which can be a protein domain, a small peptide or even a small enzyme fused at either the N- or C- terminus of the target protein, emerged as an attractive approach to orient the protein in the immobilization process.[23, 24] The ideal peptide tag does not affect the activity or the desired folding of the enzyme and they are not longer than fifteen residues whose sequence is a repetition of one or two amino acids without an ordered three-dimensional conformation.[25] Different purposes for the fusion tags have been reported over the years, from enhancing protein expression, protein solubility, purification and protein immobilization. The highly selective binding of some tags for a range of materials that display specific ligands on their surfaces -the so- called affinity tags have unique features such as one step purification and immobilization.[26] The most commonly used small peptides tags described in the literature are (I) FLAG, a short hydrophilic octapeptide (DYKDDDDK),[27] (II) c-myc, an epitope of ten peptides (EQKLISEEDL) that must be fused at either N- or C-terminus,[28] (III) S-tag, a 15-residue soluble affinity tag,[29] (IV) strep II-tag, a small affinity peptide (WSHPQFEK),[30] (V) poly-arginine (poly-Arg)[31], which typically consists of five or six consecutive arginines at the C-terminal, (VI) poly-histidine (poly-His), the most widely used with composition ranging from 3 to 10 His residues at N- or C- terminus.[24, 32]

Poly-histidine tagging is still the most versatile and widely employed for site-specific purification and immobilization using non-covalent interactions to bind with carrier surfaces due to the development of IMAC (Immobilized metal-affinity chromatography) technology. Immobilization through a histidine tag is highly specific and the histidine-tag position in the protein can be controlled by genetic engineering but they are placed on either the N- or C-terminus of recombinant proteins. This fact limits the possibility of controlling the orientation of the enzymes in the immobilization to two determined configurations that are not always the optimal configurations.

4.1.4 The Immobilized metal-affinity Chromatography (IMAC)

The Immobilized metal-affinity chromatography (IMAC) was described for first time by Porath.[33] The immobilization approach is based on a complex formation of the histidines to

a metal chelated by ligands anchored to the carrier surfaced. The stronger interaction between the histidine and the metal is due to the electron donor groups on the histidine imidazole ring and these interactions can be achieved from coordination with the divalent metal under mild conditions (Figure 22, A). Typically, the system works with peptides tags that have a sequence of consecutive histidine residues, the efficiency and the binding strength of the immobilization depends on the distance between the histidine residues and the type of metal as described by Hochuli. [34]

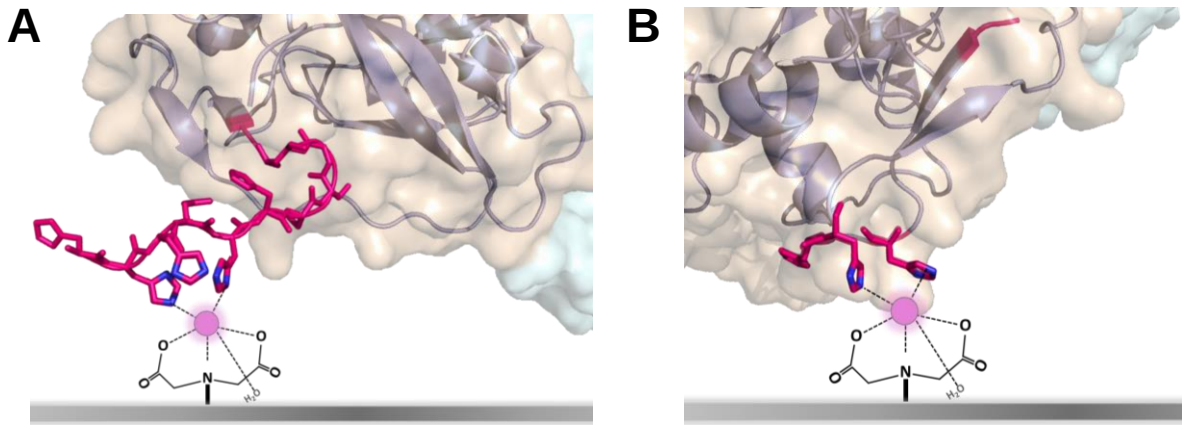

Figure 22: Immobilization through Histidine residues.

A. *Immobilization through histidine-tag at N- or C- terminus on carriers activated with divalent metals.* ***B.*** *Immobilization through surface histidine-enriched clusters on carriers activated with divalent metals.*

4.1.5 Amino acid Clusters

We want to orient proteins through any region of their 3D structure, that is, going beyond the N- and C- terminus. To that aim, the technology available to develop recombinant proteins that contain the desired residues on the target proteins would enable virtually all options for site-specific enzyme immobilization. Different research have been reported about new approaches to solve the limitation in the immobilization locations at N- or C- terminus. Some of those reports are bases in the insertions of different amino acid clusters (Xaa-rich where X refers to any type of amino acid). For example, metallothionein and phytochelatin, which are cysteine-rich proteins and play several roles such zinc-copper homeostasis, protecting against heavy metals or oxidant damage.[35] On the other hand, some glutamine-rich and asparagine-rich proteins are related with diverse protein-protein interactions probably serving as modules.[36, 37]

Histidine is an abundant amino acid in many proteins, it is also a good metal binder and just below the physiological pKa of imidazole. In nature, divers bacteria involved in the homeostasis of Ni^{2+} ion have His-rich proteins.[38] Despite the fact that the average

frequency of the histidine in all the proteins is low (approximately 2.3 %) the histidine-enriched protein is one of the most notable amino acid-enriched category.[36] The uniqueness of the histidine make them an attractive subject of study in biocatalysts research.

In the field of biocatalysts, there are few reports about the use of protein surfaces rich in amino acids to control the orientation immobilization. One of them is the work reported by Abian and colleagues where they increase the number of lysins in a defined area of the penicillin G acylase (PGA) surface to improve immobilization on glyoxyl-agarose. These new ways to drive the orientation enhance the strength of the binding and increasing the stabilization factor ranging from 4 to 11 compared with the native enzyme.[39] The same group reported that the introduction of eight additional glutamic acid residues distributed around the PGA protein surface increase the negative charge of the protein surface and improve the interactions with the cationic polymer co-immobilized in glyoxyl agarose. The introduction of these glutamic acid clusters improve the stabilization of the biocatalyst against the organic solvents. [40]

4.1.6 Computational tool: COREX/Best

As we need some structural and dynamic information to select where would be the possibilities locations for the histidine cluster insertion, for example knowing where the most flexible regions are orient the immobilization aiming at rigidifying that region and increase the overall stability of the immobilized enzymes. Under normal conditions, the structure of proteins in solution shows spontaneous transient fluctuations between the most stable, the partially unfolded and the completely unfolded states, as described by the Boltzmann distribution[41, 42] COREX/BEST (Biology using Ensemble-based Structural Thermodynamics) is a computational algorithm that describes protein dynamics. To describe such dynamics, the algorithm uses the user-supplied protein structure as a template to generate a number of possible microstates where the protein is partially folded with local fluctuations in the protein structure between the folded and native-like protein under determined conditions (e.g. pH and temperature). Therefore, COREX/BEST makes partitions of the protein structure and analyses a combination of these partition residues that could be folded or unfolded independently. The algorithm treats these fluctuations in statistical thermodynamics rather than structural terms, using the Boltzmann relation. [43, 44]

In overview, the program performs the following three calculations: I) The protein's conformational ensemble, using as a basis the "global unfolding model", the program calculates the probability of each amino acid to be in folded/unfolded state. II) Estimate the relative stability differences for the ensemble conformations within a protein`s structure defining the free energy for each ensemble state. III) Determine the temperature-dependent

stability of the conformational ensemble, the program calculates the “stability constants” for each residue in the quaternary structure of the protein and outputs the most probable low energy unfolded state of the proteins.[45] This software was employed for the first time by Godoy and colleagues to understand the directed enzyme rigidification and site-directed enzyme immobilization to get a higher enzyme stabilization.[11]

In this work, we designed different histidine clusters at the surface of the enzymes in order to drive their immobilization on solid surfaces through the regions beyond the N- and C-terminus domains (Figure 22 B). For these aim we selected the most flexible regions that were not involved in the catalytic mechanism bases on the corresponding X-ray structures. The most flexible regions were selected based on computational studies using the server COREX/Best. [43] The selection of the regions where the histidines were introduced were based on the intrinsic flexibility of specific regions calculated by accounting for their b-factor values and computing their local rigidity factors using COREX/Best algorithm. As a proof of concept, we selected two alcohol dehydrogenases: Alcohol dehydrogenase from *Bacillus steareothermophilus* (BsADH), a tetrameric enzyme of 39 kDa/subunit and alcohol dehydrogenase from *Thermus thermophiles* (Tt27-HBDH), a hexametric enzyme of 32 kDa/subunit.

4.2 Materials & Methods

4.2.1 Chemicals

Phusion High-Fidelity DNA Polymerase, FastDigest DpnI, Tris-HCl base buffer, imidazole, optical adhesive film and sealing tape from Thermo Scientific (Waltham, MA, USA), dNTPs (Deoxynucleotide triphosphates) from NZYTech (Lisboa, Portugal), NucleoSpin® Plasmid from Macherey-Nagel (Dueren, Germany). Low density (LdAG-Co^{2+},15 µmol Co^{2+}/mL (A-1061S-X), and high density (HdAG-Co^{2+},40 µmol Co^{2+}/mL) cobalt-activated agarose microbeads 6BCL were acquired from ABT technologies (Madrid, Spain). Metal ion affinity enzyme immobilization EziG1 were donated by EnginZyme (Solna, Sweden). Nicotinamide adenine dinucleotide sodium salt (NAD^+), nicotinamide adenine dinucleotide reduced disodium salt (NADH) and the inductor Isopropyl-β-D-thiogalactopyranoside (IPTG) were acquired from Gerbu Biotechnik GmbH (Wieblingen, Germany), albumin bovine serum standard (BSA), thrombin from bovine plasma, iminodiacetic acid (IDA), HEPES, SYPRO® Orange Protein Gel Stain, 1,5-pentanediol, Ethyl acetoacetate (EAA) were purchased from Sigma-Aldrich (St. Louis, IL, USA). Bradford protein assay dye reagent and micro Bio-spin columns were purchased from BIORAD (Biorad. Hercules, CA, USA). Size exclusion chromatography columns NAP, filtered plates ACroPrep™ of 0.45 µm from Avantor (2021 VWR International, LLC), µ-Slides 8 well glass bottom was purchased from Ibidi (Planegg, Germany). Trypsin Gold enzyme were supplied from Promega Corporation (Fitchburg, WI, USA). AFDye 488 maleimide were purchased from Fluoroprobes (Scottsdale, AZ, USA).

4.2.2 Design of histidine-enriched surface enzymes

The PDB from the BsADH and Tt27-HBDH model enzymes were analysed using the COREX/Best algorithm[43] on the following website (http://best.bio.jhu.edu/BEST/). The PDB file name should be short and without spaces. It must not be compressed and must have the correct PDB file format. After the file is correctly uploaded, COREX/BEST performs the calculation described above.

The COREX/Best algorithm output data was analyzed in Pymol 0.99v editing view software. Flexible regions not involved in the catalytic mechanisms were determined and, in these locations, some residues in the same spatial plane were chosen to be mutated into histidines, creating a belt of histidines on the protein surface. The four variants have been developed for this work for BsADH (Figure 23). BsADH-WT (BsADH native with 6x histidines) this is the native protein that has a tag composed with six histidines at N-terminus, BsADH-H2 (Bs-ADH-Q8H/E11H), BsADH-H2-B (BsADH-E265H/E266H), BsADH-H3 (Bs-ADH-Q8H/K10H/E11H) and BsADH-H4 (Bs-ADH-Q8H//E11H/E265H/E266H).

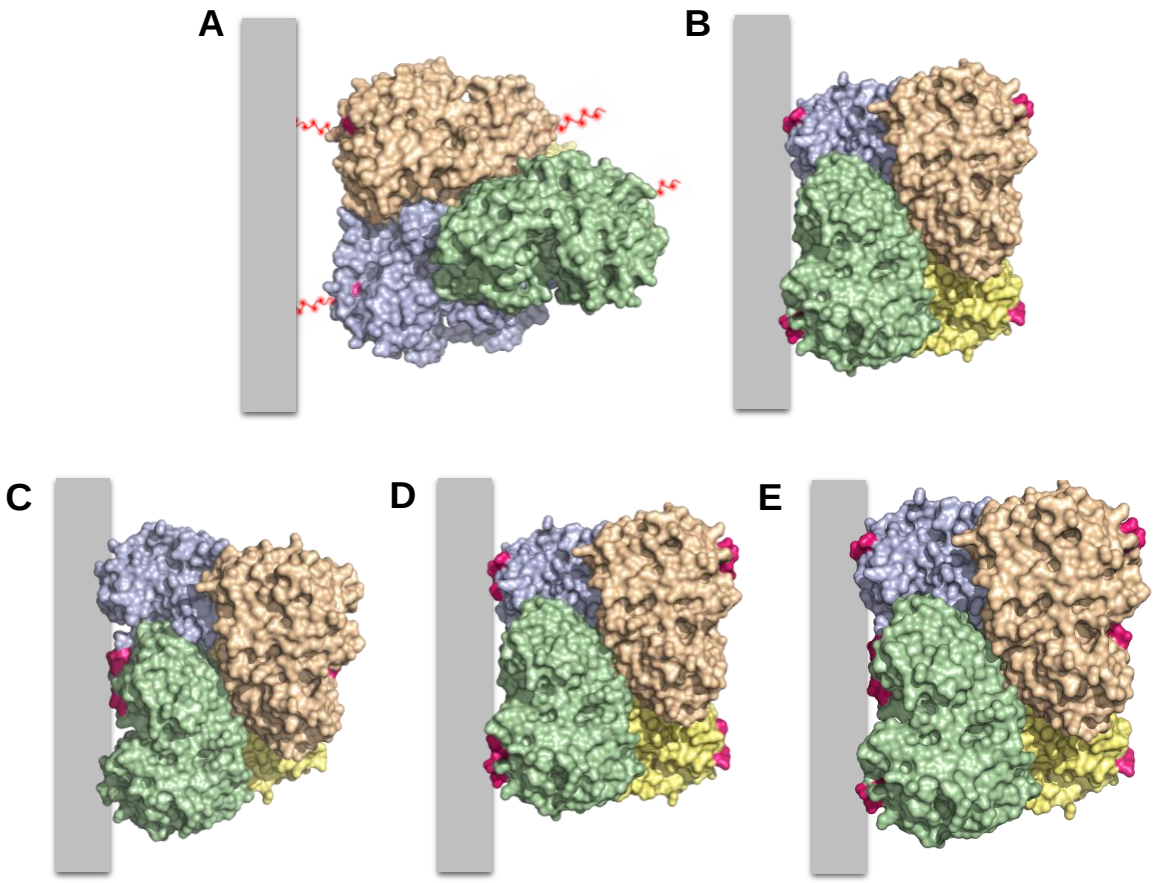

Figure 23: Model structure of the different BsADH histidine enriched variants.

Quaternary structure of the different histidine enriched cluster variants of BsADH and their orientations due to immobilization on a solid carrier. ***A.*** *BsADH-WT the positions where the 6 x histidine-tags are placed are shown in red.* ***B.*** *Variant Bs-ADH-H2.* ***C.*** *Variant Bs-ADH-H2-B.* ***D.*** *Variant Bs-ADH-H3.* ***E.*** *Variant Bs-ADH-H4. The positions where the histidines are inserted are represented in pink.*

For the Tt27-HBDH enzyme, the same analysis was undertaken and five histidine enriched cluster variants were designed including a loop of 26 amino acids with six histidines (Figure 24): Tt27-HBDH-WT (Tt27-HBDH-WT native with 6x histidines), Tt27-HBDH-H2 (Tt27-HBDH-R129H/Y130H), Tt27-HBDH-H3 (Tt27-HBDH-R99H/R129H/Y130H), Tt27-HBDH-H4 (Tt27-HBDH-R99H/R129H/Y130H/R250H) and Tt27-HBDH-loop (Tt27-HBDH-129 (6x H) 133).

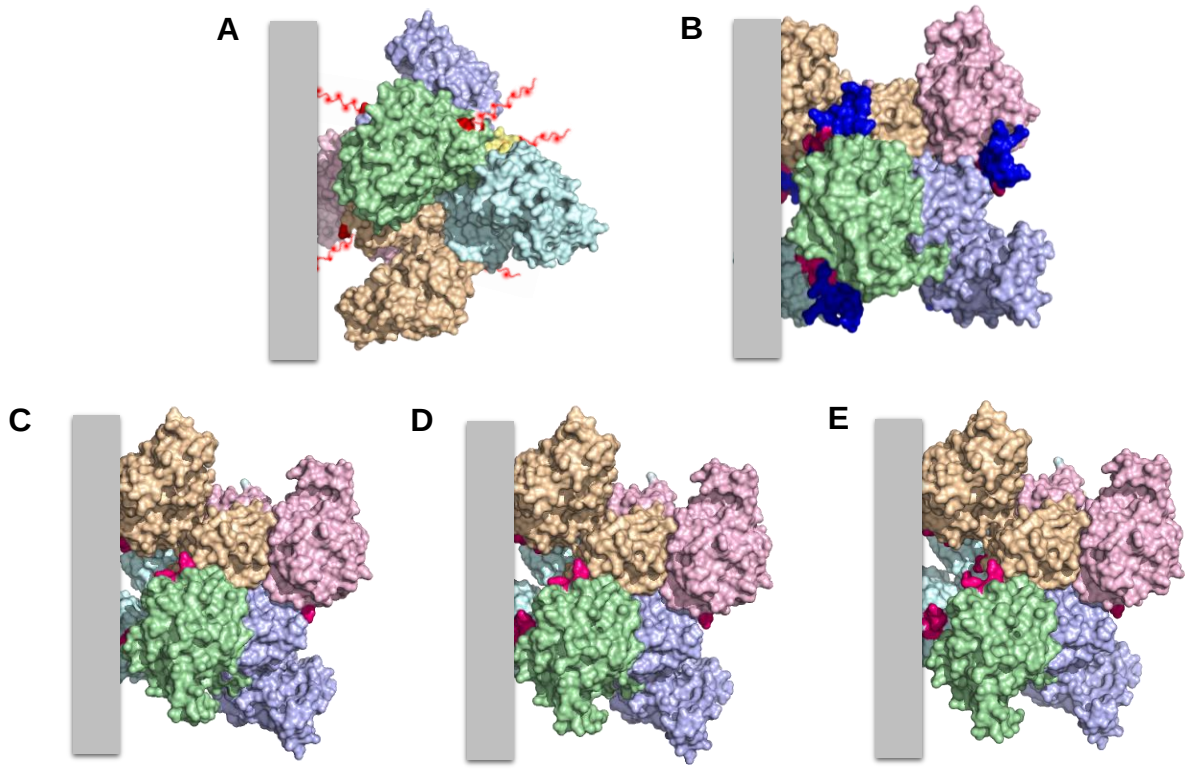

Figure 24: Model structure of the different Tt27-HBDH enriched histidine variants. *Quaternary structure of the different histidine enriched cluster variants of Tt27-HBDH and the orientation due to immobilization on a solid carrier.* ***A.*** *Tt27-HBDH -WT the positions where the 6 x histidine-tags are placed are shown in red.* ***B.*** *Variant Tt27-HBDH-loop, the loop composed by 26 amino acids has been inserted in the positions 129-133 (in blue) and contains six histidines (in pink).* ***C.*** *Variant Tt27-HBDH-H2.* ***D.*** *Variant Tt27-HBDH-H3.* ***E.*** *Variant Tt27-HBDH-H4. The positions where the histidines are inserted are represented in pink.*

4.2.3 Site-direct mutagenesis

All the plasmids in this work are cloned into a pET28b plasmid. The genetic construction for BsADH-WT was obtained from Genscript Biotech (Piscataway; NJ, USA), and the plasmid for Tt27-HBDH was developed in previous works and reported in a recent publication.[46] The primers designed for the replacement of the native amino acid by histidines are shows in the Table 11.

Table 11: Primers for site-direct mutagenesis

Nº	Primer Name	Sequence
1	PF_Bs-ADH_Q8H/E11H	GGTTGTGGAACATTTCAAACACCCGCTG
2	PR_Bs-ADH_Q8H/E11H	CAGCGGGTGTTTGAAATGTTCCACAACC
3	PF_Bs-ADH_E265H/E266H	CCTGCCACCGCATCATATGCCGAT TCC
4	PR_Bs-ADH_E265H/E266H	GGAATCGGCATATGATGCGGTGGCAGG
5	PF_Bs-ADH_K10H	GAACATTTCCATCACCCGCTGAAAATC

6	PR_Bs-ADH_K10H	GATTTTCAGCGGGTGATGGAAATGTTC
7	PF_Tt-27HBDH_R129H/Y130H	CCGCGCTGGCGCATCACAGCGGTCG
8	PR_Tt-27HBDH_R129H/Y130H	CGACCGCTGTGATGCGCCAGCGCG
9	PF_Tt-27HBDH_R99H	GCGAGAAGCATCGTCTGTTCGAACG
10	PR_Tt-27HBDH_R99H	CGTTCGAACAGACGATGCTTCTCGC
11	PF_Tt-27HBDH_R250H	GCTGCACCATGGTTTTGGCGACG
12	PR_Tt-27HBDH_R250H	CGTCGCCAAAACCATGGTGCAGC

The technique used to replace the native amino acid by histidine was the Quick-Change (QC) site-directed mutagenesis technique described elsewhere. [47] This technique allows the amino acid introduction or replacement of a site-specific position in a double-stranded plasmid by a single PCR (Polymerase Chain Reaction) amplification.

The QC reaction for replacements to histidines has been carried out in a final volume of 50 µL that contains 1X buffer Phusion DNA Polymerase, 200 µM of dNTPs, 0.02 U/µL of Phusion DNA Polymerase, 100 ng of DNA template, 0.5 µM of the primers and water. The PCR program used to amplify the DNA starts with the initial denaturalization at 98 ºC for 30 sec, followed by the denaturalization step at 98 ºC for 10 sec, the annealing step was done in a range of temperatures between 55 ºC to 72 ºC, the extension step at 72 ºC for 2 min (15 sec per kb), the program repeats the steps from the denaturalization for 30 cycles and ends with a final extension at 72 ºC for 10 min.

To achieve the QC-PCR three different strategies were employed: in the first one all the components described above were added to the same PCR Eppendorf tube, the second one, two separate PCR Eppendorf tubes were prepared using only one of the primers and run the PCR program, after that 25 µL of each mix, one with the primer forward and the other with the reverse primer were mixed and incubated at room temperature for 1 hour. In the third strategy with another 25 µL from the tubes in the second strategy, a 10-cycle PCR amplification was performed after mixed in a single PCR tube.

After the PCR amplification all the samples were treated with Fast-digest DpnI restriction enzyme to digest the non-mutated parental template in the PCR products. For that 1X buffer Fast-digest DpnI has been added followed by the addition of 2 µL of the restriction enzyme, the mix was incubated for 1 hour at 37 ºC followed by enzyme denaturalization program at 100ºC for 15 min. The final PCR product were transformed in *E. coli* DH5α competent cells (laboratory stock) using standard methods.[48] Five colonies of each PCR strategy were sent to sequencing with a previous step of plasmid DNA purification using NucleoSpin plasmid miniprep kit.

4.2.4 Protein expression

The protein expression has been done following the same protocol described in the section 3.2.3. The BsADH-WT, BsADH-H2, BsADH-H4 and Tt-HBDH variants were induced with 1 mM IPTG for 3 hours at 37 ºC and 250 rpm, while BsADH-H3 was induced with 0.1 mM IPTG and grown at 21 ºC and 250 rpm overnight.

4.2.5 Cell-free extract preparation

The resulting pellets were resuspended in purification buffer Tris-HCl buffer 25 mM at pH 7 with 150 mM of NaCl and 10 mM of imidazole. The suspension was lysed by sonication as is described in section 3.2.4. and finally centrifuged at 9391 x g at 4 ºC for 30 min to separate the soluble protein from the lysates.

4.2.6 Protein purification

BsADH histidine variants were purified by metal affinity, 5 mL of crude extract was incubated with 500 mg AG-Co^{2+} resin in a column and incubated under gentle stirring for 1 hour. After that time, the column was eluted and washed three times with Tris-HCl buffer 25 mM at pH 7 and incubated with 5 mL of 500 mM imidazole in Tris-HCl buffer 25 mM at pH 7 for 1 hour, then the solution was eluted and storage at 4 ºC. Tt27-HBDH histidine variants were purified by thermal shock. The crude extract was incubated in a thermal bath at 70 ºC for 40 min to remove all the proteins that are not thermophilic by precipitation, and the precipitated solution was centrifuged at 9391 x g at 4 ºC for 30 min to obtain the target protein and stored at 4 ºC.

4.2.7 Protein quantification

The protein concentrations were measured using Bradford's protein assay.[49] All the experiments were perform in 96 well plates. Briefly, 5 µL of pure protein solution was mixed with 200 µL of Bradford reagent and incubated at room temperature for 5 min. Then the absorbance was measured at 595 nm. A standard curve using bovine serum albumin as standard was utilized to calibrate the absorbance with the protein concentration.

4.2.8 Thrombin proteolysis and imidazole remove

A ratio of 50:1 protein: thrombin was incubated in an Eppendorf tube overnight at 4 ºC under rotation. To remove the imidazole from the purified protein a size exclusion chromatography column NAP 10 has been used. The exchange buffer used to remove the imidazole was Tris-HCl buffer at pH7 with 20 mM of imidazole.

4.2.9 Colorimetric enzyme activity assays

Enzyme activities were spectrophotometrically measured in transparent 96-well microplates using a Cell Imaging Multi-Mode Reader Cytation 7 BioTek ®. The raw data was analysed with Gen 5 software (BioTek ®).

Alcohol dehydrogenase assays

One unit of activity corresponds to the amount of enzyme needed to consume/produce 1 µmol of the corresponding nicotinamide cofactor in one minute at 30 ºC. The absorbance was monitored at 340 nm (ε= 6.22 mM^{-1} x cm^{-1}) at different times under orbital shaking (567 rpm) within the reader.

BsADH activity: 200 µL of reaction mixture containing 1 mM NAD^+, 100 mM of ethanol in 100 mM sodium phosphate buffer at pH8 were added to 5 µL of enzymatic solution or immobilized enzyme in a suspension 1:10. For the oxidation of diols, 200 µL of reaction mixture containing 1 mM NAD^+, 10 mM of 1,5-pentadiol in 50 mM Tris-HCl buffer at pH 8 was incubated with either 5 µL of free enzyme or 10 µL suspension 1:10.

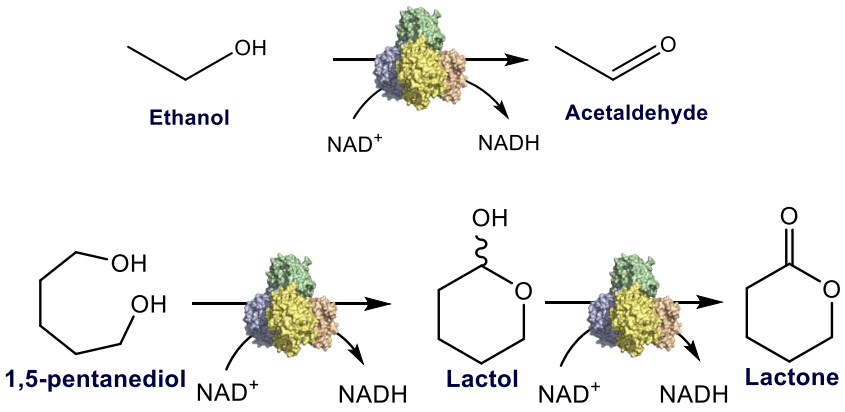

Tt27-HBDH activity: 200 µL of reaction mixture containing 0.2 mM NADH , 5 % of isopropanol and 10 mM of ethyl acetoacetate in 100 mM sodium phosphate buffer at pH 7 were added to 5 µL of enzymatic solution or immobilized enzyme in a suspension 1:10.

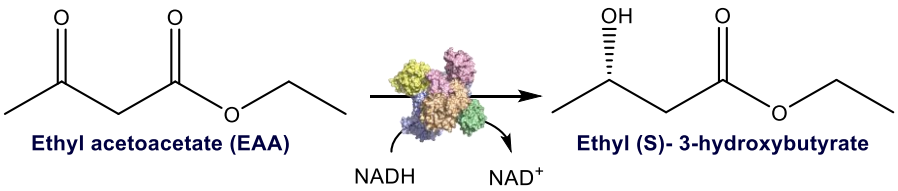

4.2.10 Circular-Dichroism (CD) spectra

CD measurements were made using a Jasco J-1500 NIR. The spectra were collected at 100 nm per min scan speed, the spectral resolution (data pitch) was 0.2 nm, 1 nm bandwidth and 10 scans were accumulated in each case. The CD spectra were plotted as molar ellipticity [θ] in deg*cm^{2}*dmol^{-1}.

$$[\theta] = \frac{\theta * 100 * MW}{c * l * n}$$

Eq (8): Molar Ellipticity

Where θ = observed ellipticity (deg), MW= Molecular mass, c = protein concentration in mg x mL^{-1}, l = path length in cm (0.001 cm) and n = number of residues. The CD spectra were recorded from 250-200 nm using 0.2-0.4 mg per mL of protein in Tris-HCl buffer at pH 7

4.2.11 Site-selective immobilization

Before immobilizing the histidine enriched variants from BsADH, the his-tag proteolysis and imidazole removal have been done as described in section 4.2.8. After, 1 mL of the untagged enzymes and the WT were offered to 100 mg of AG-Me^{2+} microbeads or EziG1 in a column under orbital rotation for 1 hour at 4 ºC. Then, the suspension was filtered and collected in a new eppendorf tube for analysis and the carrier was washed with at least 1 mL of sample buffer, 25 mM Tris-HCl buffer at pH 7 and 20 mM of imidazole, to remove the untagged protein.

4.2.12 Stability tests

The different biocatalysts were resuspended in a ratio 1:10 with 25 mM Tris-HCl buffer at pH7 for thermal inactivation. The suspension was incubated at 70 ºC for 3 hours, and the activity after this time was measured following the protocol described in the section 4.2.9. In the case of the organic solvent, the carriers were resuspended in 25 mM Tris-HCl buffer at pH7 containing 70% of isopropanol (IPA), the suspensions were incubated overnight at 4ºC. After that, the solution was eluted and the biocatalysts were resuspended keeping the ratio 1:10 with 25 mM Tris-HCl buffer at pH7, and the activity measured. For pH5, the biocatalyst was suspended in 50 mM acetate buffer pH5 and the same procedure described above was carried out. First, the recover activity after the inactivation condition were measure using the ADH colorimetric assay (section 4.2.9). The stabilization factor for the biocatalysts was calculated using the following equation.

$$Fe_{total} = \frac{\%\ Activity\ recovered_{final\ time}}{\%\ Soluble\ WT\ _{final\ time}}$$

Eq (9): Total stabilization factor

4.2.13 Kinetic thermal inactivation

The kinetic thermal inactivation of the BsADH histidine variants were carried out by incubating the suspension in a ratio 1:10 with 25 mM Tris-HCl buffer at pH7 at 70 ºC and taking points at 2, 3, 4 and 5 hours. The residual activity after the thermal inactivation were measure by the ADH activity assay (section 4.2.9). To calculate the half-life time of the biocatalysts, the kinetic inactivation model described by Aymard and colleagues were performed.[50] The model use a 3-parameters biexponential Eq (10) that describe heat-induced the enzyme activity decay.

$$\frac{(A)_t}{(A)_0} = C\ x\ e^{-\propto x\ t} + (1 - C)\ x\ e^{-\beta\ x\ t}$$

Eq (10): Model equation to adjust diversity of inactivation mechanisms

4.2.14 Differential scanning fluorimetry to calculate the enzyme melting-temperature (T_M)

Differential scanning fluorimetry (DSF) was performed using 8 µg of each BsADH/Tt27-HBDH histidine variant (soluble and immobilized on their optimal carriers, loaded at 1 mg per g of carrier). The DSF were performed using a Bio-Rad CFX Connect™ Real-Time Detection System. A final volume of 20 µL were placed on a 200 µL PCR tube containing the enzyme and 2.5 µL of SYPRO® Orange Protein Gel Stain diluted 40 times from the stock in water. The samples were heated from 25 ºC to 95 ºC using a temperature ramp rate of 0.5 ºC x min^{-1}. The first derivative (dF/dT) were plotted to obtain the maximum value that correspond with biocatalysts T_M.

4.2.15 Analysis of intrinsic Tryptophan Fluorescence

To analyse the effect in the structure of the enzymes due to the immobilization orientation change, the free enzymes and the immobilized BsADH-WT and BsADH-H3 fluorescent spectra were measured. The biocatalyst were loaded at 1 mg x g^{-1} and the measurement of the immobilized enzyme was done in a ratio 1:20 with 25 mM Tris-HCl buffer at pH7 The soluble enzyme at 0.05 mg x mL^{-1} and the immobilized enzyme were measured in a 96- well UV plate, the fluorescence were recorded with a step equal to 5 nm from 300 nm to 600 nm upon the sample excitation at 280 nm with a gain of 100. For the thermal inactivation, the suspension were incubated at 100ºC and the same protocol described above were done.

4.2.16 Protein Labelling with AFDye 488 maleimide

Fluorescent labelling of BsADH histidine enriched variants was performed using AFDye 488 as a fluorophore and the following procedures were reported elsewhere. [51] The labelling buffer employed in this process was 50 mM HEPES buffer at pH7. The 1 mg x mL^{-1} of soluble enzyme was incubated with AFDye 488 at 1:1 molar ratio (AFDye 488 stock at 10 mg x mL^{-1} in DMSO) for 15 min at room temperature under gentle shaking. The remaining unconjugated AF488 was eliminated by buffer exchange using a size exclusion chromatography column NAP 10. The labelled soluble enzymes were stored at -80 ºC using liquid N_2 to achieve a fast-freezing process.

To monitoring of the AFDye 488 fluorescence against the thermal inactivation BsADH-WT and BsADH-H3 (0.1 mg x mL^{-1}) labelled were incubated in columns with LdAG-Co^{2+} and HdAG-Co^{2+} carriers, respectively, at a 1:10 ratio for 1 hour at 4 ºC under gentle shaking. The carriers were washed with Tris-HCl 25 mM buffer at pH7 to remove the untagged protein. Finally the carrier were resuspended in a ratio (1:20) with 25 mM Tris-HCl buffer at pH7 and incubated at 100ºC. The resuspended samples were measured in a 96-well UV plate, the fluorescence were recorded with a step equal to 5 nm from 500 nm to 700 nm upon the sample excitation at 490 nm with a gain of 100.

4.2.17 Operational stability

BsADH histidine variants:

Kinetic studies were done using 50 mg of the BsADH-$WT_{Ld\text{-}AG\text{-}Co^{2+}}$,BsADH-$H3_{Hd\text{-}AG\text{-}Co^{2+}}$ and BsADH-$H4_{Hd\text{-}AG\text{-}Co^{2+}}$ biocatalysts. To each biocatalyst were added 135, 80 and 290 mg respectively of the regenerator system TtNOX/BlCAT on glyoxyl and placed into Bio-spin columns. 600 µL of the reaction mixture containing 10 mM of Diol, 1 mM of NAD^+ and 0.15 mM of FAD in 100 mM phosphate buffer at pH 8 were added to the biocatalysts. To facilitate the oxygen diffusion to the reaction, an open syringe needle were added to the columns. In the case of the batch reaction, only 25 mg of each BsADH biocatalyst were added following the same ratio described above. Again, 600 µL of the reaction mixture containing 10 mM of Diol, 1 mM of NAD^+ and 0.15 mM of FAD in mM Tris-HCl pH 8 were added to the biocatalysts, after each 24 hours of reaction, the biocatalysts were washed with Tris-HCl 25 mM at pH 7. The reaction solution were collected and analyzed by gas chromatography as is described by Santiago-Arcos and colleagues.[52]

Tt27-HBDH histidine variants:

For the Tt27-HBDH the operational study were performed using a ratio biocatalyst: reaction mix of 1:10. The biocatalyst loading employed was 10 mg per g of carrier and the reaction

mixed employed for these experiments contains 10 mM of ethyl acetoacetate, 1 mM of NADH, 5 % of isopropanol in Tris-HCl 10 mM at pH 7.For the kinetic reaction and reusability study the reaction were carried out at 60 ºC and 250 rpm and the samples were analyzed by gas chromatography as is described by Orregon and colleagues.[46]

4.2.18 Proteomic assays

To perform the proteomic assay 100 mg of biocatalyst loaded with 5 mg x g^{-1} of carrier were prepared. The biocatalysts were resuspended in a column with 200 µL of 50 mM of Tris-HCl buffer at pH 7,6 that contain 0.025 mg x mL^{-1} of trypsin. The columns are incubated overnight under gentle shaking at room temperature. Then, the solution is collected from the column and lyophilised.

4.2.19 Confocal Laser Scanning Microscopy (CLSM) of BsADH-WT and BsADH-H3 variant

The spatial distribution and organization of the BsADH-WT and the BsADH-H3 histidine cluster variants were analyzed using CLSM with a spectral ZEISS LSM 880 microscope (Carl, Zeiss, Germany). Confocal imaging was done using a 20x objective and an excitation laser of λ_{ex}: 488 nm. Image processing of confocal images were done using FIJI as is described in the section 3.2.12.

BsADH-WT and BsADH-H3 (0.1 mg x mL^{-1}) labelled with AFDye 488 were incubated in columns with LdAG-Co^{2+} and HdAG-Co^{2+} carriers at a 1:10 ratio for 15 min at 4 ºC under gentle shaking. Later, the carrier was washed with Tris-HCl 25 mM buffer at pH7 to remove the untagged protein. Finally a 1:200 (w:y) buffer (Tris-HCl 25 mM buffer at pH7) suspension containing the carrier were prepare for CLSM analysis. The ratio profile analysis were perform as is described in the section 3.2.12. Briefly, the micrographs were analyzed by FIJI with the co-localization and the fluorescence profile along the radius of single beads plugins. Whit the plugin of radial profile generation we calculate an average and normalized fluorescence of the confocal images. Then, a Gaussian fit was applied to the obtained profiles of around 10 single beads of similar size, after that, we searched for the fitted data point that corresponds to the 50% of the maximum normalized fluorescence fitted peak ($y_{max}/2$), and the corresponding radius coordinate (x) to that data point was then subtracted from the radius of the analysed bead to finally obtain the FWHM (Figure 4).

4.2.20 Single-particle immobilization assay

The immobilization of the different BsADH histidine variants was followed and recorded using a Cytation 5 cell imaging reader (Bio Tek Instruments). The immobilizations were carried out on clear bottom, black 96-well microplates. The samples were observed using

the Plan Fluorite 4X phase objective with a numerical aperture of 0.13 and coupled to an apotome grid WD with a working distance of 17 mm. The GFP (λ_{ex}:469; λ_{em}:525) imaging LED/filters pairs were used for the BsADH variants labelled with AFDye 488. All the experiments were followed in parallel by a brightfield channel to detect changes in the positions of the beads during the kinetic experiment. The experiments were performed using 195 µL of a suspension 1:400 (w:v) of microbeads (LdAG-Co^{2+} for BsADH-WT and HdAG-Co^{2+} for BsADH-H3) in 25 mM Tris-HCl at pH7 that were placed into the wells for microscopic analysis. Later, 5 µL of the labelled enzyme at 0.01 mg per mL in 50 mM of HEPES buffer at pH7 were added into the well. The kinetic were recorded following the fluorescence changes around the microbeads surface. The time-lapse images were recorded every 8 seconds for 1 hour. The image processing and analysis were performed with a FIJI plugin developed in our group.[53] From each experiment, the kinetics of 15 ROIs of different microbeads were analyzed and a non-linear curve fitting using Origin was also performed. The Eq (12) is the BoxLucas1

model that fit the data to a pseudo-first order kinetic (Eq (11): Equation, where q_t is the amount of immobilized protein at time t; q_e is the amount of protein remaining after the equilibrium of immobilization reaction and k_1 is the pseudo first order rate constant.

$$q_t = q_e(1 - e^{(-k_1 t)})$$

Eq (11): Equation of pseudo-first order kinetic model

$$y = a(1 - e^{(-bx)})$$

Eq (12): Model fitting BoxLucas1

4.2.21 Immobilization screening using a single-plate

The immobilization screening of the different Tt27-HBDH histidine variants were performed using single plates with filtered bottom. First, a suspension 1:10 of agarose microbeads activated with the different metal chelates were prepared. 200 µL of each suspension were added to the well of a filter plate AcroPrep™ and the plate was centrifuge at 1503 x g for 1 min to dry the carriers. Then, the plate bottom were covered with a sealing tape to avoid spillage through the membrane and 200 µL of each Tt27-HBDH histidine variant at 0.6 mg per mL were added finally and optical adhesive cover were used to cover the whole plate and prevent the solution from coming out as well as prevent the carrier from sticking to the film. Finally, the film were shanking gently overnight at 4 ºC.

4.3 Results & Discussion

This work sought to examine the capacity of histidine enriched clusters to control the enzyme orientation during immobilization on solid carriers activated with metals. The histidine clusters could have potential as protein engineering technology to drive the orientation of multimeric enzymes in solid carriers.

4.3.1 Development of an enzyme toolkit containing different histidine-enriched clusters

Five different BsADH histidine enriched cluster variants have been created using site-directed mutagenesis. All these variants were fused with 6x histidine tag at their N-terminus to ease the purification step. After purification the his-tag was proteolyzed using thrombin in order to not interfere with the immobilization process (Figure 25). This was possible because the plasmid encoding the wild-type BsADH was designed with a sequence encoding a recognizes thrombin between the histidine-tag sequence and the start codon of the bsadh gene. After the purification process, the specific activities (Eq (1)) of the different enzymes were measured before and after his-tag proteolysis (Table 12).

Table 12: Specific activity of BsADH histine enriched variants before and after his-tag proteolysis.

Variant	Histidine Position	Ae_s his-tag (U x mg^{-1})	Ae_s without his-tag (U x mg^{-1})
BsADH-WT	6 x his N-terminus	6.98 ± 0.13	8.20 ± 0.35
BsADH-H2	Q8H/E11H	5.47 ± 0.02	4.24 ± 0.47
BsADH-H2B	E265H/E266H	0.06 ± 0.02	0.03 ± 0.0
BsADH-H3	Q8H/K10H/E11H	12.13 ± 0.6	14.13 ± 0.79
BsADH-H4	Q8H/E11H/ E265H/E266H	9.17 ± 1.08	10.81 ± 0.23

BsADH activity was monitored at 340 nm (εNADH = 6.22 mM^{-1} x cm^{-1}), the reaction mixture containing 1 mM NAD^+, 100 mM of ethanol in 100 mM sodium phosphate at pH8. The Ae_s were calculated following the Eq (1)

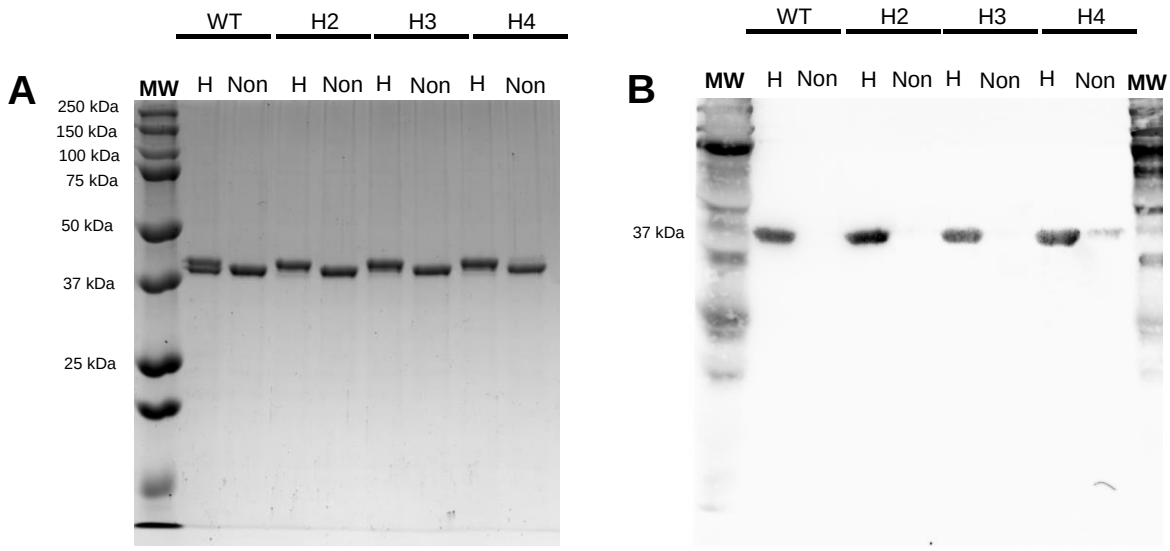

Figure 25: Histidine-tag proteolysis.

A. *SDS-Page electrophoresis gel of the pure BsADH histidine variants before (H) and after (NON) proteolysis with thrombin. The proteolysis was carried out at 4 ºC overnight in a protein: thrombin ratio of (50:1).* ***B.*** *Wester-blot analysis of the pure BsADH histidine variants before (H) and after (NON) proteolysis with thrombin.*

Removing the his-tag through thrombin proteolysis, the specific activity increases around 1.2 times in the cases of WT, H3 and H4. The H2B variant loses the activity due to replacement by histidine mutations in the positions E265H/E266H. Inspecting the quaternary structure, we saw that the glutamic acid in the position 266 has a polar interaction with the residue K241 located in the α-helix involved in the cofactor binding (Figure 26).[54] This change loses the interaction which could affect enzyme activity. Surprisingly when another two histidines are introduced, such as the case with BsADH-H4, the activity does not drop as seen with BsADH-H2-B. Due to this loss of activity seen in the BsADH-H2B variant, it was discarded for further experiments.

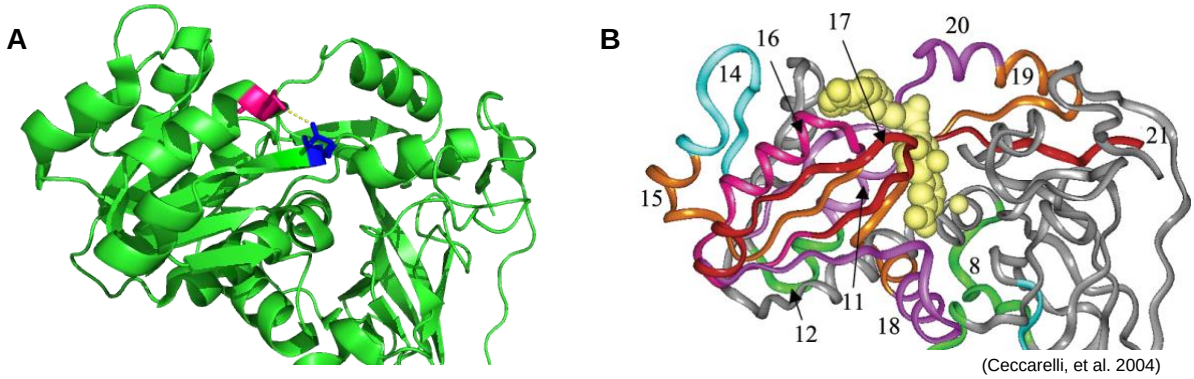

(Ceccarelli, et al. 2004)

Figure 26: Structural interaction between the peptides and the cofactor.

__A.__ Polar interaction between the residue E266 and K241. __B.__ Crystal structure described by C. Ceccarelli and co. Yellow represents the modelling cofactor NAD^+, and the peptides that are involved in the cofactor binding are coloured in orange, pink, red and magenta.

The secondary structures of the different mutants were analysed through far-UV CD spectroscopy (Figure 27) to check if the mutations significantly affect the secondary structure of the protein. The wild-type with and without histidine tag and the mutants without histidine tag were measured. On one hand, the his-tag proteolysis slightly decreases the helicity in the BsADH-WT variant. Surprisingly, the variants BsADH-H3 and BsADH-H4 are seen to conserve more helicity.

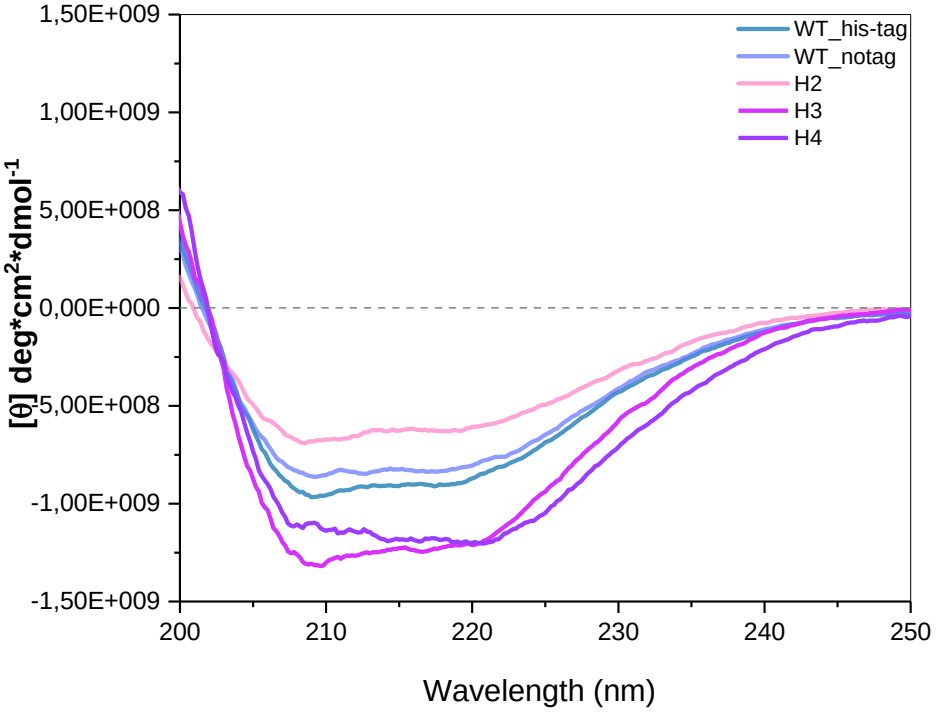

Figure 27: Circular Dichroism spectroscopy of the BsADH histidine vatiants.

4.3.2 Immobilization of BsADH histidine histidine-enriched clusters

After the characterization of the new soluble BsADH histidine enriched variants, various studies were performed to characterize and understand the behaviour of the different enzyme orientations on the immobilizations for the biocatalyst. First the immobilization parameters were analyzed to describe the differences between the common histidine-tag immobilization and the new approach of the histidine variants on different regions of the protein surface. The immobilization study of the BsADH histidine variants were achieved with porous agarose microbeads (AG functionalized with different metal chelates (AG-Me^{2+}) being Me^{2+}: Co^{2+}, Cu^{2+} and Ni^{2+} and different metal densities (15 µmol x g^{-1}: Low density (Ld), 40 µmol x g^{-1}: High density (Hd). Also, a commercial porous glass-based carrier

functionalized with Fe^{3+} catechol complex (EziG1) with a density of 10 µmol x g^{-1} were employed. To select those metals we take account of the different affinities of proteins for metal ions, due to the principles of hard and soft acids and bases (HSAB) [55] Fe^{3+}, which is classified as a hard Lewis acid, and Cu^{2+}, Ni^{2+} and Co^{2+}, which are classified as borderline acids were tested. These metal ions are commonly used in IMAC.[33] In our case, the clusters of histidines are considered a borderline base as they contain aromatic nitrogen, so the affinity with borderline acids will be favourable. The ion-metal chelates strength is Cu (II)>Ni (II)>Co (II) when they are chelating with iminodiacetate (IDA).[56]

As is described in section 4.1.4 the interaction that allows the protein immobilization to happen is between the pyrrolidine ring and the metal ions of the carrier (Figure 22). In this case, the protein must have a histidine-tag or following our approach a histidine enriched cluster on the protein surface. The first step proved that the untagged protein is not able to immobilize on the AG-Co^{2+} microbeads, the BsADH-WT and the WT untagged were immobilized and analyzed qualitatively by SDS-Page electrophoresis. Figure 28 (lanes 7 and 9) shows that all the untagged protein remained in the supernatant upon immobilization, thus they were unable to bind the AG-Co^{2+} (Figure 28, lanes 8 and 10). On the contrary, the WT his-tagged enzyme was immobilized even in presence of 20-50 mM of imidazole in the immobilization buffer (Figure 28, lanes 2 and 4).

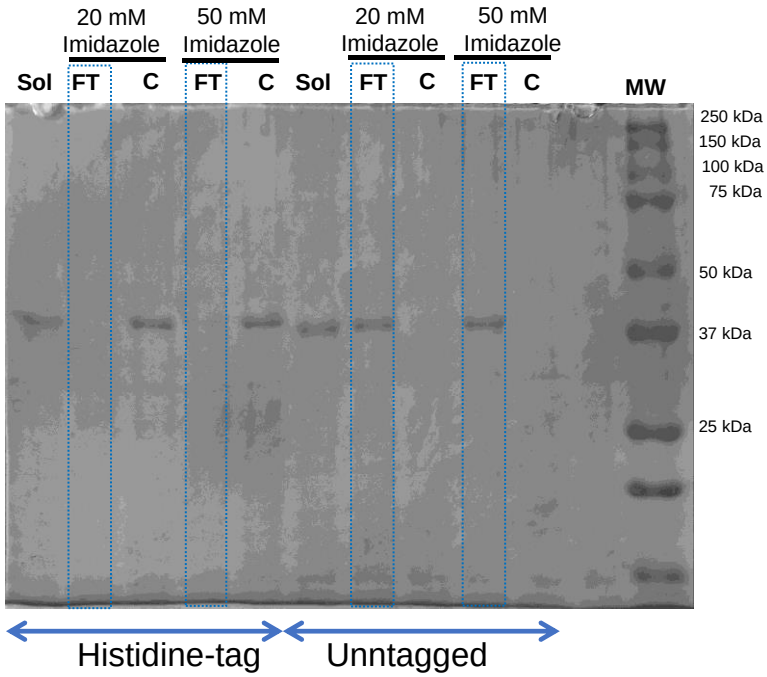

Figure 28: Immobilization of BsADH with and without histidine tag on AG-Co^{2+}.

Lane 1: *$WT_{his\text{-}tag}$ soluble (Sol) enzyme;* ***lane 2:*** *Supernatant (FT) upon immobilization in presence of 20 mM imidazole;* ***lane 3:*** *AG-Co^{2+} carrier (C) with His-BsADH immobilized in*

presence of 20 mM imidazole ; ***lane 4:*** *FT upon immobilization of His-BsADH in presence of 50 mM imidazole;* ***lane 5:*** *AG-Co^{2+} carrier (C) with His-BsADH immobilized in presence of 50 mM imidazole ;* ***lane 6:*** *non-tagged BsADH soluble (Sol) enzyme;* ***lane 7:*** *FT no tag upon immobilization of His-BsADH in presence of 20 mM imidazole;* ***lane 8:*** *AG-Co^{2+}carrier (C) with non-tagged BsADH immobilized in presence of 20 mM imidazole ;* ***lane 9:*** *FT upon immobilization of non-tagged BsADH in presence of 50 mM imidazole;* ***lane 10:*** *AG-Co^{2+} carrier (C) with non-tagged BsADH immobilized in presence of 50 mM imidazole. The FT lanes are framed in blue.*

The same analysis has been performed for the mutants BsADH-H2 and BsADH-H4 (Figure 29). The mutant BsADH-H2 was selectively immobilized on AG-Co^{2+} carrier even in the presence of 20 mM of imidazole and eluted further under denaturing conditions (Figure 29 A, lane 8). However, 50 mM imidazole was enough to almost fully avoid the immobilization of this variant (Figure 29 A, lanes 9 and 10). Surprisingly, the quadruple mutant BsADH-H4 was immobilized in negligible quantities (Figure 29 B, lanes 8 and 10) despite having a higher number of exposed histidines and sharing two histidine residues at position 8 and 11 with the H2 variant. Thus, we demonstrate that the immobilization through the histidine enriched clusters can be possible. The second step was the quantification of the immobilization parameters for the BsADH histidine variants and the different metal chelate carriers.

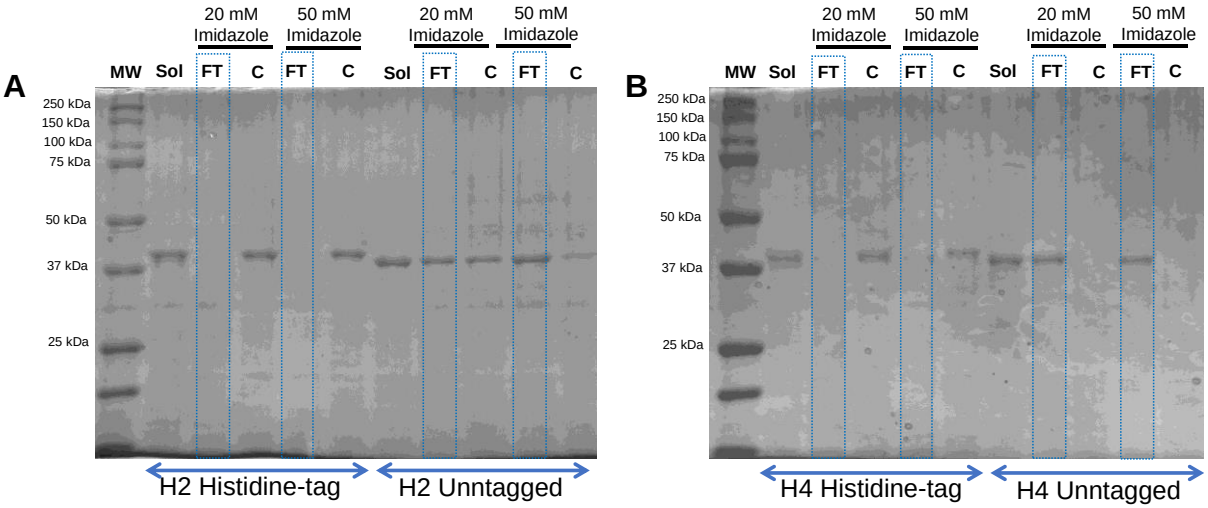

Figure 29: Immobilization of BsADH-H2 and BsADH-H4 variants with and without histidine tag on AG-Co^{2+}.

A. *BsADH-H2* ***and B.*** *BsADH-H4 variants.* ***Lane 1:*** *Soluble (Sol) His-tagged BsADH variant;* ***lane 2:*** *supernatant (FT) upon the immobilization of His-tagged variant in presence of 20 mM imidazole;* ***lane 3:*** *AG-Co^{2+} carrier (C) with His-tagged variant immobilized in presence of 20 mM imidazole ;* ***lane 4:*** *same as line 2 but with 50 mM imidazole;* ***lane 5:*** *same as line 3 but with 50 mM imidazole;* ***lane 6:*** *Free non-tagged BsADH variant;* ***lane 7:*** *supernatant (FT) upon*

the immobilization of non-tagged variants in presence of 20 mM imidazole; ***lane 8:*** *AG-Co^{2+} carrier (C) with non-tagged variants immobilized in presence of 20 mM imidazole;* ***lane 9:*** *same as line 7 but with 50 mM imidazole;* ***lane 10:*** *same line as 8 but with 50 mM imidazole. The FT are framed in blue.*

Thus, an immobilization screening was performed using agarose microbeads to chelate with the borderline acids described above, and the commercial glass-based carrier (EziG1). Additionally, in this work, different metal chelates densities were tested for Cu^{2+} and Co^{2+} chelates with 15 µmol and 40 µmol of Me^{2+} per gram of carrier (Table 13). All the carriers are able to immobilize BsADH-WT with an immobilization yield of 100%, although the recovered activity is very different with values near to 0 U x g^{-1} in the case of HdAG-Cu^{2+} and 0.65 U x g^{-1} in the case of LdAG-Co^{2+}. The metal density, in the case of BsADH-WT, seems to affect the recovery activity with a decrease of almost half of the activity expressed when is immobilized on LdAG-Co^{2+} compared to when is immobilized on HdAG-Co^{2+}. The variants BsADH-H2 and BsADH-H3 have similar behaviour upon the immobilization to the WT regardless of the ion-metal chelate or the metal density. On the contrary, the BsADH-H4 variant has a greater affinity to Ni^{2+} or Fe^{3+} over Cu^{2+} or Co^{2+}, but when the metal chelate density for Cu^{2+} and Co^{2+} is increased the immobilization yield is comparable to Ni^{2+} or Fe^{2+} with an 81 % and 99 % immobilization yield, respectively. Despite the immobilization yield of the BsADH histidine variants on the carriers with copper, low density (LdAG) (15 µmol per gram of carrier) or high density (HdAG) (40 µmol per gram of carrier) being 100 % in the variants BsADH-H2, BsADH-H3 and WT, the recover activity is lower than the activities shown in the cobalt carriers for the same variants. Considering the metal leaching from the carrier and the metal ion transfer which has been described when using immobilized metal affinity chromatography (IMAC).[57-59] we hypothesise that BsADH, as it is a metalloenzyme, could exchange the structural or catalytic zinc for copper. This phenomenon has already been reported with the insertion of Cu^{2+} ions into another alcohol dehydrogenase from horse liver, which contains four zinc ions, two catalytic and two structural. The copper ions were inserted in the catalytic sites where the catalytic site resembles Type 1 copper proteins.[60] An alternative process could happen due to the interaction between the peptide protein chain and the copper ions as they contain a wide range of potential donor groups.[61] This possible metal-peptide complex with Cu^{2+} could disturb the enzyme structure, affecting the recovered activity upon the immobilization. The activity loss shown in Table 13 is notably higher when HdAG-Cu^{2+} is used in comparison with LdAG-Cu^{2+}. However, the enzyme inactivation in HdAG-Co^{2+} is not so strong, and in the case of the variant BsADH-H4, it reaches almost 100 % of the immobilization yield and the recovery activity was 2.4 times higher than the WT variant in the same conditions.

Meanwhile, the variant BsADH-H3 recovers activity upon immobilization in all cases, with the highest activity using LdAG-Co^{2+}as a carrier.

Table 13: Immobilization parameters for BsADH variants

Variant	Metal chelate	Metal density (µmol /g)	Load ($mg_{protein}$ / g)	Ψ % Immobilization	Recovered Activity ($U/g_{carrier}$)	$Ae_{immobilized}$ (U/mg)	rRA(%)[a]
WT	Ni^{2+}	15 µmol	0.99 ± 0.16	100 ± 0	0.36 ± 0.03	0.36 ± 0.03	7
	Fe^{3+}	10 µmol	0.99 ± 0.16	100 ± 0.3	0.44 ± 0.01	0.44 ± 0.01	9
	Co^{2+}	15 µmol	0.94 ± 0.03	100 ± 0	0.65 ± 0.09	0.70 ± 0.09	41
	Co^{2+}	40 µmol	0.99 ± 0.00	100 ± 0	0.38 ± 0.05	0.38 ± 0.05	7
	Cu^{2+}	15 µmol	0.94 ± 0.03	100 ± 0	0.24 ± 0.01	0.25 ± 0.01	15
	Cu^{2+}	40 µmol	0.94 ± 0.03	100 ± 0	0.03 ± 0.01	0.03 ± 0.01	2
H2	Ni^{2+}	15 µmol	0.82 ± 0.06	100 ± 0	0.35 ± 0.05	0.42 ± 0.06	11
	Fe^{3+}	10 µmol	0.78 ± 0.01	95 ± 1.5	0.42 ± 0.05	0.53 ± 0.06	13
	Co^{2+}	15 µmol	0.82 ± 0.06	100 ± 0	0.67 ± 0.07	0.81 ± 0.09	20
	Co^{2+}	40 µmol	0.82 ± 0.06	100 ± 0	0.42 ± 0.05	0.51 ± 0.06	13
	Cu^{2+}	15 µmol	0.82 ± 0.06	100 ± 0	0.30 ± 0.07	0.36 ± 0.07	9
	Cu^{2+}	40 µmol	0.82 ± 0.06	100 ± 0	0.12 ± 0.01	0.15 ± 0.01	4
H3	Ni^{2+}	15 µmol	0.99 ± 0.06	100 ± 0	0.43 ± 0.05	0.43 ± 0.07	8
	Fe^{3+}	10 µmol	0.94 ± 0.05	98 ± 0.4	0.68 ± 0.02	0.69 ± 0.02	13
	Co^{2+}	15 µmol	1.08 ± 0.06	100 ± 0	0.91 ± 0.02	0.85 ± 0.02	57
	Co^{2+}	40 µmol	0.99 ± 0.06	100 ± 0	0.46 ± 0.06	0.46 ± 0.06	9
	Cu^{2+}	15 µmol	1.08 ± 0.06	100 ± 0	0.42 ± 0.01	0.39 ± 0.01	26
	Cu^{2+}	40 µmol	1.08 ± 0.06	100 ± 0	0.10 ± 0.01	0.09 ± 0.01	6
H4	Ni^{2+}	15 µmol	0.85 ± 0.01	88 ± 3.1	0.39 ± 0.03	0.44 ± 0.04	7
	Fe^{3+}	10 µmol	0.96 ± 0.01	99 ± 0.5	0.85 ± 0.01	0.87 ± 0.01	14
	Co^{2+}	15 µmol	0.12 ± 0.01	12.8 ± 1.3	0.12 ± 0.02	0.13 ± 0.02	3
	Co^{2+}	40 µmol	0.96 ± 0.01	99 ± 0.1	0.88 ± 0.5	0.92 ± 0.05	15
	Cu^{2+}	15 µmol	0.40 ± 0.05	43 ± 1.1	0.27 ± 0.03	0.22 ± 0.02	4
	Cu^{2+}	40 µmol	0.75 ± 0.09	81 ± 2.4	0.19 ± 0.04	0.15 ± 0.03	3

The variants and carrier pairs where the recovered activity is **higher** are showed in green. The **lower**s showed in red and the **reference** in blue.

4.3.3 Stability of BsADH variants

The first parameter analyzed for the different biocatalyst was the thermal inactivation, using 70 ºC for 3 hours of incubation as inactivation conditions. Thus, the stability of the histidine cluster variants immobilized on the different carriers were compared with the stability of the BsADH-WT immobilized on LdAG-Co^{2+} due to this biocatalyst being widely described by our group.[52, 62] With the objective to find the best balance between stability and activity, the data was plotted using the internal factor stabilization (Y axis) vs immobilized specific activity (X axis) Figure 30. The data plotted was divided in four quadrants. The upper right shows the biocatalysts that improve both the specific activity and the thermal stability in comparison with the reference. In this quadrant the variant BsADH-H3 immobilized on LdAG-$Co^{2+}$is the biocatalyst that shows the best ratio of activity/stability. The upper left quadrant shows all the biocatalysts with higher stability but that are less active than the reference, where the biocatalyst BsADH-H3 immobilized on HdAG-Co^{2+} stands out. On the contrary, the lower right quadrant shows the higher activity biocatalyst but less stable than the reference against the temperature, where BsADH-H4 immobilized on HdAG-Co^{2+} shows the highest specific activity immobilized with a stability slightly lower than the reference. Finally, the lower left quadrant shows the biocatalysts with less activity and stability than the reference against the temperature. Here, there are the biocatalyst immobilized on LdAG-Ni^{2+} and LdAG-Cu^{2+} carriers regardless the BsADH histidine variant employed. The enzymes immobilized on the commercial carrier EziG1 shows less or the same thermal stability as the reference, where the WT and the variant BsADH-H2 are also less active. The balance activity/thermal stability for BsADH-H3 is similar to the reference and the BsADH-H4 slightly improves the recovered activity mataining an thermal stability similar to the reference.

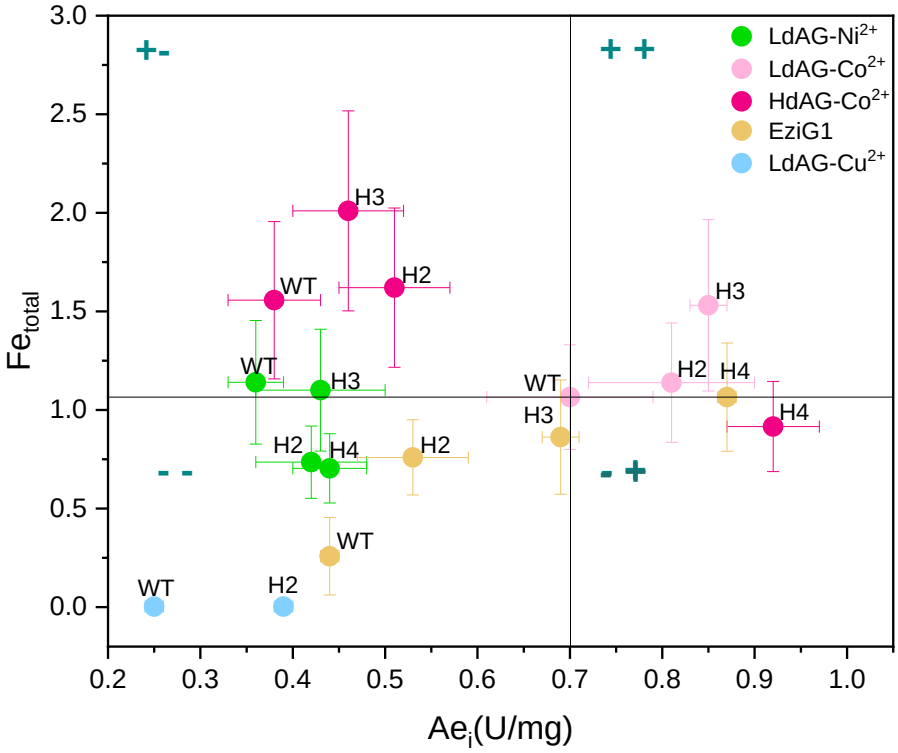

Figure 30: Stabilization factor of BsADH variants against thermal inactivation

The stability factor data is divided into four quadrants taking BsADH-WT immobilized on LdAG-Co^{2+} as reference. The ***upper left quadrant*** *shows the biocatalysts more active but less stables than the WT immobilized on LdAG-Co^{2+}.* ***The lower left quadrant*** *shows the biocatalysts less active and stable than the WT immobilized on LdAG-Co^{2}. The* ***lower right quadrant*** *shows the biocatalysts more active but less stable than the WT immobilized on LdAG-Co^{2+}.* ***The upper right quadrant*** *shows the biocatalysts more active and more stable. The thermal stability assay were carried out at 70 ºC for 3 hours. The % of the $Ae_{soluble}$ recovered after the thermal stability challenge for the reference BsADH-WT is 42 %, with initial specific activity of 8.15 U per mg.*

The same stability studies were done for common inactivation conditions in industry such as the organic solvents and the pH variations. In the case of organic solvents, the biocatalysts were incubated with a solution that contains 70 % IPA overnight (Figure 31 A). In general all the variants were more stable when they were immobilized on HdAG-Co^{2+} carriers, but the variant BsADH-H4 immobilized on HdAG-Co^{2+} also show the best balance of activity/organic solvent stability of all tested heterogeneous biocatalysts. For the pH inactivation, the biocatalysts were incubated with buffer at pH 5 overnight (Figure 31 B). Here, the variant BsADH-H3 immobilized on LdAG-Co^{2+} shows best balance activity/pH stability increasing its stability by 1.2 and 1.4 times, respectively, when compared to the reference.

In general, we observe that the worst immobilization carrier for the biocatalyst is Cu^{2+} as metal chelate when exposed to the inactivation conditions, especially with the BsADH-WT

variant. Meanwhile, BsADH-H3 immobilized on LdAG-Co^{2+} shows the best balance of activity/thermal stability and activity/pH stability. Also, the BsADH-H3 immobilized on HdAG-Co^{2+} shows a thermal stability 1.3 times higher than its counterpart on LdAG-Co^{2+} but the immobilized specific activity of the former is the half of latter. In the case of the best balance activity/organic solvent stability, the variant BsADH-H4 immobilized on HdAG-Co^{2+} shows the best behaviour. These results agree with our hypothesis about the importance of the orientation of the biocatalyst in the immobilization process.

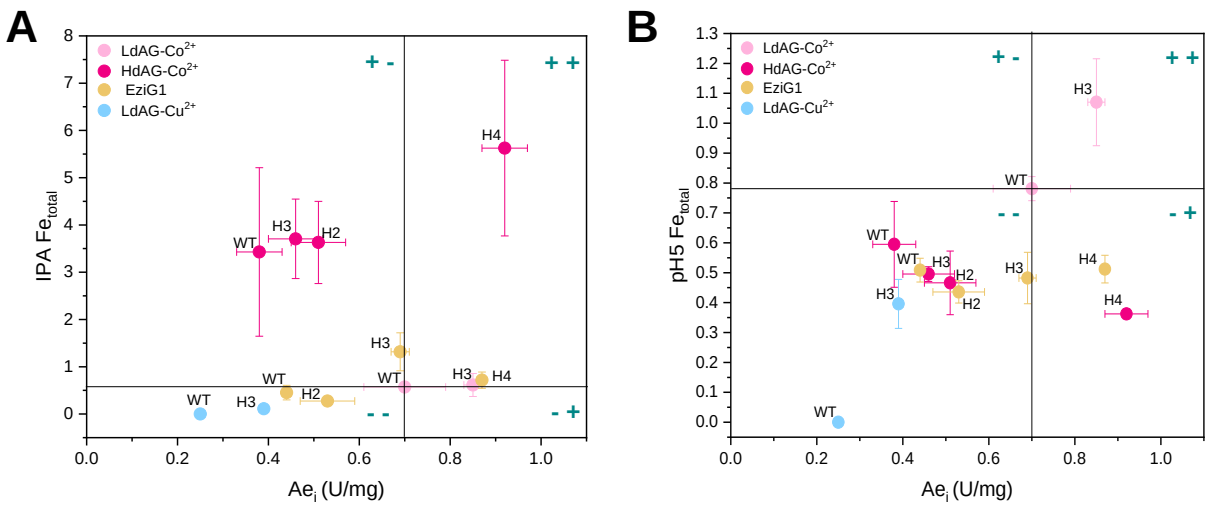

Figure 31: Stabilization factors of BsADH variants against organic solvent and pH.

A. *Stabilization factor against the organic solvent, 70 % of IPA in solution****. B.*** *Stabilization factor against the pH5. The* ***upper left quadrant*** *shows the biocatalysts more active but less stable than the WT immobilized in LdAG-*Co^{2+}*.* ***The lower left quadrant*** *shows the biocatalysts less active and stable than the WT immobilized in LdAG-*Co^{2}*. The* ***lower right quadrant*** *shows the biocatalysts more active but less stable than the WT immobilized in LdAG-*Co^{2+}*.* ***The upper right quadrant*** *shows the biocatalysts more active and more stable.*

4.3.4 Half-life time

From the observations of the different heterogeneous biocatalysts, we select the variants BsADH-H3 and BsADH-H4 on HdAG-Co^{2+} and the reference BsADH-WT on LdAG-Co^{2+} to better understand the stability behaviour of these biocatalysts. The experimental data was adjusted to Eq (10), this equation is a simplification that allows focus on the inactivation phenomenon rather than the mechanistic description of the kinetics of heat-induced enzyme inactivation. The data obtained shows that the BsADH-H3 variant immobilized on HdAG-Co^{2+} has the longest half-life time, 1.85 and 1.54 times higher than the BsADH-H4 and BsADH-WT immobilized on HdAG-Co^{2+} and LdAG-Co^{2+}, respectively (Figure 32). This thermal inactivation confirms that BsADH-H3 immobilized on HdAG-Co^{2+} is more stable than

the other histidine cluster variant BsADH-H4 immobilized on HdAG-Co^{2+} and the reference BsADH-WT on LdAG-Co^{2+} as seen in Figure 30.

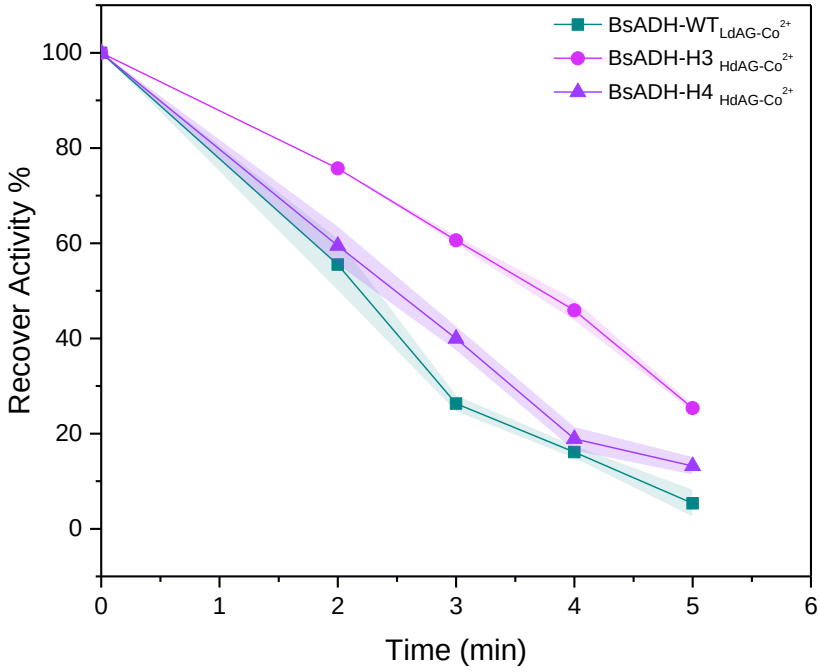

Figure 32 Thermal kinetic inactivations of the BsADH histidine variants.

The thermal inactivation was carried out at 70ºC in Tris-HCl 25 mM buffer at pH 7. The activity was measure as is described in the method section 4.2.9. The data fitting to 3-parameters biexponential kinetic inactivation model gives the half-life time of the different biocatalysts: BsADH-$WT_{LdAG\text{-}Co^{2+}}$: 2.0 ± 0.16 hours; BsADH-$H3_{HdAG\text{-}Co^{2+}}$: 3.7 ± 0.03 hours and BsADH-$H4_{HdAG\text{-}Co^{2+}}$: 2.4 ± 0.13 hours

4.3.5 Melting-Temperature (T_M) analysis

The protein melting temperature or T_M was analyzed to characterize the folding stability of the different immobilized biocatalysts. For this aim, the commercial dye SYPRO ® orange was employed. This dye is polarity-sensitive and shows bright fluorescence in the presence of a hydrophobic core. This property allows monitoring , using RT-PC, of the changes in the spectra when the dye binds hydrophobic regions in the protein that become exposed upon denaturalization. The data obtained from these experiments shows in general that the immobilization process does not increase the T_M. In the case of BsADH-WT the immobilization process decreases the T_M value by 6 ºC (from 75 ºC to 69 ºC, Figure 33 A). However, for the histidine clusters variants the T_M values are the same or slightly higher when they are immobilized. The BsADH-H3 variant shows two maximum peaks, that may be due to two different populations of immobilized enzymes. The first population in the soluble-enzyme (blue column, Figure 33 A) is less stable than the BsADH-WT, but when that population is immobilized the enzyme is 1.3 ºC more stable against the denaturalization than

the BsADH-WT immobilized on LdAG-Co^{2+}, while the second population increases the T_M value by 17 ºC (from 69 ºC to 86 ºC). This phenomenon could be due to the cluster insertion that stabilizes the protein when immobilized at temperatures of 87 ºC.

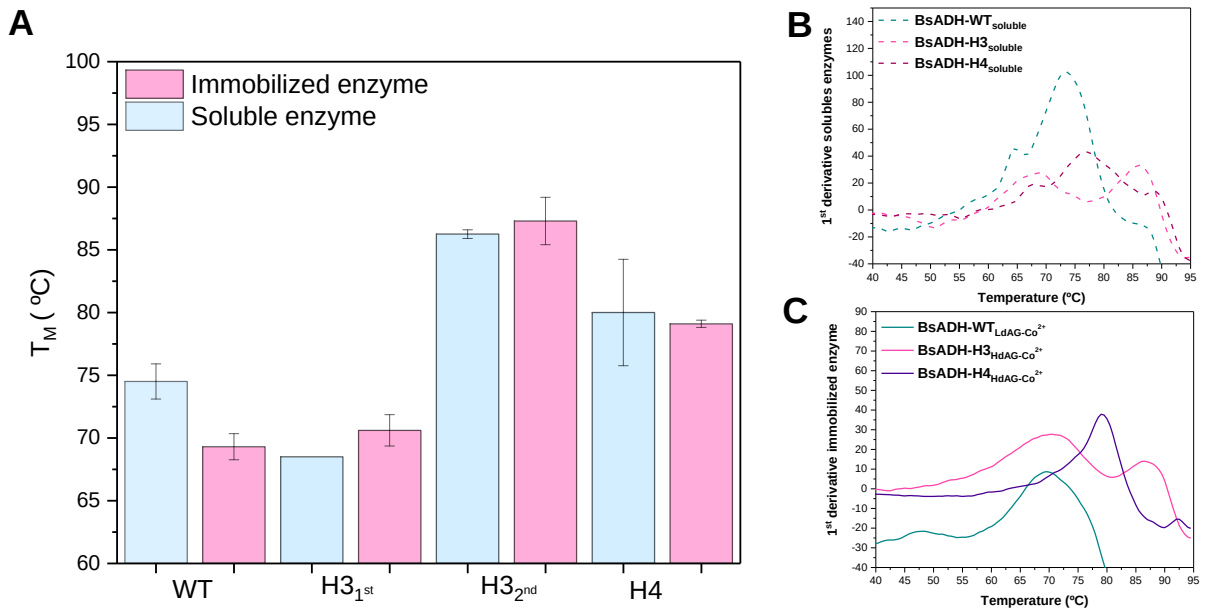

Figure 33: Melting-Temperature (T_M) of the different BsADH histidine variants.

A. *T_M values for the different BsADH variants. In blue the soluble variants and in pink the immobilized variants. BsADH-WT immobilized on LdAG-Co^{2+} and the histidine cluster variants BsADH-H3 and BsADH-H4 on HdAG-Co^{2+}. The T_M for the $BsADH\text{-}WT_{soluble}$ is 74.5 ± 1.4; $BsADH\text{-}H3_{soluble}$ has two T_M, the first one at 68.5 ± 0 and the second one 86.3 ± 0.4, the $BsADH\text{-}H4_{soluble}$ T_M at 80 ± 4.24. For the immobilized enzymes the T_M values are: $BsADH\text{-}WT_{LdAG\text{-}Co2+}$: 69.3 ± 1.0, $BsADH\text{-}H3_{HdAG\text{-}Co2+}$ also has two T_M values, the first one 70.6 ± 1.3 and the second one 87.3 ± 1.9, the $BsADH\text{-}H4_{HdAG\text{-}Co2+}$: 79.1 ± 0.29.* ***B.*** *Plot of the first derivative of the soluble enzymes.* ***C.*** *Plot of the first derivative of the immobilized enzymes. All the experiments were performed using 8 µg of protein.*

4.3.6 Tryptophan intrinsic fluorescence analysis

Tryptophan (Trp or W) is the amino acid residue that has the highest extinction coefficient and quantum yield, contributing the most to the intrinsic fluorescence in proteins. This fluorescence is also highly sensitive to the local environment of such aromatic residues. These properties were exploited to use Trp as a marker to monitor changes in the protein. [63-66] Thus, the study of Trp could give us relevant information of the changes in the protein. These changes could be due to the mutagenesis and the immobilization process. Also, this technique could give us information about the conformational changes due to the thermal inactivation to complete our previous studies. The analysis can be performed as the native enzyme has 3 Trp localized in the positions W49/W87/W167. Figure 34 shows the

locations when they are oriented immobilized on the agarose microbeads, activated with Ld of cobalt in the case of BsADH-WT and Hd in the case of BsADH-H3.

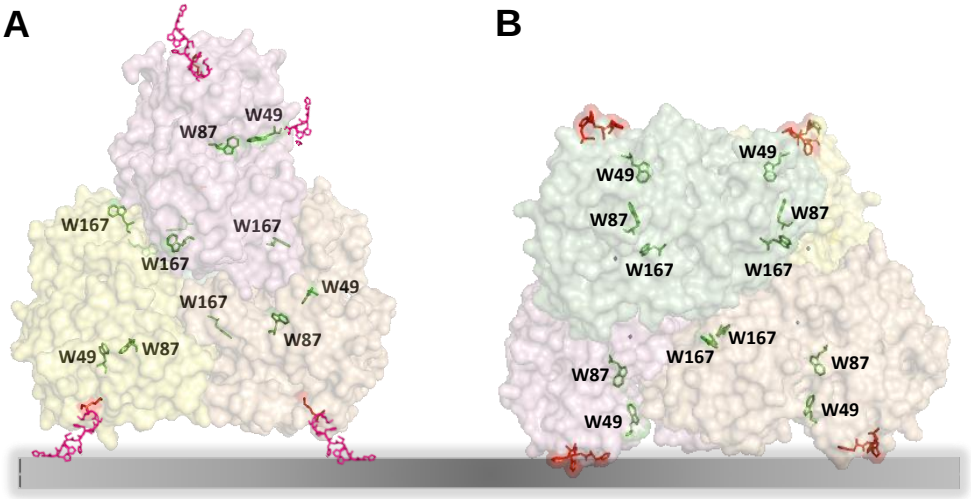

Figure 34:Tryptophan locations on BsADH enzyme

A. *BsADH-WT* ***B.*** *BsADH-H3 histidine cluster variant. The tryptophans (W) are represented in green. Each monomer contains three Trp in the positions W49/W87/W167.*

As we expected the substitution of the amino acids for histidine cluster barely perturbed the fluorescence spectrum (Figure 35 A), meaning that the mutation does not change the Trp microenvironment. The characteristic fluorescence spectra obtained from the Trp of the soluble enzyme give us one clear peak at 335 nm, this peak at shorter wavelengths typically is emitted (330-340 nm) by Trp residues that are buried in a hydrophobic core of a protein. The immobilization process changes the Trp microenvironment as observed in the Figure 35 B, where a new peak appears at larger wavelengths (red shift). This shift could be explained by the Trp microenvironment changes that the protein experiences to be immobilized on a solid carrier. The immobilized enzymes are stabilized in a different conformation than the soluble enzymes in both cases. Some of the Trp could be more exposed to the bulk, such as W49, which give us different emissions. The first peak could come from the Trp that still has a hydrophobic microenvironment, (for example the W167) and the second peak from the Trp exposed to a hydrophilic microenvironment. To demonstrate that the changes in the Trp spectra comes from changes in protein conformation, the fluorescence spectra of the soluble enzymes at 100 ºC were monitored (Figure 35 C and D). Thermal denaturalization produces protein unfolding and the Trp in the protein becomes more exposed to the bulk producing a shift to longer wavelengths (380 nm).

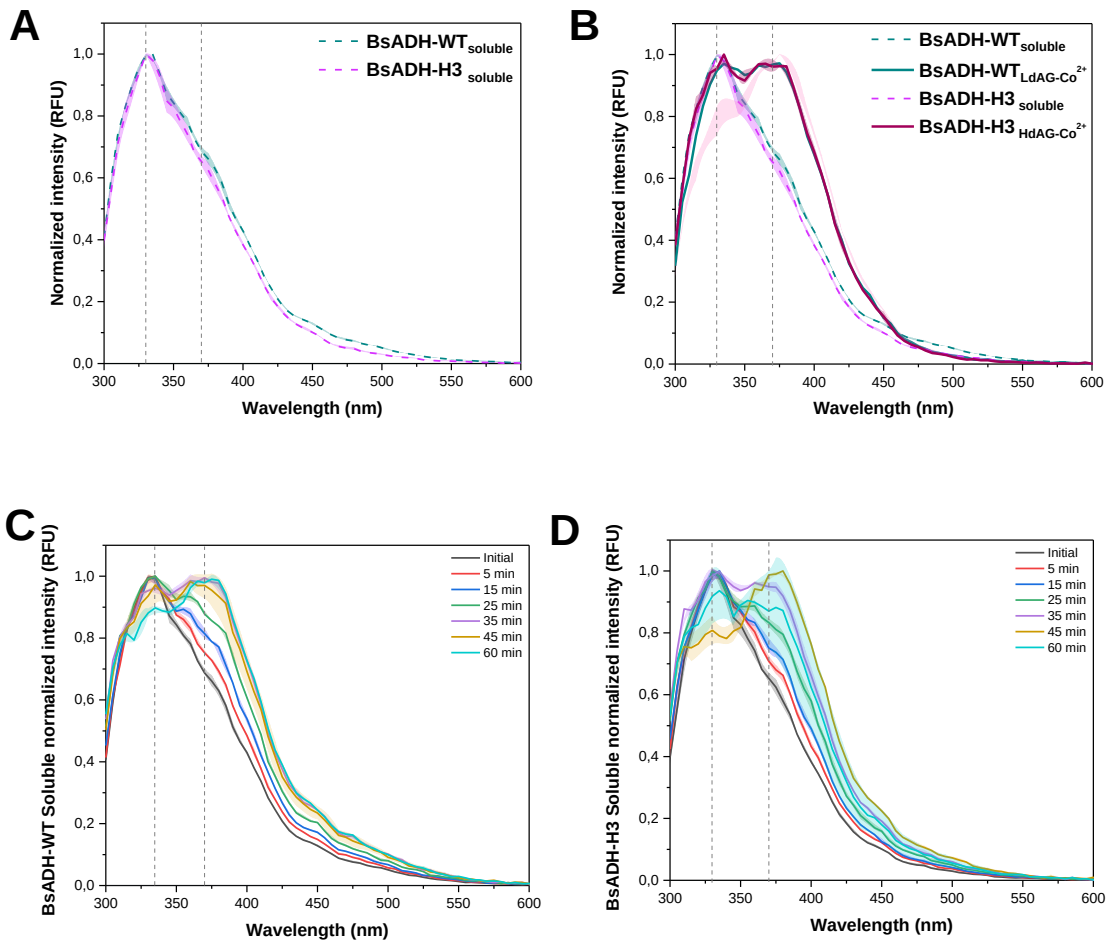

Figure 35: Tryptophan spectra of the soluble and immobilized BsADH-WT variants

A. *Tryptophan spectra of the soluble enzymes BsADH-WT and the histidine cluster BsADH-H3.****B.*** *The tryptophan spectra changes due to the immobilization process. The soluble enzymes are represented with dashed lines and the immobilized enzymes with solid lines.* ***C.*** *Changes in the Trp spectra of the soluble BsADH-WT at 100 ºC at different times.* ***D.*** *Changes in the Trp spectra of the soluble BsADH-H3 at 100 ºC at different times. Excitation wavelengths of 280 nm were used.*

The same study was done with the immobilized enzyme (Figure 36). In this case, the shift to longer wavelengths is faster than the soluble ones. When the normalized ratio between the two maximum peaks of the immobilized enzyme are compared, the structural stability of the BsADH-H3$_{HdAG\text{-}Co}^{2+}$ is clearly higher against the tryptophan exposure than the BsADH-WT $_{LdAG\text{-}Co}^{2+}$. These results correlate with the activity recovered in the thermal stability in the section 0 and 4.3.4 explained above.

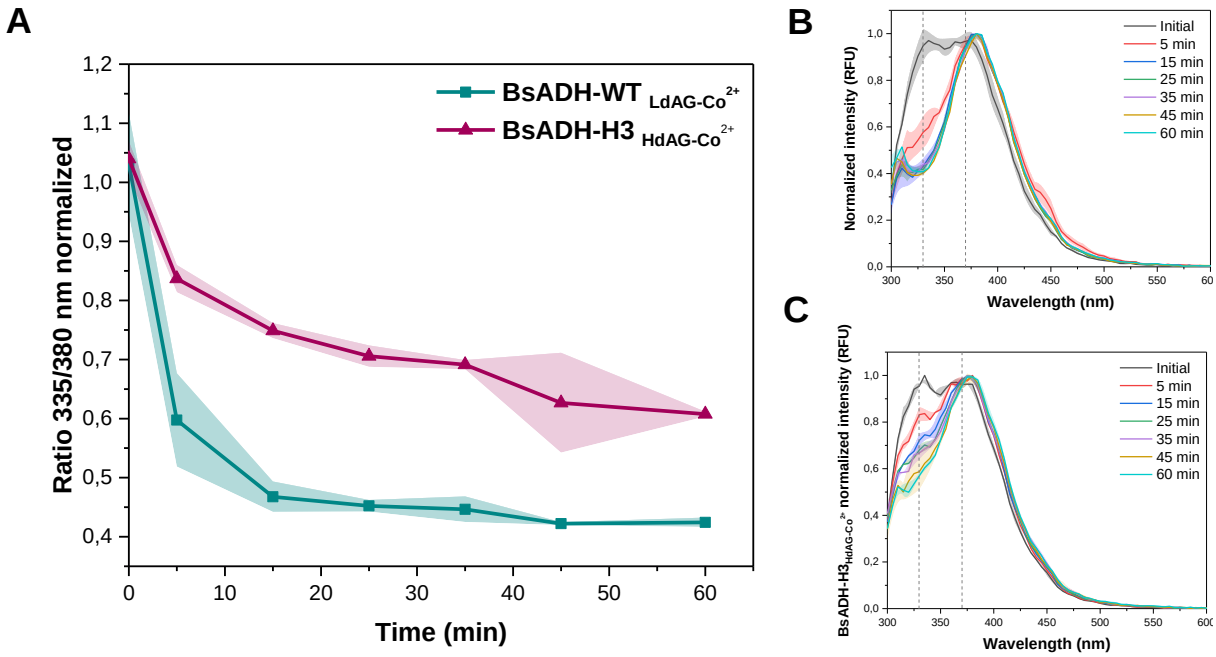

Figure 36: Thermal inactivation at 100 ºC monitored using tryptophan fluorescence spectra.

A. *Ratio normalized between the maximum peaks at 335 nm and 380 nm in the immobilized BsADH variants.* ***B.*** *Tryptophan fluorescent spectra of the BsADH-WT$_{LdAG\text{-}Co2+}$ incubated at 100 ºC.* ***C.*** *Tryptophan fluorescent spectra of the BsADH-H3$_{HdAG\text{-}Co2+}$ incubated at 100 ºC. Excitation wavelengths was at 280 nm.*

The strong quenching of the AFDye 488 dye by proximal tryptophan residues has been reported.[67] This distance-dependent quenching could be used as another approach to understand the stability of the different biocatalysts. When the protein is well-folded the distance from the native Trp and the AFDye 488 is short and the fluorophore is quenched. Whereas, when the protein is unfolded there is a higher distance between the Trp and the dye, so the fluorescence emitted is higher. Thus, both enzymes were labelled with AFDye 488 maleimide and immobilized into their corresponding carriers. The spectra obtained by the excitation at λ: 490 nm were collected and plotted as the ratio between the maximum of the fluorescence intensity at different times and the initial fluorescence intensity (Figure 37). The fitted data obtained from the measurements give us a slope that is 1.2 times higher for the BsADH-WT $_{LdAG\text{-}Co}{}^{2+}$, which also confirm the data obtained from the tryptophan analysis.

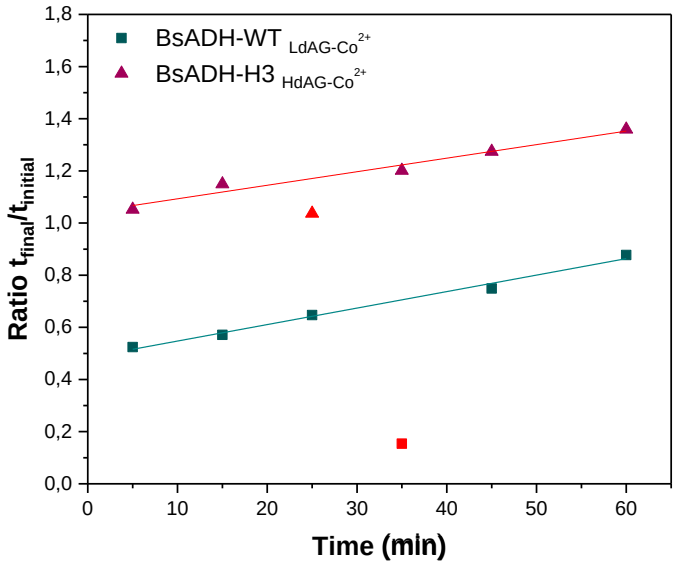

Figure 37: Changes in the ratio of the maximum emission of AFDye 488 after incubation at 100 ºC.

*The measured data was fitted to the linear equation y = a + b*x. The BsADH-WT$_{LdAG\text{-}Co}^{2+}$ is 0.063 ± 3.5 E^{-4} and the BsADH-H3$_{HdAG\text{-}Co}^{2+}$ is 0.0052 ± 5.2 E^{-4}. The red points were not considered for the fitting.*

4.3.7 Apparent kinetics parameters of soluble and immobilized BsADH-WT and BsADH-H3 variant

The apparent kinetic parameters of BsADH-WT and the variant BsADH-H3 immobilized on LdAG-Co^{2+} and HdAG-Co^{2+}, respectively, were evaluated towards different NAD^+ concentrations and compared with the parameters obtained for the soluble enzymes. Table 14 shows that K_M^{app} constant for BsADH-WT immobilized on LdAG-Co^{2+} is almost 14.5 times higher toward the NAD^+ than its soluble counterpart. Meanwhile, the BsADH-H3 variant immobilized on HdAG-Co^{2+} is 13.5 times higher. The apparent V_{max} for both variants decreases due to the immobilization 3.6 times in the case of BSADH-WT and 0.6 times for BsaDH-H3 variant. The specificity constant (k_{cat}/K_m) shows also that the variant BsADH-H3 has 2.6-fold higher affinity for NAD^+ than the BsADH-WT when they are immobilized, while in solution this constant is approximately the same.

Table 14: Michaelis-Menten kinetic parameters of soluble and immobilized BsADH-WT and BsADH-H3 variant towards NAD$^+$.

Enzyme	V_{max} (U x mg^{-1})	K_m (mM)	k_{cat} (s^{-1})	k_{cat} / K_m (mM^{-1} x s-1)
BsADH-WT $_{soluble}$	4.71 ± 0.06	0.05 ± 0.00	12.34 ± 0.16	228753 ± 10807
BsADH-H3 $_{soluble}$	5.26 ± 0.01	0.05 ± 0.01	13.31 ± 0.02	247216 ± 36197

BsADH-WT $_{LdAG\text{-}Co}^{2+}$	1.30 ± 0.0	0.72 ± 0.17	3.41 ± 0.01	4911 ± 1184
BsADH-H3 $_{HdAG\text{-}Co}^{2+}$	3.33 ± 0.03	0.67 ± 0.06	8.42 ± 0.08	12701 ± 1015

The kinetic parameters were measure with 100 mM of EtOH at pH7 and 30 ºC varying the NAD^+ concentration.

In general, the orientation upon immobilization using the histidine clusters (BsADH-H3) affects the v_{max}, which is 2.5 times higher than the BsADH-WT on LdAG-Co^{2+}. The increase in the v_{max} is related with the higher catalytic efficiency showed for the cluster variant in comparison with the typical immobilization through the poly-histidine tag.

4.3.8 Operational stability assays

The BsADH variants immobilized on the optimal carriers (BsADH-WT $_{LdAG\text{-}Co}^{2+}$, BsADH-H3 $_{HdAG\text{-}Co}^{2+}$and BsADH-H4 $_{HdAG\text{-}Co}^{2+}$) were selected to test the operational stability for the regio-selective oxidation of 1,5-pentanediol described previously by our group (Figure 38). [52] First, the different immobilized biocatalysts were tested for the regioselective oxidation of 1,5-pentanodiol into its corresponding lactone and lactone (Figure 38 A). BsADH-WT is able to sequentially catalyze the first oxidation of 1,5-pentanodiol to 5-hydroxy pentanal, which is reversibly and spontaneously transformed into tethrahydro-2H-pyran-2-ol (lactol), followed by a second, but slower, oxidation of that lactol to the d-valerolactone.[52] When comparing the reaction courses of the diol consumption, the BsADH-WT $_{LdAG\text{-}Co}^{2+}$ reached a higher conversion than the His-cluster variants. However, the variant BsADH-H4 immobilized on HdAG-Co^{2+} exerted an initial rate of diol conversion higher than the WT and the variant BsADH-H3 immobilized on their respective optimal carriers. Furthermore, when the reusability of these biocatalyst are tested in batch reaction, after 24 hours, the histidine clusters variants were more stable (Figure 38 C). This results agree with the data shown in Figure 30 where the BsADH-H4 variant immobilized on Hd-AG-Co^{2+} was the most active one, while the BsADH-H3 immobilized on Hd-AG-Co^{2+} the most thermally stable one. Nonetheless, the lower diol conversion observed with the BsADH-H4 variant immobilized on Hd-AG-Co^{2+} can be explained by product inhibition issues that limit the final substrate transformation.

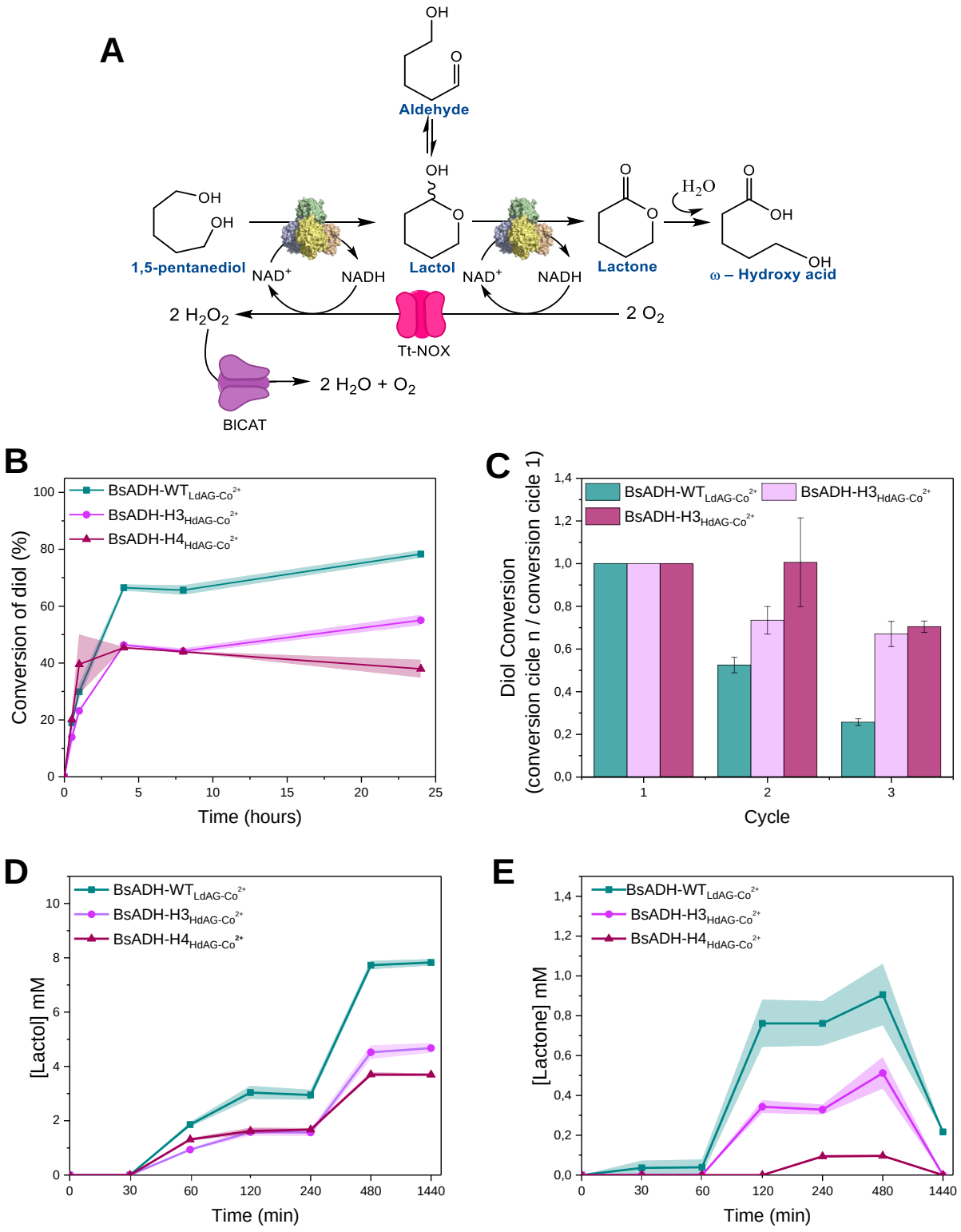

Figure 38: Operational stability of BsADH variants.

A. *Reaction scheme of the 1,5-pentanediol oxidation to lactone and further spontaneously hydrolysis* ***B.*** *Kinetics of the oxidation of 1,5-Pentanediol catalyzed by the different BsADH histidine variants with the regenerator system TtNOX/BICAT immobilized on glyoxil* ***C.*** *Reusability study in batch reaction at 24 hours of reaction.* ***D.*** *Quantification of the intermedial product (lactol) by GC.* ***F.*** *Quantification of the final product, lactone by GC.*

The possibility to analyze the intermediate product (lactol) and the final product by GC allows us to study of the product selectivity of the different heterogeneous biocatalysts. Thus, the products were quantified at different reaction times. As is shown in Figure 38 E and F, the intermediate product (lactol) start to accumulate at 60 min of reaction in all cases. This fact agrees with the previous results reported for our group where the oxidation of secondary alcohol of the lactol is slower than the oxidation of the primary alcohol of the starting diol. Remarkably, such second oxidation was more efficient when using the BsADH-WT $_{LdAG\text{-}Co}^{2+}$ biocatalyst than the other two immobilized variants. To note, the ratio of lactol/lactone is 4.5 times higher using BsADH-H4 $_{HdAG\text{-}Co}^{2+}$ biocatalyst than using the BsADH-WT $_{LdAG\text{-}Co}^{2+}$. This ratio increases along the reaction time likely due to the spontaneous hydrolysis of the lactone as previously reported.[68] This result suggests that the orientation also affects the product selectivity of the immobilized biocatalysts through likely hampering the access of the lactone to the active site when the enzymes immobilized via certain orientations.

Table 15: Ratio Lactol / Lactone at different times.

	BsADH-WT	BsADH-H3	BsADH-H4
Ratio at 480 min	8,5	8,9	38,5

4.3.9 Proteomic analysis

The immobilization results obtained above show not only that the properties of the solid carrier matter in a biocatalyst but that enzyme orientation also plays an essential role in the recovery activity, stability and selectivity towards the reaction products. To demonstrate that we can control the enzyme orientation in immobilization through the histidine clusters, the mutants BsADH-H3 and BsADH-H4 immobilized on HdAG-Co^{2+} and EziG1 were compared with the reference BsADH-WT. Proteomic analyses were performed using the immobilized biocatalysts to confirm the immobilization orientation, these experiments were carried out in collaboration with the Proteomics Platform of CIC bioGUNE.

Thus, when protein immobilization process occurs some of the protein peptides of the quaternary structure may be exposed or not due to the physical interaction between the solid carrier and the protein. Also, during the immobilization, the solid carrier could produce distortions in the protein structure which trigger the exposure of peptides. So, the partial digestion of the immobilized enzymes using a protease, such as trypsin, can generate different peptides depending on which part of the structure are exposed. The peptide pattern of the trypsinized enzyme would be different due to the conditions. This difference comes from the particular physical access of the trypsin enzyme to the quaternary structure of the protein. Based on this concept, the different orientation of the enzyme results therefore in

different trypsinized patterns, due to the different peptide exposure. So here we present the analysis of the trypsinized peptides sequences for the different variants immobilized on HdAG-Co^{2+} and EziG1.

Table 16: The most abundant peptide sequences digested with trypsin.

Code	Peptide sequence
A	AAVVEQFKEPLKIK
B	IKEVEKPTISYGEVLVRIK
C	LPLIPGHEGVGIVEEVGPGVTHLK
D	AMGLNVVAVDIGDEKLELAK
E	ELGADLVVNPLKEDAAK
F	IIGSIVGTRK
G	KDLQEALQFAAEGK
H	VKTIIEVQPLEK
I	MLKGQINGRVVLTLEDK
J	VVLTLEDK
K	ALKVTGAKPGEWVAIYGIGGLGHVAVQYAK
L	EKVGGVHAAVVTAVSKPAFQSAYNSIRR

From these analysis we found 11 most abundant peptides after the trypsinization (Table 16). On one hand, the analysis of the BsADH histidine variants immobilized on HdAG-Co^{2+} carriers are showed in the Figure 39 A. We observed that the % PMS of the C, D, K and L peptides increase their abundance in comparison with the BsADH-WT immobilized on the same carrier. However, the decrease of the peptides J and A are the most remarkable change in the proteomic analysis. The % PMS of the J peptide is 4.4-fold and 2.8-fold lower for the variants BsADH-H3 and BsADH-H4, respectively, than in the BsADH-WT immobilized on the same carrier through the histidine tag. In the case of BsADH-H3, the A peptide which correspond to the sequence where the mutations were done (Q8H/K10H/E11H, Table 16 and Figure 40 A) is exposed almost 2.5-fold less to trypsinization. This suggests that the immobilization through this zone is avoiding trypsinization and confirming the orientation. Also, the increases in the K and L peptides located in the subunit interface increase, especially in the variant BsADH-H3 which indicates a conformational change and a structural rearrangement of the subunit interface when is oriented through this histidine cluster.

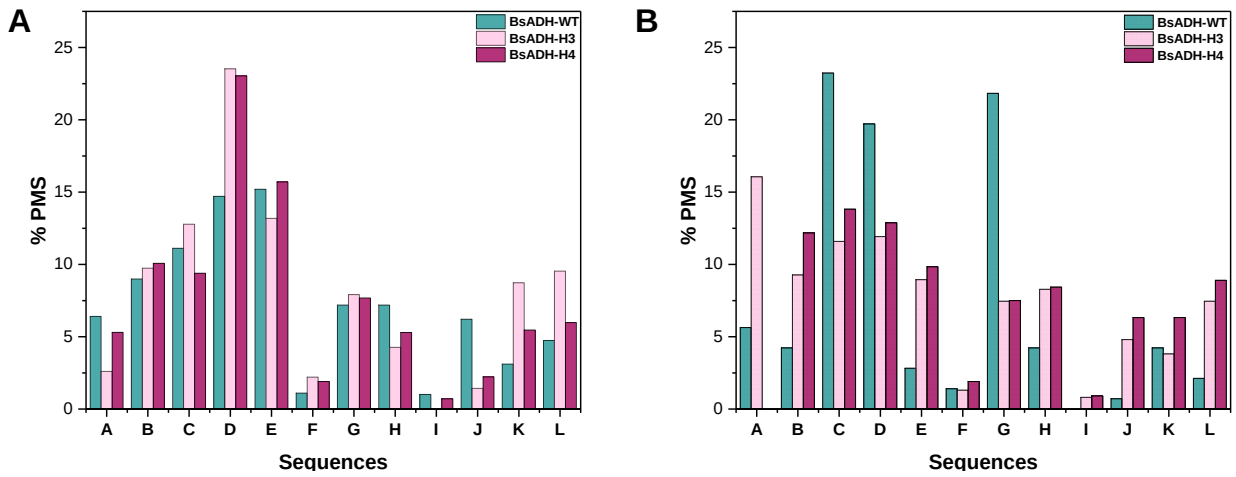

Figure 39: Percentage of the abundance of the different trypsin proteolysis peptides in the immobilized BsADH variant.

A. *BsADH variants immobilized on HdAG-Co^{2+} agarose microbeads.* ***B.*** *BsADH variants immobilized on EziG1 particles.*

On the other hand, when we used EziG1 as carrier to immobilize the different BsADH variants (Figure 39 B), we find that in general the B,E and L peptides are affected due to the conformational changes of the enzyme orientation. The % PMS of A peptide increases almost 3-fold and it is specific for the variant BsADH-H3. On the contrary, the peptide G suffers a decrease near to 3-fold in the %PMS for both variants BsADH-H3 and BsADH-H4 compared with the WT. The peptide pattern shows that EziG1 carrier generate a different interaction network with the BsADH variants in comparation with AG-Co^{2+} even when the enzymes have he same orientation. This differences may be caused by the positive charge that the EziG1 carrier have in the underneath layer of the chatecol-Fe^{3+} groups. The peptides position in the quaternary structure of the immobilized enzymes are depicted in Figure 41.

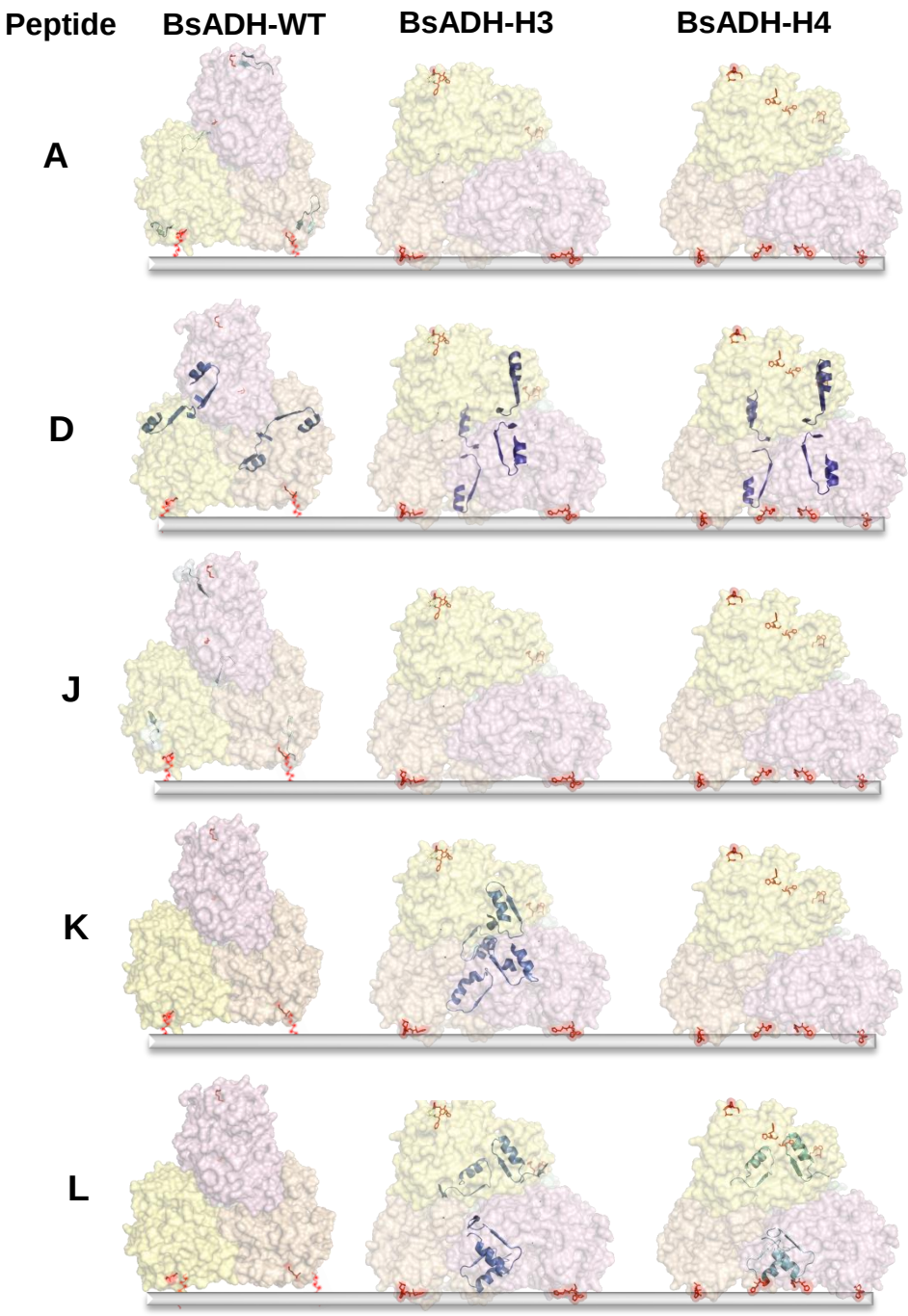

Figure 40: Peptides locations in the quaternary structure of the immobilized BsADH variants on HdAG-Co^{2+}.

The peptides more exposed to the trypsin proteolysis are represented a gradient of blues, from 6 to 8.5 % PMS in cyan, from 8.5 to 15 % PMS in blue and more than 15 % in deep blue.

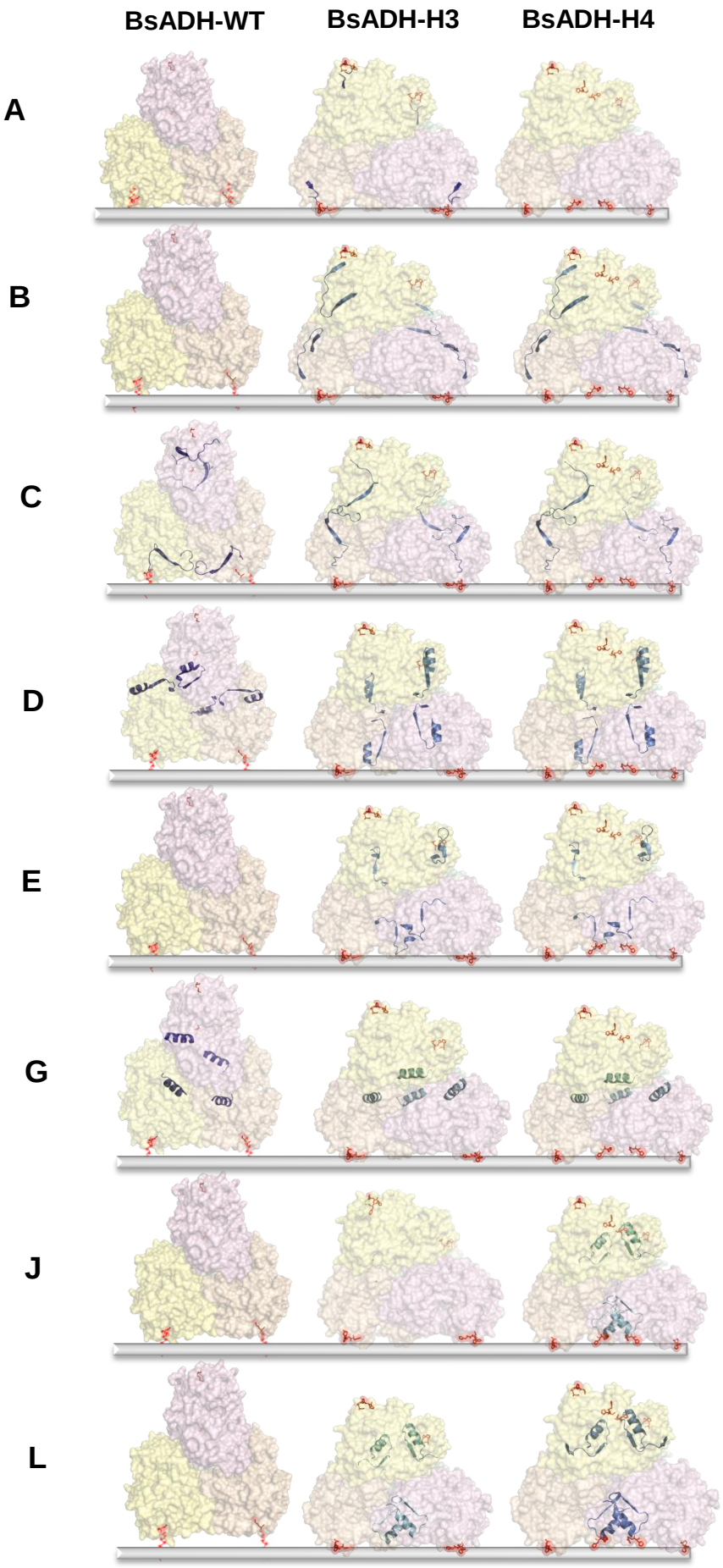
BsADH-WT
BsADH-H3
BsADH-H4
A
B
C
D
E
G
J
L

Figure 41: Peptides locations in the quaternary structure of the immobilized BsADH variants on EziG1.

The peptides more exposed to the trypsin proteolysis are represented a gradient of blues, from 6 to 8.5 % PMS in cyan, from 8.5 to 15 % PMS in blue and more than 15 % in deep blue.

In conclusion, the proteomic analysis allows us confirming that the different variants adopt different orientations on the surface of the different carriers. Moreover, the same variant can establish different interactions modes with the surface, which is reflected in the patterns of the trypsinized peptides when H3 is immobilized on either Hd-AG-Co^{2+} or EziG1. These changes in enzyme orientation are supported by the different functional properties described above for each variant immobilized one each carrier.

4.3.10 CLSM analysis

The spatial distribution of the BsADH-WT and BsADH-H3 variants immobilized on LdAG-Co^{2+} and HdAG-Co^{2+} were analyzed using labelled enzymes and CLSM images. The acquired images were processed to obtain the normalized fluoresce intensity radial profile of the different oriented biocatalysts using FIJI software.[69] A radial profile plugin that automatically performs a Gaussian fit on the normalized fluorescence intensity radial profile of single beads of the confocal images was employed to analyze single beads. Then, the plugin was used to obtain the infiltration distance profile as previously described by our group.[53, 70]

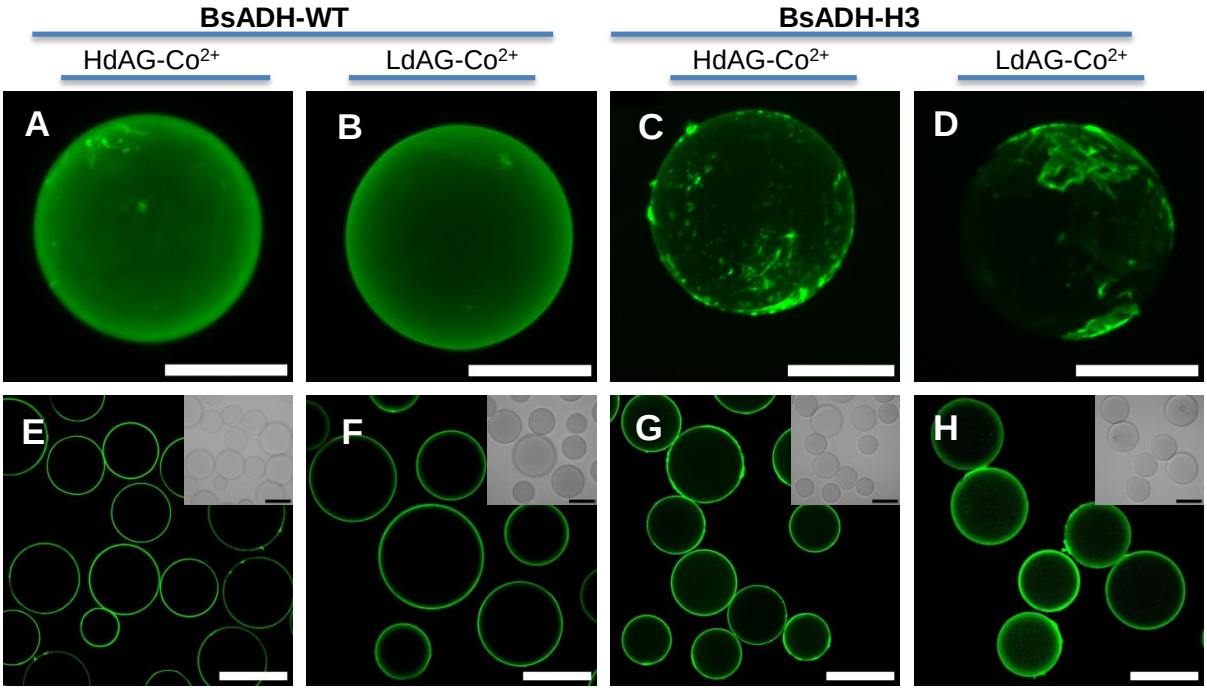

Figure 42: Fluorescent confocal images.

***A, B, C** and **D.** Confocal fluorescence microscopic Z-stack images of BsADH-WT (A) immobilized on HdAG-Co^{2+}, (B) BsADH-WT immobilized on LdAG-Co^{2+} (C) BsADH-H3 immobilized on HdAG-Co^{2+} and (D) BsADH-H3 immobilized on LdAG-Co^{2+}. Scale bar of 40 µm. **E, F, G** and **H.** Fluorescent confocal images of BsADH-WT (E and F) and BsADH-H3 (G and H) immobilized on LdAG-Co^{2+} and HdAG-Co^{2+}. Scale bar 100 µm. All enzymes were labelled with AzDye 488 (green channel, λ_{ex}: 488), objective 20x.*

The confocal images shows that BsADH-WT immobilized on HdAG-Co^{2+} and immobilized on LdAG-Co^{2+} shows similar spatial distribution of this variant across the surface of the agarose microbeads.[53, 71] In contrast the BsADH-H3 variant is distributed as non-uniform clusters at the outer surface of the agarose microbeads regardless of the cobalt-chelate density (Figure 42 B). The radial profile analysis using CLSM quantifies the average infiltration of the enzyme on the carriers as the full width half maximum (FWHM) is shown in Figure 4. The radial profile of a representative bead with the histidine-tag enzyme immobilized shows a wider profile when immobilized on LdAG-Co^{2+} than when immobilized on HdAG-Co^{2+} (Figure 43 D). This is expectedly as higher density of cobalt-chelates may promote a more rapid immobilization of the enzyme, forcing it to colonize the most outer surface of the bead. The correlation between the immobilization rate and the spatial distribution of protein across the surface of porous agarose beads has been widely reported by our group.[53, 72] The data shows a small difference between the average relative infiltration for BsADH-WT due to the metal density. Nevertheless, the average relative infiltration is double for the LdAG-Co^{2+} in the case of the BsADH-H3 variant, mainly due to population heterogeneity. The correlation between the particle size and the percentage of relative infiltration is only applicable in the case of BsADH-H3 immobilized on LdAG-Co^{2+} (Figure 43 C). The different infiltration on the BsADH-H3 immobilization may be caused by the immobilization speed, where it is slowly when the cobalt density is lower.

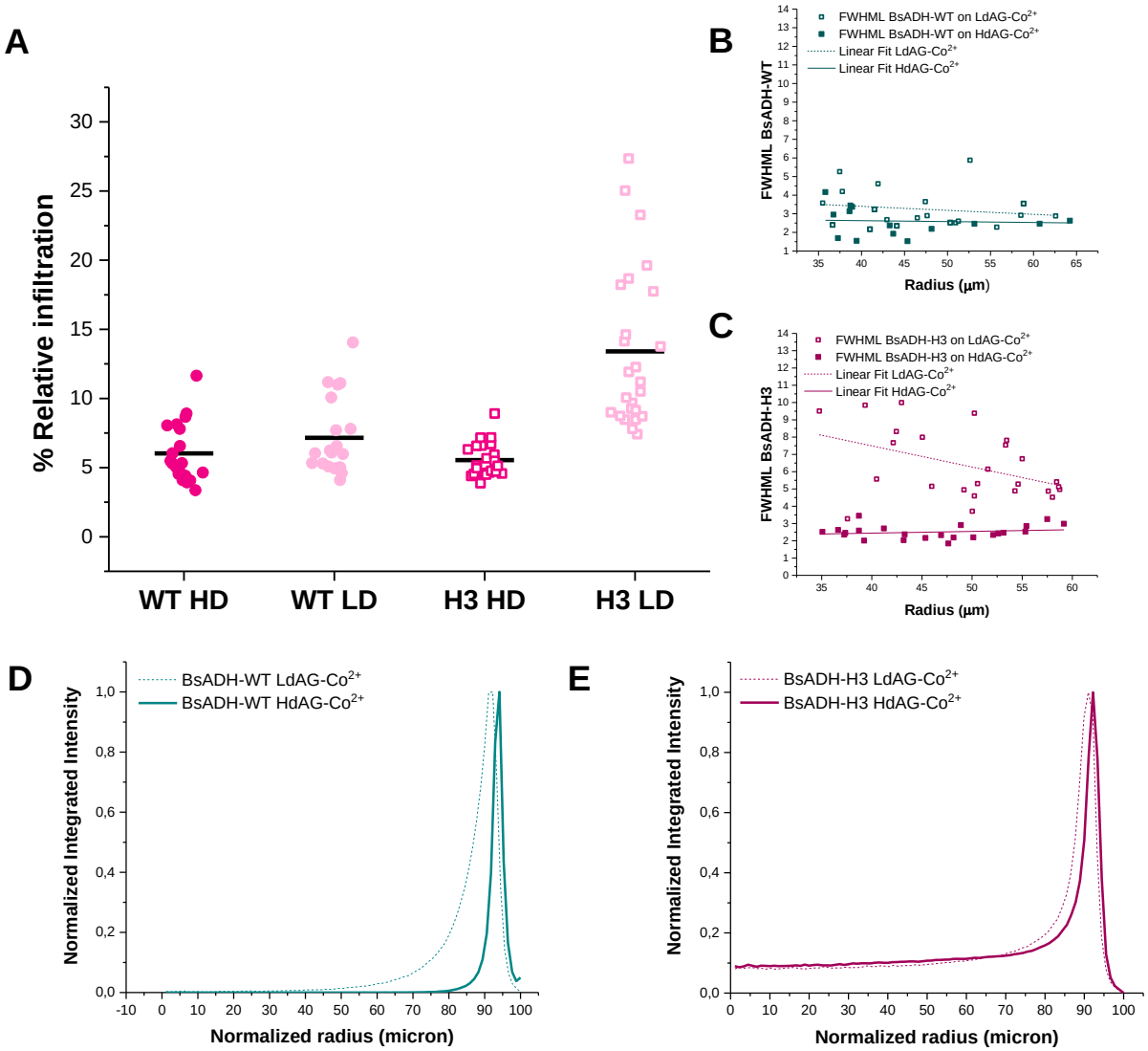

Figure 43: Radial profile of BsADH-WT and BsADH-H3 variant.

A. *Relative infiltration quantification of the BsADH variants immobilized on LdAG-Co^{2+} (LD) and HdAG-Co^{2+} (HD). The BsADH-WT represented with dots and BsADH-H3 histidine cluster represented with squares (n= ~20 agarose microbeads).* ***B.*** *and* ***C.*** *Radial profile distribution for BsADH-WT (B) and BsADH-H3 (C).* ***D.*** *and* ***E.*** *Radial profile for a representative single agarose microbead immobilized with BsADH-WT (B) and BsADH-H3 (E) on LdAG-Co^{2+} (dash) and HdAG-Co^{2+} (solid) lines.*

4.3.11 Single particle study

To continue the study on a single-particle level, we performed time-lapse fluorescence microscopy measurements to acquire the single particle immobilization kinetics as is described in section 4.2.20. This methodology allows to follow the immobilization time course in each microbead and study the population heterogeneity within the same sample during the immobilization of the different BsADH histidine variants. The immobilization kinetics for each microbead were represented as is showed in the Figure 44 and fitted to a

kinetic equation of pseudo-first order. The microbeads analyzed had a radius between 50 to 61 microns.

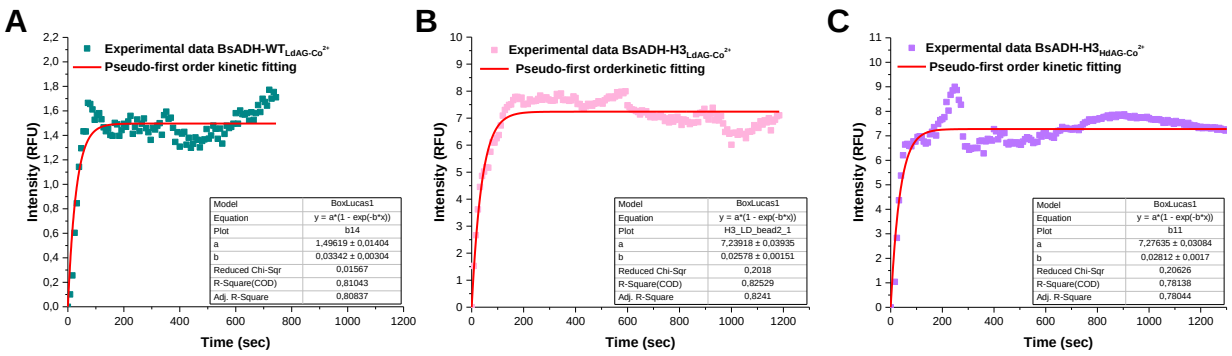

Figure 44: Single-particle kinetic immobilization.

A. *Representative kinetic immobilization of BsADH-WT labelled with AzDye 488 on LdAG-Co^{2+}.*

B. *Representative kinetic immobilization of BsADH-H3 labelled with AzDye 488 on LdAG-Co^{2+}.*

C. *Representative kinetic immobilization of BsADH-H3 labelled with AzDye 488 on HdAG-Co^{2+}.*

The red solid line represents the fitting of the pseudo-first order kinetic model.

Figure 45 shows the values for the constant k_1 obtained from the time courses of the immobilization kinetics for the BsADH histidine variants. All the variants shows a high heterogeneity in the immobilization speed values. In LdAG-Co^{2+} microbeads, the immobilization of the BsADH-WT is faster than the BsADH-H3 variants, which is supported by the larger infiltration of the BsADH-H3 in the microbeads observed in the special distribution described above. The variant BsADH-H3 shows a similar average constant k_1 no matter the metal density of the carrier, these low values could be caused by the polydisperse behaviour of this variant on the microbeads (Figure 42 C, D). This lower k_1 value could also explain the stronger interaction between the cluster histidines and the high density of cobalt in the microbead surface. In summary, the histidine tag favours a stronger interactions with the metal chelates than the histidine clusters.

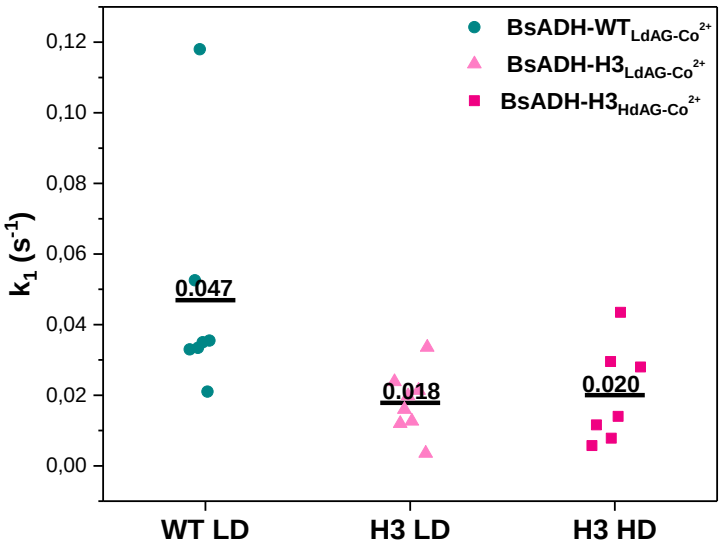

Figure 45: Values of k_1 for the immobilization on solid carriers.

The constant k_1 values were obtained after fitting the experimental data to a kinetic of pseudo-first order. The data was obtained from the analysis of 7-8 agarose microbeads of each variant with a radius around 45 to 70 micron.

4.3.12 Expanding the concept of enriched histidine clusters to other multimeric enzymes: Tt27-HBDH

With the objective of demonstrating that this new approach is viable for extrapolating other multimeric enzymes we performed a characterization of the Tt27-HBDH histidine variants. The native gene of Tt27-HBDH was cloned without any tag since all the variants can be easily purified through thermal shock. The model PDB of this enzyme was constructed using a template of the PDB from *C. acetobutylicum*, a dimeric alcohol dehydrogenase. In work later published by our group, it was characterized and elucidated that the Tt27-HBDH enzyme is actually hexameric.[46] Beside the histidine-clusters formed by his-replacement at specific positions of the primary enzyme sequence, we introduce a histidine-rich-loop between the amino acids 129-133 that contains 26 amino acids with a total of six histidines. The sequence encoding this loop was inserted by tandem insertion of the primer pairs 7 and 8 from Table 11. The specific activity of all pure variants of Tt27-HBDH are showed in the Table 17. The replacement of 4 amino acids by histidines reduced the Tt27-HBDH-WT activity almost 4 times and surprisingly, the Loop insertion exhibited 2.5 higher activity that the native counterpart.

Table 17: Specific activity for Tt27-HBDH histidine enriched variants

Variant	Histidine Position	Ae_s (U/mg)
Tt27-HBDH-WT	C-Terminus	0.106 ± 0.005
Tt27-HBDH-H2	R129H/Y130H	0.055 ± 0.004
Tt27-HBDH-H3	R99H/R129H/R130H	0.068 ± 0.002
Tt27-HBDH-H4	R99H/R129H/R130H/R250H	0.029 ± 0.002
Tt27-HBDH-Loop	Loop 129-26x-133 (6x His)	0.241 ± 0.021

Tt27-HBDH activity was monitored at 340 nm (εNADH = 6.22 mM-1 x cm-1), the reaction mixture containing 0.2 mM NADH, 5 % of isopropanol and 10 mM of ethyl acetoacetate in 100 mM sodium phosphate at pH7. The measurements have been done at 30 ºC.

The secondary structures of the different mutants were analysed through far-UV CD spectroscopy (Figure 46). The Tt27-HBDH his-tagged wild type and the loop variant present a large proportion of random coil structures compared to the other untagged variants. These results agree with the higher flexibility of both his-tagged C-terminus and the 26-extra amino acid loop that are not folded in well-defined secondary structure elements such as alpha-helix and beta-sheet.[73] Despite having more coiled structural elements, the Tt27-BHDH-Loop variant was more active. However, the lower activity of the tetra-mutant Tt27-HBDH-H4 was not due to the loss of secondary structure as is showed in the CD spectra. Therefore, there is no clear relationship between secondary structure composition and the catalytic activity of Tt27-HBDH.

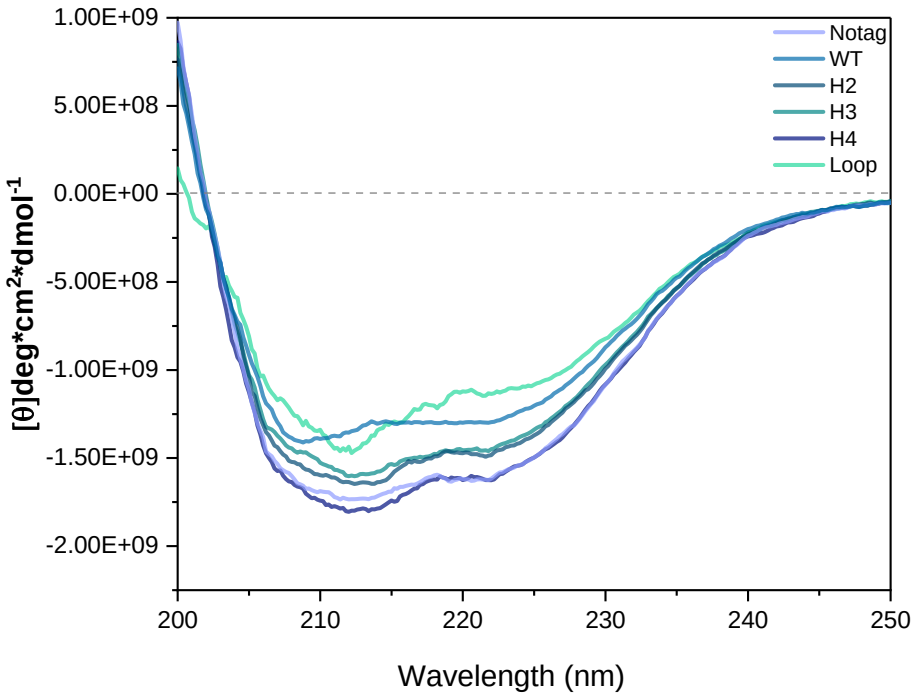

Figure 46: Circular Dichroism spectroscopy of the Tt27-HBDH histidine vatiants

Immobilization parameter for Tt27-HBDH histidine variants.

The same immobilization tests were performed for the Tt27-HBDH histidine variants. In this case we performed a fast screening of the different carriers using a 96-well plate where all immobilization and characterization was performed. The immobilizations were done using 20 mg of each carrier and 200 µL of soluble enzyme. The immobilization parameters are showed in Table 18. This fast screening allows to select the best candidates for further studies in a single experiment.. The screening results unveiled that the Tt27-HBDH loop variant can be immobilized on all the carriers herein tested like the Tt27-HBDH-WT. However, when we compare the rRA %, the Tt27-HBDH-WT generally recovers higher activity than the Tt27-HBDH-loop variant, which shows significant variation depending on the metal and density employed. When we analyse the recover activity, the only carrier that can recover activity for all the histidine variants is the Hd-AG-Cu^{2+}. Thus, copper seems to be the only divalent metal that is able to anchor the enzymes through the clusters regardless their position in the enzyme surface. However, in the case of the Tt27-HBDH-loop, the flexibility of this insertion allows a better interaction of the histidines cluster with the surface carrier, which explains the higher values of immobilization yields obtained for this variant in the different metal chelates. The recover activity for the Tt27-HBDH-loop variant immobilized on LdAG-Co^{2+} was between 2- and 3-times higher than when it is immobilized on the other carriers despite being the carrier that exhibits the lowest immobilization yield.

To sum up, the orientation of Tt27-HBDH-WT through its N-terminus requires cooper chelates to maximize its immobilization effectiveness, while orientation though the artificial loop requires cobalt chelates to recover the highest Tt27-HBDH activity at the expense of minimizing the immobilization yields. We conclude that for orienting the protein through the flexible helix 94-107 and 122-128 located in a cavity created by the quaternary structure (Figure 24), at least 4 histidines must be inserted at that region and the carriers must be functionalized with either copper or nickel chelates when the carrier is activated with a low density metal chelate. However, the immobilization did promote an increase of the specific activity of the immobilized enzymes. Thus, the single-plate immobilization screening is helpful to have a general idea about the immobilization behaviour when different carriers and enzyme variants are employed. It allows reduction of experimental and analysis time as well as the amount of carrier and enzyme to choose the best carrier option for a larger scale analysis.

Table 18: Single-plate immobilization screening.

Variant	Metal chelate	Metal density (µmol /g)	Load ($mg_{protein}$ / g)	Ψ % Immobilization	Recovered Activity ($U/g_{carrier}$)	$Ae_{immobilized}$ (U/mg)	rRA(%)[a]
WT	Ni^{2+}	15 µmol	4.73 ± 0.09	70.1 ± 6.3	0.32 ± 0.04	0.07 ± 0.01	66
	Co^{2+}	15 µmol	4.88 ± 0.07	76.3 ± 2.3	0.24 ± 0.03	0.07 ± 0.01	66
	Co^{2+}	40 µmol	4.88 ± 0.08	85.1 ± 1.7	0.28 ± 0.00	0.07 ± 0.00	55
	Cu^{2+}	15 µmol	4.73 ± 0.09	95.3 ± 4.0	0.36 ± 0.07	0.08 ± 0.02	75
	Cu^{2+}	40 µmol	4.88 ± 0.08	91.1 ± 0.9	0.25 ±0.06	0.06 ± 0.01	47
H2	Ni^{2+}	15 µmol	4.33 ± 0.07	0.00 ± 0.00	0.00 ± 0.00	0.00 ± 0.00	0
	Co^{2+}	15 µmol	4.33 ± 0.07	0.00 ± 0.00	0.00 ± 0.00	0.00 ± 0.00	0
	Co^{2+}	40 µmol	4.08 ± 0.25	0.00 ± 0.00	0.03 ± 0.00	0.00 ± 0.01	6
	Cu^{2+}	15 µmol	4.33 ± 0.07	0.00 ± 0.00	0.00 ± 0.00	0.00 ± 0.00	0
	Cu^{2+}	40 µmol	4.08 ± 0.25	73.6 ± 3.3	0.23 ± 0.01	0.08 ± 0.00	63
H3	Ni^{2+}	15 µmol	4.32 ± 0.19	0.00 ± 0.00	0.00 ± 0.00	0.00 ± 0.00	0
	Co^{2+}	15 µmol	4.32 ± 0.19	0.00 ± 0.00	0.00 ± 0.00	0.00 ± 0.00	0
	Co^{2+}	40 µmol	4.08 ± 0.11	0.00 ± 0.00	0.02 ± 0.00	0.00 ± 0.00	0
	Cu^{2+}	15 µmol	4.32 ± 0.19	79.6 ± 3.4	0.27 ± 0.00	0.08 ± 0.00	113
	Cu^{2+}	40 µmol	4.08 ± 0.11	61.1 ± 5.1	0.28 ± 0.04	0.11 ± 0.01	98
H4	Ni^{2+}	15 µmol	4.15 ± 0.04	22.4 ± 2.4	0.03 ± 0.01	0.04 ± 0.01	71
	Co^{2+}	15 µmol	4.15 ± 0.04	0.00 ± 0.00	0.00 ± 0.00	0.00 ± 0.00	0
	Co^{2+}	40 µmol	4.08 ± 0.19	0.00 ± 0.00	0.03 ± 0.01	0.00 ± 0.00	0
	Cu^{2+}	15 µmol	4.15 ± 0.04	54.0 ± 2.2	0.17 ± 0.02	0.08 ± 0.01	141
	Cu^{2+}	40 µmol	4.08 ± 0.19	67.0 ± 2.0	0.15 ± 0.05	0.06 ± 0.02	105
loop	Ni^{2+}	15 µmol	5.39 ± 0.22	91.4 ± 2.7	0.38 ± 0.07	0.08 ± 0.01	30
	Co^{2+}	15 µmol	5.39 ± 0.22	41.2 ± 5.2	0.41 ± 0.05	0.18 ± 0.02	67
	Co^{2+}	40 µmol	5.12 ± 0.06	85.3 ± 1.6	0.33 ± 0.01	0.08 ± 0.00	34
	Cu^{2+}	15 µmol	5.39 ± 0.22	96.9 ± 2.7	0.31 ± 0.01	0.06 ± 0.00	22
	Cu^{2+}	40 µmol	5.12 ± 0.06	91.3 ± 0.5	0.33 ± 0.01	0.07 ± 0.00	30

The variants and carrier pairs where the recovered activity is **higher** are showed in green.

Once we obtained a first look of the metal nature effects on the immobilization of the Tt27-HBDH histidine enriched variants, we performed the same study using Bio-Spin® columns. These experiments were performed to avoid possible problems such as inefficient or poor diffusion of the solution to the carrier. This problem could occur in the plates due to the possible ineffective agitation produced by the carrier deposition on the well bottom. These studies were performed with the candidates obtained in the single-plate screening.

Then we analyzed the immobilization parameters in the best carrier for recovery of all histidine variants Hd-AG-Cu^{2+} and they were compared with the commercial carrier EziG1. The results obtained are showed in the Table 19. The Hd-AG-Cu^{2+} is a great carrier for the immobilization of the different histidine cluster variants with yields near to the 100 % for all the variants. The commercial carrier EziG1 exhibits 100 % of immobilization, however this carrier allows higher recovery activity after the immobilization, especially in the case of Tt-27HBDH-WT, Tt-27-HBDH-H4 and Tt27-HBDH-loop.

Table 19: Tt27-HBDH histidine variants immobilization parameters on HdAG-Cu^{2+} and EziG1 carriers.

Carrier: HdAG-Cu^{2+}				
Variant	**Ψ % Immobilization**	**Recovered Activity ($U/g_{carrier}$)**	**$Ae_{immobilized}$ (U/mg)**	**rRA (%)[a]**
WT	94.2 ± 0.6	0.49 ± 0.05	0.11 ± 0.01	70
H2	87.1 ± 18.2	0.26 ± 0.01	0.05 ± 0.002	72
H3	92.6 ± 4.0	0.26 ± 0.01	0.05 ± 0.002	68
H4	100 ± 0	0.2 ± 0.02	0.05 ± 0.005	118
Loop	100 ± 0	0.28 ± 0.01	0.06 ± 0.003	16
Carrier: EziG1				
Variant	**Ψ % Immobilization**	**Recovered Activity ($U/g_{carrier}$)**	**$Ae_{immobilized}$ (U/mg)**	**rRA (%)[a]**
WT	100 ± 0	1.22 ± 0.02	0.12 ± 0.00	152
H2	92.4 ± 6.5	0.26 ± 0.06	0.05± 0.01	72
H3	94.2 ± 3.9	0.27 ± 0.05	0.06 ± 0.01	81
H4	100 ± 0	0.47 ± 0.01	0.05± 0.00	140
Loop	100 ± 0	2.77 ± 0.41	0.28 ± 0.03	321

The best performing biocatalysts for relative recovery activity (rRA) are shown in green.

4.3.13 Thermal stability of Tt27-HBDH variants

With these biocatalysts, the thermal stability analyses were performed in the same way as for BsADH variants. However, as this alcohol dehydrogenase is a thermophilic enzyme the biocatalysts were incubated at 80 ºC for 1 hour.

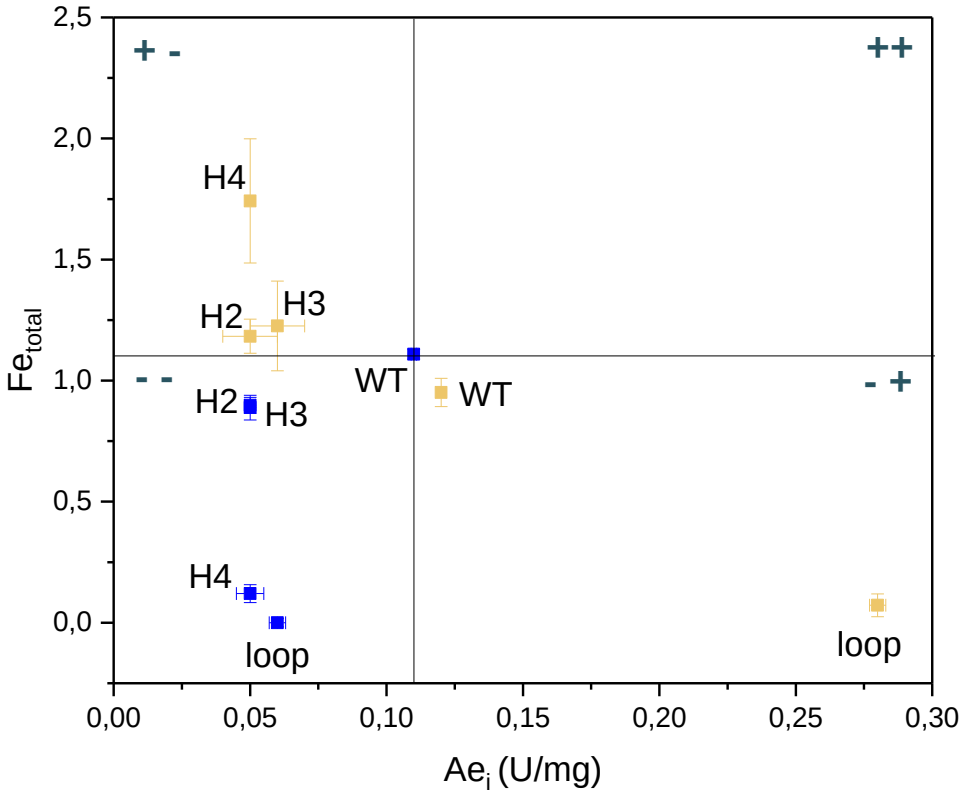

Figure 47: Thermal stability of Tt27-HBDH variants.

The stability factor data is divided into four quadrants taking Tt27-HBDH-WT immobilized on HdAG-Cu^{2+} as reference. The ***upper left quadrant*** *shows the biocatalysts more active but less stables than the WT immobilized on HdAG-Cu^{2+}.* ***The lower left quadrant*** *shows the biocatalysts less active and stable than the WT immobilized on HdAG-Cu^{2}. The* ***lower right quadrant*** *shows the biocatalysts more active but less stable than the WT immobilized on HdAG-Cu^{2+}.* ***The upper right quadrant*** *shows the biocatalysts more active and more stable. The thermal stability assays were carried out at 80 ºC for 1 hour.*

In this case, the Tt27-HBDH-WT immobilized on HdAG-Cu^{2+} was chosen as reference for the analysis of the total thermal stability factor. The analysis of the stability factor shows that the histidine clusters variants immobilized on EziG1 have higher thermal stability at 80 ºC than the reference, except for the Tt27-HBDH-loop which is less thermal stable but 2.5 times more active than the reference. It should be noted that the thermal stability of the soluble loop variant presents a very low thermal stability. The soluble loop variant recovered only 33 % of its initial activity while the WT variant recovers 99 % at 80 ºC. Meanwhile, the best histidine cluster variant Tt27-HBDH-H4 shows 1.6 times higher stability than the reference but, in contrast, has 2.2 times lower specific activity immobilized.

4.3.14 Melting Temperature (TM) analysis for Tt27-HBDH variants

To continue the biocatalyst characterization and taking account of the data obtained in the immobilization parameters, as well as the thermal stability, we decided to use the commercial EziG1 as carrier for the immobilization and the variants WT, H4 and loop as the most interesting variants for further analysis. For the experiments 8 µg of total protein were added with the commercial dye SYPRO ® orange and the same procedures described in the section 4.2.14 were performed. The T_M for the soluble enzymes are showed in the Figure 48 A and for the immobilized ones in the Figure 48 B.

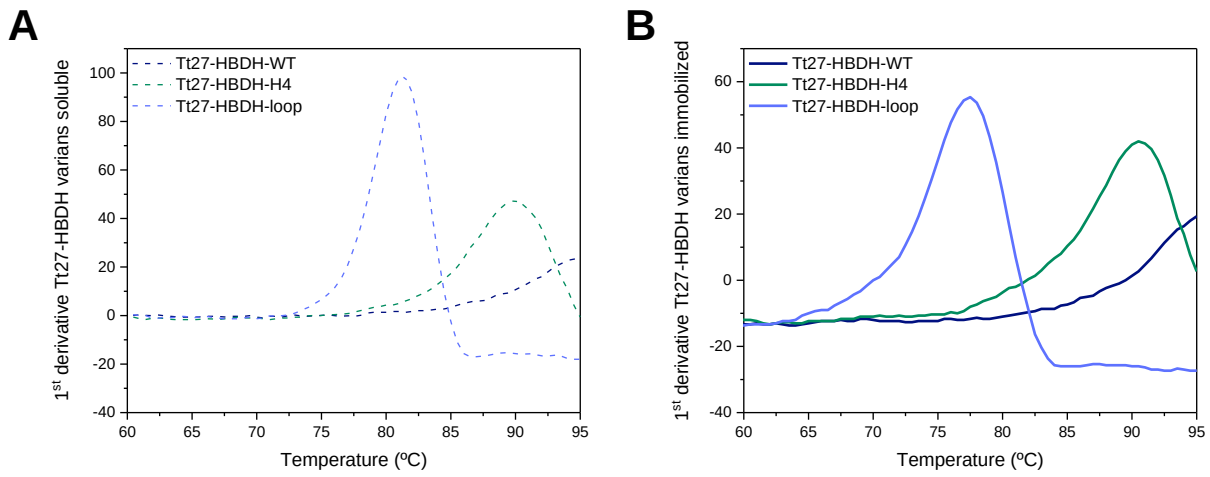

Figure 48: Melting temperature for Tt27-HBDH histidine variants.

A. *Plot of the first derivative of the soluble enzymes.* ***B.*** *Plot of the first derivative of the immobilized enzymes. All the experiments were performed using 8 µg of protein. The T_M for the soluble enzymes are 94.8 ± 0.3, 89.7 ± 0.3 and 81.5 ± 0 for the Tt27-HBDH-WT, H4 and loop respectively. For the immobilized enzyme the T_M of the variants are 95 ± 0, 90.8 ±0.6 and 77.7 ± 0.3 the Tt27-HBDH-WT, H4 and loop respectively.*

The Tt27-HBDH-WT is highly stable against the temperature and as such its Tm is not able to be measured with precision under the experimental conditions, both when they are soluble or immobilized on EziG1. The immobilization for Tt27-HBDH-H4 variant did not change the melting temperature of the enzyme, so the immobilization does not stabilize the enzyme against the thermodynamic unfolding at high temperature. However, in the case of Tt27-HBDH-loop variant, the immobilization decreases the stability of the temperature by almost 4 ºC as a result of the rigidification of the flexible loop. In short, the insertion of the mutation in the case of Tt27-HBDH enzyme does affect the resistance against the unfolding process cause by the temperature.

4.3.15 Operational stability assays for Tt27-HBDH variants

The different variants were also tested in a chemical reaction with industrial interest such is the reduction of ethyl acetoacetate (EAA) to β-hydroxyesters, ethyl (S)-3-hydroxybutyrate. This compound is widely employed in the pharmaceutical and food industries as a precursor

of functional products. Also, the capability of this alcohol dehydrogenase to perform the reaction with a high enantioselectivity towards the (S) enantiomer makes this reaction highly attractive at industrial level, as described by Orrego and co-workers. [46] The operational stability was assessed by re-using the heterogeneous biocatalysts in consecutive reaction cycles for the asymmetric reduction of ethyl acetoacetate (Figure 49 A).

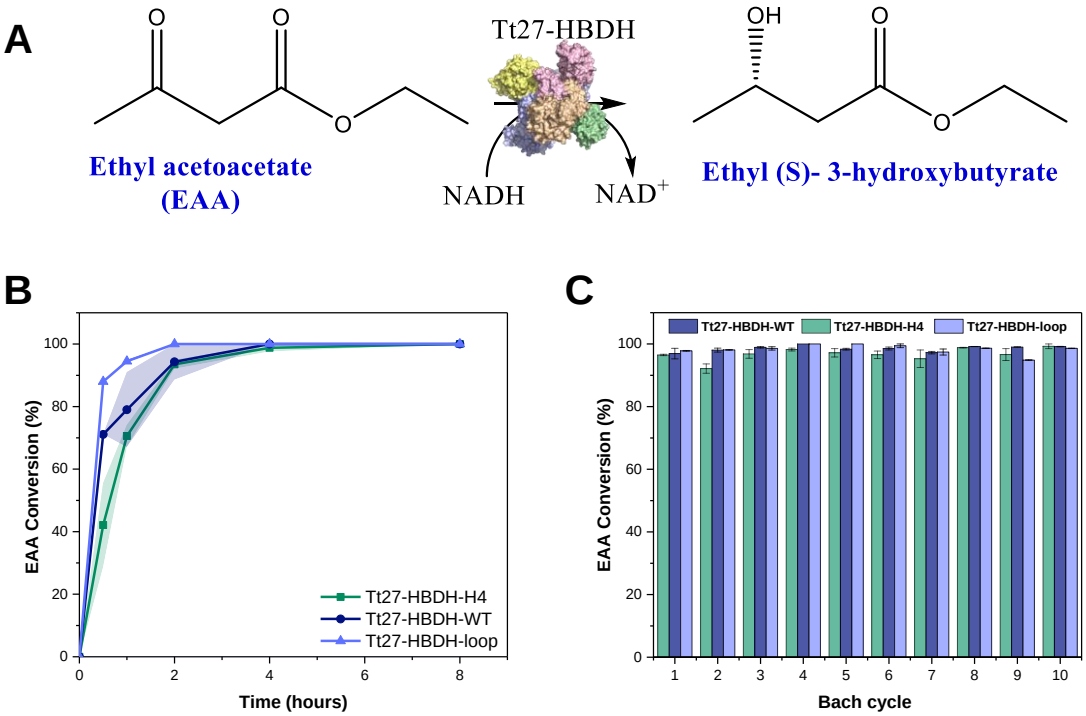

Figure 49: Operational stability of Tt27-HBDH histidine variants.

A. *Reaction scheme of the ethyl acetoacetate reduction by Tt27-HBDH histidine variants.* ***B.*** *kinetic of the EAA conversion. The reactions were carried out at 60 ºC and 250 rpm.* ***C.*** *Reusability study in batch reaction at 4 hours of reaction at 60 ºC and 250 rpm. Quantification of the EAA consumption by GC.*

First, we analyzed the time course of the first reaction cycle catalyzed by the Tt27-HBDH variant immobilized on EziG1. We found that the loop variant is faster than the Tt27-HBDH-WT variant and the Tt27-HBDH-H4 (Figure 49 B). Conversion of 100 % achieved after 2 hour of reaction for the Tt27-HBDH-loop variant, however both the WT and H4 variant needs at least 4 hours to complete the reaction. Furthermore, after 10 batch cycles, the three immobilized variants reached roughly 100 % product yield (Figure 49 C).

To further investigate the differences among the three enzyme variants herein studied, we performed the asymmetric reduction of EAA at different temperatures ranging 60-90 ºC. After 10 cycles in batch, the biocatalysts were incubated at different temperatures, from 60 to 90 ºC, to perform the catalytic reaction, the EAA conversion, for the different temperatures

for 1 hour and they are showed in Figure 50. All variants increase their activity at 70 ºC, whereas the Tt27-HBDH-loop begins to lose activity as the temperature increases, the Tt27-HBDH-WT and H4 variants are still growing with 98 and 97 % conversion, respectively in 1 hour at 90 ºC.

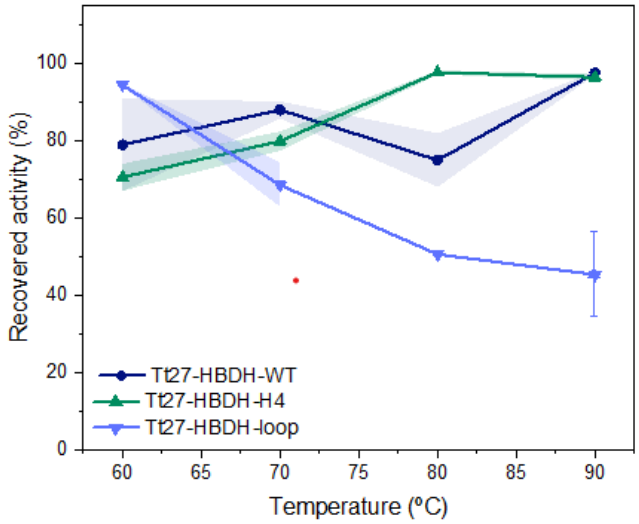

Figure 50: Temperature challenge for the Tt27-HBDH histidine variants.

4.4 Conclusions

In this chapter, we describe a new approach to control the orientation of multimeric enzymes during the immobilization procedure on solid carriers. This approach allows the rational engineering of the enzyme surface through introducing histidines clusters at different regions of their surfaces. The affinity interaction between the histidine clusters and metal chelates is, in some cases, as efficient as the widely employed enzyme immobilization driven by histidine-tags. This strategy was tested in two structurally different alcohol dehydrogenases to demonstrate its universality. Next, we studied the function/structure relationship of different His-cluster variants immobilized on agarose microbeads activated with different types and densities of metal chelates. We demonstrate that enzyme orientation can be achieved and affect biocatalyst properties. For some variants with surface histidine clusters, certain orientations lead to more active heterogeneous biocatalysts, while other orientations lead to more stable immobilized enzymes than their His-tagged counterparts immobilized on the same carriers. We also observed that the density and the nature of the metal chelates play a key role to assure an efficient immobilization (high immobilization yield, high recovered activity and high stability) of the His-cluster variants. Therefore, the best carrier for each engineered variants must be selected upon an screening that asses both the activity and the stability of the resulting heterogeneous biocatalysts.

4.5 Bibliography

[1] D.A. Cecchini, I. Serra, D. Ubiali, M. Terreni, A.M. Albertini, New active site oriented glyoxyl-agarose derivatives of Escherichia colipenicillin G acylase, BMC biotechnology, 7 (2007) 1-11.

[2] V. Grazu, F. Lopez-Gallego, T. Montes, O. Abian, R. Gonzalez, J.A. Hermoso, J.L. García, C. Mateo, J.M. Guisan, Promotion of multipoint covalent immobilization through different regions of genetically modified penicillin G acylase from E. coli, Process Biochemistry, 45 (2010) 390-398.

[3] C. Oliveira, T.Q. Aguiar, L. Domingues, Principles of genetic engineering, Current Developments in Biotechnology and Bioengineering, Elsevier2017, pp. 81-127.

[4] A.I. Freitas, L. Domingues, T.Q. Aguiar, Tag-mediated single-step purification and immobilization of recombinant proteins toward protein-engineered advanced materials, Journal of Advanced Research, 36 (2022) 249-264.

[5] C. Bernal, K. Rodriguez, R. Martinez, Integrating enzyme immobilization and protein engineering: An alternative path for the development of novel and improved industrial biocatalysts, Biotechnology advances, 36 (2018) 1470-1480.

[6] R.A. Sheldon, S. van Pelt, Enzyme immobilisation in biocatalysis: why, what and how, Chemical Society Reviews, 42 (2013) 6223-6235.

[7] R.C. Rodrigues, Á. Berenguer-Murcia, R. Fernandez-Lafuente, Coupling chemical modification and immobilization to improve the catalytic performance of enzymes, Advanced Synthesis & Catalysis, 353 (2011) 2216-2238.

[8] Y. Liu, J. Yu, Oriented immobilization of proteins on solid supports for use in biosensors and biochips: a review, Microchimica Acta, 183 (2016) 1-19.

[9] P.J. Gane, J.M. Dunwell, J. Warwickr, Modeling based on the structure of vicilins predicts a histidine cluster in the active site of oxalate oxidase, Journal of molecular evolution, 46 (1998) 488-493.

[10] D. Wasserberg, C. Nicosia, E.E. Tromp, V. Subramaniam, J. Huskens, P. Jonkheijm, Oriented protein immobilization using covalent and noncovalent chemistry on a thiol-reactive self-reporting surface, Journal of the American Chemical Society, 135 (2013) 3104-3111.

[11] C.A. Godoy, B.d.l. Rivas, V. Grazú, T. Montes, J.M. Guisán, F. López-Gallego, Glyoxyl-disulfide agarose: A tailor-made support for site-directed rigidification of proteins, Biomacromolecules, 12 (2011) 1800-1809.

[12] F. Liu, L. Wang, H. Wang, L. Yuan, J. Li, J.L. Brash, H. Chen, Modulating the activity of protein conjugated to gold nanoparticles by site-directed orientation and surface density of bound protein, ACS applied materials & interfaces, 7 (2015) 3717-3724.

[13] T. Ichihara, J.K. Akada, S. Kamei, S. Ohshiro, D. Sato, M. Fujimoto, Y. Kuramitsu, K. Nakamura, A novel approach of protein immobilization for protein chips using an oligo-cysteine tag, Journal of proteome research, 5 (2006) 2144-2151.

[14] A.I. Benítez-Mateos, I. Llarena, A. Sánchez-Iglesias, F. López-Gallego, Expanding one-pot cell-free protein synthesis and immobilization for on-demand manufacturing of biomaterials, ACS synthetic biology, 7 (2018) 875-884.

[15] G.T. Hermanson, Bioconjugate techniques, Academic press2013.

[16] V. Grazu, L. Betancor, T. Montes, F. Lopez-Gallego, J.M. Guisan, R. Fernandez-Lafuente, Glyoxyl agarose as a new chromatographic matrix, Enzyme and microbial technology, 38 (2006) 960-966.

[17] S.T. Larda, D. Pichugin, R.S. Prosser, Site-specific labeling of protein lysine residues and N-terminal amino groups with indoles and indole-derivatives, Bioconjugate Chemistry, 26 (2015) 2376-2383.

[18] R. Pagolu, R. Singh, R. Shanmugam, S. Kondaveeti, S.K. Patel, V.C. Kalia, J.-K. Lee, Site-directed lysine modification of xylanase for oriented immobilization onto silicon dioxide nanoparticles, Bioresource Technology, 331 (2021) 125063.

[19] C. Mateo, V. Grazu, J.M. Palomo, F. Lopez-Gallego, R. Fernandez-Lafuente, J.M. Guisan, Immobilization of enzymes on heterofunctional epoxy supports, Nature Protocols, 2 (2007) 1022-1033.

[20] L. Chen, S. Xu, J. Li, Recent advances in molecular imprinting technology: current status, challenges and highlighted applications, Chemical Society Reviews, 40 (2011) 2922-2942.

[21] J. Kalecki, Z. Iskierko, M. Cieplak, P.S. Sharma, Oriented immobilization of protein templates: a new trend in surface imprinting, ACS sensors, 5 (2020) 3710-3720.

[22] R. Xing, Y. Ma, Y. Wang, Y. Wen, Z. Liu, Specific recognition of proteins and peptides via controllable oriented surface imprinting of boronate affinity-anchored epitopes, Chemical science, 10 (2019) 1831-1835.

[23] S. Costa, A. Almeida, A. Castro, L. Domingues, Fusion tags for protein solubility, purification and immunogenicity in Escherichia coli: the novel Fh8 system, Frontiers in microbiology, 5 (2014) 63.

[24] C.L. Young, Z.T. Britton, A.S. Robinson, Recombinant protein expression and purification: a comprehensive review of affinity tags and microbial applications, Biotechnology journal, 7 (2012) 620-634.

[25] V. Paraskevopoulou, F.H. Falcone, Polyionic tags as enhancers of protein solubility in recombinant protein expression, Microorganisms, 6 (2018) 47.

[26] O. Barbosa, C. Ortiz, Á. Berenguer-Murcia, R. Torres, R.C. Rodrigues, R. Fernandez-Lafuente, Strategies for the one-step immobilization–purification of enzymes as industrial biocatalysts, Biotechnology advances, 33 (2015) 435-456.

[27] T.P. Hopp, K.S. Prickett, V.L. Price, R.T. Libby, C.J. March, D. Pat Cerretti, D.L. Urdal, P.J. Conlon, A short polypeptide marker sequence useful for recombinant protein identification and purification, Bio/technology, 6 (1988) 1204-1210.

[28] G.I. Evan, G.K. Lewis, G. Ramsay, J.M. Bishop, Isolation of monoclonal antibodies specific for human c-myc proto-oncogene product, Molecular and cellular Biology, 5 (1985) 3610-3616.

[29] A.C. Lellouch, R.A. Geremia, Expression and study of recombinant ExoM, a β1-4 glucosyltransferase involved in succinoglycan biosynthesis in Sinorhizobium meliloti, Journal of bacteriology, 181 (1999) 1141-1148.

[30] I.P. Korndörfer, A. Skerra, Improved affinity of engineered streptavidin for the Strep-tag II peptide is due to a fixed open conformation of the lid-like loop at the binding site, Protein science, 11 (2002) 883-893.

[31] H.M. Sassenfeld, S.J. Brewer, A polypeptide fusion designed for the purification of recombinant proteins, Bio/technology, 2 (1984) 76-81.

[32] K. Terpe, Overview of tag protein fusions: from molecular and biochemical fundamentals to commercial systems, Applied microbiology and biotechnology, 60 (2003) 523-533.

[33] J. Porath, J. Carlsson, I. Olsson, G. Belfrage, Metal chelate affinity chromatography, a new approach to protein fractionation, Nature, 258 (1975) 598-599.

[34] E. Hochuli, H. Döbeli, A. Schacher, New metal chelate adsorbent selective for proteins and peptides containing neighbouring histidine residues, Journal of Chromatography A, 411 (1987) 177-184.

[35] M. Vašák, Metallothioneins: chemical and biological challenges, JBIC Journal of Biological Inorganic Chemistry, 16 (2011) 975-976.

[36] S. Cun, Y.-T. Lai, Y.-Y. Chang, H. Sun, Structure-oriented bioinformatic approach exploring histidine-rich clusters in proteins, Metallomics, 5 (2013) 904-912.

[37] M.D. Michelitsch, J.S. Weissman, A census of glutamine/asparagine-rich regions: implications for their conserved function and the prediction of novel prions, Proceedings of the National Academy of Sciences, 97 (2000) 11910-11915.

[38] M. Rowinska-Zyrek, D. Witkowska, S. Potocki, M. Remelli, H. Kozlowski, His-rich sequences–is plagiarism from nature a good idea?, New Journal of Chemistry, 37 (2013) 58-70.

[39] O. Abian, V. Grazú, J. Hermoso, R. González, J.L. García, R. Fernández-Lafuente, J.M. Guisán, Stabilization of penicillin G acylase from Escherichia coli: site-directed mutagenesis of the protein surface to increase multipoint covalent attachment, Applied and environmental microbiology, 70 (2004) 1249-1251.

[40] T. Montes, V. Grazú, I. Manso, B. Galán, F. López-Gallego, R. Gonzalez, J.A. Hermoso, J.L. García, J.M. Guisán, R. Fernández-Lafuente, Improved stabilization of genetically modified penicillin G acylase in the presence of organic cosolvents by co-immobilization of the enzyme with polyethyleneimine, Advanced Synthesis & Catalysis, 349 (2007) 459-464.

[41] A.V. Finkelstein, A.Y. Badretdinov, A.M. Gutin, Why do protein architectures have Boltzmann-like statistics?, Proteins: Structure, Function, and Bioinformatics, 23 (1995) 142-150.

[42] Y. Bai, T.R. Sosnick, L. Mayne, S.W. Englander, Protein folding intermediates: native-state hydrogen exchange, Science, 269 (1995) 192-197.

[43] J. Vertrees, P. Barritt, S. Whitten, V.J. Hilser, COREX/BEST server: a web browser-based program that calculates regional stability variations within protein structures, Bioinformatics, 21 (2005) 3318-3319.

[44] V.J. Hilser, S.T. Whitten, Using the COREX/BEST server to model the native-state ensemble, Protein Dynamics, Springer2014, pp. 255-269.

[45] A. Prabhavadhni, T. Richa, T. Sivaraman, A Review on Computational Methods for Predicting Residue-Specific Stabilities of Proteins, Journal of Pharmaceutical Sciences and Research, 7 (2015) 159.

[46] A.H. Orrego, D. Andrés-Sanz, S. Velasco-Lozano, M. Sanchez-Costa, J. Berenguer, J.M. Guisan, J. Rocha-Martin, F. López-Gallego, Self-sufficient asymmetric reduction of β-ketoesters catalysed by a novel and robust thermophilic alcohol dehydrogenase co-immobilised with NADH, Catalysis science & technology, 11 (2021) 3217-3230.

[47] J.W. Bok, N.P. Keller, Fast and easy method for construction of plasmid vectors using modified quick-change mutagenesis, Fungal Secondary Metabolism, Springer2012, pp. 163-174.

[48] H. Malke, J. SAMBROCK, EF FRITSCH and T. MANIATIS, Molecular Cloning, A Laboratory Manual , Volumes 1, 2 and 3. 1625 S., zahlreiche Abb. und Tab. Cold Spring Harbor 1989. Cold Spring Harbor Laboratory Press. $115.00. ISBN: 0-87969-309-6, Wiley Online Library, 1990.

[49] M.M. Bradford, A rapid and sensitive method for the quantitation of microgram quantities of protein utilizing the principle of protein-dye binding, Analytical biochemistry, 72 (1976) 248-254.

[50] C. Aymard, A. Belarbi, Kinetics of thermal deactivation of enzymes: a simple three parameters phenomenological model can describe the decay of enzyme activity, irrespectively of the mechanism, Enzyme and microbial technology, 27 (2000) 612-618.

[51] K.L. Holmes, L.M. Lantz, Protein labeling with fluorescent probes, Methods in cell biology, 63 (2001) 185-204.

[52] J. Santiago-Arcos, S. Velasco-Lozano, E. Diamanti, A.L. Cortajarena, F. López-Gallego, Immobilization Screening and Characterization of an Alcohol Dehydrogenase and Its Application to the Multi-Enzymatic Selective Oxidation of 1,-Omega-Diols, Frontiers in Catalysis, (2021) 9.

[53] E. Diamanti, S. Arana-Peña, P. Ramos-Cabrer, N. Comino, D. Carballares, R. Fernandez-Lafuente, F. López-Gallego, Intraparticle Macromolecular Migration Alters the Structure and Function of Proteins Reversibly Immobilized on Porous Microbeads, Advanced Materials Interfaces, (2022) 2200263.

[54] C. Ceccarelli, Z.-X. Liang, M. Strickler, G. Prehna, B.M. Goldstein, J.P. Klinman, B.J. Bahnson, Crystal structure and amide H/D exchange of binary complexes of alcohol dehydrogenase from Bacillus stearothermophilus: insight into thermostability and cofactor binding, Biochemistry, 43 (2004) 5266-5277.

[55] R.G. Pearson, Hard and soft acids and bases, HSAB, part 1: Fundamental principles, Journal of Chemical Education, 45 (1968) 581.

[56] Z. Horváth, G. Nagydiósi, Imino-diacetic-acid-ethyl-cellulose and its chelate forming behaviour—I, Journal of Inorganic and Nuclear Chemistry, 37 (1975) 767-769.

[57] R.C.F. Cheung, J.H. Wong, T.B. Ng, Immobilized metal ion affinity chromatography: a review on its applications, Applied microbiology and biotechnology, 96 (2012) 1411-1420.

[58] J. Porath, Immobilized metal ion affinity chromatography, Protein expression and purification, 3 (1992) 263-281.

[59] E. Sulkowski, The saga of IMAC and MIT, Bioessays, 10 (1989) 170-175.

[60] W. Maret, H. Dietrich, H.-H. Ruf, M. Zeppezauer, Active site-specific reconstituted copper (II) horse liver alcohol dehydrogenase: a biological model for type 1 Cu2+ and its changes upon ligand binding and conformational transitions, Journal of Inorganic Biochemistry, 12 (1980) 241-252.

[61] C.F. Meares, Peptide–metal interactions, Encyclopedia of Inorganic Chemistry, (2006).

[62] S. Velasco-Lozano, J. Santiago-Arcos, J.A. Mayoral, F. López-Gallego, Co-immobilization and Colocalization of Multi-Enzyme Systems for the Cell-Free Biosynthesis of Aminoalcohols, ChemCatChem, 12 (2020) 3030-3041.

[63] A. Ganesan, B.D. Moore, S.M. Kelly, N.C. Price, O.J. Rolinski, D.J. Birch, I.R. Dunkin, P.J. Halling, Optical spectroscopic methods for probing the conformational stability of immobilised enzymes, ChemPhysChem, 10 (2009) 1492-1499.

[64] M.R. Eftink, C.A. Ghiron, Fluorescence quenching studies with proteins, Analytical biochemistry, 114 (1981) 199-227.

[65] E. Burstein, N. Vedenkina, i.M. Ivkova, Fluorescence and the location of tryptophan residues in protein molecules, Photochemistry and photobiology, 18 (1973) 263-279.

[66] J.T. Vivian, P.R. Callis, Mechanisms of tryptophan fluorescence shifts in proteins, Biophysical journal, 80 (2001) 2093-2109.

[67] H. Chen, S.S. Ahsan, M.E.B. Santiago-Berrios, H.D. Abruña, W.W. Webb, Mechanisms of quenching of Alexa fluorophores by natural amino acids, Journal of the American Chemical Society, 132 (2010) 7244-7245.

[68] S. Velasco-Lozano, J. Santiago-Arcos, M. Grazia Rubanu, F. López-Gallego, Cell-Free Biosynthesis of ω-Hydroxy Acids Boosted by a Synergistic Combination of Alcohol Dehydrogenases, ChemSusChem, 15 (2022) e202200397.

[69] J. Schindelin, I. Arganda-Carreras, E. Frise, V. Kaynig, M. Longair, T. Pietzsch, S. Preibisch, C. Rueden, S. Saalfeld, B. Schmid, Fiji: an open-source platform for biological-image analysis, Nature methods, 9 (2012) 676-682.

[70] N. Zeballos, E. Diamanti, A.I. Benítez-Mateos, C. Schmidt-Dannert, F. López-Gallego, Solid-phase assembly of multienzyme systems into artificial cellulosomes, Bioconjugate Chemistry, 32 (2021) 1966-1972.

[71] J.M. Bolivar, A. Hidalgo, L. Sánchez-Ruiloba, J. Berenguer, J.M. Guisán, F. López-Gallego, Modulation of the distribution of small proteins within porous matrixes by smart-control of the immobilization rate, Journal of biotechnology, 155 (2011) 412-420.

[72] E. Diamanti, J. Santiago-Arcos, D. Grajales-Hernández, N. Czarnievicz, N. Comino, I. Llarena, D. Di Silvio, A.L. Cortajarena, F. López-Gallego, Intraparticle kinetics unveil crowding and enzyme distribution effects on the performance of cofactor-dependent heterogeneous biocatalysts, AcS catalysis, 11 (2021) 15051-15067.

[73] S.M. Kelly, T.J. Jess, N.C. Price, How to study proteins by circular dichroism, Biochimica et Biophysica Acta (BBA)-Proteins and Proteomics, 1751 (2005) 119-139.

NANOPARTICLE IMMOBILIZATION

5.1 Introduction

The concept of nanotechnology was introduced for first time in 1959 by the physicist Richard Feynman.[1] However, it was not until the entrance to the XXII century that nanotechnology had become consolidated as a new field with great potential for applicability in different fields with promising advances in healthcare,[2] medicine[3, 4] and biotechnology[5] among others.[6, 7] The exponential development of this nano-based technology is facilitated by their unique general properties including the particle size, extremely high surface area to volume ratio, surface reactivity, charge and shape. They are able to increase stress resistance and decrease mass transfer resistance.[8] Nanoparticles (NPs) can also be produced with a wide range of metals and semiconductor core materials. These materials could impart useful properties such as fluorescence and magnetic behaviour.[9]

Enzymes have been incorporated into a wide range of fields and industries. However, as mentioned in previous chapters, the immobilization onto macro or micro surfaces is typically required for use in different biotechnology purposes. Nonetheless, researchers also reported some of the limitations that come with the immobilization onto planar surfaces (on macro/micro surfaces). This limitation could come from possible distortions of the native enzyme configuration, the steric hindrance or slower diffusion of the substrate to the active site or the product toward the reaction bulk. This is how, a variety of materials and carriers are currently being explored. [10, 11] Between the potential carriers reported in the literature, NPs in particular show promise as carriers to solve these problems and remain or even enhance the enzymatic activity.[12]

Thus, this recent interest in the nanotechnology promoted the development of a wealth of diverse nanocarriers that could potentially support enzyme immobilization. The use of nanocarriers could reduce diffusion limitation and maximize the enzyme loading due to maximization of the surface area. It has been reported in the literature the increase in the thermostability by increase of the surface area.[10] The enzyme-NPs conjugates also enhance the activity of diverse enzymes such as β-galactosidase, alkaline phosphatase or glucose oxidase.[13-15] Some hypotheses about the enhancements in catalysis are linked to the mobility of the NPs that could enhance the substrate-enzyme interaction due to Brownian motion on one hand,[16] and the substrate-NP interaction on the other hand.[17] Where each collision substrate-NP could generate a weak interaction such electrostatic that attraction could result in multiple binding occurrences on the NP before the substrate moves elsewhere.[17] Factors such as enzyme density, NP morphology, NP surface chemistry, mass transport, and enzyme orientation could also enhance the immobilized enzyme activity.[12]

In these terms, enzyme-nanoparticle conjugates could have great potential in biocatalysis and factors such as the correct orientation of the enzyme anchoring to a nanoparticle, which is important to keep the activity of the enzyme.[18]

5.1.1 Magnetic nanoparticles (MNPs)

In the last two decades magnetic nanoparticles have been widely utilized as nanocarriers for enzyme immobilization, and specifically in the biotechnology and biomedical fields. In the biocatalyst field, MNPs have gained interest as a solution for one of the critical and challenging aspects for biocatalysts: their lack of re-purification and efficient recovery. Thus, MNPs have become an interesting and versatile carrier for the immobilization proposes. Due to their properties as nanoparticles, such as their large surface area per volume ratio and high mass transfer, but even more so for their magnetic properties. These magnetic properties allow them to be easily separated and recovered by an external magnetic field, which has been industrially exploited for selective catalysis removal from the batch reaction mixture, which could reduce the capital and operational costs.[19, 20]

The main element that differentiates MNPs from the other NPs or materials is the magnetization cycle of hysteresis circuit, that provoke interest as these MNPs are able to retain their properties in absence of the stimulus generated.[21] These characteristics were exploited by Armenia and colleagues to produce heat under alternating magnetic field (AFM) to improve an biocatalytic process for first time.[22] They describe the activation of thermophilic enzymes immobilized on MNP under a certain alternating magnetic field, which allows the activation of the enzyme without increasing the global solution temperature. This demonstrates that it is possible to create hot spots in the local environment of the MNPs and open the gate to apply this technology to multi-enzymatic process which needs enzymes working simultaneously at different optimal temperatures. This application was also described by Ovejero and colleagues, which used fluorescent proteins as thermometers to demonstrate the heating power depends not only of the magnetic features of the MNPs but also of the intensity and frequency of the alternating magnetic field.[23]

However, MNPs have a big limitation due to aggregation issues produced by the strong magnetic attractions between particles, which limits their dispersion in aqueous media and with that their magnetic applicability.[24] It is for that reason that some modification on the MNP surface should be conducted to protect the MNPs from aggregation, oxidation and/or change of surface charge. This allows at the same time improvement of the immobilization capacity with further functionalization with specific compounds and increase of their colloidal stability.[25]

5.1.2 Effect of different enzyme orientation in the thermodynamic parameters.

Temperature is one of the critical variables for the rate reaction. The rate of reaction for a non-catalyzed chemical reaction follow the equations described by Arrhenius and Eyring[26, 27] increasing their rate exponentially when the temperature is increased. However, the effect of temperature on systems catalyzed by enzymes is complex. They have contributions from the geometry of the active site, reactivity, protein stability, conformational changes and regulations temperature-dependent that could have opposing effects. Also, changes in temperature could affect other features such as substrate binding, product release and conformational changes. Enzymes usually shows a characteristic activity/temperature profile with an increase in their activity until an optimal temperature (T_{opt}), above which the activity drops abruptly. The temperature dependence of catalytic rate is Arrhenian below the optimum temperature, which means that the enzymatic rate follows the Arrhenius law with a constant activation energy (Ea). The slope of the Arrhenius plot can provide us the activation energy Ea.

$$Ln\,(k) = -\frac{E_a}{R}\,\frac{1}{T} + \ln(A)$$

Eq (13): Arrhenius equation

This activation energy (Ea) refers to the energy difference between the reactants and the transition state. This barrier governs the catalytic rates of enzymatic reactions. Earlier works reported how the surface rigidification tunes the temperature dependence of catalytic rates tuning the entropic and enthalpic contributions and thus their activation energies.[28] Maffucci and colleagues also reported that the shifts produced in the optimal temperatures and activation energies are due to conformational changes induced by the temperature of homologous enzymes.[29]

5.1.3 Immobilization approaches

Many immobilization methods have been reported for enzyme immobilization on NPs from electrostatic attraction, [30] to the use of reactive functional groups such as thiol groups, primary amines, and carboxylate groups present on the protein surface.[31] However, one of the biggest challenges of enzyme immobilization on NPs is controlling the orientation in the immobilization. Thus, it is necessary to use molecular protein engineering to expand the range of possible functional groups in predetermined sites of the enzyme for the oriented immobilization of proteins.[32]

In the following work, we present three approaches to immobilizing the model enzyme BsADH and their variants, developed in chapters 3 and 4, on MNPs. Two of these

approaches contain the enzyme immobilized in the same orientation but with different immobilization distances to the MNP. In the other approach the enzyme is immobilized in a different orientation and at a shorter distance. The first approach has a closer immobilization to the surface using the histidine clusters (Figure 51 A), the second approach at an intermediate distance through the histidine tag (Figure 51 B) and the last one at a large distance with the system cohesin-dockerin (Figure 51 C) on MNPs previously activated with metal chelates. We hypothesise that the different orientations and distances could affect the enzyme kinetic and thermodynamic parameters. These different immobilization approaches on MNPs could affect the heat transference from the MNP to the enzyme which was described with fluorescent proteins by Ovejero and colleagues work.[23]

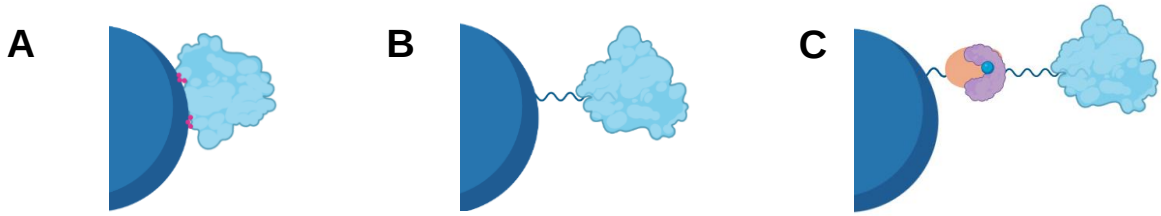

Figure 51: Scheme of the different immobilization approaches.

***A**. Immobilization through the histidine clusters (close distance to the MNP surface). **B.** Immobilization though the histidine tag (Intermediate distance to the MNP surface). **C.** Immobilization through the system cohesin-dockerin (large distance to the MNP surface).*

5.2 Materials & methods

5.2.1 Chemicals

The MNPs were kindly provide by the laboratory of Bionanosuf from the Instituto de Nanociencia y Materiales de Aragón (INMA). Tris-HCl base buffer and imidazole were purchased from Thermo Scientific (Waltham, MA, USA), Ethanol and thrombin from bovine plasma were purchased from Sigma-Aldrich (St. Louis, IL, USA). Bradford protein assay dye reagent were purchased from BIORAD (Biorad. Hercules, CA, USA) and Nicotinamide adenine dinucleotide sodium salt (NAD^+) were acquired from Gerbu Biotechnik GmbH (Wieblingen, Germany).

5.2.2 Immobilization on MNPs and characterization

The immobilization screenings were carried out in 1.5 mL Eppendorf tubes where 80 µg of MNPs and 50 µg of the corresponding enzyme was added in 25 mM of Tris-HCl buffer at pH 7 with a final volume of 200 µL. The suspension was incubated under continuous stirring at room temperature for 1 hour. Then, the solution was centrifuged at 15000 rpm for 1 hour at 4 ºC, after that, the 195 µL of the suspension was collected carefully into a new Eppendorf tube (S1 sample) for further quantification with the help of a magnet, to avoid that the MNPs leave the solution. The MNPs were resuspended with 195 µL of fresh buffer and centrifuged again for another 45 min at 15000 rpm and 4 ºC. After the solution was removed from the MNPs to remove all the unattached protein from the MNPs. The final MNPs were resuspended in 200 µL of fresh buffer and stored at 4 ºC.

The cohesin-dockerin system immobilization process was carried out in two steps. The first one, the His-D immobilization, was performed following the protocol describe above but using in the wash step Tris-HCl buffer at pH7 with 1 mM of $CaCl_2$ to allow the further interaction between the dockerin and cohesin domains. Instead of a final fresh buffer solution, the MNPs where resuspended in 200 µL of a soluble extract of C-ADH doped with 1 mM of $CaCl_2$ in Tris-HCl buffer at pH7. The mix was incubated under continuous stirring at room temperature for 1 hour and two steps of centrifugation described above were carried out. As a negative control the variant C-ADH was immobilized into MNPs that were not previously activated with the counterpart His-D.

The same process was carried out for the optimization process using instead 100 µg of MNPs and 100 µg of the BsADH-WT and BsADH-H3. In the case of the immobilization through cohesin-dockerin system the optimization was performed using 1.5 mg of His-D. The dockerin blocking was performed by the previous incubation of 1.5 mL of the C-ADH soluble extract with 0.5 µL of dockerin protein that has been removed the histidine-tag previously

(see section 4.2.8) during 15 min under continuous stirring at room temperature before been added to the activated MNPs with the His-D.

The immobilization characterization was performed by colorimetric assay, monitoring the conversion of NAD^+ to NADH at 340 nm as was described in previous chapters (section 4.2.9). In the case of C-ADH, Braford assay was used as quantification method to determine the immobilization yield of C-ADH.

5.2.3 Optimal temperature calculation

The graphic to obtain the optimal temperature was performed using a 1/3 diluted suspension of the MNPs with the corresponding enzyme variants. 2.5 µL of suspension were introduced to 200 µL PCR Eppendorf tubes and 100 µL of reaction mix added and quickly incubated for 5 min at different temperatures from 40 ºC to 98 ºC. After 5 min, 75 µL of the suspension were added to a 96 well plates and the final absorbance was measured at 340 nm.

5.2.4 Calculation of Arrhenius plot and the activation energy (Ea)

Below the optimal temperature, the temperature dependence of the catalytic rate follows the Arrhenius law. Thus, we can calculate the activation energy (Ea) of the nano-biocatalysts following Eq (13) and use a liner fitting of the experiment data.

5.2.5 Application of alternating magnetic field (AFM) experiments

For the AFM experiments, in1.5 mL Eppendorf tubes 480 µL of reaction mix was introduced followed by the addition of 20 µL of MNPs suspension and quickly inserted the tube under alternating magnetic field to produce hyperthermia. The AFM exposed were: AFM1: 146.05 Hz, AFM2: 309.50 Hz; AFM3: 772.65 Hz and 30 mT for 5 min. After that 200 µL of the suspension was added to a 96 well plate and the final absorbance measured at 340 nm.

5.3 Results & Discussion

This final experimental chapter looks to evaluate if the previous results obtained in Chapters 3 and 4 about the spatial location control and orientation control, respectively, using microscale solid carriers, can be extrapolated at the nanoscale level using MNPs.

5.3.1 Toolbox of magnetic nanoparticles (MNPs)

A toolbox of different MNPs from our collaborators in the Institute of nanoscience and materials of Aragon were employed in this work. The different MNPs were synthetized using the procedure described by Ovejero and colleagues.[23] The set of MNPs employed contain an iron oxide core (represented in grey, Figure 52) with sizes between 12 to 32 nm. The core was coated with different polymers and organic compounds. Finally, the MNP surface was engineered with divalent cobalt-nitrile acetic acid (Co^{2+}-NTA) to allow selective binding of histidine enriched proteins.

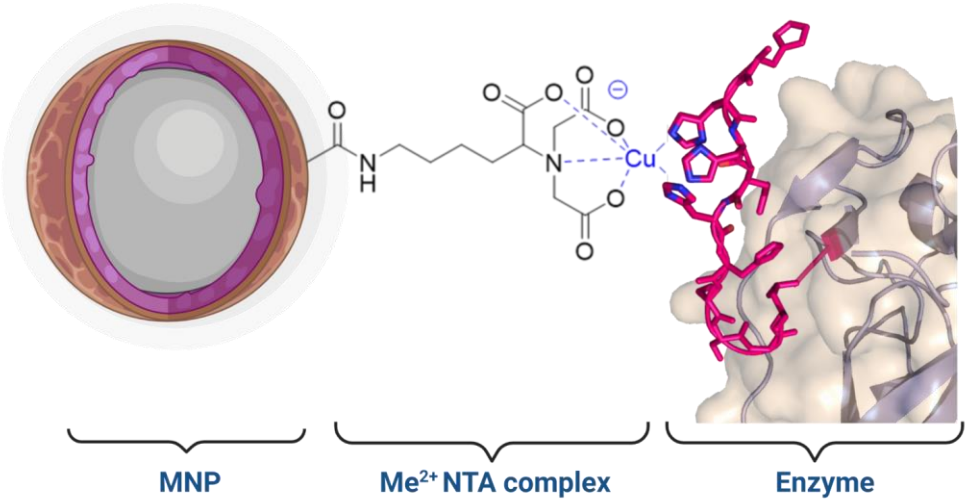

Figure 52: General scheme of the MNPs and their specific interaction with the enriched histidine proteins.

The MNPs synthesis process and their features are described in the Table 20.

Table 20: Toolbox of magnetic nanoparticles (MNPs).

MNP	Size (nm)	Z-pot (mV)	Functional Group	Features
CSIC-16	12	21	OH	Co-precipitation synthesis, -Co(OH) coating 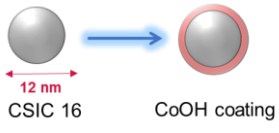

CSIC-19	32	17	OH	Oxidative precipitation synthesis, -Co(OH) coating	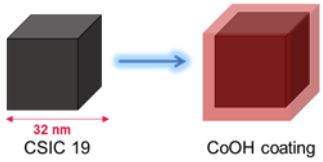
CSIC-23	15	-28	COOH/NTA	Thermal decomposition synthesis, coated with oleic acid.	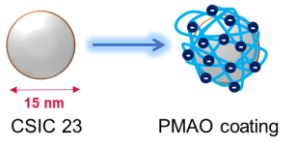
CSIC-25	15	-27	COOH/NTA	Thermal decomposition synthesis, coated with oleic acid. Doped with Mn^{2+}.	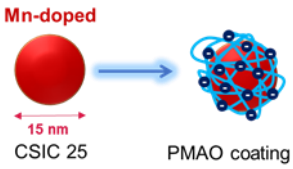

The metal chelate for all the MNPs is Co^{2+}. PMAO: Poly(malic anhydride-alt-1-actadecene)

5.3.2 Immobilization screening of the different magnetic nanoparticles (MNPs)

The first immobilization screening of MNPs were performed using the BsADH enzyme as a model. The histidine variants employed were the WT with histidine tag, WT previously removed the histidine tag (BsADH-WT-untagged) and the cluster variants developed in Chapter 4. The immobilization efficiencies and specific activities of the immobilized enzymes were followed through colorimetric assays described previously for the BsADH and the data obtained from the screening is shown in theTable 21.

Table 21: Immobilization screening of the different MNPs.

Variant	MNP carrier	Ψ (%) Immobilization	Protein immobilized (mg/mL)	Immobilized enzyme activity (U/mL)	U/mg $_{protein}$ immobilized
BsADH-WT	CSIC-16	74.9 ± 2.3	0.19	1.31 ± 0.01	6.99 ± 0.08
	CSIC-19	76.8 ± 2.9	0.19	0.94 ± 0.12	4.92 ± 0.65
	CSIC-23	82.4 ± 0.4	0.21	0.40 ± 0.02	1.96 ± 0.11
BsADH-H3	CSIC-16	79.4 ± 1.7	0.20	1.82 ± 0.04	9.16± 0.21
	CSIC-19	64.2 ± 19.1	0.16	0.93 ± 0.09	5.76± 0.56
	CSIC-23	11.7 ± 16.6	0.03	0.00 ± 0.00	0.00 ± 0.00
BsADH-H4	CSIC-16	77.7 ± 1.6	0.19	1.56 ± 0.02	8.04 ± 0.10
	CSIC-19	37.9 ± 14.2	0.10	2.39 ± 0.54	25.19 ± 5.46
	CSIC-23	0.0 ± 0.0	0.00	0.00 ± 0.00	0.00 ± 0.00
BsADH-WT untagged	CSIC-16	70.8 ± 15.3	0.18	0.00 ± 0.01	5.49 ± 0.35
	CSIC-19	26.1 ± 1.2	0.07	0.58 ± 0.09	8.83 ± 1.39
	CSIC-23	1.7 ± 0.7	0.004	0.00 ± 0.00	0.00 ± 0.00

The initial Ae_s for the different variants are: BsADH-WT: 5.6 U x mg^{-1}; BsADH-H3: 16 U x mg^{-1}; BsADH-H4: 10.2 U x mg^{-1}; BsADH-WT untagged: 8.5 U x mg^{-1}. The protein offered was 0.63 g of protein per g of NPs.

As we expected, there is possible immobilization of BsADH-WT into the MNPs using the collaborative coordination binding of the histidine-tag and the chelate divalent metals. However, not all the MNPs allow a specific immobilization through this site-specific interaction. The BsADH-WT untagged used as negative control shows that CSIC-16 is not a good carrier for a site-specific immobilization despite it showing good immobilization yields for all the variants. The immobilization screenings were also followed by SDS-page electrophoreses, the gels confirm the un-specific binding of the WT-untagged on CSIC-16 (Figure 53, A). For the same reason, CSIC-19 is not the best nanocarrier to control the site-specific immobilization.

Nevertheless, somehow these MNPs have some specificity, and it is a driving force for some interactions that we don't yet understand. The differences in the immobilization yield for the tagged protein is 3 times higher than the untagged one. Nonetheless the specific activity recovered is almost 2 times higher for the untagged enzyme. In the case of the histidine cluster variants, the immobilization yield is different from the BsADH-WT or the untagged with the higher recovered activity with the BsADH-H4 variant. The nanocarrier CSIC-23 seems to be the most specific carrier tested, however only the BsADH-WT can immobilize with good yields and recovery activity. It should be mentioned that in the immobilization process the quantification of the amount of protein is complex due to the low amount of protein in the experiment as in the immobilization protocol (section 5.2.2). Here the MNPs are separated from solution by centrifugation which causes some MNPs to be lost in the supernatants, affecting the data obtained for the immobilization yield. This is one of the issues reported in the literature when NPs are used as a nanocarrier.[13]

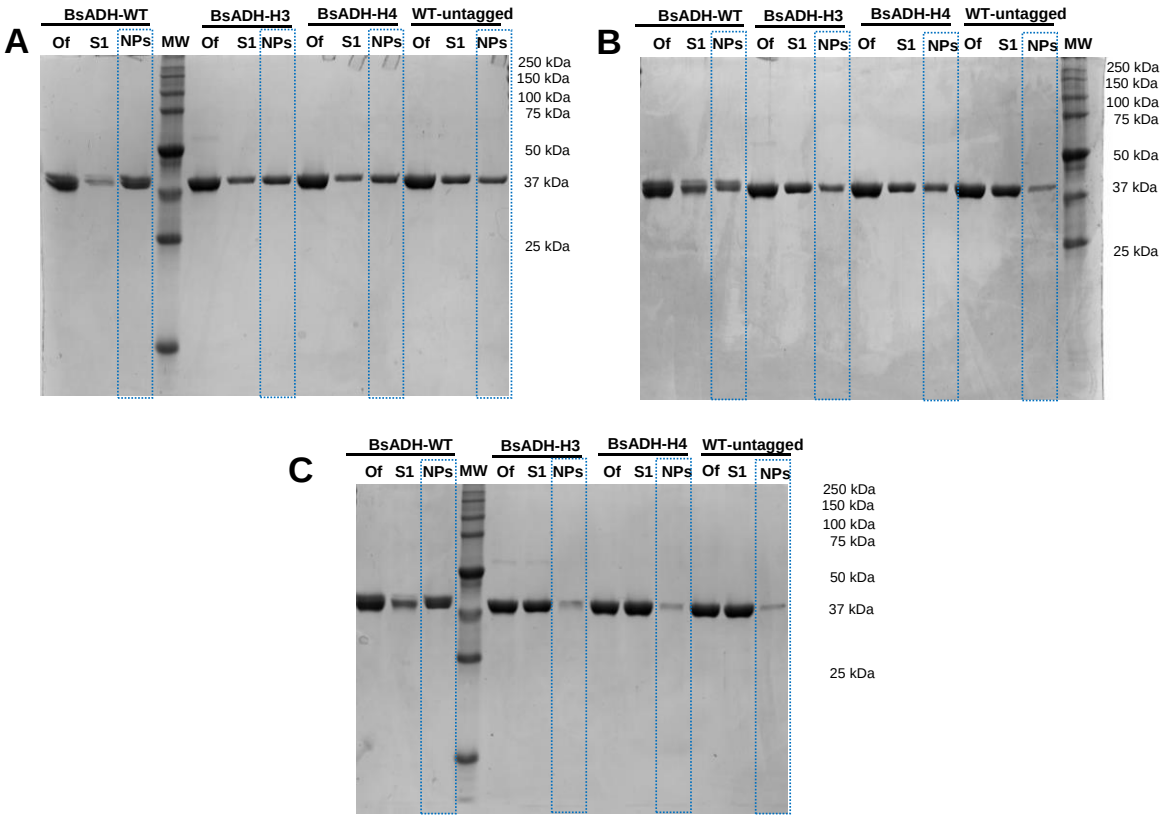

Figure 53: SDS-Page electrophoresis of immobilization on MNPs.

Immobilization of the different BsADH histidine variants on MNPs. ***A.*** *CSIC-16.* ***B.*** *CSIC-19.* ***C.*** *CSIC-23.* ***OF****: Protein offered;* ***S1:*** *Supernatant 1 after immobilization (protein non-binding to the MNPs); and* ***NPs:*** *Protein immobilized in the MNPs.*

To confirm the unspecific binding of the BsADH enzyme to the MNPs and to clarify if the binding could be through the native histidines present in the enzyme, the MNPs with untagged BsADH-WT were used. The different MNPs with untagged BsADH-WT were incubated with 0.5 M of imidazole with and without ionic strength. The results showed in Figure 54 confirm on one hand that the untagged protein is not able to attach onto the MNPs CSIC-23 activated with cobalt. However, in the cases of CSIC-16 and CSIC-19 (E1 or E2, Figure 54), the untagged protein is able to attach onto the MNPs but the results suggest that the immobilization is not through the native histidines. This is because the proteins were unable to be eluted from the MNPs with a high concentration of imidazole. Furthermore, the binding of the protein to the MNPs could be through electrostatic interactions as MNPs CSIC-16 and CSIC-19 have a positive Z-potential (Table 20) meaning that the particle are positively charged and it is already known that proteins are absorbed to positively charged surfaces. [33]

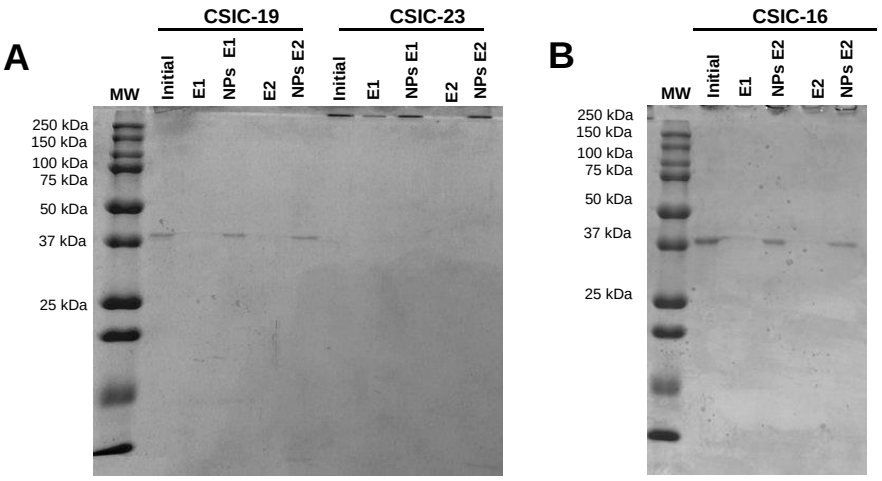

Figure 54: Study of the immobilization binding of BsADH-WT untagged into the MNPs.

A. *Immobilized on CSIC-19 and CSIC-23.* ***B.*** *Immobilized on CSIC-16.* ***Initial:*** *MNPs after the immobilization.* ***E1:*** *Eluted fraction after incubation with 0.5 M of imidazole and 50 mM of NaCl in 25 mM of Tris-HCl buffer at pH 7;* ***NPs E1:*** *MNPs after the incubation with 0.5 M of imidazole and 50 mM of NaCl in 25 mM of Tris-HCl buffer at pH 7;* ***E2****: Eluted fraction after incubation with 0.5 M of imidazole;* ***NPs E2:*** *MNPs after the incubation with 0.5 M of imidazole and 50 mM of NaCl in 25 mM of Tris-HCl buffer at pH 7.*

As described in the introduction of this chapter, colloidal stability is an important parameter when MNPs are used as nanocarriers. In our case after the immobilization process there is no aggregation observed in MNPs CSIC-16 and CSIC-19. However, for MNPs CSIC-23, aggregation issues were observed for the histidine tag variant (Figure 55, C). This phenomenon could happen as BsADH is a tetrameric enzyme, meaning it has four histidine tags per functional enzyme. We hypothesize that if the nanocarrier surface is not completely covered by the BsADH enzyme, some of the free divalent metals of the other nanoparticle could attach one of the other three histidine tags of an enzyme already immobilized in other MNPs (Figure 56).

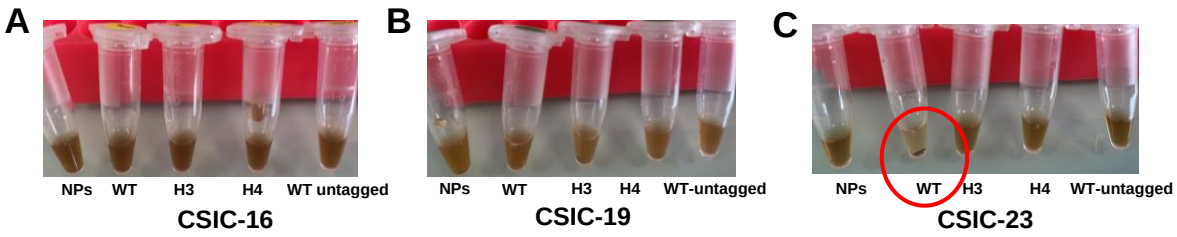

Figure 55: Colloidal stability of the MNPs after immobilization.

A. *MNPs CSIC-16.* ***B.*** *MNPs CSIC-19. And* ***C.*** *MNPs CSIC-23*

So, the results shows that CSIC-16 is not a specific nanocarrier and CSIC-19 has some specificity but is not driven by the enriched histidine moieties. Thus, these were discarded for further experiments. The MNP CSIC-23 allows a site-specific immobilization, with good yields in the case of the histidine tag, but poor colloidal stability and finally with the histidine clusters the immobilization yields are low.

5.3.3 Optimization of the enzyme immobilization

The MNP CSIC-23 was the best nanocarrier due to its specificity for collaborative coordination binding. To try increase the immobilization yield of the histidine cluster BsaDH-H3 and improve the colloidal stability, the loading protein were increased to 1 g of protein per gram of NPs. This loading increase should allow the MNPs to be more saturated with protein and avoid the intraparticle interaction (Figure 56), specifically for the BsADH-WT. Also, a same type of nanocarrier, CSIC-25, was tested. This new MNP has the same synthesis process, size and functionalization as the CSIC-23 MNP, with the difference that CSIC-25 has been dopped with Mn^{2+} in the core, which changes the magnetic properties of the nanoparticle.

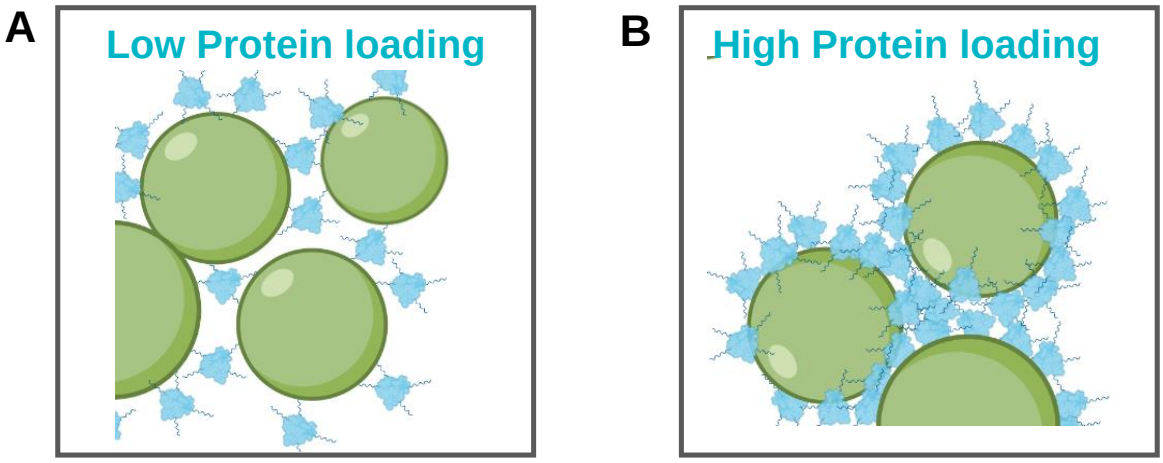

Figure 56: Colloidal stability issues due to the protein loading.

A. *Low protein loading produce aggregation of the MNPs due to the capability of intra-particle binding through the histidine-tag.* ***B.*** *High protein loading, there are not MNPs aggregated due to all the MNP surface is already saturated with the protein.*

This optimization binding process was performed with different orientations and distances, using the BsADH-WT variant oriented through the histidine tag and the BsADH-H3 variant oriented through the histidine cluster. Also, to have a similar orientation as the histidine tag variant but with a longer distance, we test the construction His-Doc/C-ADH that has been developed in Chapter 2. Here, we have a shorter distance, through the histidine clusters (BsADH-H3), intermediate distance through the histidine tag (BsADH-WT) and a longer

distance through the cohesin-dockerin interaction (His-D/C-ADH). The scheme of the different approaches is shown in Figure 51. The immobilization parameters for these variants are shown in Table 22.

Table 22: Immobilization parameters for BsADH variants in MNPs CSIC-23 and CSIC-25

Variant	MNP carrier	Ψ (%) Immobilization	Immobilized protein (mg/mL)	Activity immobilized enzyme (U/mL)	$U/mg_{protein}$ immobilized
BsADH-WT	CSIC-23	94.9 ± 0.5	0.47	1.97 ± 0.07	4.15 ± 0.15
	CSIC-25	98.5 ± 0.0	0.49	1.75 ± 0.03	3.55 ± 0.07
BsADH-H3	CSIC-23	35.4 ± 3.6	0.18	0.066 ± 0.004	0.40 ± 0.03
	CSIC-25	15.5 ± 4.8	0.08	0.125 ± 0.005	1.69 ± 0.07
His-D	CSIC-23	34.7 ± 3.2	0.17	-	-
	CSIC-25	45.2 ± 3.4	0.23	-	-
C-ADH	CSIC-23	0.0 ± 0.0	0.00	0.01 ± 0.004	-
	CSIC-25	0.0 ± 0.0	0.00	0.01 ± 0.002	-
	CSIC-23_His-D	33.3 ± 0.58	-	0.09 ± 0.015	-
	CSIC-25_His-D	34.8 ± 5.1	-	0.11 ± 0.008	-

The initial activity for the soluble fraction of C-ADH was 0.35 ± 0.018 U x mL^{-1}. The His-D protein offered was 1 g of protein per g of NPs.

The results again show a high immobilization yield for the histidine tag variant, where the immobilization yield increases slightly with the doped MNP, but the specific activity shown is lower. In the case of the histidine cluster variant, the immobilization yield improves up to 3 times when the offered protein is increased. In this case, the doped MNP CSIC-25 seems be less efficient in immobilization, but it can recover higher specific activity than the CSIC-23. In the case of cohesin-dockerin systems, the His-dockerin protein (His-D) loaded was 1 g per g of MNPs, we saw that only 35 % of the protein offered was able to immobilize in the case of CSIC-23 and nearly 45 % of the protein for the doped nanocarrier. However, the amount of cohesin-ADH (C-ADH) immobilized on both MNPs was almost the same, but with higher recovery activity in the doped MNP. Also, when this variant is offered to the initial MNPs (without His-D) there is no unspecific protein immobilization (Figure 57, C).

The immobilization process has been followed by denaturant electrophoresis. This process, allows confirmation of immobilization of different variant to the MNPs, and also confirmation of immobilization though collaborative binding of the histidine enriched moieties in the case of the histidine tag variant and the cluster of histidines (Figure 57 A and B). After immobilization the MNPs where incubated with imidazole to elute the protein, however the interaction of the BsADH is strong and there it was not possible to elute all of the

immobilized protein. The strength of the binding seems to be higher in the case of the cluster of histidines than when it binds through the histidine tag, especially for CSIC-23. The immobilization using the cohesin-dockerin system shows the specificity of the binding though cohesin-dockerin interaction as it was previously described in the Chapter 3. The electrophoresis gel also shows the strength of this interaction, as even under denaturant conditions, it was not possible to remove the protein anchored to the nanocarrier surface. The line corresponding to the His-D/C-ADH binding on both MNPs shows only a small band corresponding to the C-ADH protein. However, none of the bands corresponded to the previous immobilized His-D protein.

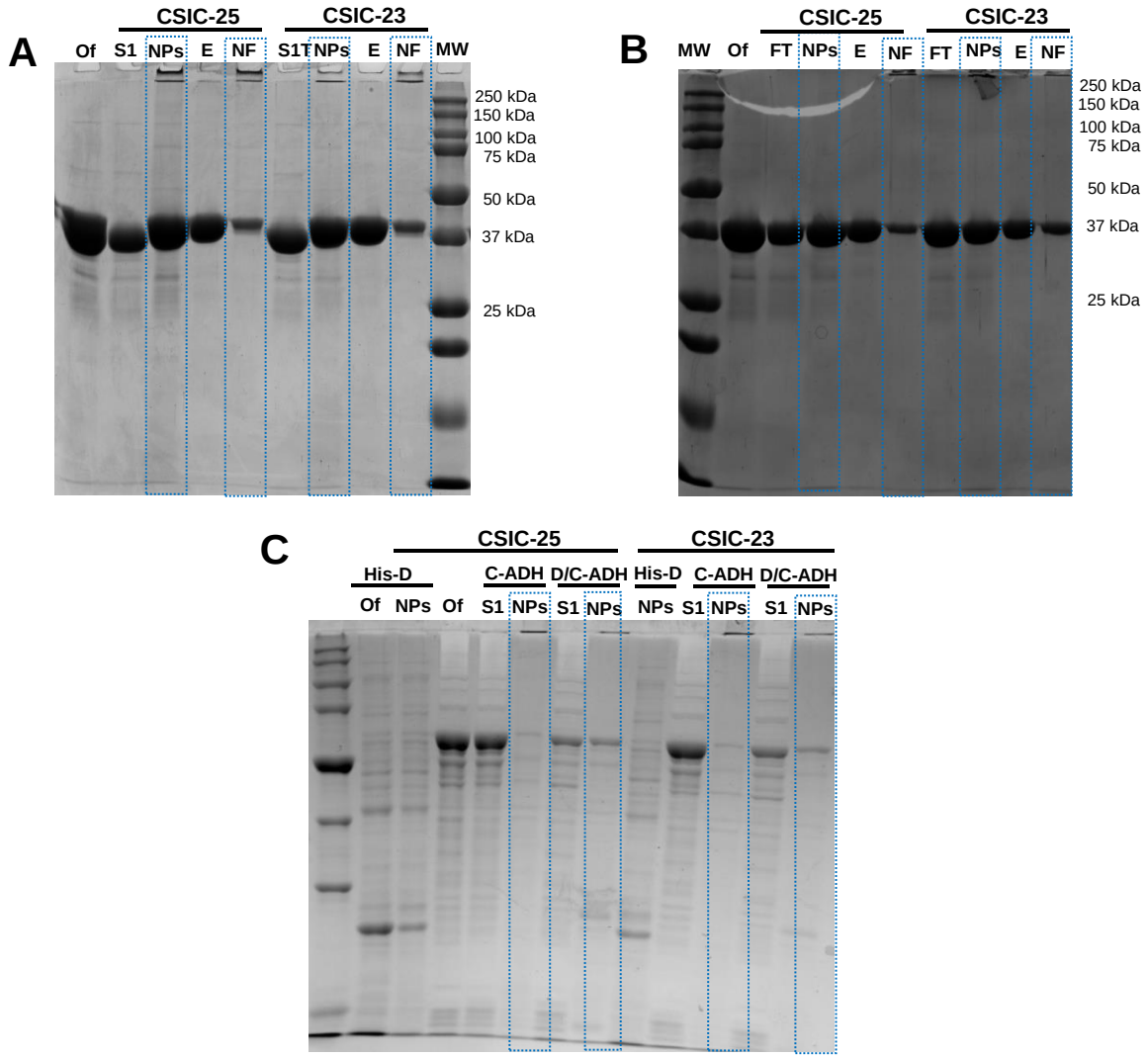

Figure 57: SDS-Page electrophoresis of the BsADH immobilization on MNPs CSIC-23 and CSIC25 with different approaches

A. *Immobilization of BsADH through the histidine tag.* ***B.*** *Immobilization though the histidine clusters.* ***C.*** *Immobilization through the cohesin-dockerin system.* ***OF****: Protein offered;* ***S1:*** *Supernatant 1 after immobilization (protein non-binding to the MNPs); and* ***NPs:*** *Protein*

immobilized in the MNPs. ***E:*** *Eluted fraction after incubation with 0.5 M of imidazole in 25 mM of Tris-HCl buffer at pH 7;* ***NF:*** *MNPs after the incubation with 0.5 M of in 25 mM of Tris-HCl buffer at pH 7.* ***His-D:*** *His-Dockerin protein offered to initial MNPs;* ***C-ADH:*** *immobilization process using the initial MNPs and offered the soluble fraction of C-ADH (Cohesin-ADH);* ***D/C-ADH****: Immobilization process using the MNPs previously activated with His-D and offered the soluble fraction of C-ADH.*

Finally, the colloidal stability after immobilization shows that increasing the loaded protein helps increase the colloidal stability (Figure 58 A). The histidine tag variant shows a better stability (darker brown colour in the MNP suspension with respect to Figure 55 C) when the protein loaded is 1 g of protein. However, in the case of C-ADH, it was not possible to completely control the amount of protein offered as it comes from a soluble fraction. Cross linking of the MNPs could be an explanation for this phenomenon as again the C-ADH variant has four cohesin domains that are able to attach to the dockerin domains of the other MNP.

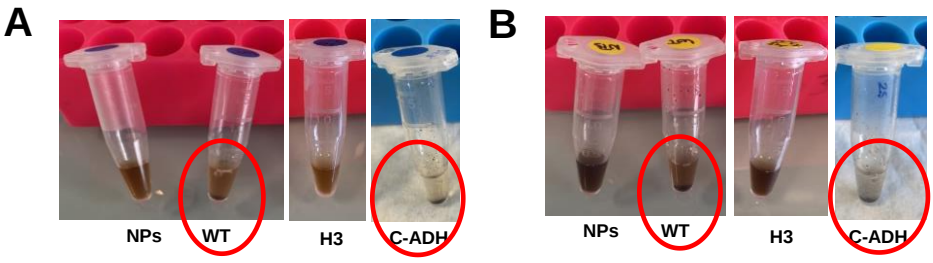

Figure 58: Colloidal stability of the immobilization on MNPs CSIC-23 and CSIC-25.

A. *BsADH variants immobilized on MNPs CSIC-23.* ***B.*** *MNPs CSIC-25*

As the increase in the protein loading woks for the histidine tag variant, we decided to increase the protein offered in the first step of MNP activation with His-D. Additionally, another alternative was tested, protecting the cohesin domains in the C-ADH protein with a previous incubation of this variant with a low and non-stoichiometric concentration of dockerin protein with the histidine tag removed as was previously described (section 4.2.8). The cohesin blocking could help to increase the colloidal stability of the MNPs (Figure 59).

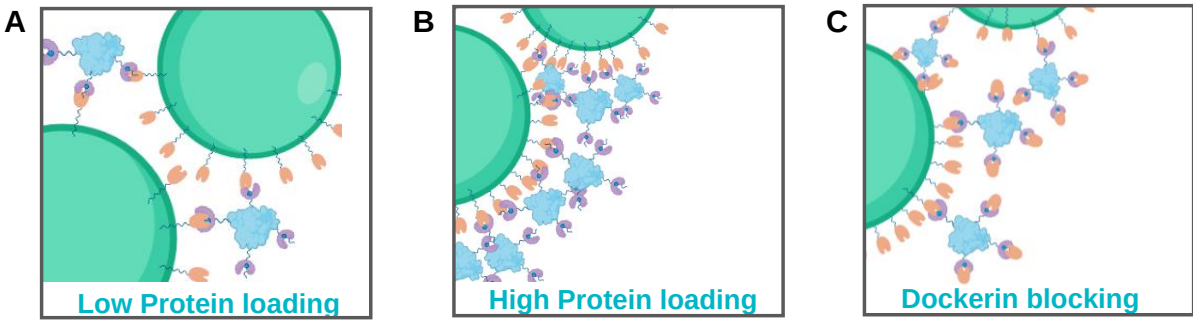

Figure 59: Improving the colloidal stability of the MNPs immobilized with BsADH through the cohesin-dockerin system.

A. *Low protein loading into the cohesin-dockerin system could cause cross-linking of the cohesin domains of the C-ADH and the free His-D on the MNPs.* ***B.*** *High protein loading could avoid the cross-linking, with protein saturation.* ***C.*** *The dockerin blocking could prevent interaction between the already immobilized cohesin in the C-ADH and the His-D of the other MNPs.*

Thus, the results obtained in the colloidal stability tests show that increase in the protein loading increases colloidal stability. Additionally, when the C-ADH protein is previously incubated with a small amount of dockerin the colloidal stability is higher as shown in the Figure 60.

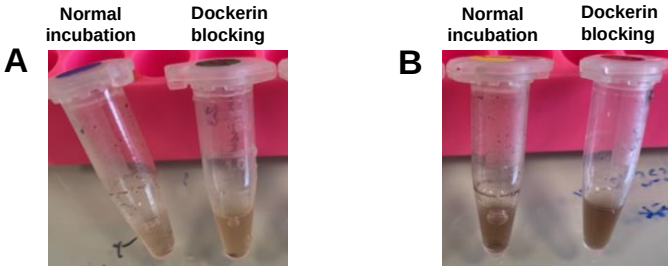

Figure 60: Colloidal stability with and without dockerin blocking on C-ADH immobilization on MNPs.

A. *C-ADH with and without dockerin blocking immobilization on MNPs CSIC-23.* ***B.*** *C-ADH with and without dockerin blocking immobilization on MNPs CSIC-25.*

The immobilization parameters with this optimization are shown in Table 23. In this case the Bradford assay was used to calculate the amount of C-ADH immobilized. The increase in quantity of His-D increases slightly the yield of immobilization. The increase seems to be helpful in the case of colloidal stability and also increases the yield of the C-ADH immobilization on MNPs CSIC-25 by 1.35 times.

Table 23: Immobilization of C-ADH with and without dockerin protection on MNPs.

Variant	MNP carrier	$\Psi_{protein}$ (%) Immobilization	Immobilized protein (mg/mL)	Activity immobilized enzyme (U/mL)	$U/mg_{protein}$ immobilized
His-D	CSIC-23	38.0 ± 0.4	0.57	-	-
	CSIC-25	54.9 ± 1.1	0.82	-	-
C-ADH	CSIC-23	32.2 ± 0.2	0.21	0.11 ± 0.01	0.52 ± 0.04
	CSIC-25	47.1 ± 4.2	0.31	0.27 ± 0.07	0.88 ± 0.23
	CSIC-23_His-D	5.0 ± 1.6	0.028	0.18 ± 0.02	6.33 ± 0.76
	CSIC-25_His-D	6.0 ± 1.6	0.034	0.19 ± 0.02	5.73 ± 0.60

The initial amount of the offered C-ADH was 0.66 mg x mL^{-1} and the concentration of the C-ADH for the dockerin blocking was 0.57 mg x mL^{-1}

The dockerin blocking strategy performed the worst in terms of quantity of enzyme immobilized as is observed in Figure 61 B. However, even with the low quantity of immobilized protein, the recovered activity on the MNPs using the dockerin blocking strategy was 1.6 times higher in the case of CSIC-23 and 0.7 times less in the case of CSIC-25, compared with immobilization without dockerin blocking (Table 23). Additionally, the specific activity immobilized of the samples using dockerin blocking are higher than the activities obtained for those using the BsADH-WT approach (Table 22). This hyperactivation of the enzyme when it is assembled through the cohesin-dockerin system but avoiding multi-attachment of the enzyme may produce a highly favourable orientation for the enzymatic reaction.

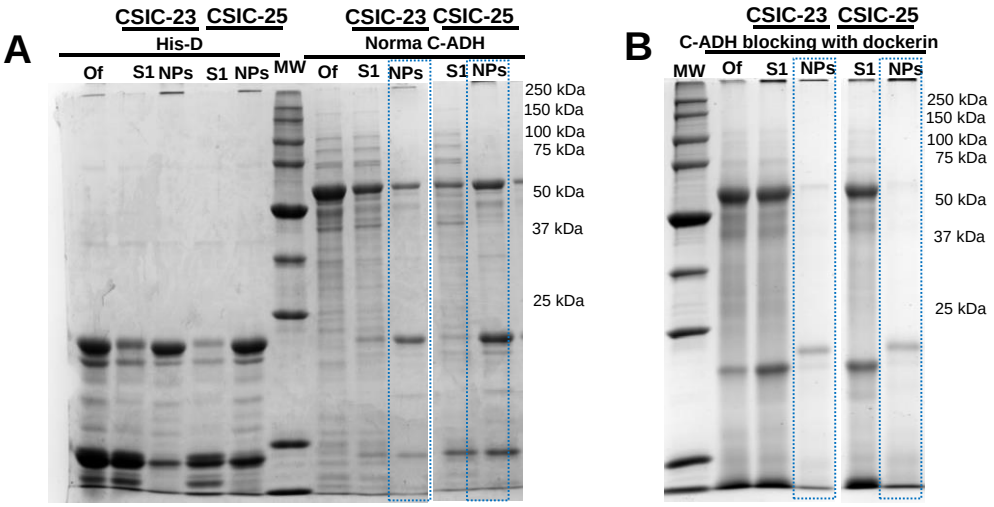

Figure 61: SDS-Page electrophoresis gel of the C-ADH immobilization with and without dockerin protection.

A. *Immobilization of the His-D protein into MNPs CSIC-23 and CSIC-25 using 1.5 g of protein and immobilization of C-ADH from the soluble crude extract immobilized into MNPs previously activated with His-D.* ***B.*** *Immobilization of C-ADH incubated with dockerin previously for 15 min and immobilized on MNPs CSCI-23 and CSIC-25.*

In summary, the capability of immobilizing the same enzyme, with different orientation and distance, has been demonstrated using two MNPs. The best candidate for both immobilization and activity is the histidine tag variant as we were able to immobilize high amount of protein and also recover high activity after the immobilization. The orientation though the histidine cluster despite immobilizing 6 times less protein, the recovered activity is only 2 times lower, which means that the enzyme is more active through this orientation than the BsADH-WT. The saturation of the MNPs with the proteins is helpful to increase the colloidal stability in both cases using the BsADH-WT or the cohesin-dockerin system. Dockerin blocking could be also used as an alternative to avoid the aggregation issues as even with a low amount of protein, the recovered activity could be comparable to the normal approach. To understand how the distance and orientation could affect the enzyme, we studied the optimal temperature of the different nano-biocatalysts: BsADH-WT, BsADH-H3 and the His-D/C-ADH with the dockerin blocking.

5.3.4 Optimal temperature measurements

The nano-biocatalyst on the MNPs were incubated at different temperatures, from 40 ºC to 100 ºC and the activity was measured by monitoring the conversion of NAD^+ to NADH after 5 min of incubation at 340 nm. The graphics obtained from the experiments are shown in the Figure 62.

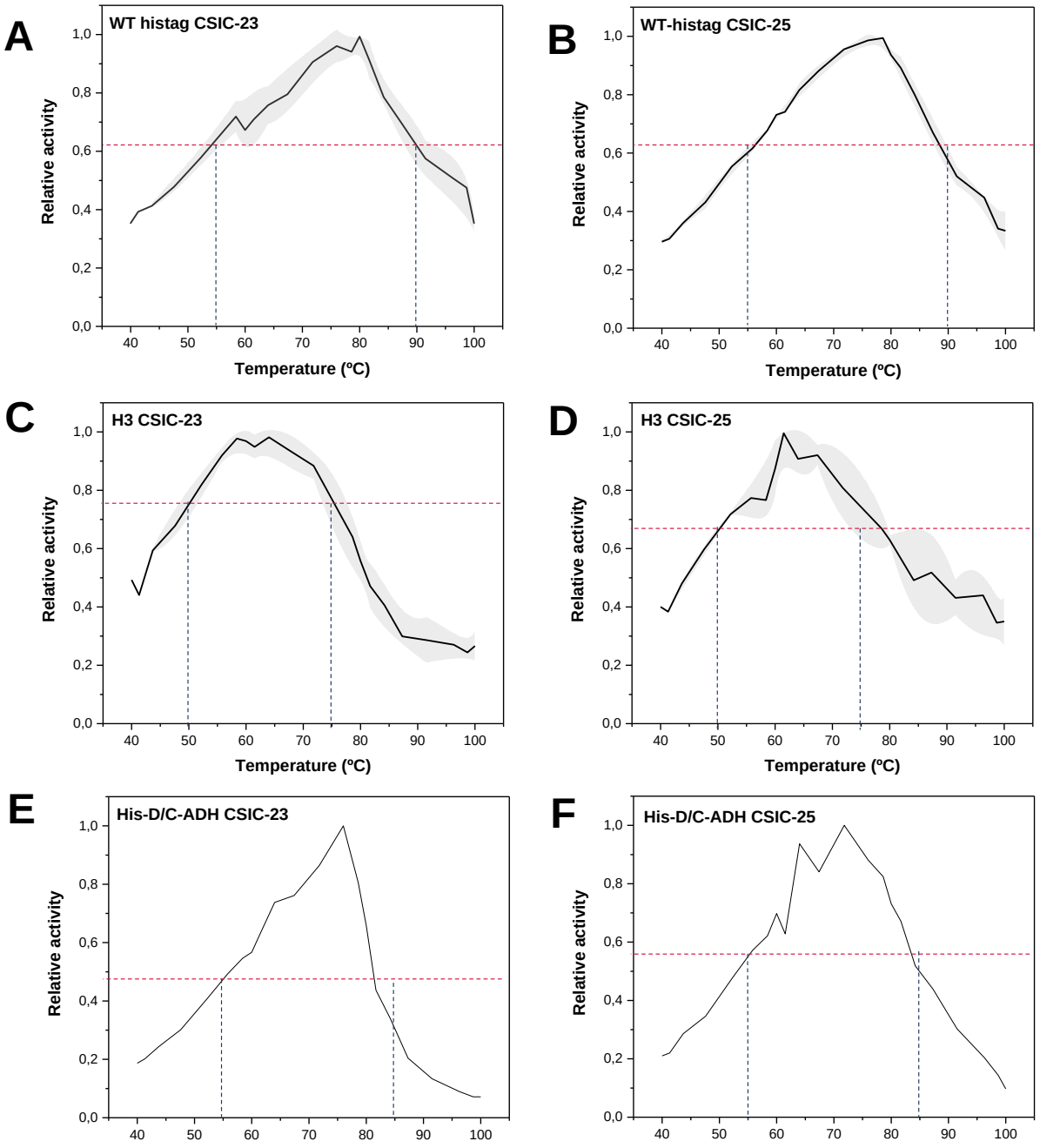

Figure 62: Optimal temperature curves of the BsADH variants immobilized onto MNPs.

A. *Relative activity of the histidine tag variant immobilized on CSIC-23.* ***B.*** *Relative activity of the histidine tag variant immobilized on CSIC-25.* ***C.*** *Relative activity of the histidine cluster variant immobilized on CSIC-23.* ***D.*** *Relative activity of the histidine cluster variant immobilized on CSIC-23.* ***E.*** *Relative activity of the cohesin-ADH variant immobilized though the cohesin-dockerin system on CSIC-23.* ***F.*** *Relative activity of the cohesin-ADH variant immobilized though the cohesin-dockerin system on CSIC-25.*

The optimal temperature for the variants in general is slightly higher when the variants are immobilized on MNPs CSIC-23. The immobilization through the histidine tag increases the

optimal temperature of BsADH to 80 ºC in the case of the MNPs CSIC-23, and 77 ºC when immobilized on MNPs CSIC-25. This increase is almost 15 ºC more than in the case of the immobilization through the histidine clusters BsADH-H3 in both MNPs (Figure 63). However, we see a small shift of 2 ºC when the enzyme is immobilized through the cohesin-dockerin system. The optimal temperature changes to 77 ºC when the enzyme is immobilized in CSIC-23 and 75 ºC when there is immobilized on CSIC-25. Also, we see that in general the optimal temperature of the immobilized enzymes is higher than its free counterpart. (70 ºC). Thus, these results suggest that the optimal temperature of the enzyme has been influenced by the orientation of the enzyme in the biocatalyst more than the distance of the enzyme to the biocatalyst.

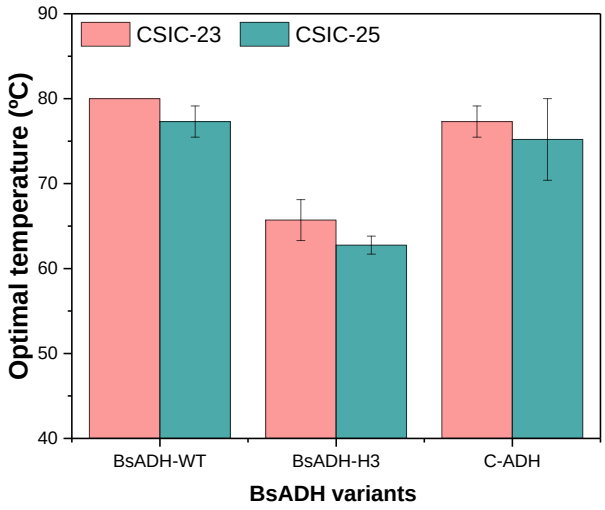

Figure 63: Optimal temperatures.

Optimal temperatures calculated from the optimal temperature curves for the different BsADH variants immobilized on MNPs CSIC-23 and CSIC-25.

After the activity curves were carried out, the Arrhenius curve were plotted following Eq (13) which helps us to calculate the activation energy (Ea) of the model enzyme under the different immobilization approaches on two MNPs. The Arrhenius plots and the Ea are shown in the Figure 64.

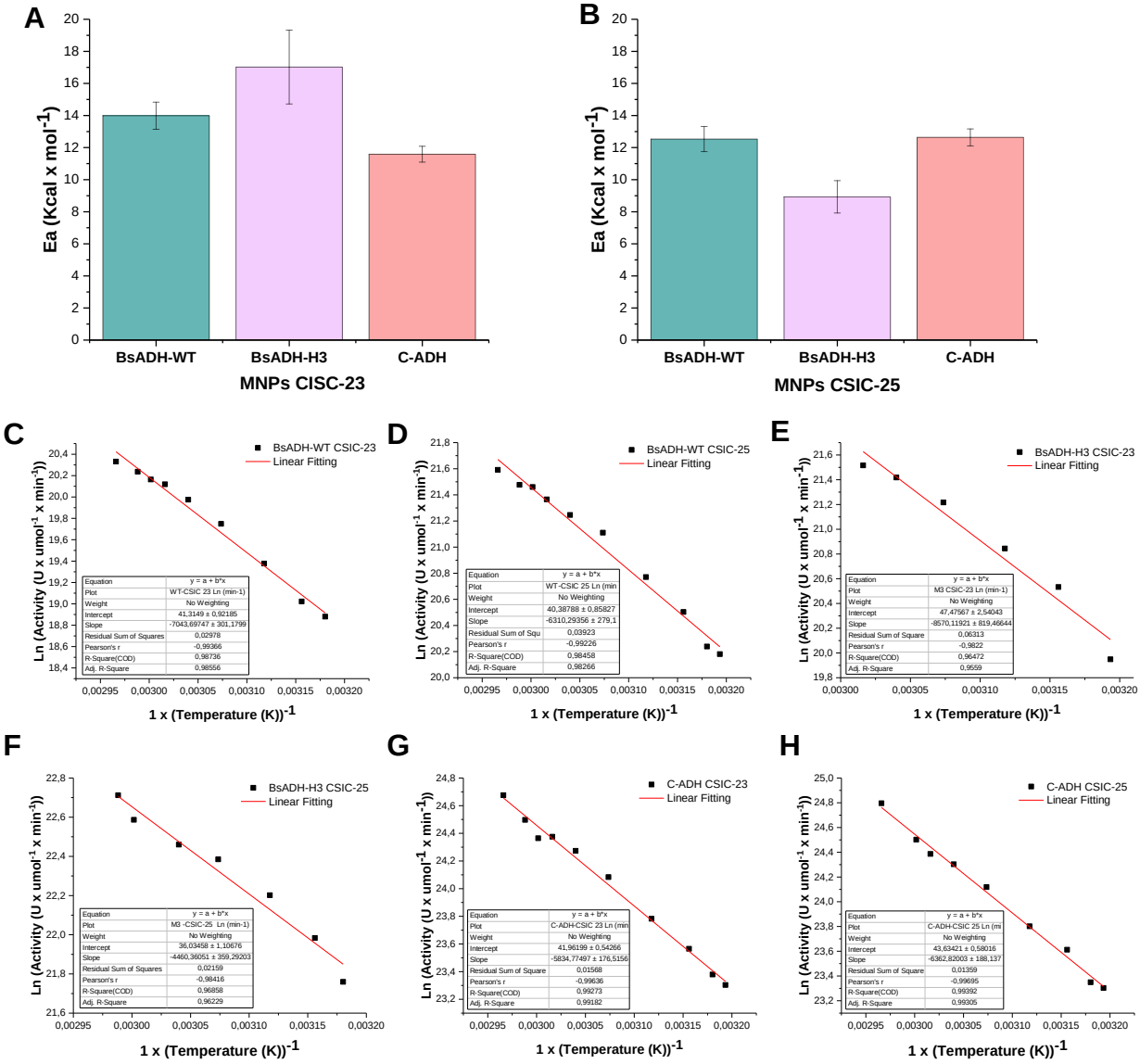

Figure 64: Activity energy (Ea) of the different immobilization approaches of the BsADH variants immobilized on two MNPs.

A. *Ea of the different nano-biocatalysts on MNPs CSIC-23.* ***B.*** *Ea of the different nano-biocatalysts on MNPs CSIC-25.* ***C.*** *Arrhenius plot fitting of BsADH-WT on CSIC-23.* ***D.*** *Arrhenius plot fitting of BsADH-WT om CSIC-25.* ***E.*** *Arrhenius plot fitting of BsADH-H3 on CSIC-23.* ***F.*** *Arrhenius plot fitting of BsADH-H3 om CSIC-25.* ***G.*** *Arrhenius plot fitting of C-ADH on CSIC-23. H. Arrhenius plot fitting of C-ADH om CSIC-25.*

As we hypothesized, the orientation plays a big factor in the thermodynamics parameters of a biocatalyst. The Ea of the enzyme oriented though the histidine cluster, BsADH-H3 shows large differences with the enzyme orientated through the histidine tag, BsADH-WT, being 0.82 times and 1.4 times higher the BsADH-WT on CSIC-23 and CSIC-25 respectively. Also, the Ea depends on the carrier where they are immobilized. Thus, the Ea of the BsADH-WT decreases as the immobilization distance increases from 17 Kcal per mol in the case of the

histidine cluster to 14 Kcal per mol in the case of histidine tag and 11.6 Kcal per mol through the cohesin-dockerin system when they are immobilized on CSIC-23. Meanwhile, in the case of CSIC-25 only the orientation plays a role in the Ea.

5.3.5 Thermal inactivation of the different BsADH variants

Taking into account the optimal temperature curves, the inactivation of the nano-biocatalyst was performed at three different temperatures: close to the T_{opt} of each variant, and two temperatures at the same relative activity value but before and after the T_{opt} (dotted lines in Figure 62).

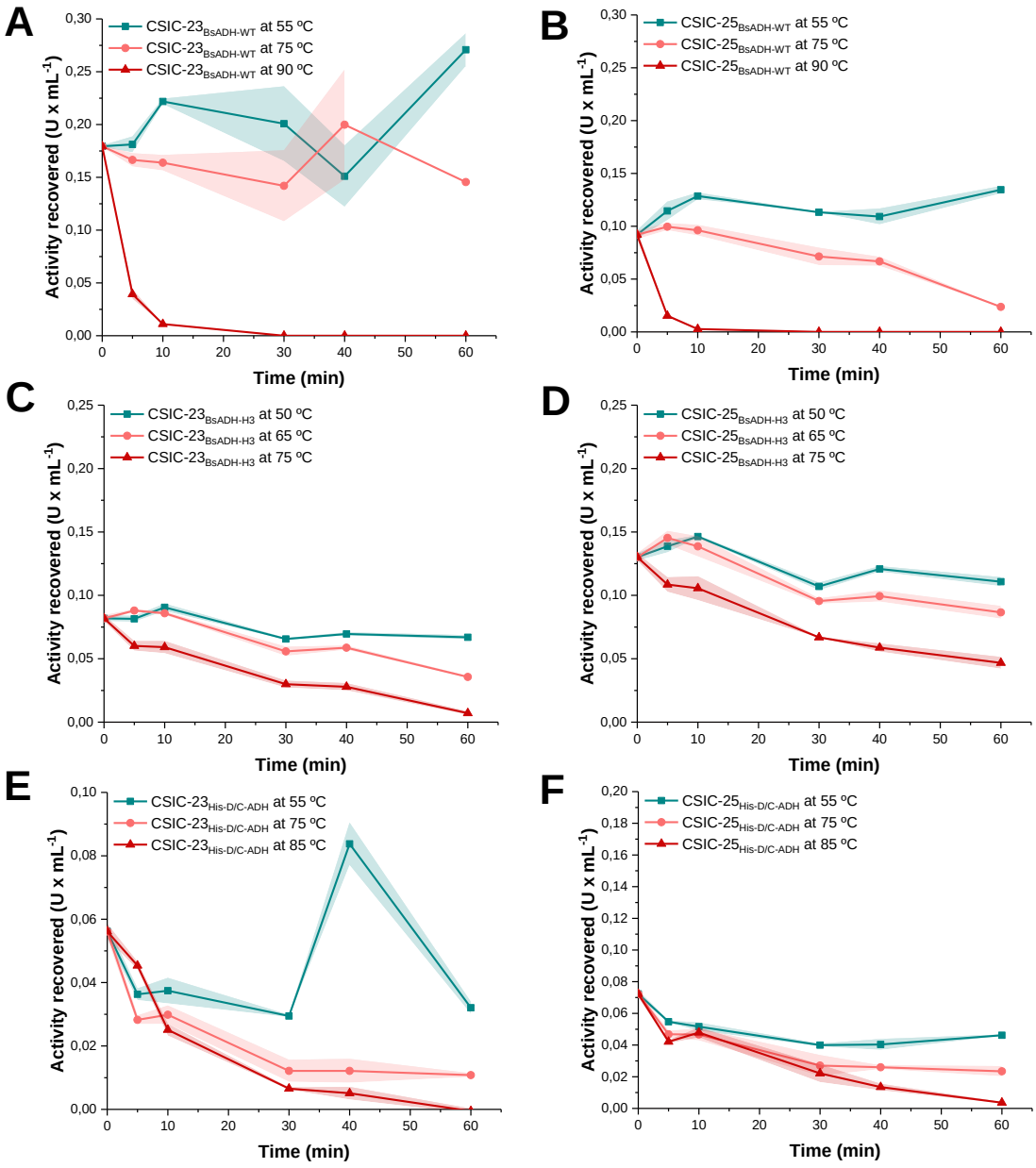

Figure 65: Thermal inactivation at three temperatures.

A. *Inactivation curves for BsADH-WT on CSIC-23* ***B.*** *Inactivation curves for BsADH-WT on CSIC-25 at 55 ºC (green line), 75 ºC (pink line) and 90 ºC (red line).* ***C.*** *Inactivation curves for BsADH-H3 variant on CSIC-23* ***D.*** *Inactivation curves for BsADH-H3 variant on CSIC-25 at 50 ºC (green line), 65 ºC (pink line) and 75 ºC (red line).* ***E.*** *Inactivation curves for His-D/C-ADH variant on CSIC-23* ***F.*** *Inactivation curves for His-D/C-ADH variant on CSIC-25 at 55 ºC (green line), 75 ºC (pink line) and 85 ºC (red line).*

As was expected the inactivation process is faster when the temperature is increased. The common temperature of inactivation for all the variants employed was 75 ºC. At this temperature, we can observe the differences between the three variants due to the orientation and the distance from the MNP. The most stable nano-biocatalyst after 30 min of inactivation was the histidine variant, BsADH-WT, which can recover almost the 80 % of its initial activity in both MNPs. However, this stability drops to almost 20 % for CSIC-23 and 40 % for CSIC-25 with the C-ADH variant., which has a larger linker and thus is further from the MNP surface. The histidine cluster orientation is also less stable against thermal inactivation than the histidine-tag orientation and recovers only 40 % of its initial activity when immobilized on CSIC-23 and 50 % on CSIC-25. (Figure 66, A). The activity of the BsADH-WT seems to increase with the temperature until 55 ºC, after that, the activity decreases abruptly with the temperature in comparison with the other variants that have gradual a decreasing (Figure 66).

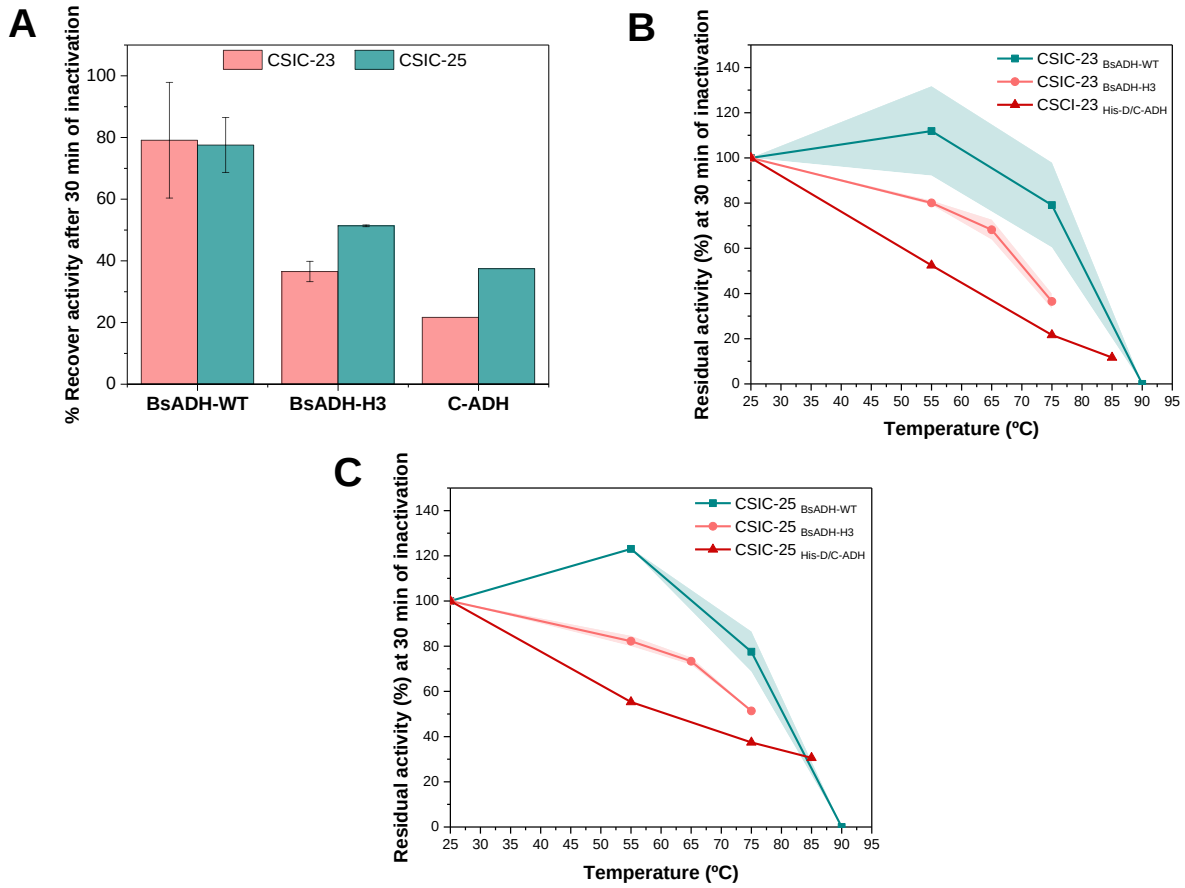

Figure 66: Thermal stability of the different approaches of immobilization after 30 min of inactivation at 75 ºC.

A. *Thermal inactivation at 75 ºC and 30 min of incubation.* ***B.*** *Thermal stability of the BsADH variants immobilized on CSIC-23 after 30 min of incubation at different temperatures.* ***C.*** *Thermal stability of the BsADH variants immobilized on CSIC-25 after 30 min of incubation at different temperatures.*

5.3.6 Inductive heating power of the MNP under alternating magnetic fields (AFM)

As was already described above, the MNPs have the capability to induce local heating by the application of alternating magnetic field. This allows regulation of enzymatic and catalytic processes without increasing the overall temperature.[22, 34] This heat depends on the MNP composite, size and shape but also the aggregation state which was described by Ovejero and colleagues.[23] As AFMs induce heating in the surface of the MNPs, we hypothesize that another important factor to take into account is the distance from the MNP surface to the enzyme. In other words, the linker used for the immobilization, due to the temperature generated at the surface of the MNP, decays rapidly a few nanometres away from the surface.

Table 24: Local temperature observed by the nano-carriers under the heating activation by the alternating magnetic field (AFM).

Variant	MNP	Frequency (Hz)	Activity (U x mL^{-1})	Temperature (°C)
BsADH-WT	CSIC-23	0	1.023 ± 0.01	35.2 ± 0.1
		146.05	0.898 ± 0.03	33.6 ± 0.4
		309.5	0.943 ± 0.08	34.2 ± 0.1
		772.65	1.055± 0.02	35.6 ± 0.2
	CSIC-25	0	1.517 ± 0.02	33.4 ± 0.2
		146.05	1.788± 0.02	32.7 ± 0.7
		309.5	1.621 ± 0.01	34.3 ± 0.1
		772.65	1.455 ± 0.06	35.8 ± 0.1
BsADH-H3	CSIC-23	0	0.312 ± 0.01	32.0± 0.2
		146.05	0.266 ± 0.01	30.3 ± 0.2
		309.5	0.299 ± 0.01	31.5 ± 0.2
		772.65	0.305± 0.01	31.8 ± 0.2
	CSIC-25	0	0.509 ± 0.00	4.5 ± 0.0
		146.05	0.473 ± 0.01	3.1 ± 0.5
		309.5	0.476 ± 0.01	3.3 ± 0.3
		772.65	0.479 ± 0.01	3.4 ± 0.3
His-D/C-ADH	CSIC-23	0	0.689 ± 0.01	31.1 ± 0.3
		146.05	0.779 ± 0.01	33.1 ± 0.1
		309.5	0.788 ± 0.03	33.3 ± 0.7
		772.65	0.709± 0.04	31.6 ± 0.9
	CSIC-25	0	1.009 ± 0.01	37.1 ± 0.1
		772.65	0.918 ± 0.00	35.7 ± 0.1
		309.5	0.969 ± 0.00	36.5 ± 0.1
		146.05	1.068 ± 0.02	38.0 ± 0.3

The temperatures were calculated using the Arrhenius plots (ln (Activity U x mL^{-1})) vs (1 x T^{-1}). The field employed on the AFM was 30 mT.

The recovered activity obtained after the incubation of the MNPs solution under AFM were interpolated into the Arrhenius plots to obtain the local temperature of the enzymes (Table 24). However, the activity of the MNPs with and without AFM does not change under any of the AFM frequencies tested. The low colloidal stability observed during the immobilization process could affect the properties of the MNPs under the AFM and may be the factor that sabotage the heating activation of the MNPs.

5.4 Conclusions

As a summary of this final chapter, we demonstrated that orientation and distance plays an important role not only in the kinetic parameters of the biocatalyst but also in thermodynamic

parameters. The BsADH variants developed in the previous chapters were studies as biocatalysts immobilized on non-porous carriers with an interesting possible application under alternating magnetic field. Unfortunately, the final applicability of the biocatalysts were not successful due to aggregation issues. To further improve the applicability of this approach, it would be necessary to reduce aggregation by modifying the composition of the MNPs' composition or by testing different additives such as Bovine serum albumin (BSA) that helps by increasing protein crowding around the surface of the MNPs. This would allow for the MNPs to have greater colloidal stability which is necessary when utilising AFM.

5.5 Bibliography

[1] R. Feynman, There's plenty of room at the bottom, Feynman and computation, CRC Press2018, pp. 63-76.

[2] S. Nakamura, M. Sato, Y. Sato, N. Ando, T. Takayama, M. Fujita, M. Ishihara, Synthesis and application of silver nanoparticles (Ag NPs) for the prevention of infection in healthcare workers, International journal of molecular sciences, 20 (2019) 3620.

[3] A.C. Anselmo, S. Mitragotri, Nanoparticles in the clinic, Bioengineering & translational medicine, 1 (2016) 10-29.

[4] A. Ito, M. Shinkai, H. Honda, T. Kobayashi, Medical application of functionalized magnetic nanoparticles, Journal of bioscience and bioengineering, 100 (2005) 1-11.

[5] M. Liong, J. Lu, M. Kovochich, T. Xia, S.G. Ruehm, A.E. Nel, F. Tamanoi, J.I. Zink, Multifunctional inorganic nanoparticles for imaging, targeting, and drug delivery, ACS nano, 2 (2008) 889-896.

[6] K.-S. Lee, M.A. El-Sayed, Gold and silver nanoparticles in sensing and imaging: sensitivity of plasmon response to size, shape, and metal composition, The Journal of Physical Chemistry B, 110 (2006) 19220-19225.

[7] A.B. Moghaddam, T. Nazari, J. Badraghi, M. Kazemzad, Synthesis of ZnO nanoparticles and electrodeposition of polypyrrole/ZnO nanocomposite film, Int. J. Electrochem. Sci, 4 (2009) 247-257.

[8] M. Seenuvasan, K.S. Kumar, A. Kumar, R. Parthiban, Review on surface modification of nanocarriers to overcome diffusion limitations: An enzyme immobilization aspect, Biochemical engineering journal, 158 (2020) 107574.

[9] M. De, P.S. Ghosh, V.M. Rotello, Applications of nanoparticles in biology, Advanced Materials, 20 (2008) 4225-4241.

[10] S.A. Ansari, Q. Husain, Potential applications of enzymes immobilized on/in nano materials: A review, Biotechnology advances, 30 (2012) 512-523.

[11] B. Brena, P. González-Pombo, F. Batista-Viera, Immobilization of enzymes: a literature survey, Immobilization of enzymes and cells, (2013) 15-31.

[12] S. Ding, A.A. Cargill, I.L. Medintz, J.C. Claussen, Increasing the activity of immobilized enzymes with nanoparticle conjugation, Current opinion in biotechnology, 34 (2015) 242-250.

[13] B.J. Johnson, W.R. Algar, A.P. Malanoski, M.G. Ancona, I.L. Medintz, Understanding enzymatic acceleration at nanoparticle interfaces: Approaches and challenges, Nano Today, 9 (2014) 102-131.

[14] J.N. Vranish, M.G. Ancona, E. Oh, K. Susumu, I.L. Medintz, Enhancing coupled enzymatic activity by conjugating one enzyme to a nanoparticle, Nanoscale, 9 (2017) 5172-5187.

[15] S.A. Ansari, Q. Husain, S. Qayyum, A. Azam, Designing and surface modification of zinc oxide nanoparticles for biomedical applications, Food and Chemical Toxicology, 49 (2011) 2107-2115.

[16] H. Jia, G. Zhu, P. Wang, Catalytic behaviors of enzymes attached to nanoparticles: the effect of particle mobility, Biotechnology and bioengineering, 84 (2003) 406-414.

[17] W.R. Algar, A. Malonoski, J.R. Deschamps, J.B. Blanco-Canosa, K. Susumu, M.H. Stewart, B.J. Johnson, P.E. Dawson, I.L. Medintz, Proteolytic activity at quantum dot-conjugates: Kinetic analysis reveals enhanced enzyme activity and localized interfacial “hopping”, Nano letters, 12 (2012) 3793-3802.

[18] F. Liu, L. Wang, H. Wang, L. Yuan, J. Li, J.L. Brash, H. Chen, Modulating the activity of protein conjugated to gold nanoparticles by site-directed orientation and surface density of bound protein, ACS applied materials & interfaces, 7 (2015) 3717-3724.

[19] K.A. Mahmoud, E. Lam, S. Hrapovic, J.H. Luong, Preparation of well-dispersed gold/magnetite nanoparticles embedded on cellulose nanocrystals for efficient immobilization of papain enzyme, ACS applied materials & interfaces, 5 (2013) 4978-4985.

[20] F. Keyhanian, S. Shariati, M. Faraji, M. Hesabi, Magnetite nanoparticles with surface modification for removal of methyl violet from aqueous solutions, Arabian Journal of Chemistry, 9 (2016) S348-S354.

[21] N.A. Frey, S. Peng, K. Cheng, S. Sun, Magnetic nanoparticles: synthesis, functionalization, and applications in bioimaging and magnetic energy storage, Chemical Society Reviews, 38 (2009) 2532-2542.

[22] I. Armenia, M.V.G. Bonavia, L. De Matteis, P. Ivanchenko, G. Martra, R. Gornati, M. Jesus, G. Bernardini, Enzyme activation by alternating magnetic field: Importance of the bioconjugation methodology, Journal of colloid and interface science, 537 (2019) 615-628.

[23] J.G. Ovejero, I. Armenia, D. Serantes, S. Veintemillas-Verdaguer, N. Zeballos, F. López-Gallego, C. Grüttner, J.M. de la Fuente, M.a.d. Puerto Morales, V. Grazu, Selective magnetic nanoheating: Combining iron oxide nanoparticles for multi-hot-spot induction and sequential regulation, Nano letters, 21 (2021) 7213-7220.

[24] J. Xu, J. Sun, Y. Wang, J. Sheng, F. Wang, M. Sun, Application of iron magnetic nanoparticles in protein immobilization, Molecules, 19 (2014) 11465-11486.

[25] O.M. Darwesh, S.S. Ali, I.A. Matter, T. Elsamahy, Y.A. Mahmoud, Enzymes immobilization onto magnetic nanoparticles to improve industrial and environmental applications, Methods in enzymology, Elsevier2020, pp. 481-502.

[26] S. Arrhenius, Über die Reaktionsgeschwindigkeit bei der Inversion von Rohrzucker durch Säuren, Zeitschrift für physikalische Chemie, 4 (1889) 226-248.

[27] H. Eyring, The activated complex in chemical reactions, The Journal of Chemical Physics, 3 (1935) 107-115.

[28] G.V. Isaksen, J. Åqvist, B.O. Brandsdal, Enzyme surface rigidity tunes the temperature dependence of catalytic rates, Proceedings of the National Academy of Sciences, 113 (2016) 7822-7827.

[29] I. Maffucci, D. Laage, F. Sterpone, G. Stirnemann, Thermal adaptation of enzymes: impacts of conformational shifts on catalytic activation energy and optimum temperature, Chemistry–A European Journal, 26 (2020) 10045-10056.

[30] F. Caruso, C. Schüler, Enzyme multilayers on colloid particles: assembly, stability, and enzymatic activity, Langmuir, 16 (2000) 9595-9603.

[31] I.A.T. Ximenes, P.C.O. de Oliveira, C.A. Wegermann, M.C. de Moraes, Magnetic particles for enzyme immobilization: a versatile support for ligand screening, Journal of Pharmaceutical and Biomedical Analysis, 204 (2021) 114286.

[32] J. Turkova, Oriented immobilization of biologically active proteins as a tool for revealing protein interactions and function, Journal of Chromatography B: Biomedical Sciences and Applications, 722 (1999) 11-31.

[33] X. Liu, L. Lei, Y. Li, H. Zhu, Y. Cui, H. Hu, Preparation of carriers based on magnetic nanoparticles grafted polymer and immobilization for lipase, Biochemical engineering journal, 56 (2011) 142-149.

[34] J. Marbaix, N. Mille, L.-M. Lacroix, J.M. Asensio, P.-F. Fazzini, K. Soulantica, J. Carrey, B. Chaudret, Tuning the composition of FeCo nanoparticle heating agents for magnetically induced catalysis, ACS Applied Nano Materials, 3 (2020) 3767-3778.

CONCLUTIONS

6 CONCLUDING REMARKS

The thesis presented here, has as its primary contribution the development and study of novel techniques for either single or multi-enzyme systems rational immobilization on solid carriers. In the case of single enzyme biocatalysts, the design of a new rational technique to control the orientation for performing a reversible affinity immobilization has been detailed. The biocatalysts developed with this technique as a model two alcohol dehydrogenases (BsADH and Tt27-HBDH) have been extensively characterized and tested with an industrially relevant reaction. In the case of multi-enzymatic systems, we describe the possibility to control the spatial distribution of the enzymes using protein scaffolds based on the cellulosome. We also examine how the spatial distribution of the enzymes affect the overall effectiveness of the reactions as well as the position between the enzymes in the multi-enzymatic system.

The main outcomes during this PhD thesis are summarized as follows:

- A protein engineering toolbox to organize multi-enzymatic systems at nanoscale level has been developed in this work, which could be used in multi-enzymatic cascades for cell-free biotransformations.

- Multi-enzymatic systems can be assembled in solid phase through the interaction cohesin-dockerin (iSECel) systems is possible. Protein scaffolds based on the binding domains from the Cellosome of *Clostridum thermocellum* were exploited. These iSECel systems` versatility has been demonstrated using two different multi-enzymatic cascades with two and three enzymes where the enzymes showed activity after the assembly.

- The co-localized assembled multi-enzymatic cascades showed better performance than the segregated system, and can be integrated into a flow-reactor for continuous synthesis with a 2-times higher specific productivity than the batch operated system.

- The expansion of the spatial organization to a three enzyme multi-enzymatic cascade, to the conversion of 1,5-pentanediol. After developing two new iSECel systems, we studied the effect of the enzyme position (iSECel-II and iSECel-III systems) on the final overall biocatalyst performance. The iSECel-II converted almost 100% of the diol compared to 60-70% achieved by the iSECel-III.

- Immobilization by controlling the orientation beyond the N- or C-terminus of multimeric enzymes on solid carriers has been successfully achieved based on the rational introduction of histidines clusters in the surface of multimeric enzymes using protein engineering.

- The enzyme variants developed in this work were immobilized on different porous carriers activated with different metals and densities. The nature and the metal density of porous carriers were recognized as important parameters to take into account for efficient immobilization of multimeric enzymes.

- We have shown that enzyme orientation modifies the characteristics of an immobilized biocatalyst. Some variants with surface histidine clusters leads to more active heterogeneous biocatalyst such BsADH-H3 or Tt27-HBDH-loop than their histidine-tagged counterpart immobilized on the same carrier.

- It was demonstrated that the enzyme orientation can increase the enzyme stability of the heterogeneous biocatalyst. Where, the oriented enzymes BsADH-H3 on Ld-AG-Co^{2+} and Hd-AG-Co^{2+} carriers showed higher stability against thermal inactivation with almost 1.3 times higher stability and Tt27-HBDH-H4 immobilized on EziG1 showed 1.85 times higher stability than their corresponding histidine-tagged counterpart immobilized on the same carrier.

- The immobilized biocatalysts, with the control of enzyme orientation, have been applied to different reactions with relevance in the chemical industry. This strategy has improved the operational stability of the immobilized enzymes and changed their product selectivity.

- The engineered variants of the model enzyme BsADH (fusing protein scaffolds and introducing histidine clusters) were tested on non-porous nano-carriers. Demonstrating, that the orientation and the distance of the enzymes from the surface carrier affects the enzyme thermodynamics of the immobilized enzymes such as the activation energy (E_A) of the biocatalyst.

The results obtained from the innovative strategies developed in this PhD thesis are the beginning of a new path for the optimization of the enzyme orientation during the immobilization of heterogeneous biocatalysts. Furthermore, this thesis also developed the

toolbox for the control of spatial distribution in complex multi-enzymatic systems which will allow the development of more efficient heterogeneous biocatalysts in the future.

Conclusiones Finales

La presente tesis doctoral tiene como principal aportación el desarrollo y estudio de nuevas técnicas para la inmovilización racional, dirigida y regio-específica de una sola enzima o de sistemas multienzimáticos en soportes sólidos. En el caso de biocatalizadores mono-enzimáticos se ha desarrollado y detallado una nueva técnica racional para el control de la orientación de la enzima usando un método de inmovilización por afinidad reversible. Los biocatalizadores desarrollados con esta técnica utilizando como modelo alcoholes deshidrogenasas (BsADH y Tt27-HBDH) han sido ampliamente caracterizados y probados frente a una reacción con aplicabilidad industrial. En el caso de los sistemas multienzimáticos, se ha demostrado la posibilidad de controlar la distribución espacial de las enzimas implicadas en la reacción utilizando andamiajes proteicos basados en el celulosoma. Estudiando cómo afecta la distribución espacial de las enzimas a la eficacia global de las reacciones, así como la posición entre las enzimas en dichos sistemas.

Los principales resultados obtenidos durante esta tesis doctoral se presentan a continuación:

- En este trabajo se ha desarrollado una caja de herramientas de ingeniería de proteínas para organizar sistemas multienzimáticos a escala nanométrica, que podría utilizarse en cascadas multienzimáticas para biotransformaciones libres de células

- Es posible ensamblar sistemas multienzimáticos en fase sólida mediante los sistemas de interacción cohesina-dockerina (iSECel). Se han explotado andamiajes proteicos basados en el dominio de unión del celulosoma de *Clostridum thermocellum.* Se ha demostrado la versatilidad de estos sistemas iSECel se utilizando dos cascadas multienzimáticas diferentes con dos y tres enzimas, en las que las enzimas mostraron actividad tras el ensamblaje.

- Las cascadas multienzimáticas ensambladas co-localizadas mostraron un mejor rendimiento que el sistema segregado y pueden ser integradas en un reactor de flujo para realizar síntesis continua con una productividad específica 2 veces mayor que el sistema operado en batch.

- Se extendió de la organización espacial a una cascada multienzimática de tres enzimas, para la conversión de 1,5-pentanediol. Tras desarrollar dos nuevos

sistemas iSECel, estudiamos el efecto de la posición de las enzimas (sistemas iSECel-II e iSECel-III) en el rendimiento global final del biocatalizador. El iSECel-II convirtió casi el 100% del diol, frente al 60-70% de conversión conseguido por el iSECel-III.

- La inmovilización controlando la orientación más allá del N- o C-terminal de enzimas multiméricas sobre soportes sólidos se ha logrado con éxito basándose en la introducción racional de clústeres de histidinas en la superficie de enzimas multiméricas utilizando ingeniería de proteínas.

- Las variantes enzimáticas desarrolladas en este trabajo se inmovilizaron en diferentes soportes porosos activados con diferentes metales y densidades. La naturaleza y la densidad metálica de los soportes porosos se reconocieron como parámetros importantes a tener en cuenta para la inmovilización eficiente de enzimas multiméricas.

- Hemos demostrado que la orientación de la enzima modifica las características de un biocatalizador inmovilizado. Algunas variantes con grupos de histidina en la superficie conducen a biocatalizadores heterogéneos más activos, como BsADH-H3 o Tt27-HBDH-loop, que su homólogo marcado con histidina inmovilizado en el mismo soporte.

- Se demostró que la orientación de la enzima puede aumentar la estabilidad enzimática del biocatalizador heterogéneo. Las enzimas orientadas BsADH-H3 en portadores Ld-AG-Co^{2+} y Hd-AG-Co^{2+} mostraron una mayor estabilidad frente a la inactivación térmica, casi 1.3 veces mayor, y Tt27-HBDH-H4 inmovilizada en EziG1 mostró una estabilidad 1.85 veces mayor que su homóloga correspondiente marcada con histidina e inmovilizada en el mismo soporte.

- Los biocatalizadores inmovilizados controlando de la orientación de las enzimas, se han aplicado a diferentes reacciones con relevancia en la industria química. Esta estrategia ha mejorado la estabilidad operativa de las enzimas inmovilizadas y ha modificado la selectividad de sus productos.

- Las variantes modificadas de la enzima modelo BsADH (fusionando andamiajes proteicos e introduciendo clústeres de histidina) se probaron en nano-soportes no porosos. Se demostró que la orientación y la distancia de las enzimas con respecto

a la superficie del soporte afectan a la termodinámica de las enzimas inmovilizadas, como la energía de activación (EA) del biocatalizador.

Los resultados obtenidos demuestran que las nuevas estrategias innovadoras desarrolladas en esta tesis doctoral son el inicio de un nuevo camino para la optimización de la orientación de las enzimas durante la inmovilización de biocatalizadores heterogéneos. Aportando además una caja de herramientas para el control de la distribución espacial en sistemas multienzimáticos complejos que permitirá el desarrollo de biocatalizadores heterogéneos más eficientes en el futuro.

ANNEXES

7 Annexes

7.1 Tables

Table A 1: Sequences of synthetic genes and proteins used in the iSECel-I system.

C-His (21.2 kDa) NdeI-Cohesin-EcoRI-linker-Histag

Gene sequence:

CATATGAGGGCAGATAAAGCCTCGAGCATTGAGCTTAAGTTTGACCGCAATAAGGGAGAAGTTGGAGATATACTTATTGGT
ACCGTAAGGATAAACAATATCAAGAATTTCGCAGGATTTCAGGTAAACATTGTATATGATCCAAAAGTCTTAATGGCTGTTG
ACCCTGAAACGGGGAAAGAATTTACTTCTTCAACATTTCCGCCAGGACGCACTGTACTGAAAAACAATGCTTACGGCCCAA
TACAGATTGCGGACAATGATCCGGAAAAAGGGATACTGAACTTCGCGCTTGCATATTCATATATTGCGGGATACAAAGAAA
CAGGAGTAGCGGAGGAAAGCGGCATAATTGCGAAAATTGGATTTAAAATACTCCAGAAAAAGAGCACTGCCGTAAAATTCC
AGGATACATTAAGCATGCCCGGAGCTATTTCGGGAACACAGCTGTTTGACTGGGACGGAGAAGTTATTACCGGATATGAG
GTAATACAGCCGGATGTGCTGAGTTTGGGTGACGAGCCTAAGAATTCGAGCTCCGTCGACAAGCTTGCGGCCGCACTCGA
GCACCACCACCACCACCACTGA

Protein sequence:

MRADKASSIELKFDRNKGEVGDILIGTVRINNIKNFAGFQVNIVYDPKVLMAVDPETGKEFTSSTFPPGRTVLKNNAYGPIQIADND
PEKGILNFALAYSYIAGYKETGVAEESGIIAKIGFKILQKKSTAVKFQDTLSMPGAISGTQLFDWDGEVITGYEVIQPDVLSLGDEPK
NSSSVDKLAAALEHHHHHH*

D-ECFP-D (67.8 kDa): N-Histag-Thrombin side- Dockerin-EcoRI-GS-BamHI-ECFP-BamHI-GS-Acc65I-Dockerin

Gene sequence:

ATGGGCAGCAGCCATCATCATCATCATCACAGCAGCGGCCTGGTGCCGCGCGGCAGCCATATGAACAAACCGGTGATTGA
AGGCTATAAAGTGAGCGGCTATATTCTGCCGGATTTTAGCTTTGATGCGACCGTGGCGCCGCTGGTGAAAGCGGGCTTTA
AAGTGGAAATTGTGGGCACCGAACTGTATGCGGTGACCGATGCGAACGGCTATTTTGAAATTACCGGCGTGCCGGCGAAC
GCGAGCGGCTATACCCTGAAAATTAGCCGCGCGACCTATCTGGATCGCGTGATTGCGAACGTGGTGGTGACCGGCGATA
CCAGCGTGAGCACCAGCCAGGCGCCGATTCATATGTGGGTGGGCGATATTGTGAAAGATAACAGCATTAACCTGCTGGAT
GTGGCGGAAGTGATTCGCTGCTTTAACGCGACCAAAGGCAGCGCGAACTATGTGGAAGAACTGGATATTAACCGCAACGG
CGCGATTAACATGCAGGATATTATGATTGTGCATAAACATTTTGGCGCGACCAGCAGCGATTATGATGCGCAGCTGGAAGA
ATTCGGTAGCGGTAGCGGTAGCTCTAGAGGATCCATGCGCAAAGGCGAAGAACTGTTTACCGGCGTGGTGCCGATTCTGG
TGGAACTGGATGGCGATGTGAACGGCCATAAATTTAGCGTGAGCGGCGAAGGCGAAGGCGATGCGACCAACGGCAAACT
GACCCTGAAATTTATTTGCACCACCGGCAAACTGCCGGTGCCGTGGCCGACCCTGGTGACCACCTTTACCTGGGGCGTGC
AGTGCTTTGCGCGCTATCCGGATCATATGAAACAGCATGATTTTTTTAAAAGCGCGATGCCGGAAGGCTATGTGCAGGAAC
GCACCATTAGCTTTAAAGATGATGGCACCTATAAAACCCGCGCGGAAGTGAAATTTGAAGGCGATACCCTGGTGAACCGCA
TTGAACTGAAAGGCATTGATTTTAAAGAAGATGGCAACATTCTGGGCCATAAACTGGAATATAACTTTAACAGCCATAACGT
GTATATTACCGCGGATAAACAGAAAAACGGCATTAAAGCGAACTTTAAAATTCGCCATAACGTGGAAGATGGCAGCGTGCA
GCTGGCGGATCATTATCAGCAGAACACCCCGATTGGCGATGGCCCGGTGCTGCTGCCGGATAACCATTATCTGAGCACCC
AGAGCGCGCTGAGCAAAGATCCGAACGAAAAACGCGATCATATGGTGCTGCTGGAATTTGTGACCGCGGCGGGCATTACC
CATGGCATGGATGAACTGTATAAACGCCCGGCGGCGAACGATGAAAACTATGCGGCGAGCGTGGGATCCGGTAGCAGCG
GTAGCAGCGGTACCATGAACAAACCGGTGATTGAAGGCTATAAAGTGAGCGGCTATATTCTGCCGGATTTTAGCTTTGATG
CGACCGTGGCGCCGCTGGTGAAAGCGGGCTTTAAAGTGGAAATTGTGGGCACCGAACTGTATGCGGTGACCGATGCGAA
CGGCTATTTTGAAATTACCGGCGTGCCGGCGAACGCGAGCGGCTATACCCTGAAAATTAGCCGCGCGACCTATCTGGATC
GCGTGATTGCGAACGTGGTGGTGACCGGCGATACCAGCGTGAGCACCAGCCAGGCGCCGATTCATATGTGGGTGGGCGA
TATTGTGAAAGATAACAGCATTAACCTGCTGGATGTGGCGGAAGTGATTCGCTGCTTTAACGCGACCAAAGGCAGCGCGA
ACTATGTGGAAGAACTGGATATTAACCGCAACGGCGCGATTAACATGCAGGATATTATGATTGTGCATAAACATTTTGGCG
CGACCAGCAGCGATTATGATGCGCAGCTGGAATAA

Protein sequence:

MGSSHHHHHHSSGLVPRGSHMNKPVIEGYKVSGYILPDFSFDATVAPLVKAGFKVEIVGTELYAVTDANGYFEITGVPANASGYT
LKISRATYLDRVIANVVVTGDTSVSTSQAPIHMWVGDIVKDNSINLLDVAEVIRCFNATKGSANYVEELDINRNGAINMQDIMIVHK
HFGATSSDYDAQLEEFGSGSGSSRGSMRKGEELFTGVVPILVELDGDVNGHKFSVSGEGEGDATNGKLTLKFICTTGKLPVPW
PTLVTTFTWGVQCFARYPDHMKQHDFFKSAMPEGYVQERTISFKDDGTYKTRAEVKFEGDTLVNRIELKGIDFKEDGNILGHKLE
YNFNSHNVYITADKQKNGIKANFKIRHNVEDGSVQLADHYQQNTPIGDGPVLLPDNHYLSTQSALSKDPNEKRDHMVLLEFVTAA
GITHGMDELYKRPAANDENYAASVGSGSGSSGTMNKPVIEGYKVSGYILPDFSFDATVAPLVKAGFKVEIVGTELYAVTDANGY
FEITGVPANASGYTLKISRATYLDRVIANVVVTGDTSVSTSQAPIHMWVGDIVKDNSINLLDVAEVIRCFNATKGSANYVEELDINR
NGAINMQDIMIVHKHFGATSSDYDAQLE

D-ωTA-D (73.9 kDa): N-Dockerin-GS-ωTA-BamHI-GS-Dockerin

Gene sequence:

ATGGGAGCTAGCCATATGAACAAACCGGTGATTGAAGGCTATAAAGTGAGCGGCTATATTCTGCCGGATTTTAGCTTTGAT
GCGACCGTGGCGCCGCTGGTGAAAGCGGGCTTTAAAGTGGAAATTGTGGGCACCGAACTGTATGCGGTGACCGATGCGA
ACGGCTATTTTGAAATTACCGGCGTGCCGGCGAACGCGAGCGGCTATACCCTGAAAATTAGCCGCGCGACCTATCTGGAT
CGCGTGATTGCGAACGTGGTGGTGACCGGCGATACCAGCGTGAGCACCAGCCAGGCGCCGATTCATATGTGGGTGGGC
GATATTGTGAAAGATAACAGCATTAACCTGCTGGATGTGGCGGAAGTGATTCGCTGCTTTAACGCGACCAAAGGCAGCGC
GAACTATGTGGAAGAACTGGATATTAACCGCAACGGCGCGATTAACATGCAGGATATTATGATTGTGCATAAACATTTTGGC
GCGACCAGCAGCGATTATGATGCGCAGCTGGAAGGCAGCGGCAGCGGCAGCTCTAGAAGATCTGCGAGCATGGATAAAG
TGTTTGCGGGCTATGCGGCGCGCCAGGCGATTCTGGAAAGCACCGAAACCACCAACCCGTTTGCGAAAGGCATTGCGTG
GGTGGAAGGCGAACTGGTGCCGCTGGCGGAAGCGCGCATTCCGCTGCTGGATCAGGGCTTTATGCATAGCGATCTGACC
TATGATGTGCCGAGCGTGTGGGATGGCCGCTTTTTTCGCCTGGATGATCATATTACCCGCCTGGAAGCGAGCTGCACCAA
ACTGCGCCTGCGCCTGCCGCTGCCGCGCGATCAGGTGAAACAGATTCTGGTGGAAATGGTGGCGAAAAGCGGCATTCGC
GATGCGTTTGTGGAACTGATTGTGACCCGCGGCCTGAAAGGCGTGCGCGGCACCCGCCCGGAAGATATTGTGAACAACC
TGTATATGTTTGTGCAGCCGTATGTGTGGGTGATGGAACCGGATATGCAGCGCGTGGGCGGCAGCGCGGTGGTGGCGCG
CACCGTGCGCCGCGTGCCGCCGGGCGCGATTGATCCGACCGTGAAAAACCTGCAGTGGGGCGATCTGGTGCGCGGCAT
GTTTGAAGCGGCGGATCGCGGCGCGACCTATCCGTTTCTGACCGATGGCGATGCGCATCTGACCGAAGGCAGCGGCTTT
AACATTGTGCTGGTGAAAGATGGCGTGCTGTATACCCCGGATCGCGGCGTGCTGCAGGGCGTGACCCGCAAAAGCGTGA
TTAACGCGGCGGAAGCGTTTGGCATTGAAGTGCGCGTGGAATTTGTGCCGGTGGAACTGGCGTATCGCTGCGATGAAATT
TTTATGTGCACCACCGCGGGCGGCATTATGCCGATTACCACCCTGGATGGCATGCCGGTGAACGGCGGCCAGATTGGCC
CGATTACCAAAAAAATTTGGGATGGCTATTGGGCGATGCATTATGATGCGGCGTATAGCTTTGAAATTGATTATAACGAACG
CAACCTGGAAGGATCCGGCAGCAGCGGCAGCAGCCATATGAACAAACCGGTGATTGAAGGCTATAAAGTGAGCGGCTATA
TTCTGCCGGATTTTAGCTTTGATGCGACCGTGGCGCCGCTGGTGAAAGCGGGCTTTAAAGTGGAAATTGTGGGCACCGAA
CTGTATGCGGTGACCGATGCGAACGGCTATTTTGAAATTACCGGCGTGCCGGCGAACGCGAGCGGCTATACCCTGAAAAT
TAGCCGCGCGACCTATCTGGATCGCGTGATTGCGAACGTGGTGGTGACCGGCGATACCAGCGTGAGCACCAGCCAGGCG
CCGATTCATATGTGGGTGGGCGATATTGTGAAAGATAACAGCATTAACCTGCTGGATGTGGCGGAAGTGATTCGCTGCTTT
AACGCGACCAAAGGCAGCGCGAACTATGTGGAAGAACTGGATATTAACCGCAACGGCGCGATTAACATGCAGGATATTAT
GATTGTGCATAAACATTTTGGCGCGACCAGCAGCGATTATGATGCGCAGCTGGAATAA

Protein sequence:

MGASHMNKPVIEGYKVSGYILPDFSFDATVAPLVKAGFKVEIVGTELYAVTDANGYFEITGVPANASGYTLKISRATYLDRVIANVV
VTGDTSVSTSQAPIHMWVGDIVKDNSINLLDVAEVIRCFNATKGSANYVEELDINRNGAINMQDIMIVHKHFGATSSDYDAQLEGS
GSGSSRRSASMDKVFAGYAARQAILESTETTNPFAKGIAWVEGELVPLAEARIPLLDQGFMHSDLTYDVPSVWDGRFFRLDDHI
TRLEASCTKLRLRLPLPRDQVKQILVEMVAKSGIRDAFVELIVTRGLKGVRGTRPEDIVNNLYMFVQPYVWVMEPDMQRVGGSA
VVARTVRRVPPGAIDPTVKNLQWGDLVRGMFEAADRGATYPFLTDGDAHLTEGSGFNIVLVKDGVLYTPDRGVLQGVTRKSVIN
AAEAFGIEVRVEFVPVELAYRCDEIFMCTTAGGIMPITTLDGMPVNGGQIGPITKKIWDGYWAMHYDAAYSFEIDYNERNLEGSG
SSGSSHMNKPVIEGYKVSGYILPDFSFDATVAPLVKAGFKVEIVGTELYAVTDANGYFEITGVPANASGYTLKISRATYLDRVIANV
VVTGDTSVSTSQAPIHMWVGDIVKDNSINLLDVAEVIRCFNATKGSANYVEELDINRNGAINMQDIMIVHKHFGATSSDYDAQLE

C-ADH (56.5kDa): N-NdeI-Cohesin-GS-BglII-ADH

Gene sequence:

CCATGGGTCGTGCGGATAAGGCGAGCAGCATTGAACTGAAATTTGATCGTAACAAGGGTGAAGTGGGTGACATTCTGATT
GGTACCGTGCGTATCAACAACATTAAGAACTTCGCGGGCTTTCAGGTGAACATCGTTTACGACCCGAAGGTGCTGATGGC
GGTTGATCCGGAAACCGGTAAAGAGTTCACCAGCAGCACCTTTCCGCCGGGTCGTACCGTGCTGAAGAACAACGCGTACG
GTCCGATCCAAATTGCGGACAACGATCCGGAAAAAGGTATCCTGAACTTCGCGCTGGCGTACAGCTATATTGCGGGCTAT
AAGGAAACCGGTGTGGCGGAGGAAAGCGGCATCATTGCGAAGATCGGTTTCAAAATTCTGCAGAAGAAAAGCACCGCGGT
TAAATTTCAAGACACCCTGAGCATGCCGGGCGCGATTAGCGGTACCCAGCTGTTCGACTGGGATGGCGAAGTTATCACCG
GTTATGAAGTGATTCAACCGGACGTTCTGAGCCTGGGCGATGAGCCGGAATTTGGTAGCGGCAGCGGTAGCAGCCGTAG
ATCTATGAAAGCCGCGGTTGTGGAACAGTTCAAAGAACCGCTGAAAATCAAAGAGGTTGAGAAACCGACCATTAGTTACGG
CGAAGTCTTGGTCCGCATCAAAGCTTGTGGTGTCTGTCACACTGATTTGCATGCGGCACACGGTGATTGGCCTGTGAAAC
CGAAACTTCCGCTGATTCCGGGGCATGAAGGCGTAGGAATCGTGGAAGAAGTGGGTCCTGGCGTTACGCACCTGAAAGT
CGGCGATCGCGTTGGTATTCCCTGGCTGTATTCAGCTTGCGGTCATTGCGACTATTGCCTCTCTGGCCAAGAAACCCTTTG
TGAACACCAGAAGAATGCGGGGTATAGCGTGGATGGCGGGTATGCGGAATACTGTCGGGCAGCAGCGGATTATGTCGTG
AAAATTCCGGACAATCTCTCGTTTGAGGAAGCAGCGCCTATCTTCTGCGCCGGTGTAACTACCTACAAAGCACTGAAAGTT
ACCGGAGCCAAACCAGGCGAATGGGTTGCGATCTACGGTATCGGTGGCCTTGGACATGTTGCCGTTCAGTATGCGAAAGC
TATGGGCTTAAACGTGGTTGCTGTGGATATTGGCGACGAAAAGCTGGAACTGGCGAAAGAGTTAGGTGCGGATTTGGTCG
TTAATCCCCTGAAAGAAGATGCCGCCAAATTCATGAAAGAGAAAGTCGGAGGTGTGCATGCAGCTGTGGTCACAGCGGTA
AGCAAACCGGCGTTTCAATCGGCCTACAACTCCATTCGCCGTGGTGGTGCCTGCGTGCTGGTAGGCCTGCCACCGGAGG
AAATGCCGATTCCGATCTTTGACACAGTGCTGAATGGGATTAAGATCATTGGCAGCATTGTAGGCACGCGTAAGGACTTAC
AGGAAGCACTGCAGTTTGCTGCCGAAGGGAAAGTCAAGACCATCATTGAGGTGCAACCACTGGAAAAGATTAACGAAGTG
TTTGATCGCATGCTCAAGGGCCAGATTAACGGCCGTGTGGTACTGACGTTAGAGGACAAATAA

Protein sequence:

MGRADKASSIELKFDRNKGEVGDILIGTVRINNIKNFAGFQVNIVYDPKVLMAVDPETGKEFTSSTFPPGRTVLKNNAYGPIQIADN
DPEKGILNFALAYSYIAGYKETGVAEESGIIAKIGFKILQKKSTAVKFQDTLSMPGAISGTQLFDWDGEVITGYEVIQPDVLSLGDEP
EFGSGSGSSRRSMKAAVVEQFKEPLKIKEVEKPTISYGEVLVRIKACGVCHTDLHAAHGDWPVKPKLPLIPGHEGVGIVEEVGPG
VTHLKVGDRVGIPWLYSACGHCDYCLSGQETLCEHQKNAGYSVDGGYAEYCRAAADYVVKIPDNLSFEEAAPIFCAGVTTYKAL
KVTGAKPGEWVAIYGIGGLGHVAVQYAKAMGLNVVAVDIGDEKLELAKELGADLVVNPLKEDAAKFMKEKVGGVHAAVVTAVSK
PAFQSAYNSIRRGGACVLVGLPPEEMPIPIFDTVLNGIKIIGSIVGTRKDLQEALQFAAEGKVKTIIEVQPLEKINEVFDRMLKGQIN
GRVVLTLEDK*

The initial and stop codons are underlined in all genes. Coh: Cohesin domain type II from *Clostridrium thermocellum* and Doc: Dockerin domain type II form *Clostridium thermocellum* (PDB ID 2B59). ADH: Alcohol dehydrogenase from *Bacillus stearothermophilus* (PDB ID: 1RJW). ωTA: ω-Transaminase from *Aspergillus Terreus* (PDB ID: 4CE5). ECFP: Enhanced cyan fluorescent protein from *Aequorea victoria* (PDB ID: 2WSN). Restriction sites and amino acids are encoded within the protein primary sequences which are highlighted in blue.

Table A 2: Sequences of synthetic genes and proteins used in the iSECel-II and iSECel-III system.

His-D (22.8 kDa) N-Histag-Thrombin side- Dockerin-EcoRI

Gene sequence

ATGGGCAGCAGCCATCATCATCATCATCACAGCAGCGGCCTGGTGCCGCGCGGCAGCCATATGAACAAACCGGTGATTGA
AGGCTATAAAGTGAGCGGCTATATTCTGCCGGATTTTAGCTTTGATGCGACCGTGGCGCCGCTGGTGAAAGCGGGCTTTA
AAGTGGAAATTGTGGGCACCGAACTGTATGCGGTGACCGATGCGAACGGCTATTTTGAAATTACCGGCGTGCCGGCGAAC
GCGAGCGGCTATACCCTGAAAATTAGCCGCGCGACCTATCTGGATCGCGTGATTGCGAACGTGGTGGTGACCGGCGATA
CCAGCGTGAGCACCAGCCAGGCGCCGATTCATATGTGGGTGGGCGATATTGTGAAAGATAACAGCATTAACCTGCTGGAT
GTGGCGGAAGTGATTCGCTGCTTTAACGCGACCAAAGGCAGCGCGAACTATGTGGAAGAACTGGATATTAACCGCAACGG
CGCGATTAACATGCAGGATATTATGATTGTGCATAAACATTTTGGCGCGACCAGCAGCGATTATGATGCGCAGCTGGAAGA
ATTCGAGCTCCGTCGACAAGCTTGCGGCCGCACTCGAGCACCACCACCACCACCACTGAGATCCGGCTGCTAA

Protein sequence:

MGSSHHHHHHSSGLVPRGSHMNKPVIEGYKVSGYILPDFSFDATVAPLVKAGFKVEIVGTELYAVTDANGYFEITGVPANASGYT
LKISRATYLDRVIANVVVTGDTSVSTSQAPIHMWVGDIVKDNSINLLDVAEVIRCFNATKGSANYVEELDINRNGAINMQDIMIVHK
HFGATSSDYDAQLEEFELRRQACGRTRAPPPPPLRSGC*

His-BpCAT-C (77.08 kDa) N-Histag-Thrombin side- BpCAT-BamHI-GS-Cohesin

Gene sequence

ATGGGCAGAGCCATCATCATCATCATCACAGCAGCGGCCTGGTGCCGCGCGGCAGCCATATGGAATTCAAAAGATCTAAT
GCGATGACCAATAAGACCCTGACCACCGCGGCGGGTGCGCCGGTTGCGGACAATAACAATACCATGACCGCGGGCCCGC
GTGGCCCGGCGCTGCTGCAGGACGTTTGGTTCCTGGAGAAGCTGGCGCACTTTGATCGTGAGCGTATCCCGGAACGTGT
GGTTCACGCGAAAGGTAGCGGCGCGTATGGCACCTTCACCGTGACCCACGACATCAGCCGTTACACCCGTGCGCGTATTT
TTGCGGAAGTGGGCAAGCAAACCCCGCTGTTCCTGCGTTTTAGCACCGTTGCGGGCGAGCGTGGCGCGGCGGACGCGG
AACGTGATGTGCGTGGTTTCGCGATCAAGTTTTATACCGACGAGGGTAACTGGGATCTGGTGGGCAACAACACCCCGGTT
TTCTTTATCCGTGACCCGCTGAAATTCCCGGATTTTATTCACACCCAGAAGCGTGACCCGAAAACCAACCTGCGTAACGCG
ACCGCGGCGTGGGATTTCTGGAGCCTGAACCCGGAGAGCCTGCACCAGGTTACCATTCTGATGAGCGACCGTGGCCTGC
CGCAAAACTACCGTCAGCAACACGGTTTCGGCAGCCACACCTATAGCTTTGTGAACGACGCGGGTGAACGTTTCTACGTTA
AGTTCCACTTCAAGAGCCAGCAAGGTATTGCGTGCTATACCGATGGTGAAGCGGCGGAACTGGTGGGTCGTGACCGTGA
GAGCGCGCAGCGTGACCTGTTCCAAAACATTGAACAGGGCCAATTTCCGCGTTGGACCCTGAAGGTGCAGGTTATGCCGG
AGGCGGAAGCGGCGACCTATCACATCAACCCGTTCGACCTGACCAAGGTTTGGCCGCACGCGGATTACCCGCTGATTGAA
GTGGGTGTTCTGGAACTGAACAAAAACCCGGAAAACTATTTCGCGGAAGTGGAACAAGCGGCGTTTACCCCGGCGAACGT
GGTTCCGGGTATTGGCTTCAGCCCGGACAAAATGCTGCAGGGTCGTCTGTTTAGCTACGGCGATACCCACCGTTATCGTC
TGGGCATCAACCACCACCAAATTCCGGTTAACGCGCCGCGTTGCCCGTTCCACAGCTTTCACCGTGACGGTATGGGTCGT
GTGGATGGTAACGGTGGCGCGACCCTGAACTACGAGCCGAACAGCTTCGGCGAGTGGCGTGAAGCGAAGCATGCGGCG
GAACCGCCGCTGGCGCTGGACGGTCAGGCGGCGGATCGTTGGAACCACCGTGTTGACGAGGATTACTATAGCCAGCCGG
GTGCGCTGTTCCGTCTGATGAACGACGATCAAAAACAGCAACTGTTTGGTAACATTGGTCGTCACATGGCGGGTGTGCCG
GAGGAAATTCAGCGTCGTCAACTGGAACACTTCCGTCGTGCGGACCCGGCGTATGCGGCGGGCGTTGCGAAAGCGCTGG
GCCTGAAATTAGGATCCGGTAGCAGCGGTAGCAGCCACATGCGTGCGGACAAGGCGAGCAGCATCGAGCTGAAGTTTGA
CCGTAACAAAGGCGAGGTGGGTGACATCCTGATTGGCACCGTTCGTATCAACAACATTAAAAACTTCGCGGGTTTCCAAGT
TAATATTGTGTATGATCCGAAAGTTTTAATGGCTGTTGATCCGGAAACCGGCAAGGAATTTACCAGCAGCACTTTTCCGCCG
GGCCGCACCGTGCTGAAAAATAATGCGTATGGCCCGATTCAGATCGCGGATAACGATCCGGAAAAGGGTATCCTGAATTT
TGCGCTGGCGTATAGCTACATTGCGGGCTATAAAGAAACCGGTGTGGCGGAAGAGAGCGGTATTATCGCGAAAATTGGCT
TTAAAATTCTGCAGAAGAAAAGCACGGCGGTTAAGTTTCAAGATACCCTGAGCATGCCGGGTGCGATCAGCGGTACCCAG
CTGTTTGACTGGGATGGTGAAGTGATTACCGGCTACGAAGTTATTCAACCGGATGTGCTGAGCCTGGGCGACGAACCGTAA
G

Protein sequence:

MGSSHHHHHHSSGLVPRGSHMEFKRSNAMTNKTLTTAAGAPVADNNNTMTAGPRGPALLQDVWFLEKLAHFDRERIPERVVH
AKGSGAYGTFTVTHDISRYTRARIFAEVGKQTPLFLRFSTVAGERGAADAERDVRGFAIKFYTDEGNWDLVGNNTPVFFIRDPLK
FPDFIHTQKRDPKTNLRNATAAWDFWSLNPESLHQVTILMSDRGLPQNYRQQHGFGSHTYSFVNDAGERFYVKFHFKSQQGIA
CYTDGEAAELVGRDRESAQRDLFQNIEQGQFPRWTLKVQVMPEAEAATYHINPFDLTKVWPHADYPLIEVGVLELNKNPENYFA
EVEQAAFTPANVVPGIGFSPDKMLQGRLFSYGDTHRYRLGINHHQIPVNAPRCPFHSFHRDGMGRVDGNGGATLNYEPNSFGE
WREAKHAAEPPLALDGQAADRWNHRVDEDYYSQPGALFRLMNDDQKQQLFGNIGRHMAGVPEEIQRRQLEHFRRADPAYAA
GVAKALGLKLGSGSSGSSHMRADKASSIELKFDRNKGEVGDILIGTVRINNIKNFAGFQVNIVYDPKVLMAVDPETGKEFTSSTFP
PGRTVLKNNAYGPIQIADNDPEKGILNFALAYSYIAGYKETGVAEESGIIAKIGFKILQKKSTAVKFQDTLSMPGAISGTQLFDWDG
EVITGYEVIQPDVLSLGDEP*

D-NOX (42.2 kDa) N-Dockerin- GS-NOX-BamHI

ATGGGAGCTAGCCATATGAACAAACCGGTGATTGAAGGCTATAAAGTGAGCGGCTATATTCTGCCGGATTTTAGCTTTGAT
GCGACCGTGGCGCCGCTGGTGAAAGCGGGCTTTAAAGTGGAAATTGTGGGCACCGAACTGTATGCGGTGACCGATGCGA
ACGGCTATTTTGAAATTACCGGCGTGCCGGCGAACGCGAGCGGCTATACCCTGAAAATTAGCCGCGCGACCTATCTGGAT
CGCGTGATTGCGAACGTGGTGGTGACCGGCGATACCAGCGTGAGCACCAGCCAGGCGCCGATTCATATGTGGGTGGGC
GATATTGTGAAAGATAACAGCATTAACCTGCTGGATGTGGCGGAAGTGATTCGCTGCTTTAACGCGACCAAAGGCAGCGC
GAACTATGTGGAAGAACTGGATATTAACCGCAACGGCGCGATTAACATGCAGGATATTATGATTGTGCATAAACATTTTGGC
GCGACCAGCAGCGATTATGATGCGCAGCTGGAAGGCAGCGGCAGCGGCAGCTCTAGAAGATCTATGGAGGCGACCCTTC
CCGTTTTGGACGCGAAGACGGCGGCCCTAAAGAGGCGTTCCATCCGGCGCTACCGGAAGGACCCCGTACCCGAGGGGC
TTCTCCGGGAAATCCTCGAGGCCGCCCTCCGGGCGCCCTCGGCCTGGAACCTCCAGCCCTGGCGGATCGTGGTGGTGC
GGGACCCCGCCACCAAGCGGGCCCTGAGGGAGGCGGCCTTCGGCCAGGCCCACGTGGAGGAGGCCCCCGTGGTCCTG
GTCCTCTACGCTGACCTCGAGGACGCCCTCGCCCACCTGGACGAGGTCATCCACCCCGGGGTCCAGGGGGAAAGGCGT
GAGGCGCAGAAGCAGGCCATCCAACGGGCCTTCGCCGCCATGGGGCAAGAGGCGCGAAAGGCCTGGGCCTCCGGGCA
GAGCTACATCCTCTTGGGCTACCTCCTTCTCCTCCTGGAGGCTTATGGCCTCGGAAGCGTCCCCATGCTGGGGTTTGACC
CCGAGAGGGTGAAGGCGATCCTGGGGCTTCCTTCCCACGCCGCCATCCCCGCCCTGGTGGCCTTGGGCTACCCGGCGG
AGGAGGGCTACCCCTCCTACCGCCTGCCCTTGGAGCGGGTGGTCCTCTGGCGCGGATCCTGA

Protein sequence:

MGASHMNKPVIEGYKVSGYILPDFSFDATVAPLVKAGFKVEIVGTELYAVTDANGYFEITGVPANASGYTLKISRATYLDRVIANVV
VTGDTSVSTSQAPIHMWVGDIVKDNSINLLDVAEVIRCFNATKGSANYVEELDINRNGAINMQDIMIVHKHFGATSSDYDAQLEGS
GSGSSRRSMEATLPVLDAKTAALKRRSIRRYRKDPVPEGLLREILEAALRAPSAWNLQPWRIVVVRDPATKRALREAAFGQAHV
EEAPVVLVLYADLEDALAHLDEVIHPGVQGERREAQKQAIQRAFAAMGQEARKAWASGQSYILLGYLLLLLEAYGLGSVPMLGF
DPERVKAILGLPSHAAIPALVALGYPAEEGYPSYRLPLERVVLWRGS*

The initial and stop codons are underlined in all genes. Coh: Cohesin domain type II from *Clostridrium thermocellum* and Doc: Dockerin domain type II form *Clostridium thermocellum* (PDB ID 2B59). BpCAT: Catalase from *Bordetella pertussis*. NOX: NADH oxidase from *Thermus thermophilus* (PDB ID 1NOX).Restriction sites and amino acids are encoded within the protein primary sequences which are highlighted in blue.

7.2 Figures

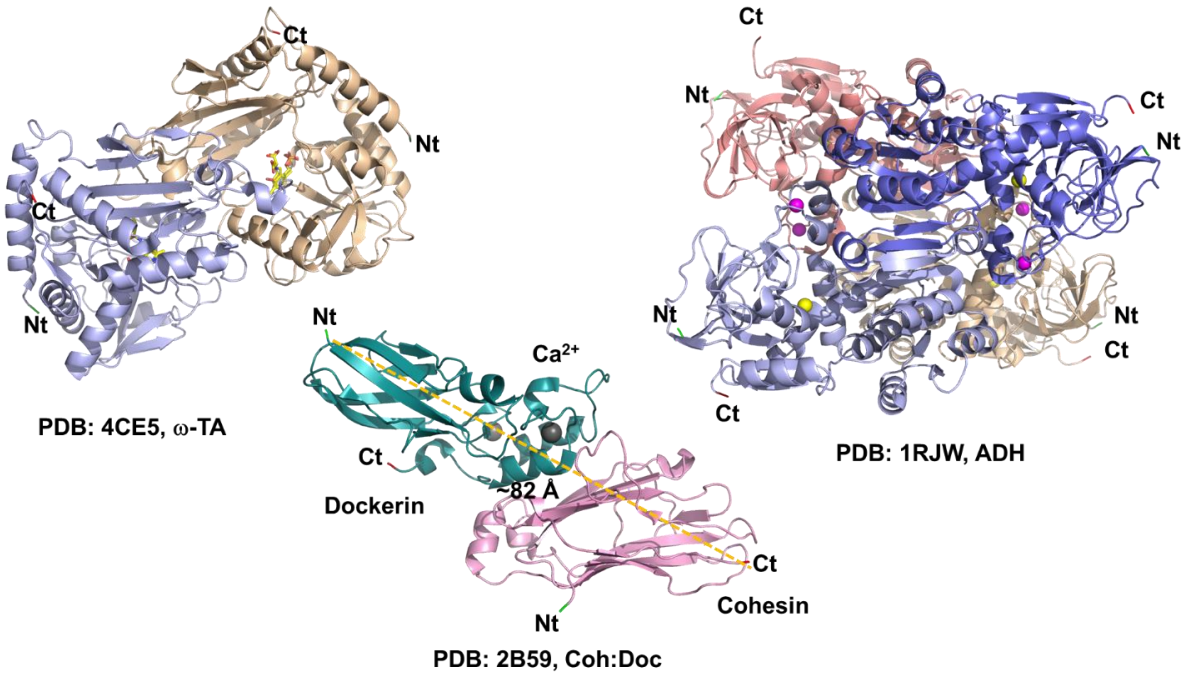

Figure A 1: Crystallographic structures of the enzymes and the cohesin-dockerin pairs

Depicts the structures of dimeric ω-TA from Aspergillus terreus, tetrameric ADH from Bacillus stearothermophilus and the cohesin-dockerin complex of Clostridium thermocellum. The transaminase is forming a stable dimer with interphase residues contributing to the enzyme function (PLP co-factor and ligand in active site is shown). Likewise, ADH is forming a stable tetramer of two functional dimers (dimer 1: light and dark blue subunits & dimer 2: salmon and wheat subunits) with structural (pink) and catalytic (yellow) Zn^{2+} atoms highlighted. Cohesin and dockerin are forming a complex with bound Ca^{2+} atoms shown in dark gray. N- and C-termini are labelled with Nt and Ct, respectively. Dashed yellow line measures the distance between the N- and C-termini for comparison purposes (1Å = 0.1 nm).